High Order Models in Diffusion MRI and Applications

Aurobrata Ghosh

PhD THESIS

prepared at
INRIA Sophia-Antipolis Méditerranée

and presented at the
University of Nice-Sophia Antipolis
Graduate School of Information and Communication Sciences

A dissertation submitted in partial fulfillment
of the requirements for the degree of

DOCTOR OF SCIENCE
Specialized in Control, Signal and Image Processing

High Order Models in Diffusion MRI and Applications

Aurobrata GHOSH

PhD thesis supervised by Dr. Rachid Deriche

Reviewers	Dr. Peter J Basser	STBB, NICHD, Bethesda, USA
	Dr. Baba C Vemuri	University of Florida, Gainesville, USA
Examiners	Dr. Habib Benali	INSERM / Pitié-Salpêtrière, Paris, France
	Dr. Pierre Comon	I3S / CNRS / University of Nice, France
	Dr. Rachid Deriche	INRIA Sophia-Antipolis Méditerranée, France
	Dr. Nikos Paragios	ECP / INRIA Saclay Ile-de-France, France

UNIVERSITÉ NICE-SOPHIA ANTIPOLIS - UFR Sciences

École Doctorale STIC
(Sciences et Technologies de l'Information et de la Communication)

THÈSE

pour obtenir le titre de
DOCTEUR EN SCIENCES
de l'UNIVERSITÉ de Nice-Sophia Antipolis
Discipline: Automatique, Traitement du Signal et des Images

présentée et soutenue par

Aurobrata GHOSH

Modèles d'ordre supérieur en IRM de Diffusion et applications

Thèse dirigée par Dr. Rachid DERICHE

Date de soutenance le 11 avril 2011

Composition du jury:

Rapporteurs	Dr. Peter J Basser	STBB, NICHD, Bethesda, USA
	Dr. Baba C Vemuri	University of Florida, Gainesville, USA
Examinateurs	Dr. Habib Benali	INSERM / Pitié-Salpêtrière, Paris, France
	Dr. Pierre Comon	I3S / CNRS / University of Nice, France
	Dr. Rachid Deriche	INRIA Sophia-Antipolis Méditerranée, France
	Dr. Nikos Paragios	ECP / INRIA Saclay Ile-de-France, France

Dedicated to The Mother and Sri Aurobindo.

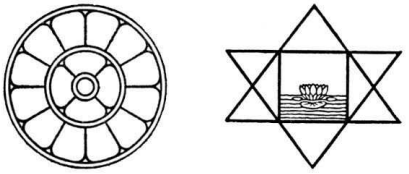

Abstract

Diffusion MRI (dMRI) is a powerful tool for inferring the architecture of the cerebral white matter in-vivo and non-invasively. Based on model assumptions, reconstructed diffusion functions can provide sub-voxel resolution microstructural information of the white matter superior to the resolution of the raw diffusion images. In the commonly used Diffusion Tensor Imaging (DTI) the diffusion function is modelled by a second order tensor. However, since it is limited in regions with fiber inhomogeneity, recent research has produced numerous reconstruction techniques that infer the fiber layout in the underlying white matter with greater accuracy. These techniques represent the diffusion function by complex shaped spherical functions. In this thesis we address two problems – first we examine one such reconstruction technique closely, and second we propose a generic way of extracting geometric features from a wide class of reconstructed diffusion spherical functions to characterize the white matter.

In this thesis we make a number of contributions. First we examine, Generalized DTI, which uses Cartesian tensors of order higher than two to model the diffusion profile (the diffusion coefficient along multiple spatial directions) in regions with fiber inhomogeneity. We propose two independent methods for estimating fourth order diffusion tensors with a positive diffusion profile, which is an important consideration since negative diffusion is non-physical. Then we propose an analytical approximation for estimating the diffusion propagator (the probability density function describing the diffusion process) from tensors of order higher than two, which allows us to measure both a modified diffusion profile and the propagator, which contain complementary information, from regions with fiber inhomogeneity. The analytical formulation allows us to efficiently estimate the propagator which is needed to infer the underlying fiber layout. Finally we propose a generic method for extracting the maxima from a wide class of diffusion spherical functions (functions on a sphere), since these indicate the fiber layout in the white matter. We also extract other geometric features from these complex shaped spherical diffusion functions to propose new biomarkers for characterizing the white matter. To illustrate the maxima-extraction, we also propose extensions to well known deterministic tractography methods where we apply maxima extraction to complex shaped orientation distribution functions (ODFs) to trace fibers through regions with fiber crossings.

Résumé

Cette thèse traite du problème de la modélisation du signal en IRM de Diffusion et à son exploitation pour caractériser au mieux le réseau de fibres de la matière blanche cérébrale. Nous examinons d'abord l'IRM du Tenseur de Diffusion Généralisé, qui utilise des tenseurs Cartésiens d'ordre supérieur à deux pour modéliser le signal de Diffusion. Nous proposons deux méthodes indépendantes pour estimer des tenseurs d'ordre 4 avec un profil de diffusion positive. Ensuite, nous proposons une approximation analytique du propagateur de diffusion de tenseurs d'ordre supérieur à deux, ce qui nous permet de mesurer à la fois un profile de diffusion modifié et le propagateur, qui contiennent des informations complémentaires. Finalement, nous proposons une méthode permettant d'extraire les maxima d'une large classe de fonctions de diffusion sphériques, que l'on peut obtenir à partir du propagateur reconstruit. Ces fonctions sont utilisées pour nous indiquer finement les directions des fibres dans la substance blanche. Nous analysons et extrayons les caractéristiques géométriques de ces fonctions sphériques et exploitons ces résultats pour proposer de nouveaux biomarqueurs pour la caractérisation de la substance blanche cérébrale. Enfin, nous exploitons l'extraction des maxima de ces fonctions pour généraliser deux méthodes de tractographie déterministe afin de permettre la gestion des singularités comme celles qui correspondent aux fibres qui se croisent.

Acknowledgments

First and foremost I would like to express my heartfelt thanks to my supervisor Dr. Rachid Deriche. I am grateful to him for his patient and endless efforts in carving out a semblance of a researcher in me. His calm and balanced leadership skills have always inspired me. I would like to thank Dr. Olivier Faugeras who in the days of Odyssée had received me in his team. Needless to say I would also like to thank the other permanent researchers of the Odyssée/Athena project-teams – Maureen, Théo, Pierre and Bruno. Two other people who have constantly made it possible to live the complex administrative part of the PhD life smoothly without making their presences ever being felt – almost being invisible themselves, have also my gratitude. They are our secretaries Marie-Cécile and Claire. I would like to also acknowledge my institute INRIA, Sophia Antipolis – Méditerranée, France, for hosting me in an environment with excellent work facilities and a charming campus. My PhD work was partially funded by the Association France Parkinson, and by the French National Research Agency (ANR, Neurodegenerative and Psychiatric Diseases).

I have been indeed fortunate to have had the opportunity to work with a number of eminent collaborators from both abroad and inside INRIA. Dr. Peter Basser, who has almost been a second mentor to me, Evren and Guan from the NIH, USA, have all three spent numerous hours with me explaining to me the intricate details of the physics of diffusion MRI. This has been crucial to my understanding of the core subject matter of this thesis. It was great to have been able to work together with Drs. Bernard Mourrain and Pierre Comon, and Elias of the INRIA project-team GALAAD. I would like to thank the reviewers and the members of the jury of my PhD for their detailed and selfless efforts.

I have had excellent colleagues at Odyssée/Athena whom I'd like to acknowledge too. Maxime who was my constant guide and helper when I had just arrived and who helped me wade through complex and endless codes, thank you for helping me out and for the great discussions we had together. I would like to thank Demian, with whom I finally had the opportunity to collaborate and whose incredible energy is an inspiration to anyone! Helping out Jian and learning from the discussions with him has been an invigorating and dynamic experience. I hope they can happen again. I would also like to acknowledge Emmanuel, Sylvain, Anne-Charlotte, Joan, Maria-Jose, Greg, James and the rest of the Odyssée/Athena family!

Then there were those who were both colleagues and friends, who moved in and out of both my professional life and my personal life – close friends who have made living here so far from home such a wonderful experience. I would like to mention the ever smiling “legend” Adan, Horacio, Émilien, Danièle (and now their “petit Olivou”), Émil, Dana, Juan-Carlos, Diana and Manolo. There is my “tea-partner” and “political-advisor” Arijit and of course Dr. Kaushik Majumdar or simply Kaushik-da who has been a constant help. Steady links to home, Pondicherry, were provided by Samarth and Ahuti in Paris, Champak with his little family in the idyllic Cevennes and now Abhinav right here. There are also my good friends and ex-flatmates Manuel, Brice and Henri. One of the best things that happened to me during my PhD life here was during the final four months when I was writing my thesis. I moved into the FJT and met a wonderful group of friends who looked after me during a difficult phase. They were Dheeraj, Sadish, Manoj, Christian, Sudarshan, Anne, Franzi and of course Ra·mo·na. Just for laughs – even my gmail account recognizes them!

A PhD is not a moment’s effort in time. It is a process of growth that spans perhaps my entire life. Although it is not possible to acknowledge them individually here, I would like to remember and thank all my teachers who nudged me along this entire process and have helped me grow until this point.

Last but most importantly I would like to mention my parents. In the crazy process of life although I have diffused further and further away from home and my source and even though my return to origin probability has dipped towards null at times, my parents have been my constant reference. In a world with ever shifting and changing coordinates they have held my foundations steady and have shown me again and again that there is more to life than simply its professional and social aspects. It was their wish that I dedicate this thesis to The Mother and Sri Aurobindo. Thank you.

Sincerely,
Auro

Contents

CHAPTER 1

INTRODUCTION

CONTEXT

Diffusion MRI (dMRI) with its ability to measure the translational diffusion of water molecules is a powerful tool for inferring the architecture of the cerebral white matter in-vivo and non-invasively. Diffusion weighted images (DWIs) measure the diffusion of water molecules along particular directions and dMRI reconstruction algorithms incorporate this partial directional information into integrated diffusion functions. As the length scale of the Brownian motion of water molecules contained in the brain is comparable to the scale of the coherent structures of the axons constituting the white matter, diffusion is a sensitive probe of the white matter's microstructure and reconstructed diffusion functions can therefore reveal microstructural details superior to the resolution of the raw DWIs. However, since the current resolution achieved by DWIs is orders of magnitude coarser than the true scale of an axon, the reconstructed diffusion functions are affected by partial voluming effects from sub-voxel resolution axonal microstructures and can at best represent the dominant axon fiber structure. Nonetheless, where invasive methods such as dissection, injection of tracers and indirect observation of changes in response due to sustained injuries or pathologies used to be the only way of studying the brain in the past, today dMRI from its ability to quantify the anisotropic diffusion of water molecules presents a unique non-invasive, although indirect, perception into the fibrous cerebral white matter.

Diffusion Tensor Imaging (DTI) is the most commonly used dMRI reconstruction technique, where the reconstructed diffusion function is represented by an ellipsoid parameterized by a second order Cartesian tensor, called the diffusion tensor. DTI's popularity can be attributed to its simple mathematical formulation and acquisition requirements and to its elegant physical interpretation of its diffusion function for inferring the microstructure of the cerebral white matter. However, due to its assumption that the underlying microstructure is homogeneous, DTI is inaccurate in regions with microstructural heterogeneity.

To overcome this limitation of DTI, other dMRI reconstruction techniques have been proposed recently, which attempt to infer heterogeneous white matter microstructures with greater accuracy. These "high order models" stem from the mathematical and physical models of the diffusion process, namely the phenomenological approach of Fick and the random walk model proposed by Einstein. These have given rise to methods that estimate the apparent diffusion coefficient (ADC) with greater accuracy and the q-space formalism, which relates the diffusion signal to the diffusion propagator or the probability density function by a Fourier Transform. While the high order ADC models measure the inherent diffusion coefficient and capture the effects of microstructural heterogeneity in the q-space, the high order diffusion propagator models capture these effects in the real space.

In this thesis, we address a number of important problems related to these high order dMRI reconstruction techniques. The starting point of this thesis is the Generalized DTI (GDTI) reconstruction approach, which uses Cartesian tensors of order higher than two (higher order tensors: HOTs) to model the ADC in regions with microstructural heterogeneity with greater accuracy than DTI. We study the problem of estimating HOTs with positive diffusion profiles or ADCs, since negative diffusion is non-physical. We show the relevance of the problem and the usefulness of the positivity constraint from the improved results of two independent solutions for estimating HOTs with positive diffusion profiles.

Next we address the important problem of estimating the high order diffusion propagator from HOTs, since the ADC represents the effects of microstructural heterogeneity in the q-space. To infer the microstructure of the cerebral white matter, it is therefore necessary to estimate the diffusion propagator, which quantifies the effects of the microstructural heterogeneity in the real space. We propose an analytical approximation of the propagator from a modified GDTI model HOTs, and we show that it is possible to infer the underlying microstructure, such as axon fiber directions, from the angular structure of the approximations.

Finally, we address the pertinent problem of extracting the complex information recovered by the high order models, which is contained in their reconstructed diffusion functions. This is a significant problem since geometric features of a wide class of diffusion functions have physical interpretations, such as for inferring the microstructure, or for characterizing the anisotropy of the cerebral white matter. We propose a complete method for the exact detection of all the maxima of a wide class of spherical diffusion functions, which we show can be used for correctly inferring the axon fiber directions and therefore also for tracing fibers. We also propose a sub-voxel resolution anisotropy measure for this class of spherical diffusion functions, to characterize the cerebral white matter in a detail commensurate with the information revealed by the high order models.

The underlying mathematical framework connecting the contributions of this thesis is the symmetric high order Cartesian tensor. The spherical projection of the Cartesian tensor or the projection of the tensor's multilinear form on a sphere, provides a substitute framework for the Spherical Harmonic basis, which has come into almost standard use in current high order dMRI reconstruction techniques. Therefore, this thesis with its predisposition towards Cartesian tensors, provides a significant alternate outlook and approach through Cartesian coordinates to the popularly used spherical coordinates in dMRI. This is an important consideration, since just as the spherical coordinates simplify the computation of angular characteristics of the underlying white matter, such as the angular moments of the diffusion propagator, which reveal the axon fiber directions, the Cartesian coordinates simplify the computation of Cartesian characteristics, such as the Cartesian moments or cumulants of the diffusion propagator, which can be used to quantify the anisotropy of the white matter.

OUTLINE

This thesis begins by exploring the physical context of the problem – the brain. Then it presents the principles of the non-invasive modality of dMRI. Finally it presents the problems related to high order dMRI reconstruction techniques that we have addressed and our solutions. This thesis contains the following chapters. An illustration of the flow of the chapters is presented in Fig-1.1.

Chapter-2 The introductory chapter is dedicated to *the brain*, which forms the physical basis of our problem of study. It presents an overview of the brain's anatomy, relevant microscopic neural tissue, and important macroscopic cerebral tissue organization, namely the major white matter pathways. These are central for understanding the diffusion of water molecules in the brain, and for understanding the usefulness of dMRI in studying the brain.

Chapter-3 This chapter presents the fundamentals of *nuclear magnetic resonance* (NMR), *diffusion* NMR (dNMR) and reviews a number of reconstruction techniques in dMRI that are used to infer the microstructure of the cerebral white matter. A major contribution of this chapter is in its observation of how the ways of modelling diffusion has influenced the reconstruction techniques in dMRI. This chapter presents the two ways of modelling diffusion, namely Fick's phenomenological approach and Einstein's random walk approach, and develops on these to show how they lead to the two ways for modelling the dNMR signal, namely the Stejskal-Tanner formulation and the q-space formalism. These two ways of modelling the dNMR signal play pivotal roles in dMRI, since almost all dMRI reconstruction techniques employ either of these signal models, or both, for reconstructing a diffusion function from the signal to infer the microstructure of the white matter. The dMRI reconstruction techniques

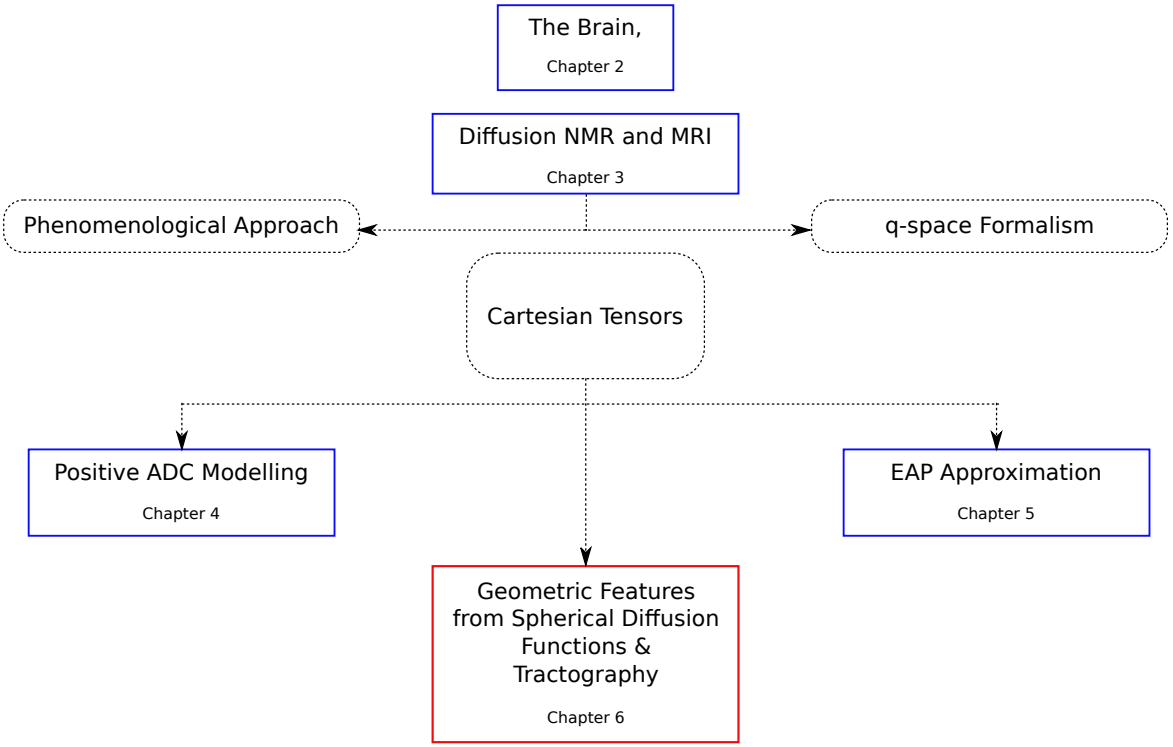

Figure 1.1: Organization of the thesis.

that are reviewed in the final part of this chapter are therefore presented under this light. Finally the review of techniques reveals the current trend towards spherical coordinates and the Spherical Harmonic basis, which motivates the work in this thesis with an alternate Cartesian coordinate approach to dMRI.

Chapter-4 This chapter addresses the problem of estimating a 4th order Cartesian tensor from the GDTI model with a positive diffusion profile since negative diffusion is non-physical. We propose two independent methods, namely a Riemannian approach based on the algebra of 4th order tensors, and a polynomial parameterization approach based on Hilbert's theorem on ternary quartics (TQ). We show that the Riemannian approach guarantees positive definite diffusion but solves a more constrained problem than implied by the GDTI model, while the TQ approach solves the correct problem but guarantees only non-negativity. However, in practice the results of the Riemannian approach are similar to the TQ approach and due to numerical computations we never find zero diffusion from the TQ approach. The relevance of the problem is motivated from the improved results.

Chapter-5 This chapter addresses the problem of estimating the higher order diffusion propagator from HOTs. Although the GDTI HOTs estimate the ADC with greater accuracy than DTI, since the ADC describes the effects of microstructural heterogeneity in the signal domain or the q-space, it is necessary to compute the dif-

fusion propagator, which describes the effects of the microstructural heterogeneity in the real space, to infer the geometry of the underlying microstructure. Therefore, while the GDTI model is based on the Stejskal-Tanner formulation of the signal, in this chapter we also employ the q-space formalism to leverage the Fourier Transform relationship between the diffusion signal and the diffusion propagator, and we propose an analytical approximation of the diffusion propagator from a modified GDTI model using 4th order tensors. We show that the approximation converges well to the true diffusion propagator and since it is analytical it is fast and can be implemented efficiently. From the results, we show that it is possible to infer the microstructure from the angular structure of the approximate diffusion propagator.

Chapter-6 In this chapter we address the problem of extracting the geometric information recovered by the higher order models. In DTI the diffusion information is represented by a diffusion ellipsoid or a 2nd order tensor, where it is straightforward to interpret its geometry from the eigen-decomposition of the tensor. However, in the higher order models, the diffusion information is generally represented by a generic function on the sphere. We propose a complete method for detecting the maxima of a wide class of spherical functions, since the maxima often represent underlying fiber directions. We show, therefore that this method can be used for tracing fibers through regions with fiber crossings by extending the standard Streamline tractography and also the Tensorline tractography to work with generic spherical diffusion functions. We also extract further geometric features from these spherical functions and propose a sub-voxel resolution anisotropy measure to characterize the cerebral white matter.

Chapter-7 The last chapter concludes the thesis by summarizing the problems we have addressed and their solutions we have proposed. In this chapter we also present perspectives and directions for developing future research, namely in further exploring the problems that can be addressed and solved by the Cartesian coordinate approach to dMRI.

CHAPTER 2

THE BRAIN

Contents

2.1 Introduction

The seat of consciousness and intelligence, the brain has tenaciously desisted generations of probing investigators, jealously guarding its secrets over centuries from inquisitive minds. Only bit by bit has it revealed the mysteries on "how it functions", and "how it is constructed". Twofold are the difficulties in investigating the brain – its sheer complexity, its sophisticated design, and the permanent damage that a direct investigation would cause to the control-center regulating the functioning of the body and hosting the perception of consciousness, resulting almost certainly in an irreversible modification of cognition or even in the death of the subject.

Our current knowledge about the brain is the result of enduring and accumulated research, primarily from dissections of the post-mortem brain – both human and animal and from experiments on animal brains, since only in these cases are invasive investigations possible or ethically accepted. A great deal about the functional characteristics of the brain has also been learned by observing animals and humans who have sustained injuries to their brains, either through accidents or diseases. This is changing with the advent of modern non-invasive and in-vivo imaging techniques of the human body such as Magnetic Resonance Imaging (MRI). While Functional MRI (fMRI), a specialized modality of MRI, addresses the brain on "how it functions", Diffusion MRI (dMRI), another specialized modality of MRI and the central topic of this thesis, is well suited for addressing "how it is connected".

This chapter is dedicated to a quick perusal of the brain – its general structure and organization, the tissues constituting it, and in highlight, it's major neuronal pathways interconnecting its various regions. This chapter aims to provide a context for understanding the general physical problem dMRI attempts to solve. The contents of this chapter have been collected from the following various sources [1, 2, 3, 4, 5, 6, 7, 8, 9, 10], and from the Internet.

2.2 The Nervous System

The role of the human nervous system is to coordinate the functions of the body, both basic or unconscious, and intricate and deliberate. It gathers information on the internal and external environment from its sensory receptors, integrates the information to determine the appropriate response, and sends out signals to muscles and glands to actuate the response. At the most fundamental level, the nervous system propagates signals from one cell to others. This is done chiefly in two ways. Nerve cells can either transmit electrochemical waves or action potentials along wire-like axons interconnecting them to send out signals to specific target cells from one point to another, or they can engage the endocrine system to activate glands that release hormones into the internal circulation that diffuse to distant cells like a broadcast system. At the global level, the nervous system not only regulates voluntary and in-

voluntary bodily functions such as breathing, the beating of the heart, blood pressure, body temperature, movement of muscles and the limbs, but also makes possible more advanced and elaborate modes of perception and communication such as awareness, emotions, languages, ideas and abstraction of concepts, transmission of cultures and other expressions of cognition, behaviour and features of society.

The nervous system is subdivided anatomically into the *central nervous system* (CNS) and the *peripheral nervous system* (PNS), and functionally into the *somatic nervous system* (SNS) and the *autonomic nervous system* (ANS). The CNS is comprised of the brain and the spinal cord and is responsible for all the central processing. The PNS is an extension of the CNS, and consists of cranial and spinal nerves emerging from the brain and the spinal cord respectively, that connect the CNS to sensory receptors, muscles and glands. Functionally the SNS is comprised of all the structures of the CNS and the PNS that convey sensory or *afferent* signals consciously or unconsciously from extremities to the CNS such as vision, pain, touch, muscle tone, etc., and those that convey motor control or *efferent* signals from the CNS to voluntary or striated muscles. The ANS on the other hand is comprised of structures of the CNS and the PNS that convey afferent input from internal organs to the CNS, and those that convey efferent signals from the CNS to involuntary or smooth muscles, such as the cardiac muscles, and glands.

2.2.1 The Brain: Anatomy

The brain is the primary building block of the nervous system and its central processing unit. The adult human brain on an average weighs 1500g. It is a soft and delicate organ that is encased within the thick bones of the cranium and is wrapped in three layers of membranes known as the *meninges*. The brain floats in the *cerebrospinal fluid* (CSF), a transparent colourless fluid, which also fills the open chambers in the brain or the ventricular system, and spaces in and around the brain. The CSF brings nutrients to the brain, removes wastes, provides an immunological protection, and supports the brain mechanically through buoyancy. It acts as a "water-jacket" or a "shock-absorber" cushioning the brain against sudden jolts and head movements. The buoyancy also reduces the weight of the brain sixty-fold to about 25g, thus protecting its soft tissue from being crushed under its own weight.

Described simply, the brain is anatomically subdivided into the *cerebrum*, the *brainstem*, and the *cerebellum*. The cerebrum, the top-most part of the brain, is constituted of two large lateral hemispheres known as the *cerebral hemispheres*, and the *diencephalon*. The surface of the cerebral hemispheres is constituted of grey matter and is topographically highly folded or wrinkled and is marked by the formation of slit-like fissures or valleys known as *sulci* and raised ridges between these fissures known as *gyri*. The mid-line or the *longitudinal fissure* separates the two hemispheres. The

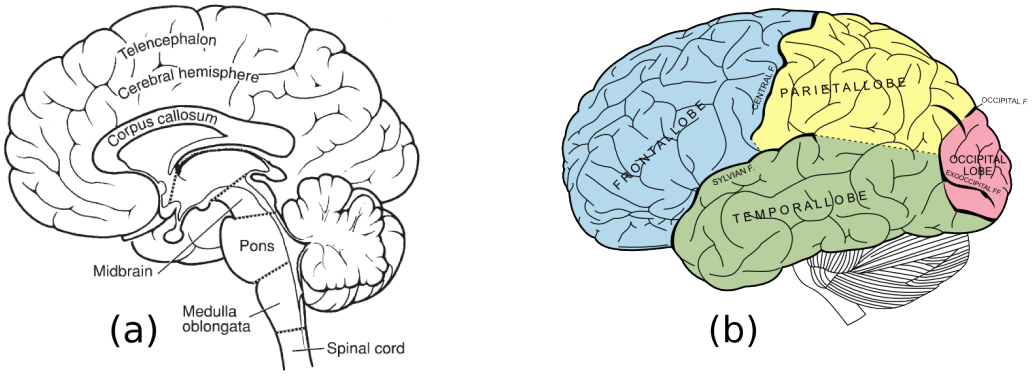

Figure 2.1: (a) The divisions of the brain, adapted from [7]. (b) The four major lobes of the cerebral cortex [6].

cerebral hemispheres are each divided into four lobes roughly separated by important sulci. These are the *frontal lobe*, the *parietal lobe*, the *occipital lobe*, and the *temporal lobe*. The frontal lobe is involved in high level thinking, planning, decision-making, and execution of movements. The parietal lobe is important in sensory perceptions such as touch and pressure, and also helps in spatial orientation and information processing. The occipital lobe is the visual centre of the brain and processes the information from the eyes. The temporal plays a key role in auditory processing and the storing of memory.

The diencephalon is mainly constituted by the *thalamus* and the *hypothalamus*, which are deep brain structures located just below the cerebral hemispheres and above the midbrain which is a part of the brainstem. The thalamus is a crucial centre for integrating and relaying motor and sensory information to the cerebral hemispheres for higher processing. It is critical for cognition and awareness. The hypothalamus regulates functions such as hunger, thirst, pain, and pleasure. One of its most important functions is to link the CNS to the endocrine system via the pituitary gland. Its influence is widespread and is even involved with emotions and behavior.

The brainstem is the bottom-most part of the brain and connects the brain to the spinal cord. It has three major parts – the *midbrain*, the *pons*, and the *medulla oblongata*. The brainstem regulates the most basic functions of the body such as consciousness, the sleep-wake cycle, and respiratory and cardiovascular control.

The cerebellum is located at the back of the head, between the cerebrum and the brainstem, behind the medulla and the pons. Its role is in controlling balance, posture, storing learned movements, and in synchronizing contractions of muscles to smooth out responses by regulating muscle tensions.

Functionally speaking, the top-most part of the brain is the most complex and has the greatest influence on conscious action. Moving lower into the brain, the parts

become increasingly primitive and are responsible for more basic functions that require less conscious control. However, all these parts have to intercommunicate to coordinate their actions for the correct overall functional responses. This communication is possible due to a network of connectivities with highly organized structures that constitute the so called white matter of the brain. Inferring the structure of this white matter non-invasively is the central problem that dMRI attempts to resolve.

2.2.2 Building Blocks: The Neuron

At a microscopic scale the brain is a network of neurons containing on an average 100 billion (10^{11}) neurons, each connected to about 1000 other neurons, totalling approximately to 100 trillion (10^{14}) synaptic connections, wired together by 150,000 – 180,000 km of nerve fibers with diameters in the range of 0.3μm – 10μm. These humongous numbers can be fully comprehended when compared to other similarly humongous numbers. It is estimated (very roughly) that the number of atoms in the

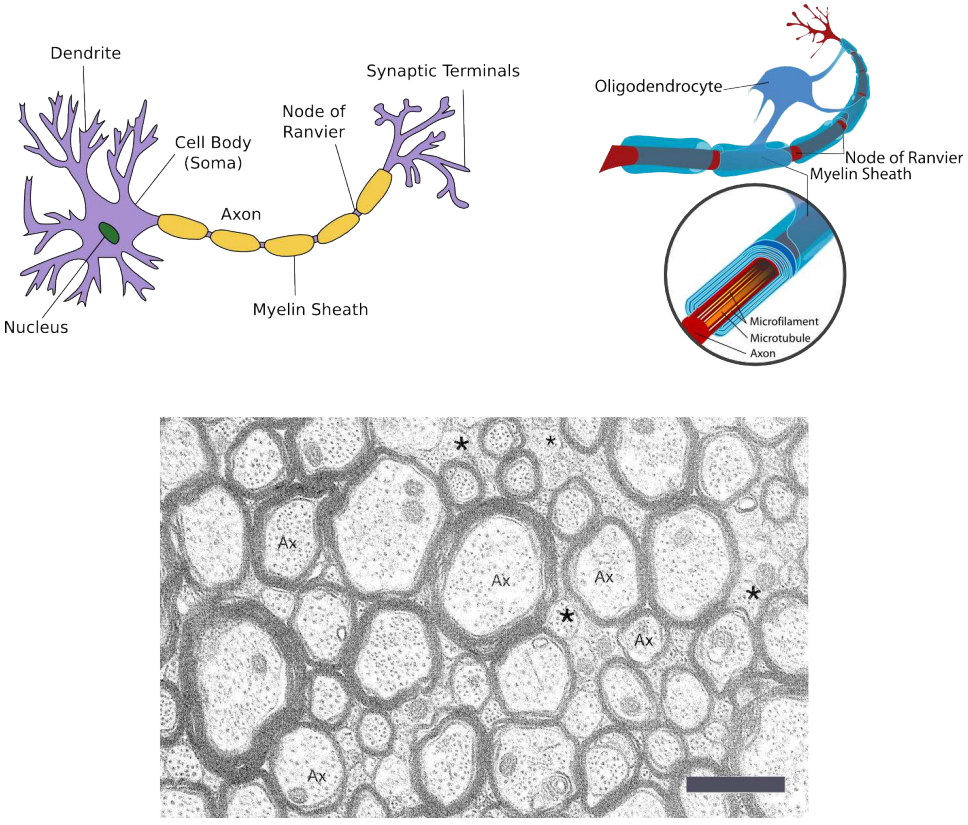

Figure 2.2: Top left: the neuron. Adapted from Wikipedia (Neuron). Top right: an oligodendrocyte creating myelin sheath to wrap the axon. Adapted from Wikipedia (Oligodendrocyte). Bottom: Electron-micrograph of axons from the Corpus Callosum. Cross section view. Myelin sheaths appear as dark bands around paler axons. Ax: axon, *: small axons that aren't myelinated, scale-bar: 1μm. Adapted from [5].

observable universe is of the order of 10^{80}, the number of stars in the observable universe is of the order of 10^{20}, and the number of stars in our galaxy, the Milky Way, is of the order of 10^{11}. Indeed, with the number of neurons comparable to the number of stars in our galaxy, interconnected by microscopic wiring with a total length of a hundred thousand kilometers, the brain is highly a complex and sophisticated organ.

The *neuron* is an electrically excitable cell capable of processing and transmitting information by electrochemical signalling. It is the fundamental processing unit of the brain. The brain is primarily constituted of neurons and glial cells which support and maintain neurons. The neurons have a cell body containing a nucleus, *dendrites*, which are short filaments attached to the body that branch out forming a tree-like structure, and a single long *axon*, a cable-like fiber extending from the neuronal body and ending in branched out synaptic terminals. The dendrites receive electrochemical stimuli from adjacent neurons via the synaptic terminals of their axons, and act as input sources for the neuronal cell body. The cell body processes this information and is then capable of retransmitting a signal via the axon. The signal travels along the axon and is transmitted via synapses at its terminals to dendrites of adjacent and connected neurons.

Axons extend over distances that can be exceedingly long when compared to their diameter of a few microns. In the human brain this can reach up to a meter, which is a difference of six orders of magnitude. However, bare axons are poor transmitters of electrochemical signals due to leakage. Special glial cells called *oligodendrocytes* wrap the axons in a fatty substance known as *myelin* to considerably improve both the efficiency and the speed of the transmission. The insulation or myelin sheaths are created in regular lengths and are separated by tiny gaps known as nodes of Ranvier. Such axons are known as myelinated axons. A loss of myelin or demyelination disrupts signal transmission and can result in functional pathologies of the brain. Myelin, which is whitish in colour, imparts a whitish tinge to myelinated axons.

Neurons differ from other cells by the fact that they don't replicate themselves. Therefore, not only do injuries to the brain and degenerative pathologies result in a permanent loss of affected neurons, but even the process of aging results in a progressive loss of neurons and axons. Between the age of twenty years and ninety years there is a loss of 9.5% of the total neurons and a loss of 40 – 50% of the total length of all the myelinated axons.

dMRI can non-invasively infer the highly organized structures formed by axons traversing the brain interconnecting its various regions. Therefore, dMRI is a suitable tool for studying the demyelination and degeneration of axons due to injuries, pathologies and aging.

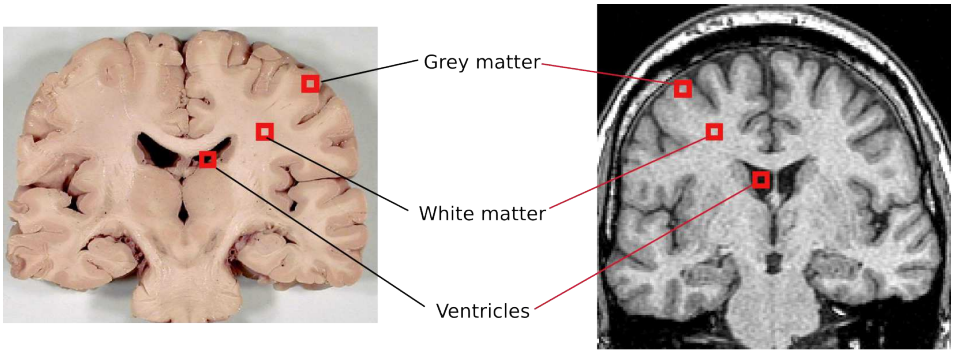

Figure 2.3: Grey & white matter and the ventricles in a coronal slice. (a) adapted from www.healcentral.org. (b) T1 image adapted from the Whole Brain Atlas.

2.2.3 Grey Matter

At a macroscopic scale the brain is made up of *grey matter* and *white matter*. Grey matter is constituted of neuron cell-bodies, dendrites, synapses, and glial cells. It is grey brown in colour due to the capillary blood vessels and the neuronal cell-bodies. White matter is constituted of myelinated axons and oligodendrocytes. Since grey matter is constituted mainly of neuronal cells, grey matter regions are the processing centres of the brain. The topographies of both grey matter and white matter are highly organized.

The largest, most important and most complex formation of grey matter is the surface of the cerebral hemispheres known as the *cerebral cortex*. The extensive wrinkling or folding of this surface increases the area of the cortex threefold and about two thirds of the grey matter of the cerebral cortex is buried in the sulci of the cerebral hemispheres. The cerebral cortex handles the most complex or highest processes of the brain. Evolutionarily speaking it is the most recently developed part of the brain, and its topographic complexity has increased over time. For example in rodents and small mammals the cerebral cortex is smooth, and it develops sulci in primates and larger mammals.

Other important regions of grey matter include the *basal ganglia* which are located deep within the cerebrum, and connected to the cerebral cortex and the thalamus. The various grey matter nuclei of the basal ganglia – the *caudate nucleus*, *putamen*, *globus pallidus*, and *substantia nigra*, are involved in voluntary motor control, eye movements, cognition and emotions. There exist other important grey matter regions such as nuclei in the thalamus and the hypothalamus, the surface of the cerebellum or the cerebellar cortex, etc.

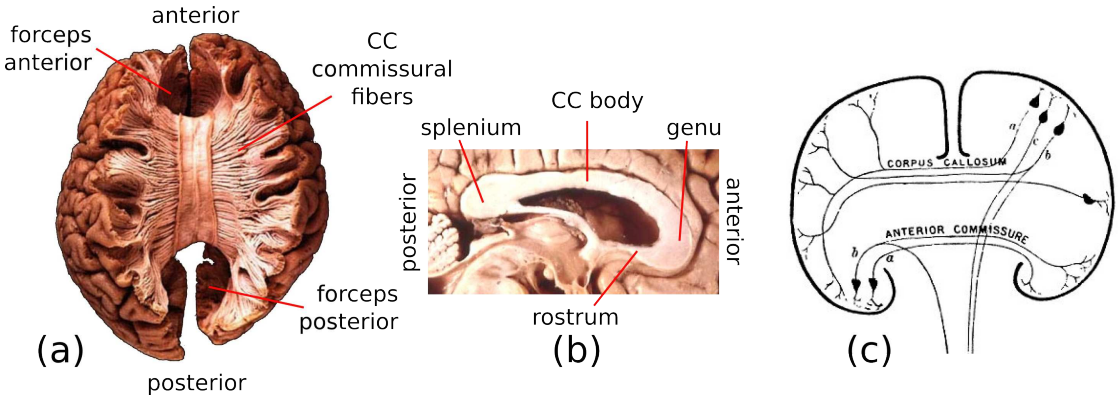

Figure 2.4: Commissural fibers. (a) top view of the Corpus Callosum (CC), adapted from [11]. (b) Divisions of the CC, adapted from www.healcentral.org. (c) The CC and the anterior commissure, adapted from www.humannervoussystem.info.

2.2.4 White Matter

While the grey matter is made up of the neuronal cell bodies, the myelinated axons originating from these neurons constitute the white matter, which gets its colour and name from the colour of the myelin sheaths. The myelinated axons interconnect various grey matter structures, and traverse the brain in highly organized conglomerations or pathways. While the surface of the cerebral hemispheres is the cerebral cortex, a grey matter structure, much of the volume beneath is formed by these white matter pathways interconnecting different regions of the cortex, and connecting the cortex to other grey matter structures such as deep brain nuclei, the cerebellum, and the spinal cord. These pathways give white matter a coherent and fibrous quality from the microscopic to the macroscopic scale. This forms the physical basis of dMRI's usefulness and suitability for studying the connectivity of the brain.

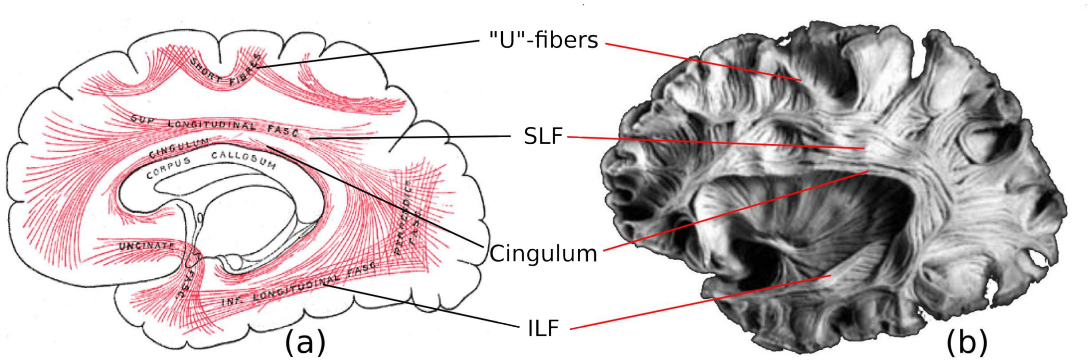

Figure 2.5: Short and long association fibers. Short or "U"-fibers, the cingulum, the superior longitudinal fasciculus (SLF), and the inferior longitudinal fasciculus (ILF). (a) Adapted from [6]. (b) Adapted from [11].

The abundantly present water molecules in the white matter diffuse in a very particular fashion within this medium. The coherent fibrous structure of white matter hinders diffusion perpendicular to its filaments and fibers, while the diffusion parallel to these structures is left relatively unaffected. In other words as water molecules diffuse in white matter due to thermally driven Brownian motion, they probe its fibrous structure. Since dMRI is sensitive to the diffusion of water molecules, it can be used to measure this constrained or anisotropic diffusion in white matter, which makes it possible to indirectly perceive the fine microstructure of the medium and to non-invasively infer the white matter pathways.

The major white matter pathways can be classified into three groups.

Commissural Fibers The commissural or transverse fibers (Fig-2.4) connect mirroring and different sites between the two cerebral hemispheres. The most important commissural structure is the *corpus callosum* (CC), which is also the largest white matter structure. It contains about three hundred million fibers. The CC is divided into the *rostrum*, the *genu*, the *body*, and the *splenium* from anterior to posterior. Commissural fibers traversing the CC in the genu and curving into the frontal lobe make up the *forceps anterior (minor)*. Similarly fibers traversing in the splenium and curving into the occipital lobe make up the *forceps posterior (major)*. Another important commissural structure is the *anterior commissure* (AC). The CC and the AC are responsible for inter-hemispheral communication.

Association Fibers The association fibers (Fig-2.5) connect regions of the cerebral cortex within the same hemisphere. Short association fibers, also known as "U"-fibers connect adjacent gyri, going around the sulcus separating them. These lie immediately beneath the grey matter of the cerebral cortex. Long association fibers

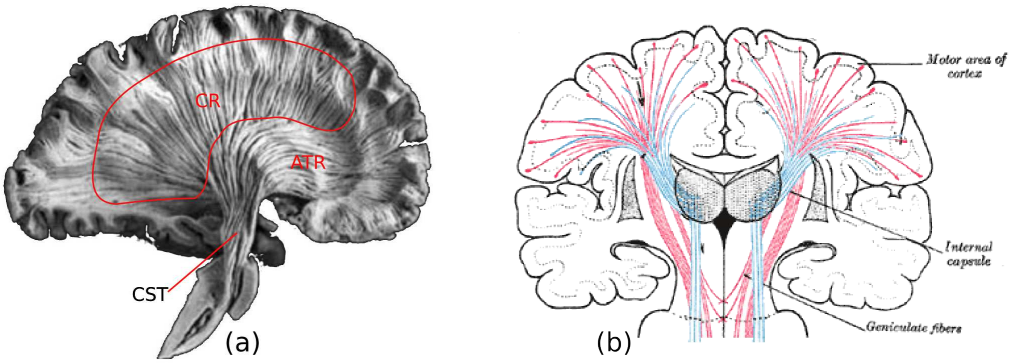

Figure 2.6: Projection fibers. (a) The corona radiata (CR), the anterior thalamic radiation (ATR), and the corticospinal tract (CST). Adapted from [11]. (b) The efferent/motor (red: CST) fibers and the afferent/sensory (blue) fibers. Adapted from [6].

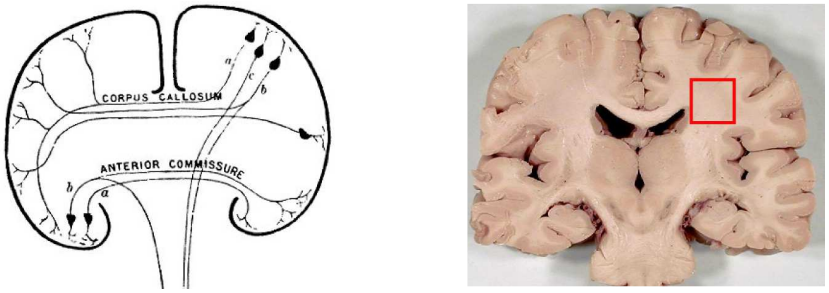

Figure 2.7: Region with three fiber bundles crossing. CST: vertically in the plane. CC: diagonally in the plane. SLF: perpendicular to the plane. Figures adapted from, left: www.healcentral.org, right: www.humannervoussystem.info.

travel greater distances to connect distant cortical regions. Some of such important association fibers are the *cingulum*, the *superior longitudinal fasciculus* (SLF), and the *inferior longitudinal fasciculus* (ILF).

Projection Fibers The projection fibers (Fig-2.6) consist of efferent and afferent fibers connecting the cerebral cortex to the cerebellum, the spine and subcortical grey matter areas such as the thalamus, and the basal ganglia. Functionally, the main efferent fibers are the motor fibers originating from the pyramidal motor cells of the cerebral cortex, that run down and converge in the *internal capsule* and travel further down the brainstem to the spine. These comprise the important *corticospinal tract* (CST) also known as the *pyramidal tract*. Structurally, the projection fibers are widely diffused just under the cerebral cortex before converging in the internal capsule. This important fanning structure is known as the *corona radiata* (CR). The CR is comprised of both efferent and afferent fibers, and handles nearly all the traffic to and from the cerebral cortex. Structures like the *anterior thalamic radiation* (ATR) connect the nuclei in the thalamus to cerebral cortex of the frontal lobe.

It must be noted that these white matter pathways or fiber tracts or simply fibers often criss-cross, resulting in geometrically complex microstructures at a scale much finer than the resolution of dMRI. This is therefore an important physical consideration in dMRI, and correctly inferring the geometry in regions with fiber-crossings is addressed as a central problem. In this respect, Fig-2.7 presents a region with fiber crossings that will be often scrutinized in this thesis. The region of interest highlighted in the coronal slice contains crossing fibers from three major pathways. Descending vertically in the plane is the CST, traversing diagonally in the plane from above the ventricles to the cerebral cortex are the lateral radiations of the CC, and within the central region of interest is the SLF perpendicular to the plane.

2.3 Summary

In this introductory chapter we briefly presented the brain with the goal of providing a physical context of the problem dMRI attempts to solve. We presented an overview of the brain's anatomy, relevant microscopic neural tissue, and important macroscopic cerebral tissue organization, namely the major white matter pathways. These are central for understanding the diffusion of water molecules in the brain, and for understanding the usefulness of dMRI in studying the brain.

At a macroscopic scale, the brain is primarily constituted of grey matter and white matter. While the grey matter contains the neuronal cell bodies and forms the main information processing centers of the brain, white matter is made up of the axons originating from the neurons, which interconnect various grey matter regions and form information carrying pathways with highly coherent fibrous structures from the microscopic to the macroscopic scale. These fibrous microstructures of the white matter form the physical basis for dMRI's usefulness in studying the brain. The Brownian motion of the water molecules contained in the brain is hindered in the white matter by these fibrous structures in a particular fashion. While the diffusion of water molecules is greatly hindered perpendicular to these structures, the diffusion parallel to these structures is relatively less affected. In other words the diffusing water molecules probe the white matter's microstructure. Therefore, since dMRI is sensitive to the diffusion of water molecules, it is used to measure the constrained or anisotropic diffusion of water molecules in the white matter, to infer its major axon fiber bundles non-invasively.

However, since the white matter axon fibers criss-cross in many regions, the cerebral white matter often contains complex structures constituted of multiple coherent microstructures at a scale that is orders of magnitude finer than the resolution achieved by current dMRI. Although the coherence or homogeneity of the multiple microstructures in such regions is visible at the fine length scale of the axons themselves, the homogeneity is lost at the resolution achieved by dMRI and such regions appear to contain heterogeneous microstructures. Therefore, the problem of accurately inferring the geometry of the microstructure in regions with fiber crossings is of central importance in dMRI. This problem is also at the heart of this thesis.

CHAPTER 3

DIFFUSION NMR AND MRI

Contents

3.1 INTRODUCTION

Only in the last century, has physics, mathematics, and technology progressed enough to be en par with the complex and involved problem of understanding the brain that has perplexed people so far. New and non-invasive approaches now provide an unprecedented power to see within this delicate organ while it functions and without harming the process of life.

Magnetic Resonance Imaging (MRI) is one such sophisticated technique, which allows to examine the brain (and also the entire body) non-invasively. At the core of MRI is the phenomenon of nuclear magnetic resonance (NMR). The NMR experiment can detect a number of different properties of a sample. For example it can detect the Brownian motion or the diffusion of the particles in the sample. This sensitivity to diffusion and the measurement of the diffusion properties from an NMR experiment is at the heart of diffusion MRI, which allows one to infer from the diffusion properties, the microstructure of the brain's white matter in-vivo and non-invasively.

This chapter is focussed on the fundamentals of NMR and diffusion NMR, and on diffusion MRI reconstruction algorithms, which are employed to infer the cerebral white matter's microstructure. This chapter opens with the NMR phenomenon and the ingenious spin-echo experiment, which forms the foundation of diffusion NMR. Then it presents diffusion NMR to show how diffusion can be measured from NMR, with an emphasis on the two ways of modelling diffusion, namely the phenomenological approach of Fick and the random walk model proposed by Einstein, since these have greatly influenced the development of diffusion NMR. These have given rise to two complementary approaches for modelling the diffusion NMR signal, namely the Stejskal-Tanner signal model, and the q-space formalism. Finally this chapter presents a number of diffusion MRI reconstruction algorithms, starting from the classical technique of diffusion tensor imaging, and then exploring various other "higher order" approaches, which attempt to describe the microstructure of the cerebral white matter with greater accuracy.

A brief history of NMR and MRI The scientific heritage of NMR and MRI is reflected by the list of Nobel laureates who contributed to their developments. The theoretical underpinnings that made NMR possible were proposed in 1924 by Wolfgang Pauli who suggested a new quantum degree of freedom that later came to be known as spin. He formulated the mathematical theory by 1927, and was awarded the Nobel prize in physics in 1945 for his contributions. The concept of spin implies that atomic nuclei bearing spins exhibit magnetic moments. The fact that protons exhibit magnetic moments had already been discovered in 1922 by Otto Stern prior to the concept of spin. Stern was awarded the Nobel prize in physics in 1943. Pauli's theory was verified in 1938 by Isidor Rabi in molecular beams. From his experiments Rabi was able to both detect the effects of spin and measure the gyromagnetic ratio

that is the characteristic signature of an atomic nucleus due to its spin. His experiments also established the concept and the technique of NMR for manipulating spins. Rabi was awarded the Nobel prize in physics in 1944.

In 1946 Felix Bloch [12] and Edward Mills Purcell [13] independently extended the techniques established by Rabi. They successfully demonstrated the magnetic resonance effect in liquids and solids. Bloch and Purcell shared the Nobel prize of 1952 in physics, and NMR was established. In his seminal paper of 1950 [14] Erwin Hahn proposed the spin echo experiment, which used a combination of 90^o and 180^o electromagnetic or radio frequency pulses to filter out effects of magnetic field inhomogeneities in the measurement of the transverse signal. Further works of Herman Carr and Purcell in 1954 [15] led to the full development of the radio frequency pulse technique introduced by Hahn. This formed the foundations of NMR.

It must be noted at this point that both the papers of Hahn [14] and Carr & Purcell [15] critically point out the observed effects of diffusion of the spin bearing nuclei in magnetic resonance experiments with a succession of radio frequency pulses. Although these papers generally perceive the diffusion effect as an unfortunate phenomenon resulting in a loss of signal, Carr & Purcell [15] in fact demonstrate that diffusion can be directly measured from NMR and go on to actually measure the diffusion constant of water at 25^oC. This forms the corner-stone of diffusion NMR.

Although NMR became a well established technique for studying various materials, it took almost three decades since the experiments of Bloch and Purcell in 1946, for MRI to be invented. NMR by itself is capable of examining a single spin ensemble or a tiny region of a sample, but it can't image the whole sample to recreate a 2D slice or a 3D volumetric image necessary to study entire biological samples like the human body. Paul Lauterbur in 1973 [16] proposed the use of magnetic gradient fields to spatially encode the positions or voxel regions of the spin ensembles. This was a remarkable invention, which made it possible to reconstruct entire slice or volumetric images from NMR data. Spatial encoding was improved in terms of frequency encoding by Richard Ernst in 1978, and phase encoding by Bill Edelstein in 1980 using pulsed gradients. In 1977 Peter Mansfield [17] developed the mathematical framework for rapidly switching gradients for spatial encoding, greatly speeding up the process of reconstructing images of an entire biological sample. This is known as *echo planar imaging* (EPI). Lauterbur and Mansfield were jointly awarded the Nobel prize in medicine in 2003 for making MRI possible. Thus modern MRI was developed from the phenomenon of NMR coupled with the method of spatial encoding.

OUTLINE

This chapter is divided into three parts dedicated respectively to NMR, diffusion NMR and diffusion MRI. Section-3.2 presents the semi-classical description of NMR

and the spin-echo experiment proposed by Hahn (section-3.2.1), which forms the corner stone for the diffusion NMR experiment. Section-3.3 presents diffusion NMR and shows how diffusion can be measured from the NMR experiment. Section-3.3.1 discusses the two main approaches for modelling diffusion mathematically, namely Fick's phenomenological approach and Einstein's random walk model. Sections-3.3.3 & 3.3.2 attempt to show how these two complementary approaches to diffusion, one macroscopic and one microscopic, have influenced the development of diffusion NMR. Finally, section-3.4 presents modern diffusion MRI reconstruction techniques where, using the diffusion NMR experiment, the diffusion measured from anisotropic media is employed to infer the microstructure of the media. A number of approaches are presented, starting from the classical diffusion tensor imaging, to more recent state-of-the-art algorithms that make use of complex models and functional bases to improve the results of diffusion tensor imaging.

3.2 Nuclear Magnetic Resonance

The principles of NMR are based on *spin*, a fundamental quantum characteristic possessed by electrons, protons, and neutrons, like electrical charge or mass. Spins come in multiples of $1/2$ and can be positive or negative. In grouped particles, e.g. atomic nuclei, opposite spin-signs can pair up to eliminate the total spin of the group. But the net spin of unpaired particles or atomic nuclei imparts a magnetic dipole moment. In other words such particles or such atomic nuclei can be influenced by an external magnetic field. In the presence of a strong magnetic field $\mathbf{B_0}$ with magnitude B_0, the magnetic dipole moment vector or the spin vector of the particle or nucleus aligns itself with $\mathbf{B_0}$ and precesses around it with an angular frequency known as the *Larmor frequency*:

$$\omega_0 = \gamma B_0,$$

where γ is the *gyromagnetic ratio*, characteristic of the particle or the nucleus. However, this cannot be observed for individual particles or nuclei. The effect is detectable when it becomes pronounced in the presence of an ample collection of spin bearing particles or nuclei with the same gyromagnetic ratio. From a macroscopic perspective, when such a collection is subjected to a magnetic field, the randomly oriented individual magnetic dipole moment vectors align themselves along $\mathbf{B_0}$, to form a resultant ensemble magnetic dipole moment vector $\mathbf{M}$, which phenomenologically satisfies:

$$\frac{d\mathbf{M}}{dt} = \gamma \mathbf{M} \times \mathbf{B_0}. \tag{3.1}$$

Although spin is a quantum characteristic, the macroscopic perspective with the resultant magnetic dipole moment vector $\mathbf{M}$, is a semi-classical description.

Of particular interest is the hydrogen nucleus ${}^1H$, which is found abundantly in nature, accounts for 99.98% of all hydrogen atoms, and also constitutes water. 60% of

the human body and 78% of the brain is water. Therefore, ^1H is a natural spin bearing nucleus of choice for MRI. ^1H is an unpaired proton with a net spin of $1/2$, and has a gyromagnetic ratio of $\gamma = 42.58$ MHz/T.

A macroscopic scale or an ensemble perspective is adopted to describe MRI instead of the quantum formulation because of its simplicity. From this point of view, MRI is explained in terms of the resultant ensemble magnetization vector $\mathbf{M}$. Under the influence of the external magnetic field $\mathbf{B_0}$, the initially randomly distributed individual spins in the ensemble, align themselves along $\mathbf{B_0}$. There are two available energy configurations or states. These are the low and high energy states depending upon whether the individual spin magnetization vectors point along the magnetic field or opposite to it. Laws of thermodynamics ensure that the number of spins N^+ in the low energy configuration slightly outnumber the number of spins N^- in the high energy configuration. However, this implies that the magnitude of the net magnetization vector $\mathbf{M}$ is only a fraction of what it would have been had all the spins been pointing along the same direction. This natural distribution of spins along or opposite $\mathbf{B_0}$ is known as the *thermal equilibrium* state.

The NMR signal is generated by exposing the ensemble of spins precessing along $\mathbf{B_0}$ to an oscillating magnetic field or an electro-magnetic (radio-frequency: RF) pulse. This is known as the excitation phase. The energy absorbed by the low energy configuration spins from this pulse tilts the magnetization vector $\mathbf{M}$ away from $\mathbf{B_0}$ towards the high energy configuration. The oscillation of the secondary magnetic field ensures that the spins (and hence $\mathbf{M}$) continue to precess around $\mathbf{B_0}$ even tilted away from it – along the surface of a cone. Once the RF pulse is switched off, the spins begin to recover their alignment with the main magnetic field $\mathbf{B_0}$, and to return to their low energy configuration or the thermal equilibrium. This is known as the relaxation phase. The signal is created as the spins precess tilted away from $\mathbf{B_0}$, and it decays as the spins relax, dissipating the absorbed energy.

This process can be better understood and put in a mathematical framework by considering the external magnetic field $\mathbf{B_0}$ to be aligned with the Z-axis. The XY-plane is then known as the transverse plane, and the net magnetization vector $\mathbf{M}$ can be separated into the *longitudinal* component $\mathbf{M}_z$, along the Z-axis (or $\mathbf{B_0}$), and the *transverse* component $\mathbf{M}_{xy}$, in the transverse plane. Or the net magnetization vector $\mathbf{M}$ can be written in terms of its components $[M_x, M_y, M_z]^T$. In this framework the low energy configuration is along the positive Z-axis, while the high energy configuration is along the negative Z-axis. {X,Y,Z} is known as the laboratory frame of reference and is considered fixed. Under the influence of $\mathbf{B_0}$, the initial net magnetization vector $\mathbf{M}$ has magnitude M_0, and is equal to its longitudinal component $\mathbf{M}_z$, while its transverse component $\mathbf{M}_{xy}$ is null.

The *excitation phase* can be understood by considering a rotating frame of reference.

Under the influence of $\mathbf{B_0}$, as the spins precess at the Larmor frequency, it is possible to envisage a rotating frame of reference {X', Y', Z' (= Z)}, with the Z'-axis aligned with the Z-axis of the fixed frame of reference. This rotating frame is taken to rotate clockwise with the spins at the Larmor frequency. In other words in the rotating frame of reference, the precessing spins appear static. Applying a secondary magnetic field in the rotating frame of reference along the X'-axis, in the transverse plane, has the effect of tilting the net magnetization vector M away from $\mathbf{B_0}$ and towards the transverse plane, which is half way to the high energy configuration. In the fixed frame of reference this is seen as the net magnetization vector M spiralling down towards the transverse plane while precessing at the Larmor frequency. In either of the reference frames this implies that the magnitude of the longitudinal component $\mathbf{M}_z$ decreases, while the magnitude of the transverse component $\mathbf{M}_{xy}$ increases.

In practice, this can be achieved by passing an alternating current through a coil aligned with the X-axis of the fixed frame of reference. When the current in the coil alternates at the Larmor frequency ω_0, the coil generates an oscillating magnetic field along the X-axis that appears static to the precessing spins. Or the precessing spins perceive the oscillating magnetic field as a static magnetic field in the rotating frame of reference. This secondary magnetic field is known as the $\mathbf{B}_1$ magnetic field or the RF pulse. The angle of the tilt experienced by the net magnetization vector M due to $\mathbf{B}_1$ depends on the magnitude and time of exposure of the RF pulse. A 90^o RF pulse tilts M into the transverse plane and zeros out its longitudinal component. A 180^o RF pulse flips M completely around and points it along its opposite direction.

The *relaxation phase* begins when the RF pulse or the secondary magnetization field is turned off. The RF pulse has the effect of disturbing the thermal equilibrium induced by the primary magnetization vector $\mathbf{B_0}$. As it is turned off the spins begin to relax and to return to their thermal equilibrium. The relaxation can also be seen in terms of its longitudinal and transverse components. However, these are governed by different phenomena and are characterized by different time signatures.

T1 Relaxation The longitudinal relaxation is known as the T1 relaxation since it is described using a time signature denoted T1. The T1 relaxation occurs as the spin ensemble radiates the energy it had absorbed from the RF pulse to the surrounding thermal reservoir or lattice and regains its thermal equilibrium with the lattice. Therefore, the T1 relaxation is also known as the *spin-lattice* relaxation. In this process the spins realign themselves with $\mathbf{B_0}$. In terms of the net magnetization vector M, this implies that the longitudinal component $\mathbf{M}_z$ progressively regains its initial magnitude M_0, while the transverse component $\mathbf{M}_{xy}$ progressively becomes null again. Phenomenologically this is described by:

$$\frac{dM_z}{dt} = -\frac{(M_z - M_0)}{T_1}, \tag{3.2}$$

where T_1 is a time constant representing the time signature T1.

T2 Relaxation The transverse relaxation involves the phenomenon of the spins regaining their thermal equilibrium amongst themselves, and is characterized by the time signature T2. Therefore it is also known as the *spin-spin* relaxation or the T2 relaxation. In the transverse plane this is interpreted by the spins losing their initial coherence. From an initial coherent transverse magnetization vector $\mathbf{M}_{xy}$, they progressively dephase as they radiate the energy they had absorbed to neighbouring spins. Phenomenologically this is described by:

$$\frac{d\mathbf{M}_{xy}}{dt} = -\frac{\mathbf{M}_{xy}}{T_2}, \tag{3.3}$$

where T_2 is a time constant that differs from T_1 and represents the time signature T2. Transverse relaxation is, however, a complex phenomenon. Although theoretically $\mathbf{B_0}$ is supposed homogeneous, in reality minor inhomogeneities exist. These inhomogeneities are relevant enough to also contribute to spins dephasing in the transverse plane, though this is not a true relaxation. Transverse relaxation is therefore a combination of spin-spin relaxation and field inhomogeneity dephasing. The pure spin-spin relaxation time is known as T2. The combined transverse relaxation time is known as T2*.

Bloch Equations The Bloch equations are a coupled set of three differential equations that combine the effects of NMR and describe the evolution of the net magnetization vector M over time. These are macroscopic and phenomenological equations that include the effects of Larmor precession and T1 and T2 relaxations. Combining Eqs-3.1, 3.2, and 3.3, they are written in the fixed frame of reference in terms of the relaxation time constants as:

$$\begin{aligned}
\frac{dM_x(t)}{dt} &= (\gamma\mathbf{M}(t) \times \mathbf{B}(t))_x - \frac{M_x(t)}{T_2} \\
\frac{dM_y(t)}{dt} &= (\gamma\mathbf{M}(t) \times \mathbf{B}(t))_y - \frac{M_y(t)}{T_2} \\
\frac{dM_z(t)}{dt} &= (\gamma\mathbf{M}(t) \times \mathbf{B}(t))_z - \frac{M_z(t) - M_0}{T_1},
\end{aligned} \tag{3.4}$$

where $\mathbf{B}(t) = \mathbf{B_0} + \mathbf{B}_1(t)$ is the total external magnetic field. These can also be rewritten in a vector form as:

$$\frac{d\mathbf{M}(t)}{dt} = \gamma\mathbf{M}(t) \times \mathbf{B}(t) + \begin{pmatrix} -\frac{1}{T_2} & 0 & 0 \\ 0 & -\frac{1}{T_2} & 0 \\ 0 & 0 & -\frac{1}{T_1} \end{pmatrix} \mathbf{M}(t) + \begin{pmatrix} 0 \\ 0 \\ \frac{M_0}{T_1} \end{pmatrix}. \tag{3.5}$$

The *signal* is generated in a receiver coil in the transverse plane when the spins precess tilted away from the Z-axis. When the magnetic moment vectors of the spins

are tilted to say the transverse plane and precess around the Z-axis, they generate an alternating current in the receiver coil at the Larmor frequency. This can be seen as the converse of the spin excitation phase where a coil in the transverse plane was used with a current alternating at the Larmor frequency to tilt the spins. The frequency of the signal current is ω_0 and its amplitude reflects the amount of magnetization of the spin ensemble. Hence, since the ^1H nucleus is chosen for imaging in MRI, the excitation RF pulse is generated at the Larmor frequency of the ^1H nucleus. Therefore, the magnitude of the signal generated from the NMR experiment reflects the density of the ^1H nucleus, or the amount of water in the tissue.

3.2.1 Spin Echo

Diffusion NMR is derived from the *spin echo* experiment that was conceived by Erwin L Hahn [14]. It combines a pair of RF pulses of different amplitudes to remove the effects of field inhomogeneities or T2* from the signal. Hahn put forth the idea that following a 90^o RF pulse that tilts the net magnetization vector to the transverse plane, the dephasing that follows caused by the field inhomogeneities, could be refocused using a second RF pulse of 180^o, thus removing the effects of the field inhomogeneities.

Again this can be understood simply in the rotating frame of reference. In this frame of reference, after the 90^o RF pulse, the spins precessing in the transverse plane should appear static. However, due to field inhomogeneities, as the spins begin to dephase, some would appear to speed up (or move ahead clockwise in the rotating frame of reference), while some would slow down (or fall back anti-clockwise in the

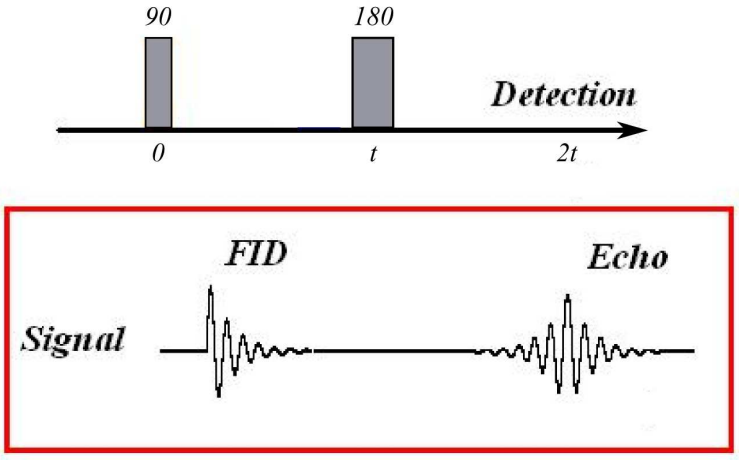

Figure 3.1: Spin Echo pulse sequence showing the Free Induction Decay (FID) after the 90^o RF pulse and the Echo signal after the 180^o RF pulse. Adapted from Wikipedia (Spin Echo Signal).

rotating frame of reference). This transverse dephasing is known as the *free induction decay* (FID) and causes the signal to decay faster than pure T2 effects. However the application of a second RF pulse of 180^o has the effect of flipping the individual spins in the transverse plane such that the "slow" spins that had fallen behind the rotating frame of reference are flipped ahead of it, while the "fast" spins that had moved ahead are flipped behind the rotating frame of reference. Indeed, the 180^o RF pulse causes the spins to refocus after a certain length of time as the fast spins catch up with the slow spins, which regenerates the signal. This is known as the *echo* and it is free of the T2* effects due to field inhomogeneities (Figure-3.1). It must be noted, however, that the echo regenerates the signal completely only under the assumption that none of the spins in the ensemble have moved. If they move then the 180^o RF pulse doesn't completely invert the spin and this results again in signal decay. However, this is not due to field inhomogeneities. As noted by Hahn [14] and Carr & Purcell [15], this is due to the translational motion of diffusion. This forms the basis of diffusion NMR.

The time between the 90^o RF pulse and the echo is known as the *echo time* (TE), and it is twice as long as the time between the 90^o and the 180^o RF pulses. In case this sequence is repeated, the time between consecutive sequences is known as the

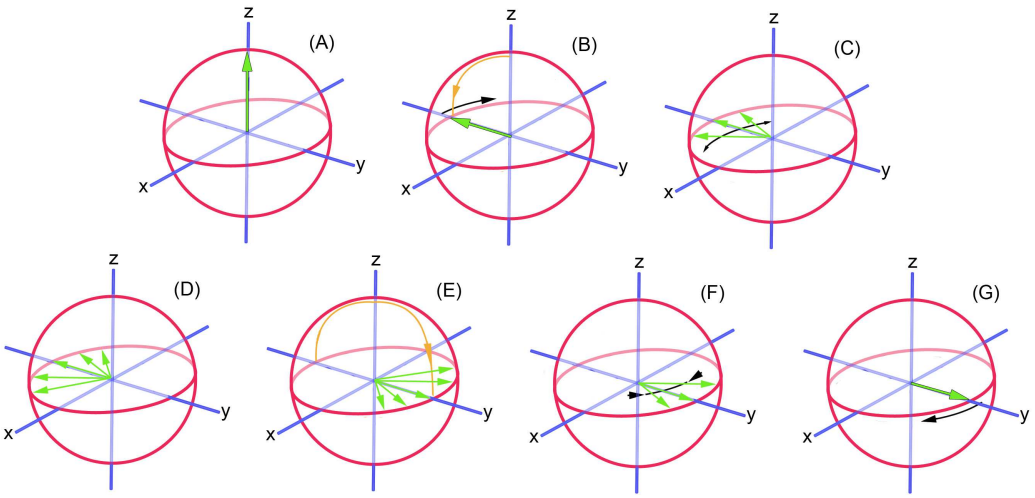

Figure 3.2: Concept of spin echo refocussing in the rotating frame of reference {X'=x, Y'=y, Z'=z}. (A) Green vector is the net magnetization vector M, initially aligned with the Z'-axis under the influence of the external magnetic field. (B) 90^o RF pulse tilts (orange arrow) M on to the transverse plane. (C) & (D) Spins dephasing due to local field inhomogeneities. Slow spins fall back, while the fast spins move ahead in the transverse plane. (E) 180^o RF pulse (orange arrow) flips the spins around such that now the slow spins are ahead and the fast spins are behind. (F) Refocussing begins as the fast spins begin to catch up the slow spins from behind. The echo begins to form. (G) The spins are completely refocussed. This is the centre of the echo and the signal is free of the effects of field inhomogeneities. From Wikipedia (Spin Echo Concept).

repetition time (TR). In fact, due to the low sensitivity of NMR, spin echo experiments are repeated a number of times and their signals added to improve the signal-to-noise (SNR) ratio. By adding the result of repeated experiments the signal adds coherently while the noise adds in random phase, improving the total SNR.

3.3 DIFFUSION NMR

Diffusion NMR (dNMR) is a modality of NMR that is sensitive to the Brownian motion of the particles in a sample. The dNMR experiment can therefore be used to measure the diffusion properties of the underlying sample. This makes dNMR central to diffusion MRI. At the heart of dNMR is the diffusion process, and understanding diffusion helps to understand how it can be measured from NMR. It leads to the critical improvements that were made by Stejskal & Tanner to the original spin echo experiments of Hahn and Carr & Purcell that opened up the domain of dNMR.

This section presents the principles of dNMR and shows how diffusion can be measured from NMR. It opens by examining the two mathematical ways for modelling diffusion, namely the phenomenological equations of Fick and the random walk model for Brownian motion proposed by Einstein. This explains the two pronged approach for modelling dNMR, namely the Stejskal-Tanner formulation for the signal and the q-space relationship between the signal and the diffusion probability density function. This also reveals the influence of these two approaches on diffusion MRI reconstruction techniques, namely the methods such as diffusion tensor imaging that estimate the apparent diffusion coefficient and the methods such as diffusion spectrum imaging that estimate the diffusion probability density function.

3.3.1 Diffusion

Diffusion is a process of mass transport that describes the random spreading of molecules or particles generally in the presence of a concentration gradient. The process of diffusion was observed, studied and mathematically described over the entire 19th century. It was initially observed in three different forms, namely heat diffusion in the presence of a temperature gradient, molecular diffusion in the presence of a concentration gradient, and Brownian motion, which occurs even in the absence of any gradients. These, apparently very different phenomena – the first, concerning the spreading of energy in a solid medium, the second, concerning the spreading of molecules from a region of high concentration to a region of low concentration in fluids, and the third, concerning the random motion of molecules and particles in fluids due to the ambient temperature – can all be described by the same diffusion equation. However, while today their correspondence is widely accepted, establishing this connection wasn't always an easily demonstrable task.

Historically, diffusion has been both observed in experiments and mathematically described in theory, in two ways – a phenomenological view point and a molecular-kinetic theory of heat view point with a "random-walk" model for the diffusing particles. The phenomenological view point corresponds to Fourier's and Fick's laws of diffusion for heat and for particles in a concentration gradient, while the random-walk model corresponds to Einstein's description of Brownian motion. This two pronged approach to diffusion, has also influenced dNMR and diffusion MRI, and has led to a two fold approach for describing it mathematically – namely the Bloch-Torrey equations, which is a phenomenological solution, and the q-space formalism, which arises from the Brownian motion of spin bearing particles.

Phenomenological approach The phenomenological equations of diffusion were proposed by Joseph Fourier in 1822 to describe the diffusion of heat in solids, and then adapted by Adolf Fick in 1855 to describe the diffusion of molecules in fluids in the presence of a concentration gradient [18]. Fick derived his "laws of diffusion" from Fourier's laws by analogy, while attempting to describe the experiments conducted by Thomas Graham in 1831 on the diffusion of gases. These laws describe the molecular transfer or diffusion that takes place in a system from regions of high concentration to regions of low concentration due to the concentration gradient. In 1D, Fick's first law relates the rate of transfer of the diffusing substance per unit area, or flux, to the concentration gradient causing the diffusion:

$$J = -D\frac{\partial C}{\partial x}, \tag{3.6}$$

where J is the flux with units (mol/m^{2}s), D is the diffusion coefficient with units (m^2/s), C is the concentration with units (mol/m^3), and x is the spatial length parameter measured in meters. Accounting for the conservation of mass during the diffusion process, which implies:

$$\partial C/\partial t = -\partial J/\partial x,$$

and combining with Eq-3.6, gives Fick's second law:

$$\frac{\partial C}{\partial t} = D\frac{\partial^2 C}{\partial x^2}, \tag{3.7}$$

when the diffusion coefficient D is constant locally. Fick's second law describes the change of the concentration field over time due to the diffusion process. Eq-3.7, which relates the time derivative of the concentration to the second order spatial derivative of the concentration is known as the *diffusion equation* – it describes diffusion phenomenologically.

In higher dimensions, e.g. 3D, Fick's laws are written as:

$$\mathbf{J} = -D\nabla\mathbf{C}, \tag{3.8}$$

$$\frac{\partial \mathbf{C}}{\partial t} = D\nabla^2\mathbf{C}. \tag{3.9}$$

D being a scalar quantity in Eqs-3.8 & 3.9 is an indication that diffusion is equal in all directions. This is known as *isotropic* diffusion. However, certain media such as crystals, textile fibers, etc. can be inherently anisotropic and can favour diffusion in a certain spatial direction while hindering it in others. This results in *anisotropic* diffusion, which is described by replacing the scalar diffusion coefficient D by a generalized *diffusion tensor* $\mathbf{D}$ in Fick's laws [18]:

$$\mathbf{J} = -\mathbf{D}\nabla\mathbf{C}, \tag{3.10}$$

$$\frac{\partial \mathbf{C}}{\partial t} = \nabla \cdot (\mathbf{D}\nabla\mathbf{C}). \tag{3.11}$$

Diagonalizing the diffusion tensor $\mathbf{D}$ into its eigenvalues and eigenvectors provides a local orthogonal coordinate system that indicates the preferential diffusion direction favoured by the anisotropy of the underlying material. This is the budding idea that indicates that diffusion can be considered as a probe of the underlying medium's microstructure. Isotropic diffusion can be understood as a special case of anisotropic diffusion when $\mathbf{D} = D\mathbf{I}$, where $\mathbf{I}$ is the identity matrix. The idea of the diffusion tensor is central to dMRI, since the fibrous quality of the cerebral white matter also exhibits directional anisotropy.

Random-walk approach Though Fick's laws are concerned with the diffusion of molecules from regions of high concentration to regions of low concentration, they essentially describe the evolution of the concentration gradient over time and space, and aren't concerned with the movements of the molecules themselves. This description of diffusion emerged with Albert Einstein in 1905 when he related the molecular-kinetic theory of heat to the observations made by Robert Brown in 1828. Brown had noted the perpetual erratic motion of pollen grains suspended in water while observing them under a microscope. This erratic movement came to be known by his name as Brownian motion. When Einstein proposed [19] that due to the thermal kinetic

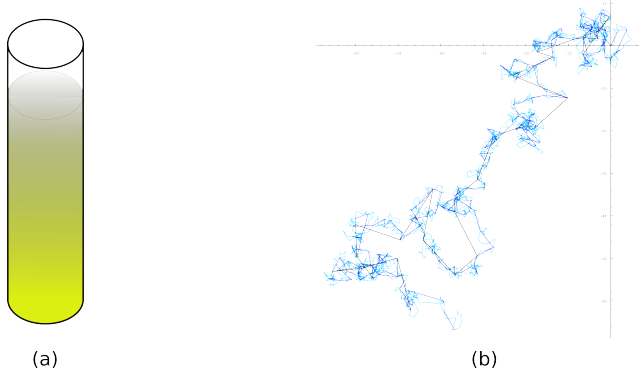

Figure 3.3: Diffusion. (a) Concentration gradient at the macroscopic scale leads to the phenomenological Fick's laws of diffusion. (b) Random-walk model of Brownian motion at a microscopic scale, adapted from Wikipedia (Brownian motion).

energy of molecules, particles suspended in a liquid large enough to be observed under a microscope would exhibit random movements governed by the probabilistic law he derived, his idea was quickly recognized to be the theoretical description of Brownian motion. It turned out that the probabilistic law of Brownian motion derived by Einstein also satisfied the diffusion equation. This provided the final link and showed that diffusion was driven by the thermal kinetic energy of molecules due to the ambient temperature, implying that diffusion, in the form of Brownian motion also occurred in the absence of a temperature or a concentration gradient. The special case of diffusion when the suspended particles belong to the liquid is known as *self diffusion*.

Essentially, the particles move erratically because they incessantly collide with the other particles in the system, which continuously changes their motion. To describe this erratic movement of a large number of particles, Einstein adopted the probabilistic approach of a random walk model. In 1D, this is modelled using two probability density functions (PDFs) – $f(x,t)$, the probability of finding a particle at the position x at a time t, and $P(\Delta x, \Delta t)$, the probability of finding a particle at a distance Δx from its initial position after a time Δt. $P(\Delta x, \Delta t)$ is a special case of the transition probability $P(\mathbf{x}|\mathbf{x}', \Delta t)$, which is the probability of a particle initially at $\mathbf{x}'$ migrating to $\mathbf{x}$ during the time Δt. $P(\mathbf{x}|\mathbf{x}', \Delta t) = P(\Delta x, \Delta t)$ when the transition probability is translationally invariant, or when the movement of a particle during a time step is independent of the movements of the other particles and also of its own position and movements in the past. $P(\Delta x, \Delta t)$ is also symmetric, such that $P(\Delta x, \Delta t) = P(-\Delta x, \Delta t)$. Then $f(x,t)$ and $P(\Delta x, \Delta t)$ are related by [19, 20]:

$$f(x, t + \Delta t) = \int_{-\infty}^{\infty} f(x - \Delta x, t) P(\Delta x, \Delta t) d(\Delta x). \tag{3.12}$$

Expanding the LHS, $f(x, t+\Delta t)$, in the powers of Δt using a Taylor expansion around t, and similarly expanding $f(x - \Delta x, t)$ in the RHS, in the powers of $-\Delta x$ using a Taylor expansion around x, and keeping only the smallest non-zero terms, the limit as $\Delta t \to 0$ is the diffusion equation:

$$\frac{\partial f(x,t)}{\partial t} = D \frac{\partial^2 f(x,t)}{\partial x^2}, \tag{3.13}$$

where:

$$D = \frac{1}{\Delta t} \int \frac{\Delta x^2}{2} P(\Delta x, \Delta t) d(\Delta x) = \frac{\left\langle (\Delta x)^2 \right\rangle}{2 \Delta t},$$

where $\langle \cdot \rangle$ signifies the expected value. It is evident that $2\Delta t D$ is the variance of the displacement Δx if its mean is zero. Comparing Eqs-3.7 & 3.13 compares the phenomenological approach to the random-walk approach, and shows that the diffusion coefficient is the variance.

The free diffusion solution The solution to the diffusion equation (Eqs-3.7 & 3.13) can be computed under given initial or boundary conditions. A number of such

solutions for various initial and boundary conditions can be found in [18]. Considering only the initial condition $f(x,0) = \delta(x)$, where δ is the Dirac delta function, and using the random-walk terminology, the solution to the diffusion equation is [19]:

$$f(x,t) = \frac{1}{\sqrt{4\pi Dt}} e^{\frac{-x^2}{4Dt}},$$

which is a Gaussian distribution with zero mean and a variance of $2Dt$. This leads to the important result in diffusion found by Einstein, which states that the mean squared displacement of a particle undergoing diffusion is: $\langle x^2 \rangle = 2Dt$.

However, of greater interest than $f(x,t)$, is $P(\Delta x, \Delta t)$, the Green's function of the diffusion equation. Under the same initial condition $f(x,0) = \delta(x)$, the transition probability turns out to be:

$$P(\Delta x, \Delta t) = \frac{1}{\sqrt{4\pi D\Delta t}} e^{\frac{-\Delta x^2}{4D\Delta t}}.$$

The Green's function is independent of the position x, and states that the displacement Δx is also governed by a Gaussian distribution. This is of greater interest than $f(x,t)$, since dMRI measures the total displacement of molecules rather than their positions.

Similarly in 3D the random-walk is described by:

$$f(\mathbf{x}, t+\Delta t) = \int_{-\infty}^{\infty} f(\mathbf{x}-\Delta\mathbf{x}, t) P(\Delta\mathbf{x}, \Delta t) d\Delta\mathbf{x} \tag{3.14}$$

Again a similar expansion of the LHS and the RHS as in the 1D case reveals the diffusion equation in 3D:

$$\frac{\partial f(\mathbf{x},t)}{\partial t} = \nabla \cdot (\mathbf{D} \nabla f(\mathbf{x},t)), \tag{3.15}$$

where [20]:

$$\mathbf{D} := \frac{1}{2\Delta t} \begin{pmatrix} \langle (\Delta x)^2 \rangle & \langle \Delta x \Delta y \rangle & \langle \Delta x \Delta z \rangle \\ \langle \Delta y \Delta x \rangle & \langle (\Delta y)^2 \rangle & \langle \Delta y \Delta z \rangle \\ \langle \Delta z \Delta x \rangle & \langle \Delta z \Delta y \rangle & \langle (\Delta z)^2 \rangle \end{pmatrix}. \tag{3.16}$$

In this case $2\Delta t\mathbf{D}$ is the *covariance* tensor. Comparing Eqs-3.11 & 3.15 compares the phenomenological approach to the random-walk approach in 3D, and shows that the diffusion tensor in the former can be seen as the covariance tensor in the latter.

The same initial condition $f(\mathbf{x},0) = \delta(\mathbf{x})$ leads to the transition probability (Green's function):

$$P(\Delta\mathbf{x}, \Delta t) = \frac{1}{(4\pi\Delta t)^{3/2} |\mathbf{D}|^{1/2}} \exp\left(-\frac{\Delta\mathbf{x}^T \mathbf{D}^{-1} \Delta\mathbf{x}}{4\Delta t} \right), \tag{3.17}$$

which is an oriented Gaussian parameterized by the covariance tensor. The random-walk Eq-3.14, satisfying the diffusion equation Eq-3.15 can be considered isotropic when $\mathbf{D} = D\mathbf{I}$. Otherwise, it is anisotropic, and the diagonalisation of $\mathbf{D}$ provides

a local orthogonal coordinate system that indicates the direction favoured by the random-walk or the diffusion.

Eq-3.17 is the solution to the 3D diffusion equation for only an initial condition and without any boundary conditions. It is, therefore, known as *free diffusion*. Including boundary conditions to solve the diffusion equation can account for restrictions, but would change the solution. Free diffusion is, therefore, described by a Gaussian PDF or a Gaussian propagator.

3.3.2 Diffusion from NMR: A Phenomenological Approach

As seen earlier, Hahn was the first to note the effects of diffusion in NMR in his spin echo experiment [14]. Carr & Purcell further measured the diffusion coefficient for the first time in NMR from their modification to Hahn's experiment by employing a temporally constant magnetic gradient field and by modelling the diffusion of spin bearing particles with discrete jumps [15] . However, the continuous description was formulated by Torrey in 1956. He modified the phenomenological differential equation of Bloch by adding to it Fick's diffusion equation (Eq.3.9) [21]. This came to be known as the Bloch-Torrey equation for describing the net magnetization vector M (without flow):

$$\frac{\partial \mathbf{M}}{\partial t} = \gamma \mathbf{M} \times \mathbf{B} + \begin{pmatrix} -\frac{1}{T_2} & 0 & 0 \\ 0 & -\frac{1}{T_2} & 0 \\ 0 & 0 & -\frac{1}{T_1} \end{pmatrix} \mathbf{M} + \begin{pmatrix} 0 \\ 0 \\ \frac{M_0}{T_1} \end{pmatrix} + D\nabla^2 \mathbf{M}, \tag{3.18}$$

where Fick's law is employed to describe the self diffusion of the net magnetization, and D is the diffusion coefficient.

About a decade later, in 1965, Stejskal & Tanner designed the *pulsed gradient spin echo* (PGSE) experiment by modifying Hahn's spin echo experiment with two identical magnetic gradients around the 180^o RF pulse to encode the transverse phase of the diffusing spin bearing particles [22, 23] (Fig-3.4). This made it easier to measure the decay in the transverse signal due to diffusion, and from there the diffusion coefficient. The PGSE experiment established the field of dNMR.

In the PGSE experiment the first gradient $\mathbf{G}$ of duration δ spatially encodes the phase of the individual spins (by dephasing them by an amount dependent on their position), and the effects of this gradient are undone by the second identical gradient after the 180^o RF pulse which flips the spins around (implying an effect $-\mathbf{G}$ from the second gradient). This results in a complete recovery of the signal since the magnitude of transverse magnetization vector $\mathbf{M}_{xy}$ depends on the phase coherence of the individual spins. However, if the individual spins move due to diffusion during the period Δ, between the two pulsed gradients, then the effects of the second gradient isn't the exact opposite of the first gradient ($-\mathbf{G}$) that was used to encode their

phases. This leads to a partial phase incoherence – resulting in a reduced transverse magnetization $\mathbf{M}_{xy}$, implying a loss in the spin echo signal. Since the signal decay is related to the rate of diffusion or the diffusion coefficient, measuring the signal decay makes it possible to measure the diffusion coefficient.

Mathematically this can be described by considering only the external magnetic field $\mathbf{B_0}$ and the diffusion encoding gradient $\mathbf{G}(t)$, both along the Z-axis. In the absence of the RF pulses, the total magnetic field experienced by a spin in position $\mathbf{r}$ is $\mathbf{B} = [0, 0, B_0 + \mathbf{r} \cdot \mathbf{G}(t)]^T$. The transverse magnetization vector $\mathbf{M}_{xy}$ can be computed for the PGSE experiment from the Bloch-Torrey equation by considering its complex form $M_+ = M_x + iM_y$, where i is the imaginary number [22, 24, 20]:

$$\frac{\partial M_+}{\partial t} = -i\gamma B_0 M_+ - \frac{M_+}{T_2} - i\gamma \mathbf{r} \cdot \mathbf{G}(t) M_+ + D\nabla^2 M_+. \tag{3.19}$$

Transforming to a frame of reference rotating at the Larmor frequency $\omega_0 = \gamma B_0$, and allowing for the T2 decay, by replacing:

$$M_+(\mathbf{r}, t) = \psi(\mathbf{r}, t) \exp\left(-i\omega_0 t - t/T_2\right),$$

the Bloch-Torrey equation simplifies to [22, 24, 20]:

$$\frac{\partial \psi}{\partial t} = -i\gamma \mathbf{r} \cdot \mathbf{G}\psi + D\nabla^2 \psi. \tag{3.20}$$

Further simplifying $\psi(\mathbf{r}, t)$ by separating the effects of diffusion into the function $A(t)$ from the solution without diffusion:

$$\psi(\mathbf{r}, t) = A(t) \exp\left(-i\gamma \mathbf{r} \cdot \mathbf{F}(t)\right),$$

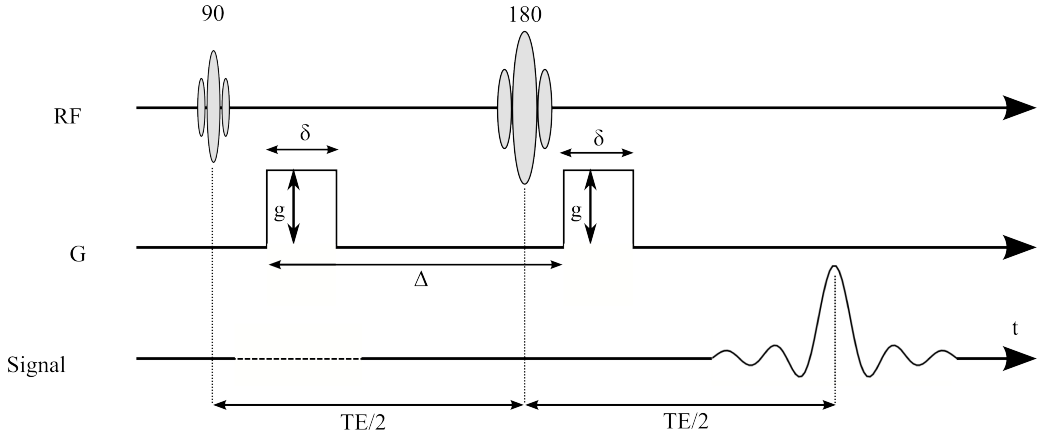

Figure 3.4: The pulsed gradient spin echo (PGSE) sequence. Two identical gradients are applied around the 180^o RF pulse of Hahn's spin echo experiment. This encodes the transverse phase of the diffusing spin bearing particles. It then becomes easier to measure the decay of the signal due to diffusion.

where [20]:

$$\mathbf{F}(t) = \int_0^t \mathbf{G}(t')dt' - 2\mathbf{H}\left(t - \frac{TE}{2}\right)\int_0^{\frac{TE}{2}} \mathbf{G}(t')dt', \tag{3.21}$$

with $\mathbf{H}(x)$ the Heaviside function which is equal to 1 for $x > 0$ and 0 otherwise, implying that the sign of $\mathbf{G}(t')$ is inverted for the gradient after the 180^o RF pulse, leads to the first order differential equation [22, 20]:

$$\frac{dA}{dt} = -\gamma^2 D|\mathbf{F}|^2 A.$$

Its solution can be found by integrating from $t = 0$ to $t = TE$, which yields Stejskal-Tanner's formulation of the PGSE signal decay due to diffusion when $\mathbf{G}(t) = \mathbf{G} = g\mathbf{g}$, where $g = |\mathbf{G}|$ and $\mathbf{g} = \mathbf{G}/|\mathbf{G}|$ [22, 20]:

$$S = S_0 \exp\left(-\gamma^2\delta^2 g^2\left(\Delta - \frac{\delta}{3}\right)D\right) = S_0 \exp\left(-bD\right), \tag{3.22}$$

where $S = A(TE)$ is the magnitude of the signal decay due to diffusion, $S_0 = A(0)$ is the magnitude of the signal in the absence of a diffusion encoding gradient, and $b = \gamma^2\delta^2 g^2\left(\Delta - \frac{\delta}{3}\right)$ is the b-value. This, therefore, makes it possible to measure the diffusion coefficient D from a PGSE and a regular spin-echo experiment in NMR.

In the same year, Stejskal further considered diffusion in anisotropic media by employing the anisotropic Fick's equation (Eq-3.11) instead of the isotropic equation (Eq-3.9), in the Bloch-Torrey equation (Eqs-3.18, 3.19), which introduces the diffusion tensor $\mathbf{D}$ [23]:

$$\frac{\partial M_+}{\partial t} = -i\gamma B_0 M_+ - \frac{M_+}{T_2} - i\gamma\mathbf{r}\cdot\mathbf{G}(t)M_+ + \nabla\cdot\mathbf{D}\nabla M_+. \tag{3.23}$$

Solving as shown in the case of the isotropic diffusion, he was able to show the modified Stejskal-Tanner equation incorporating the diffusion tensor in anisotropic media [23, 20]:

$$S = S_0 \exp\left(-\gamma^2\int_0^{TE}\mathbf{F}(t')^T\mathbf{D}\mathbf{F}(t')dt'\right), \tag{3.24}$$

$$S = S_0 \exp\left(-\gamma^2\delta^2 g^2\left(\Delta - \frac{\delta}{3}\right)\mathbf{g}^T\mathbf{D}\mathbf{g}\right) = S_0 \exp\left(-b\mathbf{g}^T\mathbf{D}\mathbf{g}\right), \tag{3.25}$$

where the second equation is again when $\mathbf{G}(t) = \mathbf{G} = g\mathbf{g}$.

However, Stejskal in this seminal paper fell short of providing a method for measuring the diffusion tensor from NMR, which could have preempted diffusion tensor imaging by almost three decades. But he did show the following relationship, which laid the foundations for the q-space formalism – under the assumption when $\delta \to 0$, but with $\delta\mathbf{G}$ finite, which implies a true "pulsed" gradient [23]:

$$S(\mathbf{G}, \Delta) = S_0 \int P_0(\mathbf{r}_0)\int P(\mathbf{r}|\mathbf{r}_0, \Delta)\exp\left(i\gamma\delta(\mathbf{r}-\mathbf{r}_0)\cdot\mathbf{G}\right)d\mathbf{r}d\mathbf{r}_0, \tag{3.26}$$

where $P(\mathbf{r}|\mathbf{r}_0, \Delta)$ is the transition probability of a spin bearing particle starting at $\mathbf{r}_0$ and migrating to $\mathbf{r}$ after the diffusion time interval Δ, and where $P_0(\mathbf{r}_0)$ is the initial spin density.

3.3.3 q-space Formalism: A Random Walk Approach

After a Fickian or phenomenological treatment of the self diffusing net magnetization, again diffusion can be viewed from a probabilistic or random-walk model driven by the thermal kinetic energy of the spin bearing particles.

The PGSE experiment (Fig-3.4) spatially encodes or labels the transverse phase of the spins using the first gradient, which results in a deliberate dephasing of the transverse magnetization. The purpose of the second gradient after the 180^o RF pulse is to undo the effects of the first gradient and rephase the transverse magnetization. However, if the spins diffuse away from their position between the two gradients, then the transverse magnetization isn't entirely rephased after the second gradient, resulting in a loss of the transverse signal. This can be described by using a random-walk approach for the spin bearing particles.

Under the assumption $\delta \ll \Delta$, which is known as the *narrow gradient pulse* (NGP) condition, which implies that the spins are static during the application of the diffusion encoding gradients $\mathbf{G}(t)$, the dephasing accrued by a spin in the initial position $\mathbf{r}_0$ during the first gradient is [24]:

$$\phi_1 = \gamma \int_0^{\delta} \mathbf{G}(t) \cdot \mathbf{r}_0 dt = \gamma \delta \mathbf{G} \cdot \mathbf{r}_0,$$

when $\mathbf{G}(t) = \mathbf{G} = g\mathbf{g}$. Similarly the dephasing accrued by the spin, now in the position $\mathbf{r}$ due to diffusion, during the second gradient is:

$$\phi_2 = \gamma \int_{\Delta}^{\Delta+\delta} \mathbf{G}(t) \cdot \mathbf{r} dt = \gamma \delta \mathbf{G} \cdot \mathbf{r}.$$

Since the second gradient is applied after the 180^o RF pulse, which flips the spins around, the net phase shift accrued by a spin is $\phi = \phi_2 - \phi_1 = \gamma \delta \mathbf{G} \cdot (\mathbf{r} - \mathbf{r}_0)$. Of course, if the spins hadn't diffused and had remained static during the period Δ (between the gradients), then the net phase shift would have cancelled out. In other words the amount of net phase shift is proportional to the diffused distance $(\mathbf{r} - \mathbf{r}_0)$.

The NGP condition $\delta \ll \Delta$ can also be interpreted in the way Stejskal proposed it $\delta \to 0$, with $\delta\mathbf{G}$ finite. Although in practice the NGP condition can never be achieved, it provides a powerful insight into the process of measuring diffusion from NMR.

The complex signal generated by individual spins with a net phase shift ϕ is $\exp(i\phi) = \exp\left[i\gamma\delta\mathbf{G} \cdot (\mathbf{r} - \mathbf{r}_0)\right]$ [25, 24]. However, the spin echo signal $E(\mathbf{G}, \Delta)$ is the averaged net signal from the spin ensemble, or it is the expected value of the complex signal given the probability of spins starting at $\mathbf{r}_0$ and diffusing to $\mathbf{r}$ in the time Δ. This probability is the product of the probabilities $f(\mathbf{r}_0, 0)$, of finding a spin initially at $\mathbf{r}_0$, and $P(\mathbf{r}|\mathbf{r}_0, \Delta)$, of a single spin starting at $\mathbf{r}_0$ and diffusing to $\mathbf{r}$ in time Δ. The product

$f(\mathbf{r}_0, 0)P(\mathbf{r}|\mathbf{r}_0, \Delta)$ introduces the random-walk model for the spin bearing particles diffusing from $\mathbf{r}_0$ to $\mathbf{r}$, and [25]:

$$E(\mathbf{G}, \Delta) = \int f(\mathbf{r}_0, 0) \int \exp\left[i\gamma\delta\mathbf{G} \cdot (\mathbf{r} - \mathbf{r}_0)\right] P(\mathbf{r}|\mathbf{r}_0, \Delta) d\mathbf{r} d\mathbf{r}_0. \tag{3.27}$$

This form of the signal corresponds to the equation (Eq-3.26) derived by Stejskal [23], with $f(\mathbf{r}_0, 0)$ as the spin density $P_0(\mathbf{r}_0)$. This also indicates that in the absence of diffusion encoding gradients:

$$E(\mathbf{0}, t) = 1. \tag{3.28}$$

In practice $E(\mathbf{G}, \Delta)$ is obtained by dividing the echo signal amplitude from a PGSE experiment with diffusion gradients by the echo signal amplitude from a Hahn spin echo experiment without gradients $E(\mathbf{G}, \Delta) = S(\mathbf{G})/S_0$.

This leads to the q-space formalism by defining a reciprocal space q where [25]:

$$\mathbf{q} := \frac{\gamma\delta\mathbf{G}}{2\pi}. \tag{3.29}$$

Inserting q in Eq-3.27 gives the q-space signal:

$$E(\mathbf{q}, \Delta) = \int f(\mathbf{r}_0, 0) \int \exp\left[i2\pi\mathbf{q} \cdot (\mathbf{r} - \mathbf{r}_0)\right] P(\mathbf{r}|\mathbf{r}_0, \Delta) d\mathbf{r} d\mathbf{r}_0. \tag{3.30}$$

Assuming the transition probability $P(\mathbf{r}|\mathbf{r}_0, \Delta)$ to be translationally invariant or that the movement of a spin is independent of the movements of the other spins and also of its own position and movements in the past – as in a random-walk, implies that $P(\mathbf{r}|\mathbf{r}_0, \Delta) = P(\Delta\mathbf{r}, \Delta)$, which is the diffusion propagator. Also since in a random-walk the movement of all the particles is independent and identical, and since the complex signal and the diffusion propagator for a spin only depend on the spin displacement $\Delta\mathbf{r} = (\mathbf{r} - \mathbf{r}_0)$, it is useful to consider the *ensemble average propagator* (EAP), which describes the average probability of any spin in the ensemble diffusing by $\Delta\mathbf{r}$ during the time Δt [25]:

$$\overline{P}(\Delta\mathbf{r}, \Delta t) = \int P(\Delta\mathbf{r}, \Delta t) f(\mathbf{r}_0, 0) d\mathbf{r}_0. \tag{3.31}$$

Combining Eqs-3.30 & 3.31 gives the main result of the q-space formalism [25]:

$$E(\mathbf{q}, t) = \int \overline{P}(\Delta\mathbf{r}, t) \exp\left(i2\pi\mathbf{q} \cdot \Delta\mathbf{r}\right) d\Delta\mathbf{r}, \tag{3.32}$$

which establishes an inverse Fourier Transform relationship between the EAP, henceforth denoted $P(\mathbf{r})$, and the normalized echo signal, henceforth denoted $E(\mathbf{q})$.

This Fourier relationship between the ensemble average diffusion propagator and the diffusion NMR signal ushers in the paradigm change that diffusion can be viewed more than just an intrinsic property, but also as a probe of the microstructure of the underlying medium. This becomes apparent when the medium is anisotropic and has a complex microstructure, which is the case in cerebral white matter where numerous

fiber bundles criss-cross at a resolution much finer than the view of dMRI. However, it is interesting to see how the diffusion coefficient or the diffusion tensor can be measured from the q-space formalism. It provides an insight into "free" diffusion.

The case of free diffusion The q-space formalism can also be used to measure the diffusion coefficient (or the diffusion tensor) just like the phenomenological approach. This can be achieved by adopting the probabilistic interpretation of the inverse Fourier Transform of the EAP (Eq-3.32). Since the EAP is real and symmetric, in probability theory its inverse Fourier Transform $E(\mathbf{q})$, is the *characteristic function* of $P(\mathbf{r})$ [24, 26]. Therefore, the *cumulant generating function* (CGF) of $P(\mathbf{r})$, which gives its cumulants, is:

$$\ln\left(E(\mathbf{q})\right) = \sum_{n=1}^{\infty} K^{(n)}_{j_1 j_2 \cdots j_n} G_{j_1} G_{j_2} \cdots G_{j_n} \frac{(i\gamma\delta)^n}{n!}, \tag{3.33}$$

where $K^{(n)}_{j_1 j_2 \cdots j_n}$ are the coefficients of the nth order cumulant tensor $\mathbf{K}^{(n)}$, G_{j_k} are the components of the gradient vector $\mathbf{G}$ constituting $\mathbf{q}$, and the repeated indices indicate summation over their entire range $K^{(n)}_{j_1 j_2 \cdots j_n} G_{j_1} G_{j_2} \cdots G_{j_n} = \sum_{j_1, j_2, \cdots, j_n} K^{(n)}_{j_1 j_2 \cdots j_n} G_{j_1} G_{j_2} \cdots G_{j_n}$. In 1D, the cumulant tensors become the scalar cumulants k_n.

Since free diffusion is described by a Gaussian distribution (Eq-3.17), and since a Gaussian distribution only has two non-zero cumulant tensors $\mathbf{K}^{(1)}_G \& \mathbf{K}^{(2)}_G$, namely the mean and the covariance tensors, Eq-3.17 implies:

$$\begin{aligned} \mathbf{K}^{(1)}_G &= \mathbf{0}, \\ \mathbf{K}^{(2)}_G &= 2\Delta t \mathbf{D}. \end{aligned} \tag{3.34}$$

Comparing the Fickian diffusion equation (Eq-3.11) to the random-walk diffusion equation (Eq-3.15) reveals that the diffusion tensor can be seen as the covariance tensor $\mathbf{K}^{(2)}_G$ or $2\Delta t \mathbf{D}$, a correspondence that had also been established in section-3.3.1 and in [27].

Therefore, if the EAP $P(\mathbf{r})$ is considered to be Gaussian (free diffusion), then the expansion of its CGF (Eq-3.33) has only two cumulant terms $\mathbf{K}^{(1)} = \mathbf{K}^{(1)}_G = \mathbf{0}$ and $\mathbf{K}^{(2)} = \mathbf{K}^{(2)}_G = 2\Delta t \mathbf{D}$, which is the diffusion tensor. However, this implies that the echo signal $E_F(\mathbf{q})$ for anisotropic free diffusion is:

$$E_F(\mathbf{q}) = \exp\left(-\gamma^2 \delta^2 \Delta D_{j_1 j_2} G_{j_1} G_{j_2}\right) \approx \exp\left(-b \mathbf{g}^T \mathbf{D} \mathbf{g}\right), \tag{3.35}$$

where the value of Δt is Δ, and the approximation $b \approx \gamma^2 \delta^2 g^2 \Delta$ reflects the NGP condition $\delta \ll \Delta$ which implies that $(\Delta - \delta/3) \approx \Delta$. When $\mathbf{D} = D\mathbf{I}$, it reveals the echo signal for isotropic free diffusion:

$$E_F(\mathbf{q}) \approx \exp(-bD). \tag{3.36}$$

These equations can be used to measure the diffusion coefficient (or the diffusion tensor) from the q-space formalism.

The random-walk approach or the q-space formalism to formulate the signal for free anisotropic diffusion reveals an interesting insight into "free" diffusion. Free diffusion was named so because its solution (Eq-3.17) was derived from only an initial condition and no boundary conditions. But indeed what is the reason for "anisotropy", if not the effect of boundaries hindering the diffusion process? This apparent contradiction is reconciled from the expansion of $P(\mathbf{r})$'s CGF (Eq-3.33). By understanding that "free" diffusion in heterogeneous media corresponds to only the first two terms in the expansion (Eq-3.34), it becomes clear that free diffusion is in fact a low order spatial approximation of the true diffusion [28]. In other words the effects of boundary conditions on the propagator-solution of the diffusion equation would be reflected by the cumulants of order higher than two in the expansion of the EAP's CGF.

Further, under the NGP condition, the correspondence between the signal for free diffusion in the q-space formalism and the signal from Stejskal-Tanner's formulation using the phenomenological approach Eqs-3.22 & 3.36 (1D) and Eqs-3.25 & 3.35 (3D), indicates the consistency between the two approaches. It also shows that under the NGP condition, the Stejskal-Tanner signal formulation or the phenomenological approach corresponds to the free diffusion or a Gaussian solution to the Fick's diffusion equation considered in the Bloch-Torrey equation. This was in fact noted by Stejskal in [23]. Therefore, under the NGP condition, the Stejskal-Tanner signal formulation does not consider boundary conditions for diffusion.

The phenomenological approach to dNMR (Stejskal-Tanner's modified signal Eq-3.25), and the random-walk approach to dNMR (Fourier relationship Eq-3.32 & free diffusion signal Eq-3.35) are complementary descriptions for dNMR. The phenomenological approach can deal with various forms of diffusion encoding gradients $\mathbf{G}(t)$, while the random-walk approach or q-space formalism assumes a NGP, which in practice cannot be achieved. In this sense the phenomenological approach is more general than the q-space formalism. However, under the NGP condition, the phenomenological approach corresponds to free diffusion. Boundary conditions would have to be included for it to be solved correctly in anisotropic media. However, when diffusion is being used as a probe for the medium's microstructure, boundary conditions are unknown, and this would present a handicap. In this respect, the q-space formalism is more general, since it presents a generic diffusion propagator that only depends on the signal, and that can be used to infer the medium's microstructure. In other words, under the NGP condition and other than in free diffusion, when inferring the microstructure of the underlying medium, the q-space formalism solves a direct problem, while the phenomenological approach or Fickian approach can be used to solve an inverse problem.

3.4 DIFFUSION MRI

Although Stejskal in [23] formulated the signal for anisotropic diffusion using a *diffusion tensor* (DT), the reason he fell short of providing a method for estimating the DT is perhaps because he was involved with dNMR. In such experiments it was generally possible to re-orient the experimental setup to align the primary anisotropy direction with the laboratory frame, sufficing it to measure the diffusion coefficient in only three directions [29, 5].

This however changed with MRI and dMRI, when large anisotropic specimen that couldn't be rotated in the scanner began to be imaged. Imaging such specimen, e.g. cerebral white matter tissue, or the entire brain, revealed that the diffusion coefficient measured in such specimen depended upon the direction of the diffusion encoding gradient. In other words the dMRI signal decay was different along different gradient directions. Or again such dMRI images revealed different contrasts as the diffusion encoding gradient was rotated. These dMRI images were called *diffusion weighted images* (DWIs). DWIs were at first cryptic because while they revealed the diffusion coefficient, they clearly also indicated that the underlying tissue was highly anisotropic, but they did not provide a method for inferring the preferential directions of this anisotropy. The diffusion coefficients computed from these DWIs using Stejskal-Tanner's isotropic signal decay formulation $S = S_0 \exp(-bD)$ (Eq-3.22) were called the *apparent diffusion coefficient* (ADC), since these changed in the highly anisotropic tissue depending on the direction of the diffusion encoding gradient. This limitation of the DWI's, and of Stejskal-Tanner's isotropic signal formulation, shifted the interest from measuring only the diffusion coefficient to inferring the preferential diffusion anisotropy directions, or to using diffusion as a probe to infer the tissue's microstructure. This brought forth a whole new meaning to Stejskal's DT formulation, and it's measurement from dMRI, since its diagonalisation provided a local coordinate system that was a good indicator of the preferential diffusion anisotropy directions or the underlying medium's microstructure.

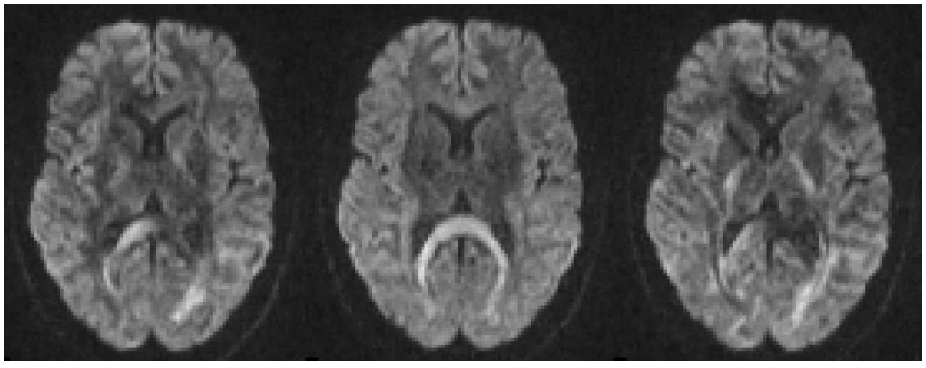

Figure 3.5: Diffusion Weighted Images (DWIs) of the brain acquired along different gradient encoding directions showing different contrasts.

This section presents modern dMRI reconstruction techniques, which are employed to infer the microstructure of the cerebral white matter. Beginning with the classical diffusion tensor imaging, this section first presents techniques based on Stejskal-Tanner's formulation for the signal. These techniques based on Fick's diffusion equations attempt to estimate the ADC with greater accuracy than DTI. Then this section presents techniques based on the q-space formalism, which leverage the Fourier relationship between the signal and the diffusion propagator. These techniques estimate either the entire propagator or its characteristics to infer the microstructure of the white matter with greater accuracy than DTI.

3.4.1 Diffusion Tensor Imaging

Diffusion tensor imaging (DTI) was introduced by Basser et al. [30, 31] in 1994, which for the first time provided a method for measuring the DT from dMRI and for inferring the local tissue microstructure from the DT. Starting from Stejskal's equation (Eq-3.24), Basser et al. defined the b-matrix, which also accounted for the imaging gradients in addition to the pure diffusion encoding gradients [30, 31]:

$$\mathbf{b} = \gamma^2 \int_0^{TE} \mathbf{F}(t')\mathbf{F}(t')^T dt', \tag{3.37}$$

where $\mathbf{F}(t)$ is defined as in Eq-3.21. They formulated the PGSE echo signal to be:

$$S = S_0 \exp\left(-tr(\mathbf{bD})\right), \tag{3.38}$$

where $tr(\mathbf{A})$ represents the trace of the matrix $\mathbf{A}$. This simplifies to Stejskal's formulation (Eq-3.25) $S = S_0 \exp\left(-b\mathbf{g}^T\mathbf{Dg}\right)$ in the absence of the imaging gradients, or under the consideration that the imaging gradients are small compared to the diffusion encoding gradients, which is mostly true [20]. Otherwise, the b-matrix has to be computed from the dynamics of the imaging and the diffusion encoding gradients.

DTI Estimation $\mathbf{D}$ is a covariance tensor, therefore, it is symmetric and positive definite. This implies that there are six unknowns to be estimated from the DTI signal in Eq-3.38. Therefore, at least six DWIs, acquired along linearly independent and non-coplanar gradient directions, and a non diffusion weighted or Hahn spin echo (S_0) image is required to measure the six unknown coefficients of $\mathbf{D}$. The linearized version of Eq-3.38 provides the simplest scheme for doing this [30, 31]:

$$\ln\left(\frac{S}{S_0}\right) = -b_{ij}D_{ij}. \tag{3.39}$$

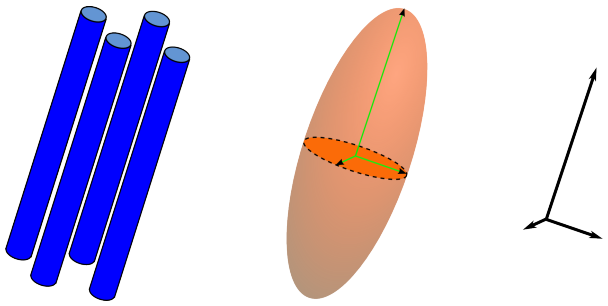

Figure 3.6: Microstructure from DTI. Coherent fibers can be inferred from the ellipsoid of the diffusion tensor (DT). The DT also provides a local coordinate system that indicates the preferential diffusion anisotropy directions.

In practice, often more than six DWIs are used to account for acquisition noise. In the case of N DWIs, the linearized equation for the signal is written in a matrix form:

$$\begin{bmatrix} -\ln(S_1/S_0) \\ -\ln(S_2/S_0) \\ -\ln(S_3/S_0) \\ \vdots \\ -\ln(S_N/S_0) \end{bmatrix} = \begin{bmatrix} b_{11}^1 & 2b_{12}^1 & 2b_{13}^1 & b_{22}^1 & 2b_{23}^1 & b_{33}^1 \\ b_{11}^2 & 2b_{12}^2 & 2b_{13}^2 & b_{22}^2 & 2b_{23}^2 & b_{33}^2 \\ b_{11}^3 & 2b_{12}^3 & 2b_{13}^3 & b_{22}^3 & 2b_{23}^3 & b_{33}^3 \\ \vdots & \vdots & \vdots & \vdots & \vdots & \vdots \\ b_{11}^N & 2b_{12}^N & 2b_{13}^N & b_{22}^N & 2b_{23}^N & b_{33}^N \end{bmatrix} \begin{bmatrix} D_{11} \\ D_{12} \\ D_{13} \\ D_{22} \\ D_{23} \\ D_{33} \end{bmatrix}, \tag{3.40}$$

$$\mathbf{X} = \mathbf{B}\mathbf{d}. \tag{3.41}$$

The easiest option for solving this is to use the least squares optimization $\mathbf{d}_{opt} = argmin_{\mathbf{d}}||\mathbf{X} - \mathbf{B}\mathbf{d}||^2$, which translates to the Moore-Penrose pseudo-inverse solution:

$$\mathbf{d} = (\mathbf{B}^T\mathbf{B})^{-1}\mathbf{B}^T\mathbf{X}.$$

Due to its linear form which only involves matrix manipulations, this solution is extremely rapid. However, it doesn't account for the signal noise or of the distortion to the noise it introduces while taking the logarithms of the signal in the linearization process. Due to DTI's popularity and maturity as a technique of probing tissue microstructures, a number of sophisticated solutions exist for measuring $\mathbf{D}$ from the dMRI signal. These range from Basser's original weighted least squares approach [30] which accounts for the logarithmic distortion of the signal noise, to non-linear optimization approaches that account for signal noise, spatial smoothing, and also for constraining the DT to be positive definite [32, 33, 34, 35, 36, 37, 1].

Microstructure from DTI The consistency between the phenomenological approach and the q-space formalism, under the NGP condition, implies that the propagator describing the diffusion measured by DTI is the Gaussian PDF (Eq-3.17):

$$P(\Delta\mathbf{x}, t) = \frac{1}{(4\pi t)^{3/2}|\mathbf{D}|^{1/2}} \exp\left(-\frac{\Delta\mathbf{x}^T\mathbf{D}^{-1}\Delta\mathbf{x}}{4t}\right).$$

This is an oriented Gaussian parameterized by the DT $\mathbf{D}$, or its inverse. The orientation of the PDF can be deduced from the eigen-decomposition of the DT. The eigenvalues and eigenvectors of $\mathbf{D}$ form a local coordinate system that indicates the preferential diffusion direction orienting the Gaussian PDF. In other words it indicates the diffusion direction favoured by the microstructure of the medium. This preferential orientation of the microstructure can be visually represented by the ellipsoid represented by $\mathbf{D}$ whose implicit quadratic form is [31]:

$$\frac{\mathbf{x}^T\mathbf{D}^{-1}\mathbf{x}}{2t} = 1. \tag{3.42}$$

Since $\mathbf{D}$ is symmetric it can be diagonalized $\mathbf{D} = \mathbf{W^T\Lambda W}$, where $\mathbf{W}$ are its orthonormal eigenvectors and $\mathbf{\Lambda}$ is a diagonal matrix whose diagonal elements are its eigenvalues. The canonical form of the diffusion ellipsoid defined by $\mathbf{D}^{-1}$ emerges in the coordinate frame of its eigenvectors:

$$\left(\frac{x'}{\sqrt{2\lambda_1 t}}\right)^2 + \left(\frac{y'}{\sqrt{2\lambda_2 t}}\right)^2 + \left(\frac{z'}{\sqrt{2\lambda_3 t}}\right)^2 = 1.$$

To infer the microstructure of the cerebral white matter from DTI, the fundamental assumption is that the coherent fiber bundle structures formed by the axons hinder the perpendicular diffusion of water molecules (spin bearing ^1H atoms) more than the parallel diffusion. Therefore, the elongation and orientation of the DT are good indicators of these coherent structures or fiber bundles locally. The eigenvector corresponding to the largest eigenvalue, the major eigenvector, indicates the main fiber direction, while the other eigenvectors and eigenvalues indicate diffusion anisotropy in the perpendicular plane.

Scalar Measures The microstructure of the medium or the white matter can be further characterized from a number of rotationally invariant scalar measures derived from the DT that reveal diffusive properties of the underlying tissue. Two such scalar measures are of primary importance since they are often used as bio-markers. The first is *mean diffusivity* (MD) which is $\overline{\lambda} = tr(\mathbf{D})/3$ [38].

Fractional anisotropy (FA) is the other measure which describes the amount of anisotropy presented by the microstructure. It too is derived from the eigenvalues of $\mathbf{D}$ [38]:

$$\text{FA} = \sqrt{\frac{3}{2}}\sqrt{\frac{(\lambda_1 - \overline{\lambda})^2 + (\lambda_2 - \overline{\lambda})^2 + (\lambda_3 - \overline{\lambda})^2}{\lambda_1^2 + \lambda_2^2 + \lambda_3^2}}.$$

There also exist a number of other scalar measures [39].

Tracing Fibers from DTI When DTI is performed on the brain, the DT in every voxel is a local indicator of coherent structures or fiber bundles in the cerebral white matter. However, the process of reconstructing the global structures of fiber bundles by connecting the local information is known as fiber tracing or *tractography*. Tractography graphically reconstructs the connectivity of the cerebral white matter by

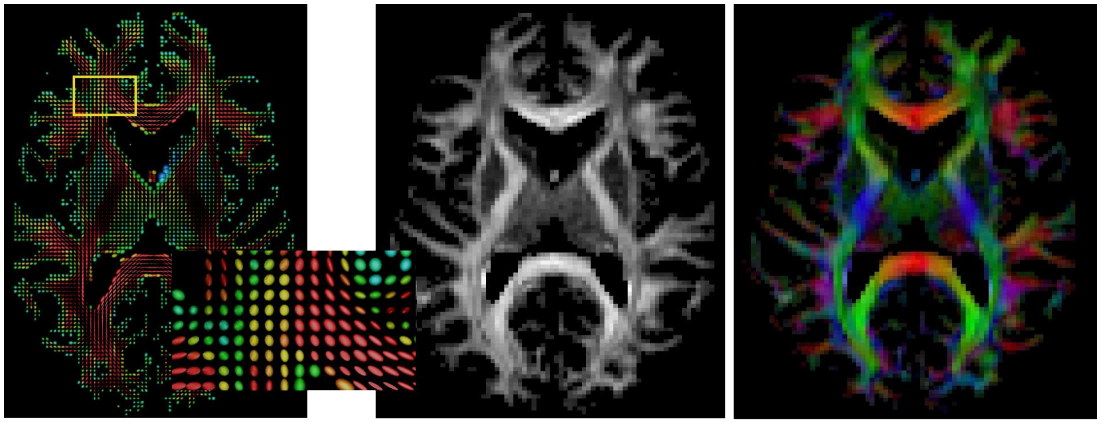

Figure 3.7: Diffusion Tensor Imaging (DTI). (a) DTI ellipsoids from an axial slice of the brain, with zoom. (b) Fractional Anisotropy (FA). (c) Colour FA where the colour components RGB represent the unit major eigenvector of the diffusion tensor $\mathbf{e}_1 = [r, g, b]^T$ weighted by FA. Or the colours indicate the preferential diffusion anisotropy directions.

integrating along the direction indicated by the local geometry of the DT. It is a tool that is unique in the sense that it permits an indirect dissected visualization of the brain in-vivo and non-invasively [40]. The underpinnings of tractography are also based on the fundamental assumption of dMRI mentioned above, i.e. that the diffusion of water molecules is hindered to a greater extent perpendicular to coherent fiber bundle structures than parallel to these. Therefore, following the geometry of the local DT and integrating along reveals the continuous dominant structure of the fiber bundle. Tractography became possible once DTI was established.

Of the many tractography algorithms, the continuous deterministic tractography is a widely used scheme that was proposed for DTI [41]. It considers a fiber tract as a 3D space curve parametrized by its arc-length, $\mathbf{r}(s)$, and describes it by its Frenet equation:

$$\frac{d\mathbf{r}(s)}{ds} = \mathbf{t}(s) = \epsilon_1(\mathbf{r}(s)),\ \mathbf{r}(0) = \mathbf{r}_0 \tag{3.43}$$

where $\mathbf{t}(s)$ the tangent vector to $\mathbf{r}(s)$ at s is equal to the unit major eigenvector $\epsilon_1(\mathbf{r}(s))$ of the DT at $\mathbf{r}(s)$. This implies that fiber tracts are locally tangent to the major eigenvector of the DT.

Integrating the differential equation Eq.3.43 generates individual fiber tracts starting from seed voxels $\mathbf{r}_0$. There exist various schemes for numerical integration, for estimation of a spatially continuous tensor field from a discrete DTI tensor field, and for stopping the integration process heuristically [41]. These influence the quality of the fibers that are traced from the DTI.

3.4.2 ADC & Generalized DTI

The usage of the ADC was prevalent even before the advent of DTI. It was defined from Stejskal-Tanner's isotropic signal formulation (Eq-3.22):

$$S = S_0 \exp\left(-b.\mathrm{ADC}\right).$$

The diffusion coefficient measured from Eq-3.22 in anisotropic media was named the ADC since its value changed depending upon the direction in which it was measured, or equivalently on the direction of the diffusion encoding direction. The ADC was replaced by DTI since DTI could express a more complex ADC than the previous scalar value, namely the ADC in DTI is described by the spherical function:

$$\mathrm{ADC} = \mathbf{g}^T \mathbf{D} \mathbf{g}.$$

However, interest returned to the ADC, when it was realized that the complexity of the cerebral white matter's microstructure was sometimes beyond the scope of DTI or the free diffusion Gaussian propagator. Since the fiber bundles in the white matter criss-crossed at a resolution finer than that of dMRI, the DT was only an average description of the true microstructure. Therefore, when fiber bundles crossed

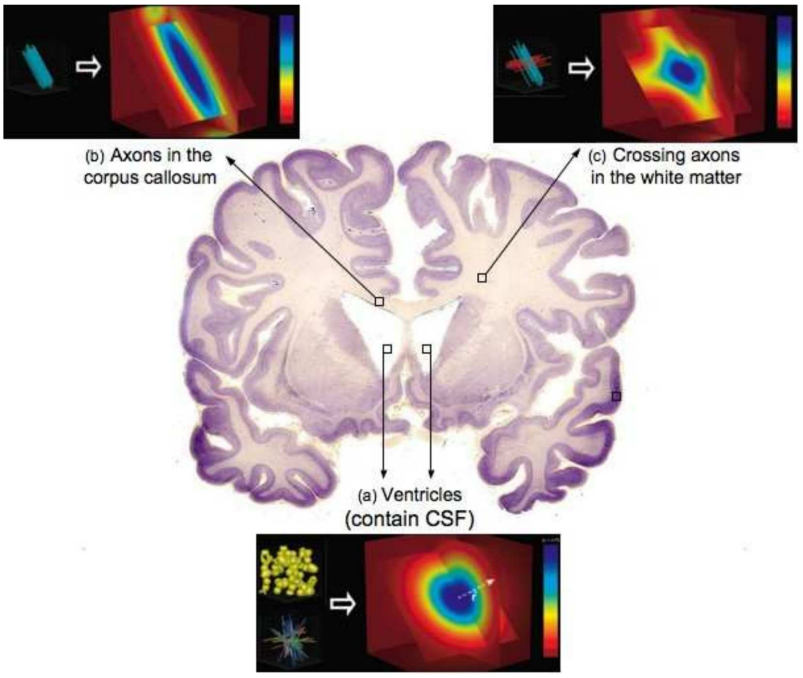

Figure 3.8: Microstructural complexities in the cerebral white matter due to the criss-crossing of fibers at a resolution finer than that of dMRI. Regions with isotropic diffusivity, regions with simple unidirectional anisotropic diffusivity, and regions with complex multi-directional anisotropic diffusivity. From [3], with original figures adapted from [42] and from Brain Museum.

within a voxel, even though they presented locally, within the voxel, two independent preferential directions of anisotropy, the DT perceived this as isotropy, and failed to discern the independent preferential directions of anisotropy.

This can be understood in two ways. Mathematically, the preferential direction indicated by a DT can be understood from either its eigen-decomposition or equivalently from its quadratic form describing its ellipsoid Eq-3.42. Since the quadratic form is nothing but a 2nd order homogeneous polynomial, it is clearly limited to only a pair of antipodally symmetric maxima. The presence of additional anisotropy directions makes the quadratic form more isotropic. From a physical view point, as seen previously, Gaussian diffusion or free diffusion was derived from the diffusion equation without boundary conditions. However, in the presence of such boundaries or criss-crossing fibers, Gaussian diffusion is a low order spatial approximation of the true diffusion when viewed from the q-space formalism. Therefore, DTI is inherently limited in voxels with complex fiber bundle configurations, such as crossings.

However, this microstructural complexity could be seen in the ADC. Returning interest in the ADC brought along the novel concept of general spherical functions described mathematically by different functional bases to describe the richer geometries of the microstructure probed by diffusion. Frank introduced the *Spherical Harmonic* (SH) basis for the first time in 2002 to model the ADC [43]. Although the ADC was soon abandoned since, SHs turned out to be an invaluable contribution to the field of dMRI. Similarly Ozarslan [44] and Liu [45] introduced Cartesian *higher order tensors* (HOTs) for modelling the ADC.

ADC was soon abandoned because although it was sensitive to complex fiber configurations, it wasn't well suited for inferring these fiber directions. Unlike DTI, it wasn't a good indicator of the medium's microstructure since its maxima weren't aligned with the preferential anisotropy directions [46]. However, before q-space became popular in dMRI, two methods generalizing the DTI-ADC, $D(\mathbf{g}) = \mathbf{g}^T\mathbf{D}\mathbf{g}$, were proposed to overcome its shortcoming.

GDTI1 GDTI1 (so called in this thesis) was proposed by Ozarslan in 2003 [44]. Essentially it considers a modified Fick's second law Eq-3.9, generalized such that the diffusion coefficient is replaced by a spherical function parameterized by a Cartesian HOT, in the Bloch-Torrey equation (Eq-3.19). The generalized diffusion term in the Bloch-Torrey equation is:

$$\frac{\partial M_+}{\partial t} = D^{(n)}_{j_1 j_2 \cdots j_n} g_{j_1} g_{j_2} \cdots g_{j_n} \nabla^2 M_+,$$

where $D^{(n)}_{j_1 j_2 \cdots j_n}$ are the coefficients of an nth order tensor $\mathbf{D}^{(n)}$, g_{j_k} are the components of the unit gradient vector $\mathbf{g} = \mathbf{G}/|\mathbf{G}|$ when the gradient vector is $\mathbf{G}$, and the repeated

indices indicate summation over their entire range. Solving the Bloch-Torrey equation along the lines of Stejskal and Tanner gives a generalized Stejskal-Tanner signal formulation, which in the absence of imaging gradients is [44]:

$$-\ln\left(\frac{S}{S_0}\right) = b \cdot D^{(n)}_{j_1 j_2 \cdots j_n} g_{j_1} g_{j_2} \cdots g_{j_n},$$

where b is the b-value. This shows that the generalized ADC is the spherical diffusion function that was used to modify Fick's law:

$$D(\mathbf{g}) = D^{(n)}_{j_1 j_2 \cdots j_n} g_{j_1} g_{j_2} \cdots g_{j_n}.$$

Since negative diffusion is non-physical, naturally the HOT $\mathbf{D}^{(n)}$, parameterizing the ADC, is of even order. $\mathbf{D}^{(n)}$ is also symmetric, such that its coefficients are invariant under any permutations of the indices. When $n = 2$ this becomes the DTI-ADC:

$$D(\mathbf{g}) = \sum_{i=1}^{3}\sum_{j=1}^{3} D_{ij} g_i g_j = \mathbf{g}^T \mathbf{D} \mathbf{g}.$$

This forms an alternate basis to the SH basis for modelling complex ADCs.

Interestingly, when viewed under the NGP condition, which is not a requirement of this method, it reveals that to account for complex microstructures, this method doesn't really consider boundary conditions. It accounts for complex microstructure by using a spherical diffusion function that reflects the form of the complex ADC. However, under the q-space formalism the ADC (or the signal) is in the Fourier space of the EAP. Therefore, the spherical diffusion function describes the effects of complex microstructures in the Fourier domain.

GDTI2 GDTI2 (so called in this thesis) was proposed by Liu also in 2003 [45]. This is perhaps the first approach that attempted to recover the diffusion EAP using basis functions to describe the signal and the EAP. This is of utmost value in the q-space formalism, since a correct choice of basis functions in the signal domain can lead to an analytical form for the Fourier Transformed EAP. This lies at the heart of modern q-space techniques. However, the complex fashion in which GDTI2 compares the phenomenological Bloch-Torrey equation to the q-space formalism in the case of non-free diffusion to achieve its results, is perhaps an indicator of the phase when dMRI transitioned from the phenomenological approach to the q-space formalism, which was also referred to as "higher order descriptions" in the dMRI terminology.

GDTI2 employs both the q-space formalism and the phenomenological approach. Therefore, it assumes the NGP condition. From the q-space perspective it relies on the CGF of the EAP (Eq-3.33). In the phenomenological approach, GDTI2 like GDTI1 doesn't consider boundary conditions for the diffusion equation, and instead modifies

the diffusion equation itself. In the derivation of the diffusion equation in the random-walk model, the passage from Eq-3.14 to Eq-3.15 was made by considering only the smallest non-zero terms in the Taylor expansions of Eq-3.14. GDTI2 modifies this by considering all the terms in the Taylor expansion of the spatial component, i.e. the RHS of Eq-3.14. This leads to the diffusion equation:

$$\frac{\partial C}{\partial t} = \sum_{n=2}^{\infty} \left[D^{(n)}_{j_j i_2 \ldots j_n} \nabla^{(n)}_{j_1 j_2 \ldots j_n} C \right],$$

where $D^{(n)}_{j_1 j_2 \ldots j_n}$ are the coefficients of an n-th order three dimensional Cartesian diffusion tensor $\mathbf{D}^{(n)}$, the repeated indices indicate summation over their entire range, and by an abuse of notation:

$$\nabla^{(n)}_{j_1 j_2 \ldots j_n} C = \frac{\partial^{(n-1)} C}{\partial x_{j_2} \partial x_{j_3} \ldots \partial x_{j_n}}.$$

Using this diffusion equation in the Bloch-Torrey equation and again solving along the lines of Stejskal and Tanner gives another generalized Stejskal-Tanner equation, which in the presence of imaging gradients has the form:

$$\ln\left(\frac{S}{S_0}\right) = \sum_{n=1}^{\infty} \left[i^n D^{(n)}_{j_1 j_2 \ldots j_n} b^{(n)}_{j_1 j_2 \ldots j_n} \right],$$

where $b^{(n)}_{j_1 j_2 \ldots j_n}$ are the coefficients of the nth order $\mathbf{b}^{(n)}$-tensor which is a generalization of the b-matrix.

Comparing this to the CGF expansion of the EAP in Eq-3.33, where in both the expansions only the even terms are non-zero (since for the CGF expansion, the EAP is considered symmetric, and for the random-walk formulation expansion, the transition probability is considered symmetric), reveals their similarity and leads to:

$$\begin{aligned} K^{(n)}_{l_1 l_2 \ldots l_n} &= (-1)^n n! D^{(n)}_{l_1 l_2 \ldots l_n} \left(\Delta - \frac{n-1}{n+1} \delta \right) \\ &\approx (-1)^n n! D^{(n)}_{l_1 l_2 \ldots l_n} \Delta, \end{aligned} \tag{3.44}$$

where the approximation is due to the assumed NGP condition.

What this procedure reveals is that the cumulant tensors in the q-space formalism can be measured from the higher order diffusion tensors in the modified phenomenological formulation under the NGP condition. However, since the NGP condition is assumed it is already possible to measure the cumulant tensors directly from the CGF of the EAP in Eq-3.33, which connects the signal to the cumulant tensors. The process of generalizing the diffusion equation is a remnant from the pre-q-space days of dMRI.

Interestingly GDTI2 then reconstructs the EAP analytically from the cumulant tensors using a Gram-Charlier approximation:

$$P(\mathbf{r}) \approx N(0, \mathbf{K}^{(2)}) \times \left(1 + \frac{K^{(4)}_{j_1 j_2 j_3 j_4}}{4!} H_{j_1 j_2 j_3 j_4}(\mathbf{r}) + \ldots \right), \tag{3.45}$$

where $N(0, \mathbf{K}^{(2)})$ is the Gaussian distribution with zero mean and covariance tensor $\mathbf{K}^{(2)}$, and $H_{j_1 j_2 j_3 j_4}(\mathbf{r})$ are the components of the n-th order Hermite tensor $\mathbf{H}^{(n)}(\mathbf{r})$.

3.4.3 Diffusion Spectrum Imaging

Diffusion spectrum imaging (DSI) introduced by Wedeen et al. [47, 28] in 2000, was the first dMRI method that applied the q-space formalism to measure or estimate the EAP in biological tissue. The forte of the q-space formalism, where diffusion could reveal more than just the intrinsic properties like the diffusion coefficient, and show how it could probe the complex microstructure of the underlying tissue, became quickly apparent. Crossing fiber microstructures were clearly revealed by the geometric forms of the measured EAPs, or their characteristics. Such EAPs clearly represented non-free diffusion and were non-Gaussian. DSI was based on the Fourier Transform relationship between the signal and the EAP described in Eq-3.32. Although in practice it couldn't satisfy the NGP condition required by the q-space formalism, DSI essentially imaged the q-space densely and reconstructed the EAP via a fast Fourier Transform (FFT). In fact, $\delta \approx \Delta$ in the DSI experiments conducted in [47, 28, 48]. Nonetheless, the angular results produced by such DSI experiments clearly spoke in favour of q-space imaging – as seen in [49].

DSI, however, considered the modulus Fourier Transform:

$$P(\mathbf{r}) = \int |E(\mathbf{q})| \exp\left(-i2\pi\mathbf{q}\cdot\mathbf{r}\right) d\mathbf{q},$$

in place of the true Fourier Transform, justifying that in the case of pure diffusion the

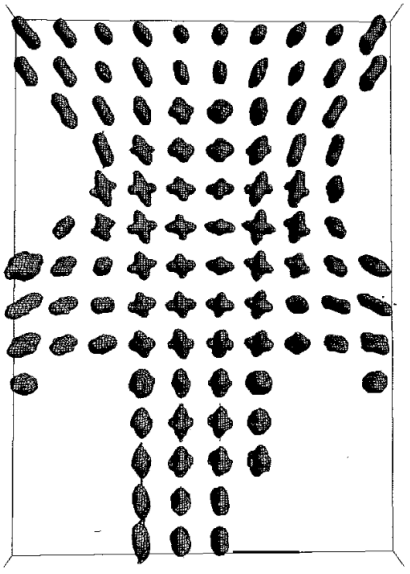

Figure 3.9: DSI diffusion PDFs from [47]. Corticospinal tract (orientations sup.-inf.) and pontine decussation (left-right).

modulus Fourier Transform is equal to the true Fourier Transform. This was done to counter biological motion such as cardiac pulsation, which tended to contaminate the phase of the signal.

Initially visualizing iso-surfaces of the estimated EAP [47], DSI techniques later introduced the *orientation distribution function* (ODF), to emphasize the angular results, which indicated underlying fibers. Two ODFs were used, namely [48]:

$$\Psi_{SA}(\mathbf{u}) = \int_{\mathbf{R}^+} P(r\mathbf{u})r^2 dr, \quad \mathbf{u} = \mathbf{r}/|\mathbf{r}|, \tag{3.46}$$

and the one introduced by Tuch [28]:

$$\Psi_{T}(\mathbf{u}) = \int_{\mathbf{R}^+} P(r\mathbf{u})dr, \quad \mathbf{u} = \mathbf{r}/|\mathbf{r}|. \tag{3.47}$$

However, DSI had severe acquisition setbacks. To correctly estimate the EAP, the q-space had to be densely sampled, and also at very high b-values. The DSI sampling scheme was a Cartesian grid inside a sphere in q-space, where both the radius of the sphere – the maximum b-value, and the number of grid-points – the number of acquisitions played important roles in determining the accuracy of the estimated EAP. For example in [47, 48], the maximum b-value was in the range of 20,000 s/mm^2, and the number of acquisitions were more than 500. In comparison, DTI acquisitions are done for b-values of 1000 s/mm^2, and only require a minimum of 6 acquisitions. These demanding requirements played unfavourably for DSI, since its clinical viability was near impossible.

However, DSI was the proof of concept for q-space imaging, which quickly became the popular approach for dMRI, and gave rise to a plethora of techniques for estimating complex EAPs or their characteristics like the ODF. These q-space techniques were developed to overcome the acquisition limitations of DSI.

3.4.4 Other Methods

A selected number of popular approaches are presented here that have been used in dMRI for inferring the underlying microstructure or fiber distribution. Some are based on the q-space formalism while others aren't, some are model based while others are model-free.

Multi-Tensor model The multi-tensor method is a model based approach introduced by Tuch et al. [46] as a direct extension to DTI to overcome its inherent limitation in regions with fiber heterogeneity. Simply put it considers the EAP to be a sum

of free diffusion Gaussian processes, implying the signal to be:

$$E(\mathbf{g}) = \sum_{j=1}^{n} f_j \exp\left(-b\mathbf{g}^T\mathbf{D}_j\mathbf{g}\right),$$

where $\mathbf{g} = \mathbf{G}/|\mathbf{G}|$ when $\mathbf{G}$ is the diffusion encoding gradient, n are the number Gaussian distributions comprising the EAP or equivalently the number of fibers or oriented free diffusion subsets, f_j the corresponding weights, such that their sum is unity, thus ensuring the PDF property of the Fourier Transform of this signal, and $\mathbf{D}_j$ are the DTs characterizing the anisotropies or orientations of the Gaussian distributions. The straightforwardness of this formulation, however, hides a number of technical difficulties. First, unlike the DTI signal, this signal cannot be linearized in the unknowns of the DTs $\{\mathbf{D}_j\}$. Therefore, a non linear gradient descent optimization approach has to be adopted to measure the DTs. However, such methods are inherently unstable. Next, the number of fibers have to be predefined (usually chosen as 2), and this can render the estimation scheme numerically unstable, especially when the actual fiber population is smaller than the predefined number of fibers – leading to spurious results. Various improvements and specializations in the form of constraints, regularizations, and automatic selection of the number of fibers have been proposed [5] (and references therein).

However, this model is often used as the ground truth for the signal, the EAP and the ODF in synthetic data experiments, since all these have simple analytical forms.

Diffusion Kurtosis Imaging *Diffusion Kurtosis Imaging* (DKI) was proposed by Jensen et al. [50] to quantify and measure the EAP's departure from the Gaussian distribution. DKI uses a 2nd order 3D Cartesian tensor to measure the ADC or the covariance of the unknown EAP and a 4th order 3D Cartesian tensor to measure the *excess kurtosis*, which measures the unknown EAP's departure from the Gaussian distribution. DKI is closely related to GDTI2. Both estimate the higher order cumulants of the EAP and use the expansion of the CGF (Eq-3.33). Therefore, DKI also relies on the q-space formalism. But GDTI2 and DKI differ in two respects. While GDTI2 estimates the cumulants – only the second and the fourth cumulants in practice, to reconstruct the EAP, DKI estimates the second and the fourth cumulants to measure the departure of the EAP from the Gaussian distribution. Also DKI doesn't employ the phenomenological approach like the modified Fick's equations used by GDTI2, and measures the higher order cumulants directly from the signal using the CGF expansion of the EAP using the q-space formalism.

In DKI the CGF expansion of the EAP is truncated to the fourth order, which includes only the second and the fourth cumulants of the EAP (Eq-3.33):

$$\ln\left(E(\mathbf{q})\right) = -\frac{(\gamma\delta g)^2}{2!}K^{(2)}_{j_1j_2}g_{j_1}g_{j_2} + \frac{(\gamma\delta g)^4}{4!}K^{(4)}_{j_1j_2j_3j_4}g_{j_1}g_{j_2}g_{j_3}g_{j_4},$$

where the gradient vector $\mathbf{G} = g\mathbf{g}$, $\mathbf{g} = \mathbf{G}/|\mathbf{G}|$, and the repeated indices again indicate summation over their range. However, DKI measures the excess kurtosis, which is defined as the standardized fourth order cumulant $\widetilde{k_4} = k_4/k_2^2$ in 1D. It's equivalent in 3D is defined along particular gradient directions $\mathbf{g}$, as $\widetilde{K_4}(\mathbf{g})$, the projection of the fourth order cumulant $\mathbf{K}^{(4)}$ along $\mathbf{g}$ divided by the squared projection of the second order cumulant $\mathbf{K}^{(2)}$ along $\mathbf{g}$:

$$\widetilde{K_4}(\mathbf{g}) = \frac{K^{(4)}_{j_1j_2j_3j_4} g_{j_1} g_{j_2} g_{j_3} g_{j_4}}{\left(K^{(2)}_{j_1j_2} g_{j_1} g_{j_2}\right)^2} = \frac{\left(tr(\mathbf{K}^{(2)})/3\right)^2 \cdot W^{(4)}_{j_1j_2j_3j_4} g_{j_1} g_{j_2} g_{j_3} g_{j_4}}{\left(K^{(2)}_{j_1j_2} g_{j_1} g_{j_2}\right)^2},$$

where [50] defines $W^{(4)}_{j_1j_2j_3j_4}$ as the coefficients of the *kurtosis tensor* $\mathbf{W}^{(4)}$. Replacing the fourth order cumulant tensor $\mathbf{K}^{(4)}$ by the kurtosis tensor $\mathbf{W}^{(4)}$, and the second order cumulant tensor $\mathbf{K}^{(2)}$ by the covariance matrix $2\Delta\mathbf{D}$, where $\mathbf{D}$ is the diffusion tensor, in the CGF expansion allows to estimate the diffusion tensor and $\mathbf{W}^{(4)}$ from the signal [50]:

$$\ln\left(E(\mathbf{q})\right) = -b \cdot D^{(2)}_{j_1j_2} g_{j_1} g_{j_2} + \frac{b^2 \left(tr(\mathbf{D})/3\right)^2}{6} \cdot W^{(4)}_{j_1j_2j_3j_4} g_{j_1} g_{j_2} g_{j_3} g_{j_4},$$

which allows to measure the excess kurtosis or the departure from the Gaussian distribution along any direction.

QBI *Q-Ball Imaging* (QBI) was proposed by Tuch [28, 51] spurred by the facts that DSI had severe acquisition requirements, and that the DSI result of interest wasn't the estimated EAP itself, but rather its radial projection – the ODF, which emphasized angular details. His idea was to retrieve the same angular result with reduced acquisition requirements. His initial attempt was the model based multi-tensor approach which was stricken with instabilities induced by the assumed model. Therefore, he proposed QBI, a model free method that sampled q-space only on a sphere or q-shell with fixed q-radius with high angular resolution. Such *high angular resolution diffusion imaging* is known as HARDI.

QBI like DSI is based on the q-space formalism and shows promising results, although like DSI, in practice it cannot satisfy the NGP condition [28]. However, QBI became a forerunner to a plethora of q-space methods that attempted to reconstruct the EAP or its characteristics from partial sampling of the q-space. QBI, itself maps spherical acquisitions in q-space to the ODF – a spherical function in real space.

QBI is based on the *Funk Radon transform* (FRT), which is a mapping from a sphere to a sphere $\mathcal{G} : S^2 \to S^2$. To a point on the sphere, called the pole, the FRT of a spherical function f, assigns the value of the integral of the spherical function along the equator on the plane that has for normal the vector connecting the centre of the sphere to the pole (Fig-3.10):

$$\mathcal{G}[f(\mathbf{u})](\mathbf{u}) = \int_{S^2} f(\mathbf{u}) \delta(\mathbf{u}^T \mathbf{w}) d\mathbf{w},$$

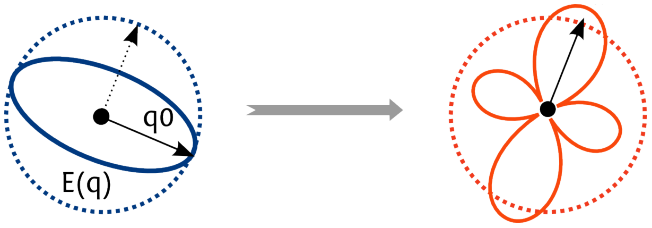

Figure 3.10: The Funk Radon Transform of a spherical function f, assigns the value of the integral of the spherical function along the equator on the plane that has for normal the vector connecting the centre of the sphere to the pole.

where $\mathbf{u}, \mathbf{w} \in S^2$. Using the Fourier slice theorem, Tuch was able to show that the FRT of the signal acquired on a q-sphere was equal to the ODF in Eq-3.47 blurred by a zeroth-order Bessel function, where the blurring or the width of the Bessel function was inversely proportional to the radius of the acquisition q-sphere.

QBI, therefore, made it possible to reconstruct the angular result of DSI, i.e. the ODF, with fewer acquisitions and without assuming any models. QBI was further boosted by [52, 53, 54], where an analytical solution was proposed independently by the authors, by using the SH basis. It was shown that the SHs are the eigenfunctions of the FRT [54]. Aganj et al. [55] recently proposed an analytical solution to QBI using SHs to compute the ODF in Eq-3.46, under a mono-exponential assumption of the signal. The ODF in Eq-3.46 takes into account the solid angle factor during the radial integration, therefore, it is a true marginal density function of the EAP, and is called the ODF-SA henceforth. This solution was also proposed by Vega et al. in [56]. The ODF in Eq-3.47 proposed by Tuch on the other hand doesn't account for this solid angle, and therefore needs to be numerically normalized after estimation [51]. It is henceforth referred to as the ODF-T. Typically the ODF-SA produces sharper peaks than the ODF-T.

PAS-MRI PAS-MRI proposed by Janson and Alexander [57] attempts to recover a certain characteristic of the EAP called the *persistent angular structure* (PAS) from the dMRI signal. Since QBI like acquisitions often sampled q-space densely on a sphere, it seemed natural like in QBI to try and recover angular properties of the EAP – the PAS, rather than its radial information. Therefore, assuming that the angular and the radial parts of the EAP are independent:

$$P(\mathbf{r})_{PAS} = \frac{1}{\mathbf{r}_0^2}\hat{p}(\hat{\mathbf{r}})\delta(|\mathbf{r}| - \mathbf{r}_0),$$

where $\hat{p}$ is the PAS, and $\hat{\mathbf{r}} = \mathbf{r}/|\mathbf{r}|$, the PAS for the radius $\mathbf{r}_0$ is estimated by best fitting the Fourier Transform of $P(\mathbf{r})_{PAS}$ to the measured q-space signal. This was done using a maximum entropy cost function and a non-linear iterative algorithm. Although

the original implementation was slow, this was improved upon by the realization that recovering the PAS could be reformulated as a spherical deconvolution problem [58].

Spherical Deconvolution Spherical Deconvolution (SD), proposed by Tournier et al. [59] attempts to infer directly the fiber orientation distribution function (fODF), which is the distribution of the underlying fibers, from the signal, without involving either the EAP or the ODF. Essentially this approach considers the signal to be the convolution of the fODF with the signal from a single fiber on the sphere [5]:

$$E(\mathbf{q}) = \int_{S^2} f(\mathbf{u}) R(\mathbf{q}, \mathbf{u}) d\mathbf{u},$$

where $\mathbf{u}$ is a unit-norm vector, $f(\mathbf{u})$ is the fODF, and $R(\mathbf{q}, \mathbf{u})$ is the signal from a single fiber oriented along $\mathbf{u}$ also called the "response function". Therefore, the fODF is recovered from the signal by deconvolving it with the response function. This deconvolution can be computed by simple matrix manipulations when the signal is described in the SH basis and the response function in the rotational harmonics basis.

The SD method, however, assumes the same response function model for all the underlying fibers, which can be estimated directly from the signal in voxels with very high anisotropy. However, there also exist a number of other models for estimating the response function [3]. SD is also highly sensitive to signal noise, and when high order SHs are considered, it produces spurious peaks and also negative values on the sphere, which are non-physical. A number of methods to improve this by using constraints and regularizations have also been proposed to improve SD [3, 5] (and references therein).

3.4.5 EAP Estimation

A number of methods have been recently proposed for recovering the complete EAP in dMRI. Like DSI, these methods make use of the q-space formalism, which relates the EAP to the diffusion signal via a Fourier Transform. However, unlike DSI which proceeds by sampling the q-space densely, which is its major disadvantage, these recent methods employ functional bases to model the q-space signal resulting in a continuous signal function from relatively few q-space samples, when compared to the requirements of DSI. These methods differ from each other in the way the signal is modelled using the functional basis of their choice, and in their choices of the functional bases used to represent the signal function.

Since the relationship between the EAP and the signal is a Fourier Transform, which was a hurdle crossed by DSI using a numerical fast Fourier Transform (FFT), choosing the functional bases rightly can help in solving the Fourier Transform analytically, by understanding that the Fourier Transform is a linear operator. This was in

fact highlighted by the GDTI2 approach, where the standard polynomial basis (with cumulants as coefficients) was used to model the signal, and the EAP was analytically computed in the Hermite polynomial basis (with again the same cumulants as coefficients). Therefore, choosing the functional bases rightly facilitates the Fourier Transform passage.

However, while GDTI2 inherently modelled the signal in the Cartesian coordinate system, and solved the Fourier Transform in the Cartesian coordinate system, these recent methods are all expressed in the spherical coordinate system, to separate the angular diffusion profile from the radial diffusion profile. Further, all these methods (except DOT) make use of the SH basis to fit the angular part of the continuous signal function, since the SH basis is a complete orthonormal basis for L2 integrable functions on the sphere, and also since in the spherical coordinates, the SHs are eigenfunctions of the angular part of the Fourier Transform – implying an easy and analytical angular transformation. The DOT uses the SH basis to fit the angular part of the signal's logarithm.

DOT The *diffusion orientation transform* (DOT) was proposed by Ozarslan et al. [60] as an analytical method for transforming the diffusivity (ADC) profile to probability profiles or the EAP. The DOT addresses a geometrically complex ADC profile in the SH basis, therefore the signal has the form:

$$E(\mathbf{q}) = e^{-bD(\mathbf{g})},$$

where $\mathrm{g} = \mathbf{G}/|\mathbf{G}|$ when $\mathbf{G}$ is the gradient encoding direction, and $D(\mathbf{g})$ is the ADC profile in the SH basis. This continuous signal function is used to compute its Fourier Transform in the spherical coordinates which provides an analytical solution for spherical profiles of the EAP also in spherical coordinates. Therefore, the DOT signal model is based on the ADC, and its signal function is a mono-exponential decay which was also generalized to a multi-exponential decay.

DPI *Diffusion propagator imaging* (DPI) was proposed by Descoteaux et al. [61], where the signal was written in the *solid harmonics* basis which are the general solutions of Laplace's equation in spherical coordinates:

$$E(\mathbf{q}) = E(q\mathbf{u}) = \sum_{j=0}^{\infty} \left[\frac{c_j}{q^{l+1}} + d_j q^l \right] Y_j(\mathbf{u}) \quad \text{for} \quad q > 0,$$

where c_j and d_j are the coefficients which fit the signal to this functional form, and Y_j are real and symmetric SHs. The solid harmonics are generalizations of the SHs. However, this signal model implies that the signal satisfies Laplace's equation, implying a heat diffusion like behaviour of the signal in q-space. Such an assumption is,

however, not verifiable physically. But using boundary conditions provided by multiple q-shells, since Laplace's equation requires boundary conditions to be solved, it is possible to fit a continuous signal function to the signal samples. This functional basis also admits an analytical Fourier Transform in the spherical coordinates, making it possible to estimate the EAP analytically, when the signal is described in this functional basis.

SHORE The *simple harmonic oscillator based reconstruction and estimation* (SHORE) of the EAP was proposed by Ozarslan et al. [62], where for the first time a complete orthogonal function basis was used to estimate the signal function from the signal samples. Since the basis used is complete for L2 integrable functions in $\mathbf{R}^3$, the signal is model free and is treated as is. The orthogonal basis used by SHORE is:

$$\Phi_{jlm}(u, q\mathbf{g}) = i^{-l}\sqrt{4\pi}(2\pi^2u^2q^2)^{l/2}\exp\left(-2\pi^2u^2q^2\right)L_{j-1}^{l+1/2}(2\pi^2u^2q^2)Y_{lm}(\mathbf{g}),$$

where u is a tuning parameter, $L_{j-1}^{l+1/2}(\cdot)$ is the Associated Laguerre polynomials and $Y_{lm}(\cdot)$ is the SH. While the SHs form a complete orthogonal basis on the sphere, the Associated Laguerre polynomials form a complete orthogonal basis on $[0, \infty)$. Since this basis has also an analytical Fourier Transform in spherical coordinates, the signal written in this basis also leads to an analytical expression for the EAP.

SPFI Closely related to the SHORE method is the method proposed by Assemlal et al. in [63]. This method proposes another basis, very similar to the SHORE basis, to estimate the signal function from the signal samples. This basis too is orthogonal and complete:

$$\Psi_{nlm}(u, q\mathbf{g}) = \left[\frac{2n!}{u^{3/2}\Gamma(n+3/2)}\right]^{1/2}\exp\left(\frac{-q^2}{2u}\right)L_n^{1/2}\left(\frac{q^2}{u}\right)Y_{lm}(\mathbf{g}),$$

where again u is a tuning parameter, and $Y_{lm}(\cdot)$ is the SH. However, in this basis, $L_n^{1/2}(\cdot)$ is the generalized Laguerre polynomial. Again since this basis is complete, estimating the signal in this basis requires no model assumptions and signal samples are treated as is for fitting. Although Assemlal et al. did not propose an analytical Fourier Transform for this basis, Cheng et al. proposed an analytical Fourier Transform in spherical coordinates in [64]. He called this the *spherical polar Fourier imaging* (SPFI). Therefore, again an analytical estimation of the EAP can be computed by fitting the signal in this basis.

3.5 SUMMARY

This chapter presented the fundamentals of the NMR phenomenon, the diffusion NMR experiment, and reviewed a number of diffusion MRI reconstruction algorithms. The NMR experiment can recover several different physical properties

from samples which contain spin bearing particles by simply applying a set of magnetic fields and gradients. This forms the core of the non-invasive nature of MRI. However, NMR can only examine a tiny region of a sample or a single spin ensemble and cannot image an entire biological specimen. This is made possible by the spatial encoding technique of MRI, which allows to spatially encode various juxtaposed regions or spin ensembles where NMR can be applied independently. This is done in MRI again using magnetic gradients. Therefore, this allows MRI to examine entire biological specimen, like the brain or the body, in-vivo and non-invasively.

One of the properties that NMR can be sensitized to is the Brownian motion of the spin bearing particles in a sample. Therefore, NMR can be used to measure the diffusion properties of a sample by modelling the diffusion of the spin bearing particles in the sample. Since diffusion has been historically modelled in two different ways, namely the Fick's phenomenological laws of diffusion and Einstein's random walk model of Brownian motion, the diffusion NMR signal is also modelled in two ways, namely the Stejskal-Tanner formulation and the q-space formalism. These approaches provide complementary ways to measure the diffusion properties of a sample from the NMR experiment, which have strongly influenced the development of diffusion MRI reconstruction techniques.

However, diffusion of water molecules, which are spin bearing particles, in a biological specimen is an intricate phenomenon since biological tissues are composed of complex microstructures. This microstructure causes diffusion to be anisotropic in biological tissues. This leads to the idea that diffusion can be viewed as more than just an intrinsic property of a sample, but can be further interpreted as a sensitive probe of the sample's microstructure. Therefore, measuring the anisotropic diffusion from a sample makes it possible to infer the microstructure of the sample. This is the principle behind diffusion MRI, where diffusion measured from juxtaposed spin ensembles using the diffusion NMR experiment and the spatial encoding of MRI, is employed to infer the complex microstructure of the cerebral white matter in-vivo and non-invasively.

Diffusion tensor imaging was the first diffusion MRI technique that was proposed to infer the tissue microstructure. It is the most commonly used technique since its mathematical framework is simple, it has few acquisition requirements and has a number of powerful and practical applications. However, it is limited in regions with microstructural heterogeneity. Many "higher order" techniques have been therefore proposed recently in diffusion MRI to overcome this limitation of diffusion tensor imaging, and to infer the microstructure of the cerebral white matter with greater accuracy.

A trend for using the spherical coordinates emerges from the (incomplete) review of recent higher order dMRI reconstruction techniques. This can be seen in the exten-

sive usage of the SH basis either for estimating characteristics of the diffusion EAP, e.g. in the analytical solution of QBI, PAS-MRI, SD, or for the estimation of the complete EAP, like in the methods in section-3.4.5. This is perhaps due to the importance given to recovering underlying axon fiber directions. These fiber directions correspond to angular properties, e.g. angular profiles of the EAP and angular marginal moments of the EAP, which are easier to compute in the spherical coordinates.

In this respect, the techniques presented in this thesis, contribute to an important alternate approach to dMRI using Cartesian coordinates. While the spherical coordinates simplify the computation of angular properties, the Cartesian coordinates simplify the computation of Cartesian properties like the "cumulants" of the EAP, as can be seen from DKI. The Cartesian properties are relevant since these can also be used to characterize the white matter, such as its anisotropy. Finally, as shown in GDTI2, and as will be shown in chapters-4 & 5, the Cartesian approach can also be used to infer the underlying axon fiber directions.

CHAPTER 4

HIGH ORDER SYMMETRIC TENSORS AND POSITIVE ADC MODELLING

Contents

4.1 INTRODUCTION

Diffusion Tensor Imaging (DTI) [30, 31] has become the de facto standard today in diffusion MRI (dMRI) for investigating the complex microstructure of the cerebral white matter in-vivo and non-invasively. Its tremendous popularity is due to its simplicity in acquisition requisites and elegance in interpretation, which makes it easy to implement the technique and infer the white matter microstructure, in particular the underlying fiber orientations. Based on Fick's phenomenological anisotropic diffusion equation, the DTI signal for the diffusion gradient $\mathbf{G}$, is described by the modified Stejskal-Tanner equation parameterized by the diffusion tensor $\mathbf{D}$ [23]:

$$S = S_0 \exp\left(-b\mathbf{g}^T\mathbf{D}\mathbf{g}\right),$$

where $b = \gamma^2\delta^2 g^2\left(\Delta - \frac{\delta}{3}\right)$, $g = |\mathbf{G}|$, and $\mathbf{g} = \mathbf{G}/|\mathbf{G}|$. In DTI, the apparent diffusion coefficient (ADC) is modelled by the spherical function:

$$D(\mathbf{g}) = \mathbf{g}^T\mathbf{D}\mathbf{g}.$$

However, in spite of its usefulness, it is well known that DTI is inherently limited in regions with heterogeneous fiber distributions, such as in fiber-crossings. In such regions DTI can neither accurately model the complex shape of the resulting ADC, nor correctly infer the underlying fiber bundle layout.

Generalized DTI (GDTI1: section-3.4.2) [44], was proposed to overcome this limitation by modelling the complex shaped ADC with greater accuracy using Cartesian tensors of order higher than two, the so called higher order (diffusion) tensors (HOTs). GDTI1, like DTI, is also based on Fick's phenomenological laws of diffusion, where the diffusion tensor is replaced by a spherical diffusion function parameterized by a HOT, or as its projection on to the unit sphere. The GDTI1 signal along the gradient direction $\mathbf{G}$ is similarly described by:

$$S = S_0 \exp\left(-b \sum_{j_1=1}^{3}\sum_{j_2=1}^{3}\cdots\sum_{j_k=1}^{3} D_{j_1,j_2\ldots j_k} g_{j_1} g_{j_2}\ldots g_{j_k}\right), \tag{4.1}$$

where, $D_{j_1,j_2\ldots j_k}$ are the coefficients of the kth order, three dimensional, diffusion HOT $\mathbf{D}^{(k)}$, and g_{j_i} are the components of the unit gradient vector $\mathbf{g}$. The complex shaped ADC is described in GDTI1 by:

$$D(\mathbf{g}) = \sum_{j_1=1}^{3}\sum_{j_2=1}^{3}\cdots\sum_{j_k=1}^{3} D_{j_1,j_2\ldots j_k} g_{j_1} g_{j_2}\ldots g_{j_k}. \tag{4.2}$$

Since $\mathbf{g}$ is a unit norm vector, it can also be described by the two parameters $\theta \in [0, \pi]$ and $\phi \in [0, 2\pi)$ as $\mathbf{g} = [\sin\theta\cos\phi, \sin\theta\sin\phi, \cos\theta]^T = [g_x, g_y, g_z]^T$, which shows that the ADC or the spherical diffusion function is the projection of $\mathbf{D}^{(k)}$ on to the unit sphere.

This form of the diffusion function helps derive certain properties of the diffusion HOT which greatly simplifies the GDTI1 model [44]. First, when k is odd :

$$D(-\mathbf{g}) = -D(\mathbf{g}).$$

However, since negative diffusion is non-physical, this implies that k can only be even, or only even ordered HOTs are of interest in modelling the ADC. Second, although a kth order 3D HOT can have 3^k independent coefficients, since only its projection along a vector g is of interest – $\mathbf{D}^{(k)}$ has to be symmetric – or its coefficients should be equal under any permutation σ, of the coefficient indices:

$$D_{j_1,j_2\ldots j_k} = D_{\sigma(j_1,j_2\ldots j_k)}.$$

This reduces the number of independent coefficients of the kth order HOT to a more tractable:

$$N_k = \frac{(k+1)(k+2)}{2}. \tag{4.3}$$

In other words, to describe the ADC more accurately using GDTI1, it is required to estimate from the diffusion signal the coefficients of a 3D symmetric HOT of even rank, such that the diffusion function or the estimated ADC is positive.

The independent coefficients of the kth order diffusion HOT are in practice estimated using the least squares (LS) approach [44] in a fashion almost identical to the approach for estimating the six coefficients of the diffusion tensor in DTI (section-3.4.1, Eq-3.41). The LS approach, although, rapid, since it involves only linear matrix operations, does not guarantee that the estimated HOT will result in a positive diffusion function even when k is considered even. In other words, the reason for considering k to be even, i.e. the estimated ADC should be positive, is not satisfied by the LS estimation process.

In this chapter we present two estimation approaches for measuring, in particular 4th order, diffusion HOTs from the diffusion signal that guarantee that the estimated ADC or the diffusion function is positive. In the first method, we take recourse to the fact that 3D symmetric 4th order tensors can be rewritten through a mapping as 6D symmetric 2nd order tensors. This makes it possible to reformulate the problem of estimating a 4th order tensor with a positive diffusion profile, to a problem of estimating a 2nd order tensor with a positive diffusion profile, albeit in 6D. We solve this problem by applying the Riemannian framework developed for symmetric positive definite (SPD) tensors of order 2, for estimating DTI diffusion tensors with positive diffusion profiles.

In the second method, we base ourselves on the polynomial interpretation of HOTs. Therefore, the diffusion function $D(\mathrm{g})$ is re-interpreted as a homogeneous polynomial in the components of the unit norm gradient vector g. This allows for a powerful parameterization of the diffusion signal, which ensures that the estimation process

guarantees a 4th order HOT with a positive diffusion profile. This parameterization comes from the properties of ternary quartics, which was first pointed out in [65, 66]. Also it has been proposed in [67] that the affine invariant Riemannian metric may not be well suited for diffusion data. The polynomial parameterization, therefore, provides an alternative approach for estimating 4th order diffusion tensors with positive diffusion profiles, which employs the Euclidean metric that is better suited for handling diffusion data [67].

4.2 A Riemannian Approach for Symmetric Positive Definite 4th Order Diffusion Tensors

The problem of estimating a diffusion tensor from the signal, which satisfies the positive diffusion profile has been extensively considered in DTI. Negative diffusion, which is non-physical, can also be a problem while estimating a 2nd order diffusion tensor $\mathbf{D}$, which happens when the DTI-ADC $\mathbf{g}^T\mathbf{D}\mathbf{g} < 0$, for some gradient direction $\mathbf{g}$. This can occur since the LS estimation process (section-3.4.1, Eq-3.41) doesn't guarantee that the diffusion tensor will have a positive diffusion profile. This condition requires a dedicated mathematical framework which constraints the estimation process to only diffusion tensors $\mathbf{D}$ such that $\mathbf{g}^T\mathbf{D}\mathbf{g} > 0,\ \forall \mathbf{g} \in S^2$.

An adequate framework for such an estimation was proposed by identifying the appropriate set of 2nd order tensors that satisfy the positive quadratic form, namely $\mathcal{S}ym_n^+$, the set of SPD matrices, which satisfy $\mathbf{x}^T\Sigma\mathbf{x} > 0,\ \forall \mathbf{x} \in \mathbf{R}^n \backslash \{\mathbf{0}\}$, and $\Sigma \in \mathcal{S}ym_n^+$. In other words, if the estimation process were to only operate in the space of $\mathcal{S}ym_3^+$ (in the case of DTI, $n = 3$), then the estimated diffusion tensor would satisfy the positive diffusion profile. The mathematical framework that was proposed, which allows to do this consists of an affine invariant metric of $\mathcal{S}ym_n^+$, the Riemannian metric [35, 36, 37, 1], and a similarity invariant metric of $\mathcal{S}ym_n^+$, the Log-Euclidean metric [68], which naturally confine operations on SPD matrices, such as geodesic computation, to the space of $\mathcal{S}ym_n^+$.

Deriving an equivalent Riemannian metric for the space of 4th order diffusion tensors would, however, be far more involved due to the increase in order or the multi-linear property of HOTs. Nonetheless, such a metric would be the right framework to use in the estimation process of the 4th order diffusion tensor, since it would ensure that the estimated HOT satisfies the positive diffusion profile. However, given the symmetry condition of a diffusion HOT, this problem can be simplified by reformulating the diffusion profile of a 4th order HOT (Eq-4.2) to a bilinear form dependent on a 2nd order tensor. Mathematically, this would convert the problem to the case of estimating a 2nd order tensor in $\mathcal{S}ym_n^+$, like in DTI. However, the conversion from a symmetric 4th order 3D tensor, results in a symmetric 2nd order tensor in 6D [69, 70]. Therefore, we would have to consider the space of $\mathcal{S}ym_6^+$ instead of the space of $\mathcal{S}ym_3^+$.

In this section, we propose to use this approach of transforming a symmetric 3D 4th order Cartesian diffusion tensor to a symmetric 6D 2nd order tensor, and of applying the Riemannian metric of the space $\mathcal{S}ym_6^+$, to estimate a 4th order diffusion tensor from the signal with a positive diffusion profile in GDTI1 [71].

4.2.1 Algebra of 2nd Order Tensors

To understand the algebra of 4th order tensors, which is required to manipulate these entities, and to transform them to isometrically equivalent 2nd order tensors, we start with 2nd order tensors, which are well studied and intuitively easy to understand. Much of the following formulation of Cartesian 2nd and 4th order tensors in an Euclidean space can be found in [69, 70], where, essentially a tensor is used interchangeably with the matrix of a linear transformation.

Given an n dimensional inner product space (vector space with an inner product) V, an nD 2nd order tensor $\mathbf{A} = \mathbf{A}^{(2)}$ is defined as the $n \times n$ matrix of the linear transformation:

$$A : V \to V, \quad \text{st} \quad \mathbf{x} \to \mathbf{A}\mathbf{x}, \ \mathbf{x} \in V.$$

The transpose of the linear transformation, with matrix $\mathbf{A}^T$, can be defined from the inner product of V as:

$$\left\langle \mathbf{x}, \mathbf{A}^T\mathbf{y} \right\rangle = \left\langle \mathbf{A}\mathbf{x}, \mathbf{y} \right\rangle, \quad \forall \mathbf{x}, \mathbf{y} \in V.$$

The space of linear transformations from V to V, itself forms a vector space, which can be called $\mathrm{Lin}(V) = \{A : V \to V\}$. The transpose of A can be used to define a natural inner product on $\mathrm{Lin}(V)$:

$$\langle \mathbf{A}, \mathbf{B} \rangle := tr(\mathbf{A}^T\mathbf{B}) = \sum_{i,j} A_{ij}B_{ij}, \quad A, B \in \mathrm{Lin}(V).$$

If V is $\mathbf{R}^n$, then $\mathrm{Lin}(V)$ is $\mathbf{R}^{n\times n}$, and it is isomorphic to $\mathbf{R}^{n^2}$. Therefore a tensor $\mathbf{A}$ in $\mathbf{R}^{n\times n}$ can be written as a vector $\mathbf{a}$, in $\mathbf{R}^{n^2}$. Furthermore, the isomorphism is an isometry, since:

$$\langle \mathbf{a}, \mathbf{b} \rangle = \langle \mathbf{A}, \mathbf{B} \rangle,$$

where the first inner product is the natural inner product of the vector space $\mathbf{R}^{n^2}$, and the second inner product is the newly defined inner product of $\mathrm{Lin}(V) = \mathbf{R}^{n\times n}$.

A symmetric linear transformation A from V to V, can be defined from the transpose of its corresponding 2nd order tensor, as $\mathbf{A} = \mathbf{A}^T$, which in terms of its components can be described by $A_{ij} = A_{ji}$. It is then possible to decompose a 2nd order tensor (or linear transformation) into its symmetric and skew-symmetric parts by $\mathbf{A}^s = (\mathbf{A} + \mathbf{A}^T)/2$ and $\mathbf{A}^a = (\mathbf{A} - \mathbf{A}^T)/2$ respectively, such that $\mathbf{A} = \mathbf{A}^s + \mathbf{A}^a$.

Finally the space of symmetric linear transformations $\mathrm{Sym}(V) = \{A \in \mathrm{Lin}(V) | \mathbf{A} = \mathbf{A}^T\}$, forms a subspace of $\mathrm{Lin}(V)$. Since, an nD symmetric 2nd order tensor has $n(n+$

$1)/2$ independent coefficients, if V is $\mathbf{R}^n$, then $\mathrm{Sym}(V)$ is isomorphic to $\mathbf{R}^{n(n+1)/2}$, and this mapping can be established in such a fashion that it is also an isometry, just like in the case of $\mathrm{Lin}(V)$, or $\langle \mathbf{a}_s, \mathbf{b}_s \rangle = \langle \mathbf{A}^s, \mathbf{B}^s \rangle$, for $\mathbf{a}_s, \mathbf{b}_s \in \mathbf{R}^{n(n+1)/2}$ and $A^s, B^s \in \mathrm{Sym}(V)$. An example for such an isometric mapping when $n = 3$, can be established between a symmetric 3D 2nd order tensor $\mathbf{B}$, and $\mathbf{b}$, a vector or a 6D 1st order tensor:

$$\mathbf{b} = [B_{xx}, B_{yy}, B_{zz}, \sqrt{2}B_{xy}, \sqrt{2}B_{xz}, \sqrt{2}B_{yz}]^T, \tag{4.4}$$

where B_{ij} are the coefficients of $\mathbf{B}$.

4.2.2 Algebra of 4th Order Tensors

The background for understanding the algebra of 4th order tensors is formed by the definition of the inner product, the isometric mapping to vectors (1st order tensors) of higher dimensions, and the symmetry properties, in particular $\mathrm{Sym}(V)$, of the space of 2nd order tensors or $\mathrm{Lin}(V)$. In an analogous way, we will define 4th order tensors as linear transformations from a vector space onto itself, define an inner product for the vector space of these linear transformations, study their symmetries, and establish an isometric mapping from the linear transformations to a vector space of lower order and higher dimension, which will allow us to manipulate 4th order tensors as 2nd order tensors.

The algebra of 4th order tensors can be described by proceeding in exactly the way as done above for 2nd order tensors, but with $\mathrm{Lin}(V)$ as the vector space in place of V. Let an nD 4th order tensor $\mathcal{A} = \mathbf{A}^{(4)}$ be defined as the $n \times n \times n \times n$ transformation array of the linear transformation:

$$\mathrm{A} : \mathrm{Lin}(V) \to \mathrm{Lin}(V), \quad \mathbf{C} \to \mathcal{A}\mathbf{C} = \sum_{k,l} A_{ijkl} C_{kl}, \ \mathbf{C} \in \mathrm{Lin}(V).$$

Since an inner product for $\mathrm{Lin}(V)$ exists, it can be used to define the transpose of the linear transformation, with the transformation array $\mathcal{A}^T$, as:

$$\left\langle \mathbf{D}, \mathcal{A}^T \mathbf{C} \right\rangle = \left\langle \mathcal{A}\mathbf{D}, \mathbf{C} \right\rangle, \quad \forall \mathbf{C}, \mathbf{D} \in \mathrm{Lin}(V).$$

Again the space of linear transformations from $\mathrm{Lin}(V)$ to $\mathrm{Lin}(V)$ forms a vector space, which can be called $\mathcal{L}in(V) = \{\mathrm{A} : \mathrm{Lin}(V) \to \mathrm{Lin}(V)\}$, and again the transpose of A can be used to define an inner product on $\mathcal{L}in(V)$:

$$\langle \mathcal{A}, \mathcal{B} \rangle := tr(\mathcal{A}^T \mathcal{B}) = \sum_{ijkl} A_{ijkl} B_{ijkl}, \quad \mathcal{A}, \mathcal{B} \in \mathcal{L}in(V).$$

If V is $\mathbf{R}^n$, then $\mathrm{Lin}(V)$ is $\mathbf{R}^{n \times n}$, and $\mathcal{L}in(V)$ is $\mathbf{R}^{n \times n \times n \times n}$, which is isomorphic to $\mathbf{R}^{n^4}$. Therefore an nD 4th order tensor can be written as a vector in $\mathbf{R}^{n^4}$. However, of greater interest is that $\mathcal{L}in(V)$ is also isomorphic to $\mathbf{R}^{n^2 \times n^2}$, which implies that an

nD 4th order tensor $\mathcal{A}$ can be written as an n^2D 2nd order tensor $\mathbf{A}$. Furthermore, this isomorphism is also an isometry:

$$\langle \mathbf{A}, \mathbf{B} \rangle = \langle \mathcal{A}, \mathcal{B} \rangle .$$

Symmetries of 4th order tensors present a richer set of possibilities than the symmetry of 2nd order tensors, since a number of symmetries can be defined by applying different "symmetry rules" on the four coefficient indices. Indeed, we shall present the major symmetry, the minor symmetry and the total symmetry. Total symmetry is, however, the symmetry of interest to us, which in the mathematical approach to tensors is the *definition of symmetry* of a HOT, where the coefficients of the HOT remain unchanged under any permutation of the coefficient indices. This is also the symmetry condition required by the diffusion HOT in GDTI1, as implied by its properties. However, this symmetry is best called total symmetry (or complete symmetry or super-symmetry), to differentiate it from the other possible symmetries that are derived from physics and that carry important physical interpretations.

We shall, however, not present such physical interpretations here, but content ourselves with counting the number of independent coefficients of a 4th order tensor under the various symmetries. To do this we will require the formula for counting the number of ways of choosing m elements from n elements without order and with repetition (combination):

$$S_{m,n} = \left(\begin{array}{c} n+m-1 \\ m \end{array} \right).$$

Major symmetry of an nD 4th order tensor $\mathcal{A}$ is defined by the index symmetry rule $A_{ij,kl} = A_{kl,ij}$. To count the number of independent coefficients of $\mathcal{A}$, which satisfies major symmetry, we consider the isometrically equivalent n^2D 2nd order tensor $\mathbf{A}$, which has only two indices $I = ij$ and $J = kl$. Therefore, major symmetry of $\mathcal{A}$ can be translated as the index symmetry rule of $\mathbf{A}$ as $\hat{A}_{IJ} = \hat{A}_{JI}$, where $\hat{A}_{o_1 o_2}$ are the coefficients of $\mathbf{A}$, which implies that $\mathbf{A} = \mathbf{A}^T$. Therefore, the number of independent coefficients of $\mathcal{A}$, which satisfies major symmetry, is:

$$N_{\overline{M}} = \frac{n^2(n^2+1)}{2}.$$

Note that major symmetry for $\mathcal{A}$, corresponds to the regular notion of symmetry for the 2nd order tensor $\mathbf{A}$. Therefore, symmetry properties of $\mathbf{A}$, such as decomposition into a symmetric part and a skew symmetric part and eigen-decomposition, can be attributed to the 4th order tensor $\mathcal{A}$ by isomorphism. Major symmetry also corresponds to the notion of symmetry induced by the definition of the transpose of a 4th order tensor, or a linear transformation from $\mathrm{Lin}(V)$ to $\mathrm{Lin}(V)$.

Minor symmetry of an nD 4th order tensor $\mathcal{A}$ is defined by the index symmetry rule $A_{ij,kl} = A_{ji,kl} = A_{ij,lk}$. To count the number of independent coefficients of $\mathcal{A}$, which satisfies minor symmetry, the index rule can be seen as first choosing 2 index values $\{ij\}$ from n index values without order and with repetition, and then again choosing 2 index values $\{lk\}$ under the same condition. However, since $\{ij\}$ and $\{lk\}$ don't swap, their mutual order is important. Therefore, the number of independent coefficients of $\mathcal{A}$, which satisfies minor symmetry is:

$$N_{\underline{M}} = \left(\begin{array}{c} n+2-1 \\ 2 \end{array} \right)^2 = \frac{n^2(n+1)^2}{4}.$$

The number of independent coefficients of an nD 4th order tensor with combined major and minor symmetries can be computed by combining the reasonings of the individual counts. First choose 2 index values $\{ij\} = I$ or $\{lk\} = J$ from n index values without order and with repetition, which gives $\sqrt{N_{\underline{M}}}$. Then choose 2 index values $\{IJ\}$ from these $\sqrt{N_{\underline{M}}}$ index values without order and with repetition. Therefore, the number of independent coefficients of $\mathcal{A}$, which satisfies both major and minor symmetries is:

$$N_{(\overline{M}+\underline{M})} = \left(\begin{array}{c} \sqrt{N_{\underline{M}}}+2-1 \\ 2 \end{array} \right).$$

Total symmetry or just symmetry, is defined for an nD 4th order tensor $\mathcal{A}$ by the index symmetry rule $A_{ijkl} = A_{\sigma(ijkl)}$, where $\sigma(ijkl)$ is any permutation of the indices $\{ijkl\}$. This is the symmetry satisfied by any HOT in the GDTI1 model, which implies from Eq-4.3, that the number of independent coefficients for a 3D kth order GDTI1 HOT is N_k. However, the number of independent coefficients of an nD 4th order tensor $\mathcal{A}$, which satisfies total symmetry can also be counted as the number of ways of choosing 4 index values from n possible index values, therefore:

$$N_T = \left(\begin{array}{c} n+4-1 \\ 4 \end{array} \right).$$

If we consider $k = 4$, it implies $N_k = 15$, and if we consider $n = 3$, it implies $N_T = 15$. This establishes the consistency between N_k and N_T.

Any 4th order tensor $\mathcal{A}$ satisfying major and minor symmetries can be decomposed in a unique manner into a totally symmetric 4th order tensor $\mathcal{A}^s$ and its asymmetric part $\mathcal{A}^a$ such that $\mathcal{A} = \mathcal{A}^s + \mathcal{A}^a$. The coefficients of the totally symmetric part and the asymmetric part can be computed from [69]:

$$\begin{aligned} A^s_{ijkl} &= \tfrac{1}{3}\left(A_{ijkl} + A_{ikjl} + A_{ilkj}\right) \\ A^a_{ijkl} &= \tfrac{1}{3}\left(2A_{ijkl} - A_{ikjl} - A_{ilkj}\right). \end{aligned}$$

These, alongwith the definition of the inner product between two 4th order tensors can be used to show that:

$$\langle \mathcal{A}^s, \mathcal{B}^a \rangle = tr(\mathcal{A}^s \mathcal{B}^a) = 0. \tag{4.5}$$

These symmetries greatly reduce the number of independent coefficients of an nD 4th order tensor from the total number of possible independent coefficients, which is n^4. Of particular interest are the 4th order tensors which satisfy both major and minor symmetries. These form a subspace of $\mathcal{L}in(V)$, called:

$$\mathcal{S}ym_{(\overline{M}+\underline{M})}(V) = \{\mathrm{A} : \mathcal{L}in(V) \rightarrow \mathcal{L}in(V) | \mathcal{A} \text{ satisfies major \& minor symmetries}\},$$

which is isometrically isomorphic to $\mathbf{R}^{N_{(\overline{M}+\underline{M})}}$.

When $n = 3$, $N_{\underline{M}} = 36$, and $N_{(\overline{M}+\underline{M})} = 21$. Therefore, $\mathcal{S}ym_{(\overline{M}+\underline{M})}(V)$ is isomorphic to $\mathbf{R}^{21}$, which is the space of symmetric 6D 2nd order tensors. An example of an isometric isomorphism that can be established in this case between a 3D 4th order tensor $\mathcal{A}_{(\overline{M}+\underline{M})}$ and a 6D 2nd order tensor $\mathbf{A}$ is [72]:

$$\mathbf{A} = \begin{pmatrix} A_{xxxx} & A_{xxyy} & A_{xxzz} & \sqrt{2}A_{xxxy} & \sqrt{2}A_{xxxz} & \sqrt{2}A_{xxyz} \\ A_{xxyy} & A_{yyyy} & A_{yyzz} & \sqrt{2}A_{yyxy} & \sqrt{2}A_{yyxz} & \sqrt{2}A_{yyyz} \\ A_{xxzz} & A_{yyzz} & A_{zzzz} & \sqrt{2}A_{zzxy} & \sqrt{2}A_{zzxz} & \sqrt{2}A_{zzyz} \\ \sqrt{2}A_{xxxy} & \sqrt{2}A_{yyxy} & \sqrt{2}A_{zzxy} & 2A_{xyxy} & 2A_{xyxz} & 2A_{xyyz} \\ \sqrt{2}A_{xxxz} & \sqrt{2}A_{yyxz} & \sqrt{2}A_{zzxz} & 2A_{xyxz} & 2A_{xzxz} & 2A_{xzyz} \\ \sqrt{2}A_{xxyz} & \sqrt{2}A_{yyyz} & \sqrt{2}A_{zzyz} & 2A_{xyyz} & 2A_{xzyz} & 2A_{yzyz} \end{pmatrix}, \tag{4.6}$$

where A_{ijkl} are the independent coefficients of $\mathcal{A}_{(\overline{M}+\underline{M})}$. This map, along with the map in Eq-4.4, which transforms a symmetric 2nd order tensor to a vector or a 1st order tensor, allows us to isometrically rewrite the effects of a linear transformation $\mathbf{A}_{(\overline{M}+\underline{M})}$ in $\mathcal{S}ym_{(\overline{M}+\underline{M})}(V)$ on a symmetric linear transformation B^s in $\mathrm{Sym}(V)$, as a matrix vector product when $n = 3$:

$$\mathcal{A}_{(\overline{M}+\underline{M})}\mathbf{B}^s = \mathbf{A}_{(\overline{M}+\underline{M})}\mathbf{b}^s, \tag{4.7}$$

$$\left\langle \mathbf{D}^s, \mathcal{A}_{(\overline{M}+\underline{M})}\mathbf{B}^s \right\rangle = \mathbf{d}^{s^T}\mathbf{A}_{(\overline{M}+\underline{M})}\mathbf{b}^s. \tag{4.8}$$

However, since diffusion HOTs from the GDTI1 model have to satisfy total symmetry, we are interested in the space of 3D 4th order tensors, which satisfy total symmetry. These also form a subspace of $\mathcal{L}in(V)$, called:

$$\mathcal{S}ym_T(V) = \{\mathrm{A} : \mathcal{L}in(V) \rightarrow \mathcal{L}in(V) | \mathcal{A} \text{ satisfies total symmetry}\},$$

which is isometrically isomorphic to $\mathbf{R}^{15}$, since $N_T = 15$ when $n = 3$. Although $\mathbf{R}^{15}$ corresponds to the space of symmetric 5D 2nd order tensors, the isometry to symmetric 6D 2nd order tensors (Eq-4.6) can be modified to represent $\mathcal{S}ym_T(V)$, with the added equalities:

$$\begin{array}{lll} A_{xxyy} = A_{xyxy}; & A_{xxzz} = A_{xzxz}; & A_{yyzz} = A_{yzyz} \\ A_{xxyz} = A_{xyxz}; & A_{yyxz} = A_{xyyz}; & A_{zzxy} = A_{xzyz}. \end{array}$$

Applying these equalities to $\mathbf{A}$ in Eq-4.6, is equivalent to decomposing the 3D 4th order tensor $\mathcal{A}_{(\overline{M}+\underline{M})}$, with major and minor symmetries, into its totally symmetric part $\mathcal{A}^{s}_{(\overline{M}+\underline{M})}$ [69]. In other words, an isometry from $\mathcal{S}ym_T(V)$ to the space of symmetric 6D 2nd order tensors can be established by considering the totally symmetric part of the equivalent 3D 4th order tensor with only major and minor symmetries.

The final isometry between $\mathcal{S}ym_T(V)$ and the space of symmetric 6D 2nd order tensors is the transformation that converts a 3D 4th order diffusion tensor from the GDTI1 model to an isometrically equivalent symmetric 6D 2nd order tensor. This allows us to use the Riemannian metric on the space of $\mathcal{S}ym_6^+$, to estimate the 4th order diffusion tensor with a positive diffusion profile.

4.2.3 Riemannian Framework for Symmetric Positive Definite Matrices

Second order tensors that satisfy the positive quadratic form required by the diffusion profile of the tensor, are the set of symmetric matrices whose bilinear form is always positive, i.e. the set of SPD tensors or $\mathcal{S}ym_n^+$. We consider only the set of symmetric tensors, since the symmetry is implied by the physical problem. The space $\mathcal{S}ym_n^+$, however, isn't complete under the metric induced by the natural inner product defined on the space, which is $\langle \mathbf{A}, \mathbf{B} \rangle = tr(\mathbf{A}^T\mathbf{B}) = tr(\mathbf{AB}),\ \forall \mathbf{A}, \mathbf{B} \in \mathcal{S}ym_n^+$. In fact $\mathcal{S}ym_n^+$ is known to be an open cone under this metric, also known as the Euclidean metric, whose closure is $\mathcal{S}ym_n$[36], where $\mathcal{S}ym_n$ corresponds to $\mathrm{Sym}(V)$ defined in the section above when $V = \mathbf{R}^n$. Therefore, to operate exclusively in $\mathcal{S}ym_n^+$, it is either required to explicitly consider a constraint, like in optimization, which confines the operation artificially to $\mathcal{S}ym_n^+$, or it is required to consider $\mathcal{S}ym_n^+$ as a manifold with its own metric, which can be computed from the geometry of the manifold, and which, therefore, renders $\mathcal{S}ym_n^+$ complete – thus naturally confining every operation to $\mathcal{S}ym_n^+$. This metric, which depends on the geometry of $\mathcal{S}ym_n^+$, is known as the Riemannian metric and it associates a new inner product to each point of $\mathcal{S}ym_n^+$. The manifold $\mathcal{S}ym_n^+$ with the new metric is known as a Riemannian manifold. In the following, we present briefly the salient features of the Riemannian framework for $\mathcal{S}ym_n^+$, which can be found in greater detail in [36, 37, 1].

More generally, a Riemannian manifold $\mathcal{M}$ is a real differentiable manifold in which each tangent space is equipped with an inner product, a Riemannian metric, which varies smoothly from point to point. This smooth variation of the tangent planes and their inner products over the manifold, allows to generalize a number of pointwise concepts to a finite neighbourhood. For example, given a smooth curve $\alpha(t),\ t \in [0, 1]$, on the manifold, it is possible to compute at each point of the curve $x = \alpha(t_x)$, its tangent $\alpha'(t_x)$, in the tangent space at x, $T_x\mathcal{M}$, and the norm of the tangent $||\alpha'(t_x)||$, which is induced by the inner product of $T_x\mathcal{M}$. Therefore, integrating the norm of

	Vector Space	Riemannian manifold
subtraction	$\overrightarrow{xy} = y - x$	$W = \log_x(y)$
addition	$y = x + \overrightarrow{xy}$	$y = \exp_x(W)$
distance	$\|\|y - x\|\|$	$\|\|W\|\|_x$
gradient descent	$x_{t+\epsilon} = x_t - \epsilon\nabla C(x_t)$	$x_{t+\epsilon} = \exp_{x_t}(-\epsilon\nabla C(x_t))$

Table 4.1: Comparison of vector operations in a vector space with the equivalent operations in a Riemannian manifold [73].

the tangent vector along the curve, it is possible to define a length for the curve. This can be used to define the distance between two points in $\mathcal{M}$ as the minimum length of all the curves joining the two points. The distance renders the manifold into a metric space, and the minimum length curve is known as the geodesic. When the geodesic corresponding to the distance exists in the Riemannian manifold, the manifold is known as geodesically complete. It can also be shown that this implies metric completeness, which is the result of the Hopf-Rinow theorem.

Conversely, given a point x of the manifold $\mathcal{M}$, and a tangent vector W in $T_x\mathcal{M}$, there exists a unique geodesic $\Gamma_{x,W}(t)$, such that $\Gamma_{x,W}(0) = x$ and $\Gamma'_{x,W}(0) = \mathrm{W}$. In other words, there exists a unique geodesic that passes through x, and at x has the tangent vector W. The *exponential map* projects the tangent vector W from $T_x\mathcal{M}$ to a point along the geodesic on $\mathcal{M}$ such that $\exp_x(W) = \Gamma_{x,W}(1) = y,\ y \in M$. The inverse of this map is known as the *log map* and it projects a point $y \in M$ on to a tangent vector in the tangent space at x by $W = \log_x(y),\ W \in T_x\mathcal{M}$. When $\mathcal{M}$ is geodesically complete, it implies that the exponential map at x is defined on the entire tangent space $T_x\mathcal{M}$. However, even then the exponential map is injective only in a local neighbourhood of x in $T_x\mathcal{M}$. In this neighbourhood, $\exp_x$ establishes a local diffeomorphism from $T_x\mathcal{M}$ to a neighbourhood of x in $\mathcal{M}$, and $T_x\mathcal{M}$ is a kind of "linearization" of the manifold $\mathcal{M}$. Or, intuitively, in this neighbourhood geodesics in $\mathcal{M}$ correspond to tangent vectors in $T_x\mathcal{M}$. The points where the exponential map fails are known as the *tangential cut locus*, and their image by the exponential map is the *cut locus*.

The concepts of vectors in an Euclidean space can be extended locally to Riemannian manifolds with the help of the local tangent spaces, the geodesics and the exponential and the log maps. This is summarized in Table-4.1 [73].

A Riemannian metric for $\mathcal{S}ym_n^+$ can be defined, when the metric is considered to be affine invariant, or invariant under the action of the linear group GL_n, where the group action is $\phi : \mathbf{S} \rightarrow A\mathbf{S}A^T,\ A \in GL_n, \mathbf{S} \in \mathcal{S}ym_n^+$. This invariance defines an inner product for each tangent space, where the tangent space of $\mathcal{S}ym_n^+$ at any point $\mathbf{S} \in \mathcal{S}ym_n^+$ is identically equal to $\mathcal{S}ym_n$ [35]. Therefore, the affine invariant inner

product in $T_{\mathbf{S}}\mathcal{S}ym_n^+ = \mathcal{S}ym_n$, is [73]:

$$\langle X, Y\rangle_{\mathbf{S}} = \left\langle \mathbf{S}^{-\frac{1}{2}} X \mathbf{S}^{-\frac{1}{2}}, \mathbf{S}^{-\frac{1}{2}} Y \mathbf{S}^{-\frac{1}{2}} \right\rangle_{\mathrm{Id}} = tr\left(\mathbf{S}^{-\frac{1}{2}} X \mathbf{S}^{-1} Y \mathbf{S}^{-\frac{1}{2}}\right), \quad X, Y \in \mathcal{S}ym_n,$$

where $\mathbf{S}^{-\frac{1}{2}}$ & $\mathbf{S}^{-1}$ exist since $\mathbf{S}$ is a SPD tensor, and Id is the $n \times n$ identity matrix.

The geodesic in $\mathcal{S}ym_n^+$ at Id, with the tangent vector W is given by [73]:

$$\Gamma_{\mathrm{Id},W}(t) = \exp(tW).$$

Therefore, by the affine invariance property of the Riemannian metric, the geodesic at any point $\mathbf{S} \in \mathcal{S}ym_n^+$ with the tangent vector X is:

$$\Gamma_{\mathbf{S},X}(t) = \mathbf{S}^{\frac{1}{2}} \Gamma_{\mathrm{Id},\left(\mathbf{S}^{-\frac{1}{2}} X \mathbf{S}^{-\frac{1}{2}}\right)} \mathbf{S}^{\frac{1}{2}} = \mathbf{S}^{\frac{1}{2}} \exp\left(t\mathbf{S}^{-\frac{1}{2}} X \mathbf{S}^{-\frac{1}{2}}\right) \mathbf{S}^{\frac{1}{2}}.$$

The matrix or tensor exponentials can be computed from the Taylor expansion of the exponential function, which forms a well defined matrix polynomial. This polynomial is further simplified to the operation of only considering the exponentials of the eigenvalues of the matrices, since the matrices considered are all symmetric.

The geodesic defines the exponential and the log maps in $T_{\mathbf{S}}\mathcal{S}ym_n^+$, for $W \in T_{\mathbf{S}}\mathcal{S}ym_n^+$ and $\mathbf{C} \in \mathcal{S}ym_n^+$:

$$\exp_{\mathbf{S}}(W) = \mathbf{S}^{\frac{1}{2}} \exp\left(\mathbf{S}^{-\frac{1}{2}} W \mathbf{S}^{-\frac{1}{2}}\right) \mathbf{S}^{\frac{1}{2}}, \qquad \log_{\mathbf{S}}(\mathbf{C}) = \mathbf{S}^{\frac{1}{2}} \exp\left(\mathbf{S}^{-\frac{1}{2}} \mathbf{C} \mathbf{S}^{-\frac{1}{2}}\right) \mathbf{S}^{\frac{1}{2}}.$$

The exponential map can be used along with the formulation of the gradient descent in Table-4.1 to design the appropriate gradient descent operation in the Riemannian manifold of $\mathcal{S}ym_n^+$:

$$\mathbf{S}_{t+1} = \Gamma_{\mathbf{S}_t, \nabla f(\mathbf{S}_t)}(-\epsilon) = \mathbf{S}_t^{\frac{1}{2}} \exp\left(-\epsilon \cdot \mathbf{S}_t^{-\frac{1}{2}} \nabla f(\mathbf{S}_t) \mathbf{S}_t^{-\frac{1}{2}}\right) \mathbf{S}_t^{\frac{1}{2}}, \tag{4.9}$$

where $f(\mathbf{S}) : \mathcal{S}ym_n^+ \rightarrow \mathbf{R}$ is the objective function that needs to be optimized, and ∇f is the gradient of f in the Riemannian manifold $\mathcal{S}ym_n^+$, which is defined $\forall \mathbf{S} \in \mathcal{S}ym_n^+$ by the directional derivative $\langle \nabla f, X\rangle_{\mathbf{S}}$ in the tangent plane $T_{\mathbf{S}}\mathcal{S}ym_n^+$. This can be understood as following backwards at every iteration the geodesic with the Riemannian gradient of the objective function as its tangent vector.

Therefore, the Riemannian metric of $\mathcal{S}ym_n^+$ allows us to design a gradient descent algorithm that guarantees to confine the 2nd order tensor estimated in each iteration to $\mathcal{S}ym_n^+$. In other words the Riemannian gradient descent allows us to find a solution, to the minimization of a function of SPD 2nd order tensors, in $\mathcal{S}ym_n^+$.

4.2.4 Estimating a SPD 4th Order Diffusion Tensor

We now connect the dots and show how to use the isometric map, between totally symmetric 4th order tensors and 6D 2nd order tensors, along with the Riemannian

metric on $\mathcal{S}ym_6^+$, to estimate the 4th order diffusion tensor in the GDTI1 model with a positive profile. First we re-write the diffusion function in Eq-4.2, which is written in terms of the coefficients of the kth order tensor $\mathbf{D}^{(k)}$ and of the unit gradient vector g, in the tensor terminology when $k = 4$:

$$D(\mathbf{g}) = \langle \mathcal{D}, \mathcal{G} \rangle, \qquad \text{where } \mathcal{G} = \mathbf{g} \otimes \mathbf{g} \otimes \mathbf{g} \otimes \mathbf{g} \tag{4.10}$$

$$= \langle \mathbf{B}, \mathcal{D}\mathbf{B} \rangle, \qquad \text{where } \mathbf{B} = \mathbf{g} \otimes \mathbf{g} \tag{4.11}$$

$$= \left\langle \mathbf{b}, \widehat{\mathbf{D}}\mathbf{b} \right\rangle = \mathbf{b}^T \widehat{\mathbf{D}} \mathbf{b}, \tag{4.12}$$

where $\mathcal{D} = \mathbf{D}^{(4)}$ is the 4th order diffusion HOT in GDTI1, $\mathcal{G}$ is a totally symmetric 4th order tensor computed from the outer products "$\otimes$" of the gradient vector, similarly $\mathbf{B}$ is a symmetric 2nd order tensor computed from the outer products of g, b is the vector form of $\mathbf{B}$ using the isometric map from Eq-4.4, and $\widehat{\mathbf{D}}$ is the symmetric 6D matrix form of $\mathcal{D}$ using the isometric map from Eq-4.6. The first two equalities can be derived from the coefficients' equation in Eq-4.2, and the third equality can be derived from Eqs4.7 & 4.8. Therefore, the diffusion signal from the GDTI1 model (Eq-4.1) when $k = 4$, can be written in tensor form as:

$$S = S_0 \exp\left(-b \mathbf{b}^T \widehat{\mathbf{D}} \mathbf{b}\right). \tag{4.13}$$

In this form, the problem of estimating the 4th order diffusion tensor $\mathcal{D}$, from the signal, with a positive diffusion profile can be solved by estimating the 2nd order tensor $\widehat{\mathbf{D}}$, from the signal, in $\mathcal{S}ym_6^+$.

The objective function we minimize to estimate $\widehat{\mathbf{D}}$ from N diffusion weighted images (DWIs) is the linearized form of the modified GDTI1 Stejskal-Tanner equation:

$$E(\widehat{\mathbf{D}}) = \frac{1}{2} \sum_{i=1}^{N} \left(\frac{1}{b} \ln\left(\frac{S_i}{S_0}\right) + \mathbf{b}_i^T \widehat{\mathbf{D}} \mathbf{b}_i \right)^2.$$

To estimate $\widehat{\mathbf{D}}$ in $\mathcal{S}ym_6^+$, we have to consider the Riemannian manifold of $\mathcal{S}ym_6^+$, and the appropriate gradient descent in that manifold, namely Eq-4.9. This requires computing the gradient of $E(\widehat{\mathbf{D}})$ in that manifold, which at every point in $\mathcal{S}ym_6^+$ is defined from the directional derivatives in the corresponding tangent plane.

To compute $\nabla E(\widehat{\mathbf{D}})$ at $\widehat{\mathbf{D}}$, we therefore consider a geodesic $\Gamma_{\widehat{\mathbf{D}},W}(t)$ originating from $\widehat{\mathbf{D}}$ with the tangent vector $W = \Gamma'_{\widehat{\mathbf{D}},W}(0)$ at $\widehat{\mathbf{D}}$ in the tangent space $T_{\widehat{\mathbf{D}}}\mathcal{S}ym_6^+$. The derivative of $E(\widehat{\mathbf{D}})$ along the geodesic $\Gamma_{\widehat{\mathbf{D}},W}(t)$ is therefore the directional derivative of $E(\widehat{\mathbf{D}})$ along W. Therefore, computing the derivative $\frac{d}{dt}E(\Gamma_{\widehat{\mathbf{D}},W}(t))$, and equating it to the directional derivative $\left\langle \nabla E(\widehat{\mathbf{D}}), W \right\rangle_{\widehat{\mathbf{D}}}$, it is possible to compute the gradient of

$E(\widehat{\mathbf{D}})$ at $\widehat{\mathbf{D}}$ in the manifold $\mathcal{S}ym_6^+$ [1]:

$$\begin{aligned}\nabla E(\widehat{\mathbf{D}}) &= \sum_{i=1}^{N}\left(\frac{1}{b}\ln\left(\frac{S_i}{S_0}\right)+\mathbf{b}_i^T\widehat{\mathbf{D}}\mathbf{b}_i\right)\cdot(\widehat{\mathbf{D}}\mathbf{b}_i)(\widehat{\mathbf{D}}\mathbf{b}_i)^T,\\ &= \widehat{\mathbf{D}}\left[\sum_{i=1}^{N}\left(\frac{1}{b}\ln\left(\frac{S_i}{S_0}\right)+\mathbf{b}_i^T\widehat{\mathbf{D}}\mathbf{b}_i\right)\cdot(\mathbf{b}_i\mathbf{b}_i^T)\right]\widehat{\mathbf{D}},\end{aligned} \tag{4.14}$$

where the second equality comes from the fact that $\widehat{\mathbf{D}} \in \mathcal{S}ym_6^+$. Therefore, $\nabla E(\widehat{\mathbf{D}}) \in \mathcal{S}ym_n$, which is the tangent space at $\widehat{\mathbf{D}}$. Therefore, it is now possible to plug this gradient into Eq-4.9 to compute the appropriate gradient descent in the Riemannian manifold $\mathcal{S}ym_6^+$:

$$\widehat{\mathbf{D}}_{t+1} = \widehat{\mathbf{D}}_t^{\frac{1}{2}}\exp\left(-\epsilon\cdot\widehat{\mathbf{D}}_t^{\frac{1}{2}}\left[\sum_{i=1}^{N}\left(\frac{1}{b}\ln\left(\frac{S_i}{S_0}\right)+\mathbf{b}_i^T\widehat{\mathbf{D}}\mathbf{b}_i\right)\cdot(\mathbf{b}_i\mathbf{b}_i^T)\right]\widehat{\mathbf{D}}_t^{\frac{1}{2}}\right)\widehat{\mathbf{D}}_t^{\frac{1}{2}}. \tag{4.15}$$

Minimizing the objective function $E(\widehat{\mathbf{D}})$ in this way, it is possible to estimate $\widehat{\mathbf{D}}$ in $\mathcal{S}ym_6^+$ from the diffusion signal. Since $\widehat{\mathbf{D}}$ is isometrically equivalent to a 4th order tensor $\mathcal{D}$ with major and minor symmetries, $\mathcal{D}$ is guaranteed to have a positive diffusion profile. Finally we extract the totally symmetric part of $\mathcal{D}$ to compute the totally symmetric 4th order GDTI1 diffusion tensor $\mathcal{D}^s$, which, due to the Riemannian estimation framework, is also guaranteed to have a positive diffusion profile.

4.2.5 Experiments and Results

We test the Riemannian approach for computing 4th order tensors by first conducting experiments on synthetic data, where the ground truth ADC is known. On this simulated data, we compare the Riemannian approach to two other methods for estimating the 4th order GDTI1 diffusion tensor, namely the standard Euclidean LS approach and a spherical harmonics (SH) basis approach. Then we test the Riemannian approach on a biological phantom data created from excised rat spinal cords, and on two in-vivo human cerebral datasets.

We generate the synthetic dataset using the multi-tensor model described in Appendix-A.0.1, where we use the diagonal tensor $\mathbf{D} = \mathrm{diag}(1390, 355, 355) \times 10^{-6}$ mm^2/s for the profile of a single fiber, and $\mathbf{D} = \mathrm{diag}(700, 700, 700) \times 10^{-6}$ mm^2/s for the profile of an isotropic voxel. Crossing fibers are simulated with equal volume fractions for each fiber. The purpose behind using the multi-tensor model is that it is easy to compute both the signal and the ADC analytically from this model [3]. Therefore, we use the ground truth ADC from the model as the reference for comparing the diffusion function generated by the 4th order GDTI1 diffusion tensor estimated from the synthetic signal using a particular estimation method. We use this comparison between the ground truth ADC and the estimated diffusion function to guage

the estimation method. In this way, we compare the Riemannian approach to two other methods of estimating a 4th order GDTI1 diffusion tensor that do not enforce the positive diffusion profile constraint.

As the first method we use the Euclidean LS approach with the linearized version of the modified GDTI1 Stejskal-Tanner equation, which requires only computing the Moore-Penrose pseudo-inverse of the measurements' matrix. As the second method, we use the SH basis to estimate the diffusion function as proposed in [74]. However, we consider only a real and symmetric sub-basis of SHs like in [75, 76], since the ADC is real and symmetric. Estimating the diffusion profile in this modified SH basis can also be achieved by a linear LS fitting, which requires only matrix manipulations. It is, therefore, efficient and fast. But, this LS fitting in the SH basis also doesn't guarantee that the estimated diffusion function has a positive profile. We then convert the modified SH basis expansion to a symmetric HOT basis description. It has been shown in [44, 75], that the truncated real symmetric SH basis of maximal rank-l is bijective to a symmetric lth order HOT. In other words, when the rank of the SH basis is equal to the order of the HOT, both of these form equivalent bases for functions defined on the sphere. This is described further in section-6.2.1. Therefore, by choosing $l = 4$, we estimate a 4th order GDTI1 diffusion tensor from a rank-4 SH basis estimation via a simple linear transformation. We call this the SH to HOT approach.

To compare these approaches, we generate a number of test voxels with various fiber configurations, namely isotropic voxels, single fiber voxels, two-fiber voxels, and three fiber voxels, where the multi-fiber voxels simulate fibers crossing perpendicularly. These configurations and the underlying fiber directions are generated randomly for each test voxel, and we store the ground truth ADCs for later comparison. We corrupt the signal generated from these voxels by adding Rician noise with known signal-to-noise-ratio (SNR), and from the noisy signal we estimate 4th order diffusion tensors using the three approaches. Finally we compare the diffusion functions generated by the estimated 4th order diffusion tensors to the ground truth ADC to evaluate the effects of noise, in the signal, on the three methods. We compare the ground truth ADC and the diffusion functions by first min-max normalizing them on the sphere and then considering the mean squared difference (or error) along discrete directions. We choose the directions from an icosahedral discretization of the sphere, with 642 vertices on a hemisphere.

We conduct this experiment for two different b-values, with a range of SNR values for each. For the b-value of 1000 s/mm^2, we generate 100 test voxels, where the random configurations consist of 36 isotropic voxels, 24 single fiber voxels, 20 two-fiber voxels and 20 three-fiber voxels. For the b-value of 3000 s/mm^2, we also generate 100 test voxels, where the random configurations consist of 25 isotropic voxels, 23 single fiber voxels, 28 two-fiber voxels, and 24 three-fiber voxels. The mean squared difference and the standard deviations of the squared difference of the min-max normalized

ADCs for the three methods in these tests are presented in Fig-4.1. It is clear that a positive diffusion profile constraint has a beneficial influence on the estimated ADC in the presence of signal noise.

Next we test the three approaches, the Euclidean LS, the SH basis, and the Riemannian methods for positive diffusion function profiles by conducting experiments on an in-vivo human cerebral dataset. The dataset is described in Appendix-A.0.4. We consider a masked region from this dataset, with 249352 voxels of interest. For these voxels, we estimate the 4th order GDTI1 diffusion tensors from the 41 DWIs, using the three approaches. We then evaluate the diffusion profiles from these estimated tensors along 81 pairs of directions on a sphere for negative diffusion. The results are described in Table-4.2. The Riemannian approach is the only method, which guarantees positive diffusion, since it takes into account the positivity constraint by identifying the space of 4th order tensors with positive multi-linear forms, and using the appropriate metric.

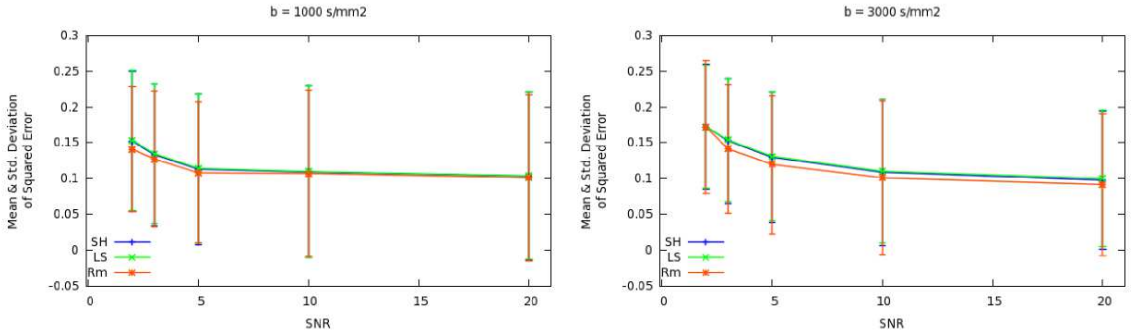

Figure 4.1: Synthetic Dataset. Comparing the effects of signal noise on the Riemannian, the Euclidean least squares (LS), and a spherical harmonic (SH) basis approaches for estimating a 4th order GDTI1 diffusion tensor. The graphs compare the squared difference of the min-max normalized ground truth ADC and the similarly normalized estimated diffusion functions. A positive diffusion profile constraint has a beneficial influence on the estimated ADC when the signal is noisy.

(81 dirs)	LS	SH	RM
Positive	181757	249263	249352
Negative	67595	89	0

Table 4.2: Real dataset. The estimated diffusion functions from 249352 4th order GDTI1 tensors checked for positive diffusion profile on a set of 81 pairs of directions distributed evenly on a sphere. The Riemannian approach is the only method, which guarantees positive diffusion.

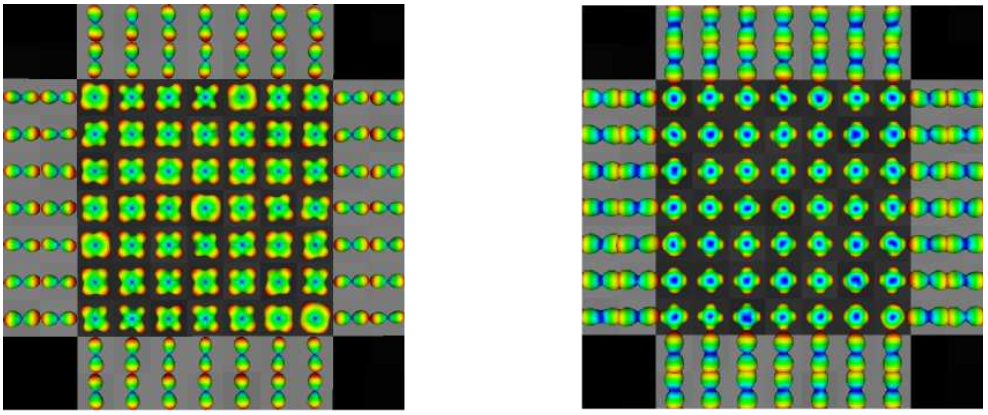

Figure 4.2: Synthetic Dataset. (a) The diffusion function and (b) the diffusion probability density function or ensemble average propagator (EAP) computed from 4th order GDTI1 diffusion tensors, which were estimated using the Riemannian approach.

Although, the shape of the ADC or diffusion function that is estimated by a 4th order GDTI1 diffusion tensor is more complex and accurate than the ADC of the DTI model, it is well known that the geometry of the higher order ADC doesn't correspond to the underlying fiber bundle directions. The fiber bundle directions can be inferred from the diffusion displacement probability density function $P(\mathbf{r})$, or the ensemble average propagator (EAP). Under the q-space formalism, it is possible to compute the EAP from the diffusion signal, $E(\mathbf{q}) = \frac{S_i(\mathbf{q})}{S_0}$, from a Fourier Transform $P(\mathbf{r}) = \int E(\mathbf{q}) \exp\left(-2\pi i \mathbf{q}^T \mathbf{r}\right) d\mathbf{q}$ [25]. Therefore, to detect the underlying fiber bundle directions, we compute the EAP, by assuming the q-space formalism, and by evaluating the Fourier Transform of the signal generated from the estimated 4th order GDTI1 diffusion tensors, using Eq-4.1. Fig-4.2, shows the results on a synthetic dataset that was also generated using the multi-tensor model of Appendix-A.0.1. Both the ADC or the diffusion functions and the computed EAPs are shown, where the underlying 4th order GDTI1 diffusion tensors were estimated from the synthetic signal using the Riemannian approach.

We test the EAP computation from 4th order diffusion tensors further on the in-vivo dataset from the previous experiment (Appendix-A.0.4). This experiment is conducted to evaluate the effect of negative diffusion profiles, or rather the absence of a positive diffusion constraint, on the computed EAP. Therefore we compute the EAP from the 4th order tensors estimated by the Euclidean LS approach, which doesn't apply the positive diffusion profile constraint, and from the tensors estimated by the Riemannian framework, which automatically confines the estimation process to 4th order tensors with a positive diffusion profile. The results are presented in Fig-4.3, where the EAP $P(\mathbf{r})$, has been evaluated for the constant displacement radius of $|\mathbf{r}| = 17$ μm. Note that no spatial regularization was used in any of the computations.

The improvement in the results in the Riemannian approach is only from the positivity constraint. This shows the impact of the positivity constraint in estimating the 4th order diffusion tensor on the computation of the EAP. This indicates the need for applying this positivity constraint, and the usefulness of the Riemannian framework.

We also compare the computation time for estimating the 4th order diffusion tensors that have been visualized in Fig-4.3, since, applying the Riemannian framework naturally increases the complexity in the estimation process. The simplicity and efficiency of the Euclidean LS method is in fact one of its main supporting factors. For the visualization of Fig-4.3, we computed 987 4th order tensors. On our computer, a Dell D630 Latitude laptop with Intel(R) Core(TM)2 Duo CPU @ 2.20GHz and 2GB RAM, the Euclidean LS method estimated these tensors in about 6 s, while the Riemannian approach took about 35 s. Although this is a six fold increase in the estimation time for the Riemannian approach, it is still tractable.

Next we conduct an experiment on a biological phantom data that was produced from excised rat spinal cords. Only two cords were used to create a fiber crossing configuration with known physical directions. The phantom dataset is described in Appendix-A.0.2. In this experiment we estimate 4th order GDTI1 diffusion tensors from the phantom dataset using the Riemannian approach. We then compute the EAPs from the tensors to validate the coherence of their geometry with the known layout of the phantom, and to see if it is possible to infer the underlying fiber bundle directions. For the sake of comparison we also present the result of the orientation distribution function (ODF) computed from the analytical q-ball estimation technique in [55], which is an angular marginal distribution of the true and unknown EAP under a mono-exponential decay model that corresponds to the GDTI1 model. The ODFs were directly estimated from the signal using the approach in [55].

The results are presented in Fig-4.4. The geometry of the EAPs computed from the 4th order tensors are coherent with the underlying phantom model, and also agree with the geometry of the ODFs. It is interesting to note that since the ODFs are angular marginal distributions of the true EAPs, the radial information of the true EAPs has been marginalized out by a radial integration. Therefore, although the ODFs' angular structures resemble the angular structures of the EAPs computed from the 4th order tensors, the ODFs do not reveal anything about the magnitude of diffusion due to the heterogeneous structure of the underlying tissue. This is visible in the EAPs computed from the tensors from the size or volume of the displacement probability at a constant displacement radius. Also as seen by comparing (b) and (c) in Fig-4.4, it is possible to recover sharper angular details from the EAP by increasing the displacement radius from $|\mathbf{r}| = 17$ μm to 20 μm.

Finally, we conduct a similar comparison between the EAP computed from the 4th order GDTI1 diffusion tensor, and the ODF, on another in-vivo human cerebral dataset.

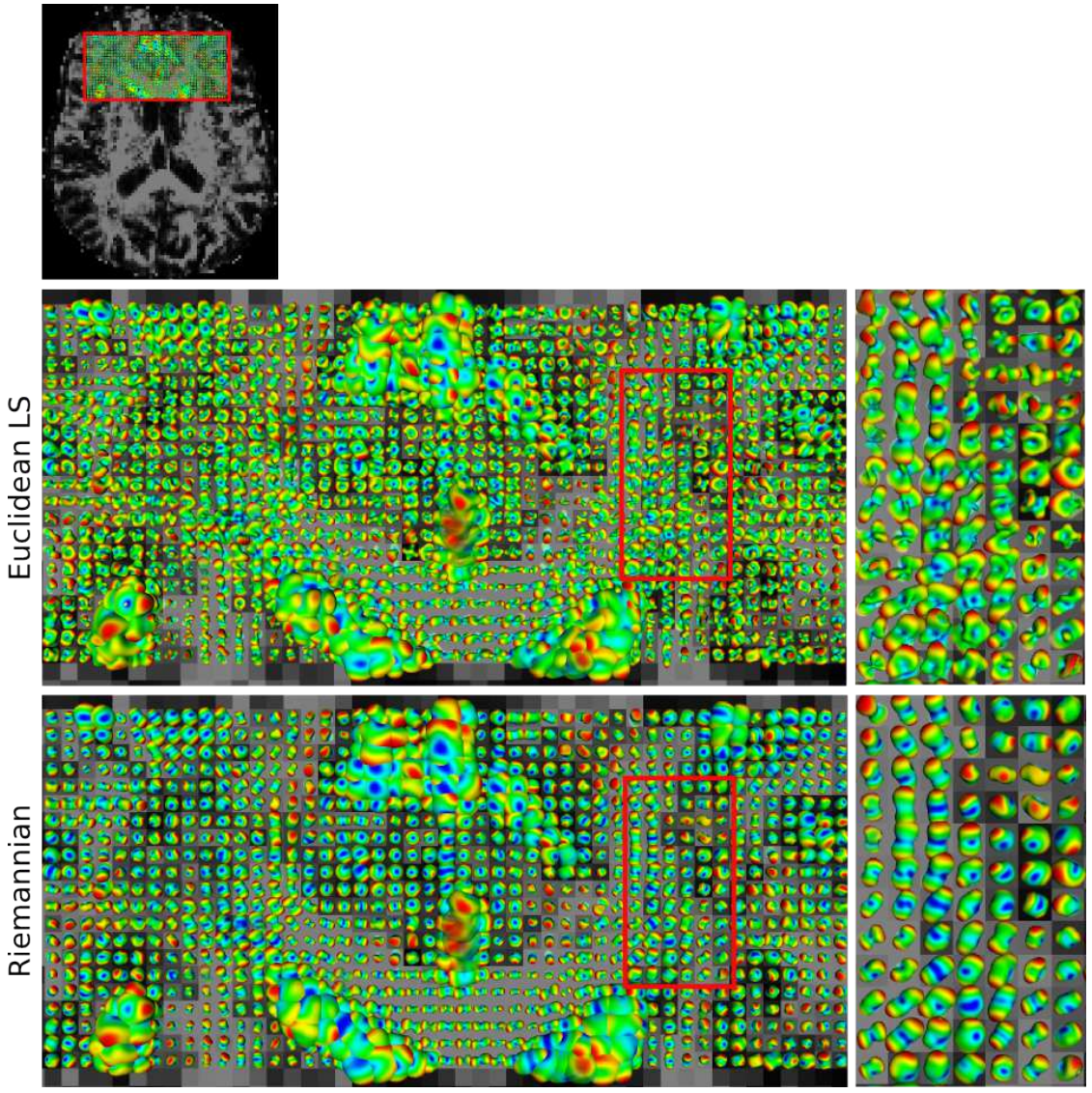

Figure 4.3: In-vivo Human Cerebral Dataset. Effects of positive diffusion profile constraint seen on the EAPs computed from 4th order GDTI1 diffusion tensors that were estimated using the Euclidean LS approach, which doesn't apply any positivity constraint, and the Riemannian approach, which naturally confines all tensor computations to the space of 4th order diffusion tensors with positive diffusion profiles. Note that no spatial regularization was used in any of the computations. The improvement in the results of the Riemannian approach is only due to the positivity constraint. The tensors were estimated from the dataset in Appendix-A.0.4.

The dataset is described in Appendix-A.0.3, and the 4th order tensors were estimated from this dataset using the Riemannian approach, while the ODFs were estimated directly from the signal. The results are presented in Fig-4.5, which shows a region of interest on a coronal slice where three major fiber bundles are known to intersect. These are the cortico-spinal tract, the corpus callosum, and the superior longitudinal

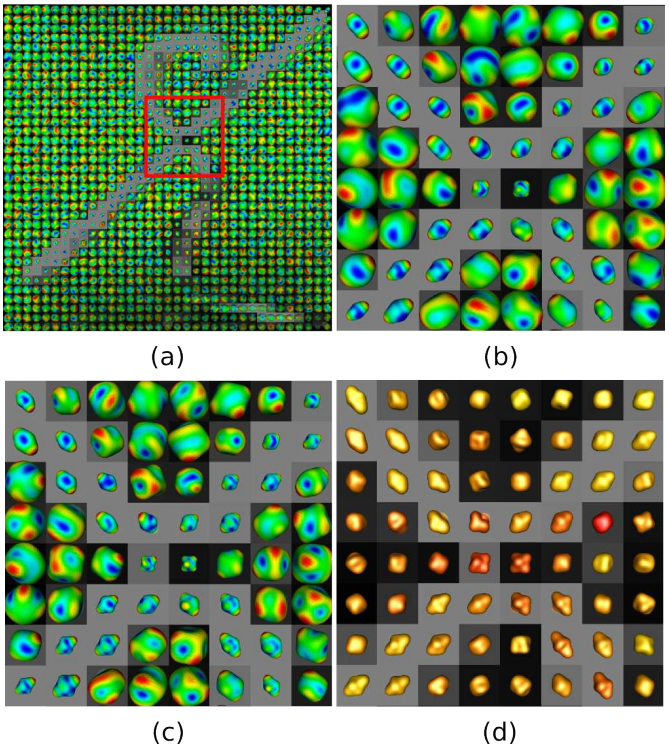

Figure 4.4: Biological Phantom Dataset. (a) The layout of the two excised rat spinal cords that constitute the phantom, and the zoom region. (b) The EAP $P(\mathbf{r})$, computed from 4th order GDTI1 diffusion tensors, evaluated for $|\mathbf{r}| = 17$ μm. (c) The EAP $P(\mathbf{r})$, evaluated for $|\mathbf{r}| = 20$ μm. (d) ODFs, estimated from an analytical q-ball approach, such that they represent the angular marginal distributions of the true and unknown EAPs. The 4th order diffusion tensors were estimated from the signal using the Riemannian approach. The ODFs were estimated directly from the signal.

fasciculus. Again we note the agreement between the geometry of the EAPs computed from the 4th order tensors, and the ODFs, which are the angular marginal distributions of the true and unknown EAPs. We also note the lack in radial information in the ODFs, which is visible in the EAPs from their size or volume.

4.2.6 Discussion

The GDTI1 model was proposed to overcome the inherent limitation of the popular DTI, in regions with heterogeneous fiber configurations. GDTI1 can describe the complex shaped ADC in such regions with greater accuracy by using Cartesian tensors of order higher than two to model Fick's diffusion equation. The ADC or the diffusion function is represented by a homogeneous polynomial parameterized by the coefficients of the HOT in GDTI1. However, a general kth order HOT in 3D can have a large number of independent coefficients, with an upper limit of 3^k. But this can be greatly simplified from the physical design of the problem. Since, only the spherical

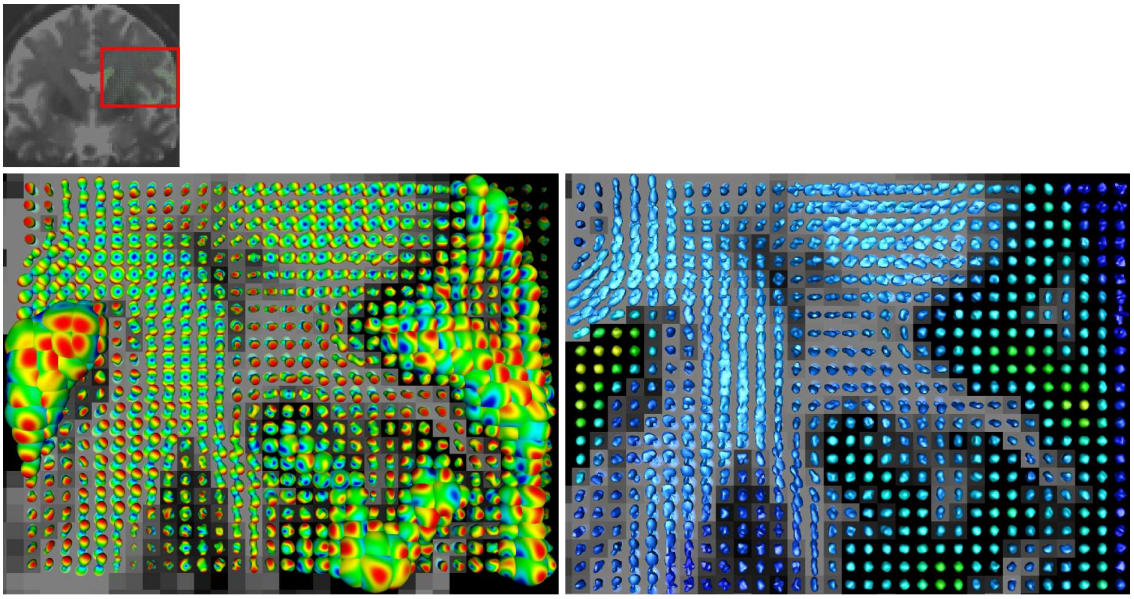

Figure 4.5: In-vivo Human Dataset. (a) EAPs computed from 4th order GDTI1 diffusion tensors that were estimated using the Riemannian approach. (b) ODFs that were estimated directly from the signal, and which are the angular marginal distributions of the true and unknown EAPs. The coronal slice presents a region of interest where three major fiber bundles, namely the cortico-spinal tract, the corpus callosum and the superior longitudinal fasciculus, intersect.

profile of the HOT is of relevance, only totally symmetric HOTs can satisfy the GDTI1 model. Similarly, since negative diffusion is non-physical, only even ordered HOTs can be considered. This reduces the number of independent coefficients that need to be estimated from the GDTI1 model significantly. However, although negative diffusion is non-physical, the generally used Euclidean LS approach does not guarantee an estimated diffusion HOT with a positive diffusion profile.

In this section, we proposed a Riemannian framework for estimating a 4th order GDTI1 diffusion HOT, which guarantees a positive diffusion profile. By studying the algebra and symmetries of HOTs when the order is 4, we first remapped 3D 4th order tensors satisfying major and minor symmetries to symmetric 6D 2nd order tensors using an isometrically isomorphic map. This transformed the problem of estimating a 4th order tensor satisfying a positive diffusion profile, to estimating a 6×6 symmetric matrix that is positive definite. We then applied the Riemannian framework that was developed to estimate symmetric positive definite 2nd order diffusion tensors to the space of 6D symmetric matrices to confine all matrix operations to the space of symmetric positive definite matrices. Using this framework, and the appropriate gradient descent method, we estimated symmetric positive definite 6×6 matrices, or equivalent 4th order tensors with major and minor symmetries and positive diffusion

profiles from the diffusion signal. Finally, by extracting the totally symmetric part of this 4th order tensor with only major and minor symmetries, we estimated the totally symmetric 4th order GDTI1 diffusion tensor with a positive diffusion profile.

We motivated the need for considering tensors with positive diffusion profiles by conducting experiments on synthetic and on real in-vivo data. On the synthetic data we compared the diffusion profiles of the estimated 4th order diffusion tensors against the known ground truth ADC, where the tensors were estimated using methods that don't guarantee a positive diffusion profile and the Riemannian approach, which inherently satisfies this condition. The positive influence of the Riemannian approach on the estimated ADC became clear when we tested for various SNRs and different b-values. On the real in-vivo human cerebral data, we computed the EAPs from the signal generated by the estimated 4th order tensors, and compared the EAPs visually when the tensors were estimated using an Euclidean LS approach and the Riemannian approach. Clearly again the improved results of the Riemannian approach indicated the contribution of the positive diffusion constraint in the computation of the EAP and the usefulness of the Riemannian framework. Computationally, although the Riemannian approach represents a more complex approach, the estimation time for about 1000 tensors was tractable.

We then conducted experiments on a biological phantom data and another in-vivo human cerebral data, where we evaluated the geometry of the EAPs computed from the 4th order tensors that were estimated using the Riemannian approach. We found the geometry of the EAPs to be in coherence with the phantom layout, which allows to infer the underlying fiber directions. We also compared these EAPs to ODFs that represent the angular marginal distribution of the true and unknown EAPs, when the ODFs were directly estimated from the signal. We found that the angular structure of the EAPs was in agreement with the angular structure of the ODFs. However, the ODFs didn't contain any radial or diffusion magnitude information, which was also visible in the computed EAPs from their size and volume. We found similar results on another in-vivo human cerebral data, where we again compared the computed EAPs to ODFs, where the EAPs were computed from 4th order tensors that were estimated from the diffusion signal using the Riemannian approach.

4.3 A Ternary Quartic Approach for Symmetric Positive Semi-Definite 4th Order Diffusion Tensors

In this section, we revisit the problem of estimating a symmetric higher order Cartesian tensor with a positive diffusion profile from the GDTI1 model, using a polynomial approach. In this approach we consider the polynomial interpretation of HOTs instead of considering the algebra of HOTs, and look at a polynomial solution to the

positivity problem. In particular, we consider 4th order GDTI1 diffusion tensors, where the diffusion function of such tensors can be seen as trivariate homogeneous polynomials of degree 4 in the coefficients of the gradient vector. In this class of polynomials, also known as ternary quartics, we consider the positive semi-definite, or non-negative diffusion profile constraint, which is slightly weaker in theory, but almost equivalent to the positive diffusion profile constraint in practice. Relying on Hilbert's theorem on non-negative ternary quartics [65, 66], we propose a parameterization of the 4th order GDTI1 diffusion tensor, which allows us to estimate such tensors with non-negative diffusion profiles from the signal. We test this approach on synthetic data, biological phantom data and in-vivo human cerebral data, to motivate the need for a positive or a non-negative diffusion profile constraint, and to demonstrate the applicability of this approach on real data. Finally, this approach is based on the Euclidean metric, which, as proposed in [67], is better suited for diffusion data, than the previously used affine invariant Riemannian metric.

Polynomials form an alternate way of expressing the multi-linear form of HOTs. This expression was indicated in the original GDTI1 paper [44], but was used for applying the positivity constraint for the first time in [65]. To make the relationship between the coefficients of a HOT and the coefficients of a homogeneous polynomial more evident, the diffusion function of GDTI1 (Eq-4.2) was rewritten in [65] as:

$$D(\mathbf{g}) = \sum_{m+n+p=k} D_{m,n,p}\, g_1^m g_2^n g_3^p, \tag{4.16}$$

where $D_{m,n,p}$ are the coefficients of the kth order tensor $\mathbf{D}^{(k)}$ by a re-arrangement of the indices.

In this form, it is clear that the diffusion function, which was considered as the projection of the of a kth order HOT on to a unit sphere, is a trivariate homogeneous polynomial of degree k in the three coefficients of the unit gradient vector $\mathbf{g} = [g_1, g_2, g_3]^T$, where the coefficients of the polynomial are the coefficients of the HOT. Since $D(\mathbf{g})$ is a homogeneous polynomial of even degree, the problem of a positive diffusion profile on the unit sphere, $D(\mathbf{g}) > 0,\ \forall \mathbf{g} \in \mathbf{R}^3$ st. $||\mathbf{g}|| = 1$, is equivalent to the problem of finding a polynomial $D(\mathbf{x}) > 0,\ \forall \mathbf{x} \in \mathbf{R}^3/\{\mathbf{0}\}$. This is exactly the same equivalence that was used in DTI, where the problem of positive diffusion from a second order tensor, $\mathbf{g}^T\mathbf{D}\mathbf{g} > 0,\ \forall \mathbf{g} \in S^2$, was recast as the problem of finding a positive definite second order tensor, $\mathbf{x}^T\mathbf{D}\mathbf{x} > 0,\ \forall \mathbf{x} \in \mathbf{R}^3/\{\mathbf{0}\}$, which entailed the Riemannian framework for $\mathcal{S}ym_3^+$. Therefore, in this section we consider a method of estimating the coefficients of a positive polynomial from the diffusion signal, to estimate a GDTI1 HOT with a positive diffusion profile.

It is interesting to note at this juncture, when $k = 4$, how the Riemannian approach presented in the previous section compares to the polynomial formulation. When $k = 4$, the goal of the polynomial formulation, as we have just seen, is to find a

trivariate homogeneous polynomial of degree 4, $D_4(\mathbf{x})$, where the coefficients of the polynomial are the coefficients of the 4th order GDTI1 diffusion tensor $\mathbf{D}^{(4)}$, such that:

$$D_4(\mathbf{x}) > 0, \quad \forall \mathbf{x} \in \mathbf{R}^3/\{\mathbf{0}\}.$$

In comparison, the Riemannian approach, using an isometric map, tries to find a symmetric 6D 2nd order tensor $\widehat{\mathbf{D}}$ in $\mathcal{S}ym_6^+$:

$$\mathbf{c}^T\widehat{\mathbf{D}}\mathbf{c} > 0, \quad \forall \mathbf{c} \in \mathbf{R}^6/\{\mathbf{0}\},$$

where the coefficients of the totally symmetric 4th order GDTI1 diffusion tensor can be extracted from the coefficients of $\widehat{\mathbf{D}}$. However, although, this quadratic form resembles the diffusion profile from a totally symmetric 4th order tensor, $\mathbf{b}^T\widehat{\mathbf{D}}\mathbf{b}$ (Eq-4.12), estimating $\widehat{\mathbf{D}}$ in $\mathcal{S}ym_6^+$ isn't equivalent to the problem of computing a 4th order GDTI1 diffusion tensor $\mathbf{D}^{(4)}$, with a positive diffusion profile. This can be seen from the isometrically equivalent inner product formulation of the quadratic form:

$$\langle \mathbf{C}, \mathcal{D}\mathbf{C} \rangle > 0, \quad \forall \mathbf{C} \in \mathcal{S}ym_3/\{\mathbf{0}\}.$$

The positive diffusion profile constraint on the other hand only implies the condition:

$$\langle \mathbf{B}, \mathcal{D}\mathbf{B} \rangle > 0, \quad \text{where } \mathbf{B} = \mathbf{g} \otimes \mathbf{g},$$

which can be seen in Eq-4.11. Since the 2nd order tensor $\mathbf{B}$ in the diffusion profile is only of rank-1, it is rank deficient, whereas in general the 2nd order tensor $\mathbf{C}$, in the quadratic form would include both full rank, and rank deficient tensors. In other words, the positive quadratic form condition is much stronger than the positive diffusion profile constraint. Therefore, although the positive quadratic form constraint would entail the positive diffusion profile constraint, the solutions found from this approach – the Riemannian approach, would only belong to a subset of all the solutions possible from only the positive diffusion profile constraint.

This can also be seen through examples, shown in [65, 66], by inspecting the isometric map in Eq-4.6 which transforms a 4th order tensor into a 2nd order tensor. When this 6×6 matrix is positive definite it cannot represent valid totally symmetric 4th order tensors whose homogeneous polynomials are of the type $P(\mathbf{g}) = ag_1^4 + bg_2^4 + cg_3^4$, or $P(\mathbf{g}) = (ag_1^2 + bg_2^2)^2 + cg_3^4$, etc., because these require the matrix to be semi-definite [66]. Since, the Riemannian framework pushes such matrices away to an infinite distance from the estimation tensor $\widehat{\mathbf{D}}$, the solutions found by the Riemannian estimation only form a subset of all the solutions that are possible.

In our experiments on synthetic data, this translates to a swelling effect in the ADCs and the EAPs estimated by the Riemannian approach when compared to the polynomial formulation for estimating 4th order GDTI1 HOTs, which we propose in this section. However, the overall angular structure is preserved. Similar effects are seen

in the results of tests conducted on phantom and in-vivo data. These results are presented in section-4.3.2.

We now return to the problem of estimating a positive trivariate homogeneous polynomial of degree k from the signal. A particular aspect of this problem has been addressed in [77], which describes a framework for estimating symmetric GDTI1 HOTs of any even order k and with a positive definite diffusion profile *on a unit sphere*. This paper proposes that any polynomial (the GDTI1 HOTs) that is positive definite on a unit sphere can be written as sums of squares of polynomials of lower order:

$$P^{(k)}(\mathbf{x}) = \sum_{i=1}^{M} Q_i^{(k/2)}(\mathbf{x}),$$

where k is even, $P^{(k)}(\mathbf{x})$ denotes a multi-variate polynomial of degree k, $\{Q_i^{(k/2)}(\mathbf{x})\}$ denote M multi-variate polynomials of degree $k/2$, and only an upper bound is known for M. Therefore, in [77], the authors propose to estimate the coefficients of the polynomials $Q_i^{(k/2)}(\mathbf{x})$ from the signal to estimate a polynomial $P^{(k)}(\mathbf{x})$ (or a GDTI1 HOT) with a positive definite diffusion profile.

Since M is not known exactly, the authors in [77] proceed by oversampling M, or rather densely sampling the space of possible polynomials of lower order $Q_i^{(k/2)}(\mathbf{x})$. It is claimed that increasing the density of the sampling increases the accuracy of the decomposition of $P^{(k)}(\mathbf{x})$. However, it also increases the number of unknown coefficients of the set $\{Q_i^{(k/2)}(\mathbf{x})\}$, which need to be estimated from the signal. The authors then propose heuristically measured approximations M' for M, for different values of k, from tests on synthetic data. However, even such approximations M', which can only be mathematically inexact and can at best depend on the synthetic data, result in a much larger number of unknowns to be estimated from the signal than the number of coefficients of the original polynomial which is positive definite on a unit sphere and of degree k (or kth order HOT).

When we have to deal with the general problem of estimating a positive homogeneous polynomial of degree k using similar decompositions into sums of squares of polynomials of lower degree, we are, however, restricted to only certain specific classes of non-negative multi-variate polynomials. To our knowledge, decompositions of polynomials into sums of squares of lower order polynomials only deal with non-negative polynomials and not positive definite polynomials [78]. Furthermore, [78] provides examples of non-negative polynomials that cannot be written as sums of squares of lower order polynomials, which implies that not all non-negative polynomials can be decomposed into sums of squares of lower order polynomials. The same article [78] also elaborates on Hilbert's theorem, which identifies all the classes of non-negative multi-variate polynomials that can always be decomposed as sums of squares of lower order polynomials. Such polynomials are, however, all of degree four or less.

In fact, Hilbert's theorem states that degree 4 trivariate polynomials that are non-negative *and* homogeneous, can always be written as a sum of squares of quadratic homogeneous polynomials, where the number of terms in the sum is also known and is exactly three ($M = 3$) [78]:

Theorem (Hilbert): If $P(x, y, z)$ is homogeneous, of degree 4, with real coefficients and $P(x, y, z) \geq 0$ at every $(x, y, z) \in \mathbf{R}^3$, then there are quadratic homogeneous polynomials f, g, h with real coefficients, such that:

$$P = f^2 + g^2 + h^2. \tag{4.17}$$

Trivariate polynomials of degree 4 are known as *ternary quartics*. All other classes of non-negative polynomials that can be decomposed into sums of squares of lower order polynomials are all of degree less than four [78].

In this section, we, therefore, turn to Hilbert's theorem on non-negative, or positive semi-definite (PSD) ternary quartics, for a parameterization of the GDTI1 HOT when it is of order 4, to estimate 4th order diffusion tensors with a non-negative diffusion profile. Since such tensors are symmetric and non-negative, these are known as symmetric positive semi-definite (SPSD) tensors. Hilbert's theorem on non-negative ternary quartics was first used in [65] and later in [66] to the same end – that of estimating 4th order diffusion tensors from the GDTI1 model with a non-negative diffusion profile. [65] and [66] proposed two different parameterizations of the 4th order tensor. We revisit this problem and propose a third parameterization [79].

As a final remark, we note that by adopting the polynomial formulation for the GDTI1 HOT, we have gained over the Riemannian framework proposed in the previous section from the fact that we address the exact problem of estimating a diffusion HOT with a positive diffusion profile, whereas the Riemannian approach addressed a more constrained problem. However, given the results on polynomials, namely Hilbert's theorem on ternary quartics, we concede to the Riemannian approach by the fact that we can only address the problem of a non-negative diffusion profile with the polynomial formulation, whereas the Riemannian approach addressed the positive definite diffusion profile constraint. However, we shall consider this a "negligible" loss, since in practice, due to numerical computations, we have never come across a diffusion profile that is exactly zero even along a single direction.

4.3.1 Estimating a SPSD 4th Order Diffusion Tensor

The basic approach behind all three "ternary quartic" methods, namely the two in [65, 66] and the one proposed here, is the same. The idea is to consider the diffusion profile of a 4th order GDTI1 tensor as a homogeneous trivariate polynomial in the coefficients of the gradient vector g (Eq-4.16), and to apply Hilbert's theorem on

non-negative ternary quartics to rewrite it as a sum of squares of three quadratic homogeneous polynomials. Therefore, by estimating the coefficients of these quadratic homogeneous polynomials from the signal, it is possible to reconstruct the 4th order diffusion tensor by computing its coefficients from the coefficients of the quadratic forms, a process also known as the Gram-matrix approach [65, 80], such that the estimated 4th order tensor has a PSD diffusion profile. The three methods differ from each other in the way they parameterize the quadratic homogeneous polynomials to estimate their coefficients from the diffusion signal.

In [65], the diffusion profile of a 4th order GDTI1 tensor is written as:

$$\begin{aligned} D(\mathbf{g}) &= (\mathbf{v}^T\mathbf{c}_1)^2 + (\mathbf{v}^T\mathbf{c}_2)^2 + (\mathbf{v}^T\mathbf{c}_3)^2, && (4.18)\\ &= \mathbf{v}^T\mathbf{C}\mathbf{C}^T\mathbf{v}, && (4.19)\\ &= \mathbf{v}^T\mathbf{G}\mathbf{v}, && (4.20) \end{aligned}$$

where $\mathbf{v} = [g_1^2, g_2^2, g_3^2, g_1g_2, g_1g_3, g_2g_3]^T$ contains the monomials formed by the coefficients of the gradient vector $\mathbf{g}$, $\mathbf{v}^T\mathbf{c}_i$ are the three quadratic forms from Hilbert's theorem, and $\mathbf{G}$ is known as the Gram matrix. The column vectors $\mathbf{c}_i$ contain the coefficients of the quadratic forms, which have to be estimated from the signal, $\mathbf{C} = [\mathbf{c}_1|\mathbf{c}_2|\mathbf{c}_3]$ is a 6×3 matrix, which assembles these coefficients to compute the rank deficient or PSD 6×6 Gram matrix, which is used to compute the coefficients of the 4th order diffusion tensor from the coefficients of the quadratic forms. This ensures that the 4th order diffusion tensor estimated from the signal has a non-negative diffusion profile.

The authors in [65] use the Eq-4.19 to parameterize the ternary quartic decomposition by Hilbert's theorem, and estimate $\mathbf{C}$ from the DWIs, and compute the 4th order tensor from $\mathbf{G}$. However, this parameterization is problematic since it produces an infinite solution space, which can be seen by decomposing $\mathbf{C}$ into two blocks $\mathbf{C} = [\mathbf{A}, \mathbf{B}]^T$ where $\mathbf{A}$ and $\mathbf{B}$ are 3×3 matrices. Then $\mathbf{CO}$, for any 3×3 orthogonal matrix $\mathbf{O}$, also results in the same Gram matrix, since $\mathbf{CO}(\mathbf{CO})^T = \mathbf{CC}^T = \mathbf{G}$. In other words, in this parameterization, $\mathbf{C}$ is unique only up to the equivalent class of orthogonal matrices $O(3)$. But as $\mathbf{C}$ is estimated from the DWIs from a minimization problem, such an infinite space of solutions can result in the optimization algorithm getting stuck in a degenerate subspace of the solution space, without ever being able to minimize its objective function.

In [65], the authors overcome this degenerate subspace issue by considering the $\mathbf{QR}$-decomposition (or $\mathbf{RQ}$-decomposition) of the 3×3 submatrix $\mathbf{A}$ of $\mathbf{C}$, where $\mathbf{Q}$ is an orthogonal matrix and $\mathbf{R}$ is an upper triangular matrix. This implies that $\mathbf{C} = [\mathbf{RQ}, \mathbf{B}]^T = [\mathbf{R}, \mathbf{BQ}^T]^T\mathbf{Q}$. Therefore, $\mathbf{CC}^T = [\mathbf{R}, \mathbf{BQ}^T]^T\mathbf{Q} \cdot \mathbf{Q}^T[\mathbf{R}, \mathbf{BQ}^T] = [\mathbf{R}, \mathbf{BQ}^T]^T \cdot [\mathbf{R}, \mathbf{BQ}^T]$, which effectively quotients out the orthogonal group from the computation of the Gram matrix $\mathbf{G}$ and resolves the issue of the infinite degenerate subspace.

In the paper [66], the authors overcome this same issue in Eq-4.19 by applying certain constraints on $\mathbf{C}$ from the properties of the Gram matrix, to remove the ambiguity of the class of orthogonal matrices $O(3)$. Since the rank of the rank deficient Gram matrix is known apriori from Hilbert's theorem to be three, they identify and isolate the positive definite part of the PSD Gram matrix using a modified Iwasawa decomposition [81], which is then parameterized uniquely by a Cholesky decomposition. In other words, they first collect the rank-3 positive definite part of $\mathbf{G}$ into a 3×3 matrix $\mathbf{W}$, and then decompose $\mathbf{W}$ using a Cholesky decomposition as $\mathbf{W} = \mathbf{L}\mathbf{L}^T$. This effectively equates the 3×3 matrix $\mathbf{A}$, from the paragraph above, where $\mathbf{C} = [\mathbf{A}, \mathbf{B}]^T$, to the triangular matrix with positive diagonal elements $\mathbf{L}$. In short, this procedure determines a unique $\mathbf{C}$ in the infinite space of solutions $\{\mathbf{CO}\}$ from the previous approach, and removes the ambiguity of the class of orthogonal matrices $O(3)$. Therefore, the authors in [66] effectively estimate $\mathbf{C} = [\mathbf{L}, \mathbf{B}]^T$ from the DWIs. Furthermore, the Cholesky decomposition also distinguishes $\mathbf{C}$ from $-\mathbf{C}$, although both result in the same Gram matrix. The authors then use this uniqueness property of $\mathbf{C}$ to design a spatial regularization of the field of estimated 4th order diffusion tensors as a function of $\mathbf{C}$.

We propose a third parameterization for the ternary quartic decomposition of Hilbert's theorem that naturally has no ambiguity from the class of orthogonal matrices $O(3)$, and therefore, is unique and can be solved easily. We essentially use Eq-4.18 to parameterize the Hilbert decomposition, and we estimate the $\mathbf{c}_i$ directly from the DWIs and assemble these afterward to reconstruct $\mathbf{C}$. From there we follow the same procedure as the two other methods, and reconstruct the Gram matrix and compute the coefficients of the 4th order diffusion tensor.

Materials and Methods From Hilbert's theorem on non-negative ternary quartics we write the diffusion function of a 4th order diffusion tensor as $D(\mathbf{g}) = \psi_1^2(\mathbf{g}) + \psi_2^2(\mathbf{g}) + \psi_3^2(\mathbf{g})$, where:

$$\begin{aligned}
\psi_i(\mathbf{g}) &= a_i g_1^2 + b_i g_2^2 + c_i g_3^2 + 2\alpha_i g_1 g_2 + 2\beta_i g_1 g_3 + 2\gamma_i g_2 g_3, && (4.21)\\
&= [a_i, b_i, c_i, \sqrt{2}\alpha_i, \sqrt{2}\beta_i, \sqrt{2}\gamma_i] && (4.22)\\
&\qquad \cdot [g_1^2, g_2^2, g_3^2, \sqrt{2}g_1 g_2, \sqrt{2}g_1 g_3, \sqrt{2}g_2 g_3]^T, && (4.23)\\
&= \mathbf{x}_i^T \mathbf{v} && (4.24)
\end{aligned}$$

are the quadratic forms. Note that we have modified the form of the vector $\mathbf{v}$ by multiplying certain terms by $\sqrt{2}$, this is a minor difference in the notation convention from [65, 66]. Each quadratic form is known if its six unknown coefficients in $\mathbf{x}_i$ can be estimated from the DWIs. Therefore, the diffusion profile can be written as a

function of the unknowns to be estimated as:

$$
\begin{aligned}
D(\mathbf{x}_1, \mathbf{x}_2, \mathbf{x}_3) &= \mathbf{x}_1^T \mathbf{v}\mathbf{v}^T \mathbf{x}_1 + \mathbf{x}_2^T \mathbf{v}\mathbf{v}^T \mathbf{x}_2 + \mathbf{x}_3^T \mathbf{v}\mathbf{v}^T \mathbf{x}_3, && (4.25)\\
&= [\mathbf{x}_1^T, \mathbf{x}_2^T, \mathbf{x}_3^T] \begin{bmatrix} \mathbf{v}\mathbf{v}^T & \mathbf{0} & \mathbf{0} \\ \mathbf{0} & \mathbf{v}\mathbf{v}^T & \mathbf{0} \\ \mathbf{0} & \mathbf{0} & \mathbf{v}\mathbf{v}^T \end{bmatrix} \begin{bmatrix} \mathbf{x}_1 \\ \mathbf{x}_2 \\ \mathbf{x}_3 \end{bmatrix} && (4.26)\\
&= \mathbf{X}^T \mathbf{V} \mathbf{X}. && (4.27)
\end{aligned}
$$

Comparing Eq-4.27 to Eq-4.19 provides an insight into the simplicity of the modification that we have proposed by considering the coefficients of the quadratic forms as the unknowns. Eq-4.19 can be interpreted as the projection of $\mathbf{C}\mathbf{C}^T$ along the 6D vector $\mathbf{v}$, however, since $\mathbf{v}$ is known, and the unknowns are in $\mathbf{C}$, this is like projecting the squares of the unknowns along a known vector. On the other hand in Eq-4.27, we rightly identify the unknowns as $\mathbf{x}$, and consider the projection of the known monomials of the coefficients of the gradient vector along the unknown vector. This naturally resolves the ambiguity of the orthogonal matrices in Eq-4.19. Furthermore, it is easy to reconstruct $\mathbf{C}$ by writing $\mathbf{C} = [\mathbf{x}_1, \mathbf{x}_2, \mathbf{x}_3]$, and to recompute the Gram matrix once the unknowns coefficients of the quadratic forms have been estimated separately.

To estimate the unknown coefficients $\mathbf{x}_i$ of the homogeneous quadratic forms from a set of DWIs, we minimize the objective function based on the modified and linearized Stejskal-Tanner equation:

$$
E(\mathbf{X}) = \frac{1}{2} \sum_{i=1}^{N} \left(\frac{1}{b} \log \left(\frac{S_i}{S_0} \right) + \mathbf{X}^T \mathbf{V}_i \mathbf{X} \right)^2, \tag{4.28}
$$

where N is the number of DWIs and $\mathbf{V}_i$ corresponds to the monomials from the gradient direction $\mathbf{g}_i$. Although here we use the linearized form of the Stejskal-Tanner equation, it is equally possible to use the non-linear form. The gradient of the objective function with respect to the unknowns $\mathbf{X}$ is computed to be:

$$
\nabla E(\mathbf{X}) = \sum_{i=1}^{N} \left(\frac{1}{b} \log \left(\frac{S_i}{S_0} \right) + \mathbf{X}^T \mathbf{V}_i \mathbf{X} \right) \left(\mathbf{V}_i + \mathbf{V}_i^T \right) \mathbf{X}. \tag{4.29}
$$

In our implementation we use the well known Broyden-Fletcher-Goldfarb-Shanno (BFGS) method [82], which is a sophisticated quasi-Newton optimization algorithm for non-linear problems.

Finally we compute the 15 independent coefficients A_{ijkl} of the 4th order GDTI1 diffusion tensor $\mathbf{A}^{(4)}$ from the coefficients of the Gram matrix $\mathbf{G}$, by using Eq-4.20, which equates $D(\mathbf{g})$, the multi-linear form of $\mathbf{A}^{(4)}$, to the quadratic form of the Gram matrix. We use a mapping very similar to the one presented in [65, 80], where the

inverse mapping, i.e. $\mathbf{G}$ in terms of A_{ijkl} is given by:

$$\mathbf{G} = \begin{pmatrix} A_{xxxx} & a & b & \frac{1}{4}A_{xxxy} & \frac{1}{4}A_{xxxz} & d \\ a & A_{yyyy} & c & \frac{1}{4}A_{yyxy} & e & \frac{1}{4}A_{yyyz} \\ b & c & A_{zzzz} & f & \frac{1}{4}A_{zzxz} & \frac{1}{4}A_{zzyz} \\ \frac{1}{4}A_{xxxy} & \frac{1}{4}A_{yyxy} & f & \frac{1}{4}(A_{xyxy} - 2a) & \frac{1}{8}(A_{xyxz} - 4d) & \frac{1}{8}(A_{xyyz} - 4e) \\ \frac{1}{4}A_{xxxz} & e & \frac{1}{4}A_{zzxz} & \frac{1}{8}(A_{xyxz} - 4d) & \frac{1}{4}(A_{xzxz} - 2b) & \frac{1}{8}(A_{xzyz} - 4f) \\ d & \frac{1}{4}A_{yyyz} & \frac{1}{4}A_{zzyz} & \frac{1}{8}(A_{xyyz} - 4e) & \frac{1}{8}(A_{xzyz} - 4f) & \frac{1}{4}(A_{yzyz} - 2c) \end{pmatrix}, \tag{4.30}$$

where $\{a, b, c, d, e, f\}$ are six free parameters that determine the rank of the matrix. In this case, since the rank of $\mathbf{G}$ is known to be three, the free parameters are determined from the construction of the Gram matrix, i.e. $\mathbf{G} = \mathbf{C}\mathbf{C}^T$. Therefore these can be used to compute the coefficients A_{ijkl}.

In comparison to the approach in [66], since we estimate all the coefficients of the three quadratic forms without any constraints, in effect we estimate 18 unknowns from which we recover the 15 unknowns of the 4th order diffusion tensor. This actually leaves us three degrees of freedom that can be applied as suitable constraints. Also this approach doesn't distinguish between $\mathbf{C}$ and $-\mathbf{C}$. However, since we only deal with the estimation problem of the 4th order diffusion tensor, and do not execute any further operations like spatial regularization as a function of $\mathbf{C}$ this isn't important since both $\mathbf{C}$ and $-\mathbf{C}$ give the same Gram matrix, and hence the same 4th order tensor. But if such were desired, the three degrees of freedom could be explored, to distinguish between $\mathbf{C}$ and $-\mathbf{C}$. This is a problem we haven't yet addressed.

4.3.2 Experiments and Results

We first conduct experiments on a synthetic dataset, where the ground truth ADC is known, to compare the non-negative ternary quartic approach, denoted henceforth as the "Ternary Quartic" (TQ) approach, to the Euclidean LS and the SH to HOT approaches, which estimate 4th order GDTI1 diffusion tensors without any positive or non-negative diffusion profile constraints. We then experiment on a biological phantom data and two in-vivo human cerebral datasets, where we test for non-negative diffusion and computation time. We also compare the EAPs computed from the estimated 4th order tensors on these datasets. Although we do not extensively compare the Riemannian approach to the Ternary Quartic approach, we however, visualize the EAPs computed from the Riemannian approach alongwith the EAPs computed from the Ternary Quartic approach for a visual inspection.

First on a synthetically generated data we compare the diffusion profiles of 4th order tensors estimated from the Ternary Quartic approach, which ensures a non-negative diffusion profile, to the diffusion profiles of tensors estimated using the Euclidean

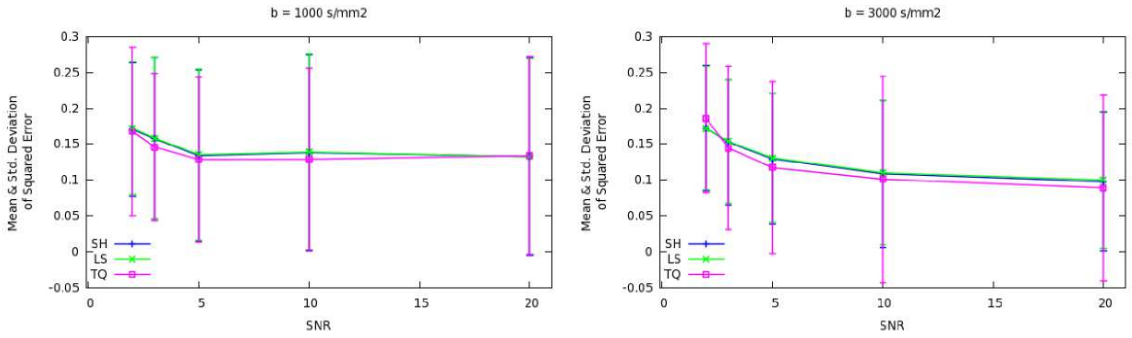

Figure 4.6: Synthetic Dataset. Comparing the effects of signal noise on the Ternary Quartic, the Euclidean least squares (LS), and a spherical harmonic (SH) basis approaches for estimating a 4th order GDTI1 diffusion tensor. The graphs compare the squared difference of the min-max normalized ground truth ADC and the similarly normalized estimated diffusion functions. A non-negative diffusion profile constraint has a positive influence on the estimated ADC when the signal is noisy.

LS approach and the SH to HOT approach, which don't account for any positivity or non-negativity constraints. Since we know the ground truth ADC of the synthetic dataset, we use it as the benchmark, and compare the diffusion functions of all the tensors estimated using the different methods to the ground truth ADC.

We generate the synthetic dataset using the multi-tensor model described in Appendix-A.0.1, where we use the diagonal tensor $\mathbf{D} = \mathrm{diag}(1390, 355, 355) \times 10^{-6}$ mm^2/s for the profile of a single fiber, and $\mathbf{D} = \mathrm{diag}(700, 700, 700) \times 10^{-6}$ mm^2/s for the profile of an isotropic voxel. Crossing voxels are simulated with equal volume fractions for each fiber, where all crossings are perpendicular. We generate 100 test voxels with random fiber configurations, i.e. isotropic voxels, single fiber voxels, two fiber voxels and three fiber voxels, and with random fiber directions. From these test voxels, we generate the diffusion signal using the two b-values of 1000 s/mm^2 and 3000 s/mm^2, and we add a range of Rician noise to the signal. The noise free ADC of the multi-tensor model is easy to compute, and we call this the ground truth ADC.

We estimate 4th order GDTI1 diffusion tensors from this synthetically generated noisy signal using the Ternary Quartic, the Euclidean, and the SH to HOT approaches. We then compute the mean and the standard deviation of the squared difference or error between the min-max normalized ground truth ADC and the min-max normalized spherical profiles of the estimated 4th order tensors along 642 pairs of directions from an icosahedral discretization of the sphere. This is done to evaluate the impact of noise in the signal on the estimation process. The mean and standard deviation of the squared error are presented in Fig-4.6. In these experiments, the random fiber configurations in the 100 test voxels consisted of 25 isotropic voxels, 27

single fiber voxels, 22 two fiber voxels, and 26 three fiber voxels for the b-value of 1000 s/mm^2. For the b-value of 3000 s/mm^2 there were 20 isotropic voxels, 37 single fiber voxels, 24 two fiber voxels, and 19 three fiber voxels. It is clear, that although the non-negativity constraint is slightly weaker than the positive definite constraint, this constraint on the diffusion profile nonetheless has a positive influence on the estimation process when the signal is noisy.

At this juncture, before conducting further experiments on phantom data and in-vivo human data, we visually compare the Riemannian approach, which guarantees a positive definite diffusion profile but solves a more constrained problem, to the Ternary Quartic approach, which guarantees only a positive semi-definite diffusion profile but solves the problem in the correct space. We again generate a synthetic dataset using the multi-tensor model, where we simulate two fiber bundles crossing perpendicularly. The profile for the single fiber is taken from the diagonal tensor $\mathbf{D} = \mathrm{diag}(1700, 300, 300) \times 10^{-6}$ mm^2/s, and crossing voxels are generated using equal fiber volume fractions. The signal is generated for a b-value of 3000 s/mm^2. The diffusion profiles of the estimated 4th order GDTI1 tensors and the EAPs computed thereof are presented in Fig-4.7.

We notice that the ADCs and the EAPs of the Ternary Quartic approach are a little sharper than the Riemannian counterparts. It can be surmised that this is due to the fact that the Riemannian approach cannot estimate certain types of 4th order tensors that can have positive or non-negative diffusion profiles, since these tensors require to have a semi-definite representation in the symmetric 6D 2nd order tensor formulation used by the Riemannian estimation. Such semi-definite 6D 2nd order tensors are, however, pushed to an infinite distance from the estimation tensor by the Riemannian metric. Nonetheless, the overall angular structure of the two methods remain comparable.

We now return to testing the Ternary Quartic method. In the next experiment, we test the Ternary Quartic method on the in-vivo human cerebral dataset described in Appendix-A.0.4 for non-negative diffusion. In this dataset we consider exactly the same masked region with 249352 voxels of interest that we had considered for

(81 dirs)	LS	SH	RM	TQ
Positive	181757	249263	249352	249352
Negative	67595	89	0	0

Table 4.3: Real dataset. The estimated diffusion functions from 249352, 4th order GDTI1 tensors checked for positive diffusion profile on a set of 81 pairs of directions distributed evenly on a sphere. The Ternary Quartic and the Riemannian approaches are the only methods, which guarantee non-negative diffusion.

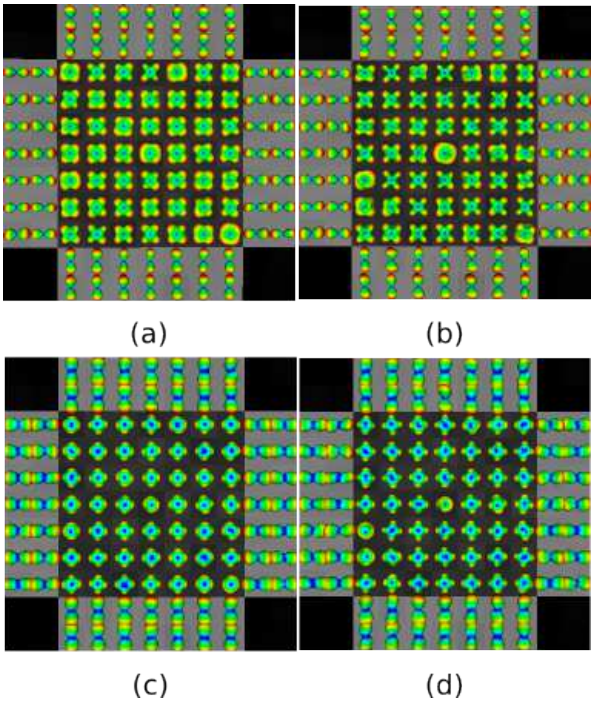

Figure 4.7: Synthetic Dataset. Comparing the diffusion profiles and the EAPs from the Riemannian approach and the Ternary Quartic approach. (a) ADC Riemannian. (b) ADC Ternary Quartic. (c) EAP Riemannian. (d) EAP Ternary Quartic. The Riemannian approach guarantees positive diffusion, but solves a more constrained problem. The Ternary Quartic approach guarantees only a positive semi-definite diffusion, but solves the problem in the correct space.

the Riemannian approach, and we estimate 4th order GDTI1 diffusion tensors using the Ternary Quartic approach. We then evaluate the diffusion profiles of these tensors along 81 pairs of directions on a sphere for negative diffusion. We include the results of the Euclidean LS approach, the SH to HOT approach and the Riemannian approach to summarize the results from all the methods. These are presented in Table-4.3. The Ternary Quartic and the Riemannian methods are the only approaches that guarantee positive diffusion. We note here that in these tests we also explicitly checked for zero diffusion. However, although the Ternary Quartic method guarantees only non-negative diffusion, we never came across zero diffusion. This is understandable, since in practice, due to numerical computations, the possibility of computing exactly zero diffusion is rare. As stated earlier, we therefore consider the non-negative condition only "negligibly" weaker than the positive definite constraint.

On this human cerebral dataset, we also compute the EAPs from the estimated 4th order tensors by computing the Fourier Transform of the signal generated by the estimated tensors using Eq-4.1. To evaluate the impact of the non-negative constraint in the estimation of the tensors on the EAPs computed from these tensors, we compare the EAPs computed from the 4th order tensors estimated using the Eu-

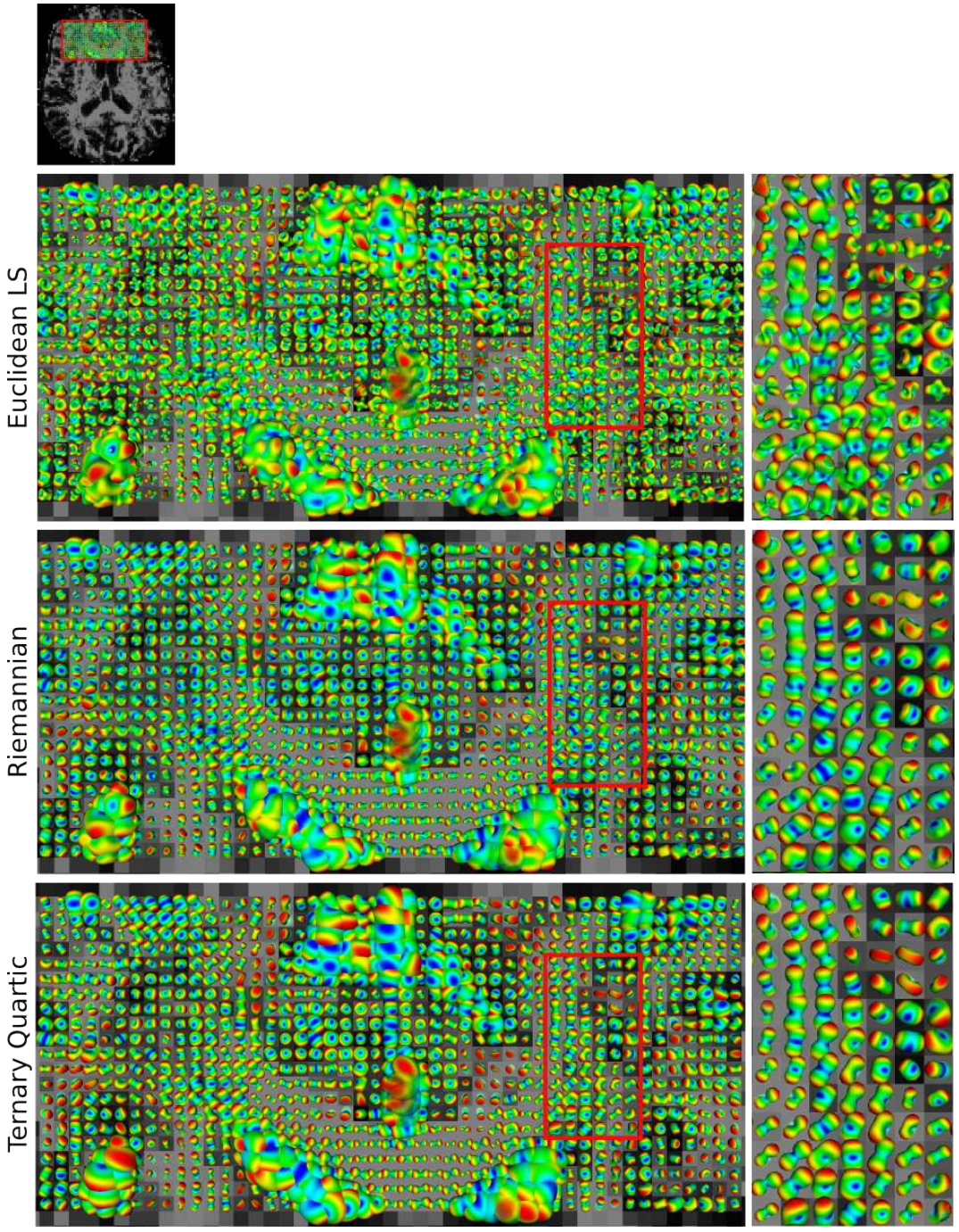

Figure 4.8: In-vivo Human Cerebral Dataset. Effects of the non-negative and the positive definite constraints that are guaranteed by the Ternary Quartic approach and the Riemannian approach are evaluated on the EAPs computed from the estimated tensors. EAPs computed from tensors estimated using the Euclidean LS approach, which doesn't consider any constraints, are shown for comparison. No spatial regularization was used. The improvement in the results is only due to the non-negativity constraints. The dataset used is described in Appendix-A.0.4.

(987 tensors)	LS	Rm	TQ
Estimation	6s	35s	102s

Table 4.4: Real dataset. Comparison of the time for estimating 987, 4th order diffusion tensors that are visualized in Fig-4.8.

clidean LS method, which doesn't consider any constraints. For comparison, we also include the results of the Riemannian method. The results are presented in Fig-4.8. No spatial regularization was used in either the estimation of the 4th order tensors or in the computation of the EAPs. The improved results are only due to the non-negativity and positivity constraints applied by the Ternary Quartic and the Riemannian methods. The result from the Ternary Quartic method confirms the result of the Riemannian method, which implies that applying a non-negative or positive-definite constraint in the estimation process of the 4th order tensors greatly improves the results. However, these constraints also entail increased computational complexity. To evaluate this we present the estimation time of the 987 4th order diffusion tensors in Table-4.4 whose EAPs were visualized.

Next, we conduct an experiment on the biological phantom described in Appendix-A.0.2 to evaluate the geometry of the EAPs computed from 4th order tensors estimated using the Ternary Quartic approach. The phantom was produced using two excised rat spinal cords that were embedded in agar to produce a crossing fiber configuration. Since the layout of this phantom is known, we evaluate the concurrence of the EAPs' geometry with this phantom's layout. In the previous section, we had included the ODFs, which represent the angular marginal distribution of the true and unknown EAPs, as a comparison to the EAPs computed from the tensors estimated using the Riemannian approach. In this experiment, we include the latter – the EAPs computed from tensors estimated using the Riemannian approach as a comparison to the EAPs computed from tensors estimated using the Ternary Quartic approach. The results are presented in Fig-4.9. The EAPs computed from the tensors estimated using the Ternary Quartic method have geometries or angular structures that are coherent with the underlying phantom layout, indicating that it is possible to infer the fiber directions correctly. The geometry of the EAPs computed from the tensors estimated using the two different methods also seem to be in overall agreement. These seem to match both in terms of angular structure and radial size.

Finally, we conclude the experiments, by computing the EAPs from tensors estimated using the Ternary Quartic method from the in-vivo human cerebral dataset described in Appendix-A.0.3. For comparison we include the EAPs computed from tensors estimated using the Riemannian method. The results are presented in Fig-4.10, where a region of interest on a coronal slice is shown. This is the same region of interest that was chosen in the previous section, where for comparison we had shown the ODFs

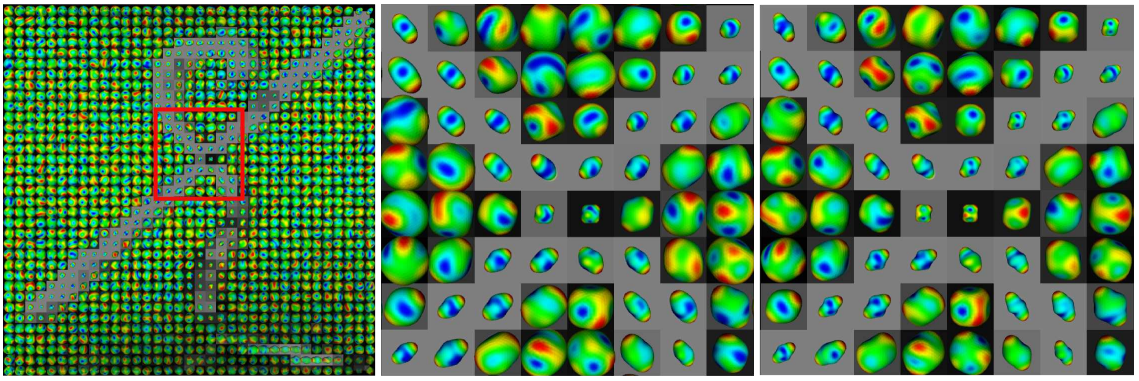

Figure 4.9: Biological Phantom Dataset. (a) The layout of the phantom created using two excised rat spinal cords. (b) EAPs computed from 4th order tensors estimated using the Riemannian approach for comparison. (c) EAPs computed from 4th order tensors estimated using the Ternary Quartic approach. The EAPs were evaluated at the constant probability radius of $|\mathbf{r}| = 17\ \mu$m.

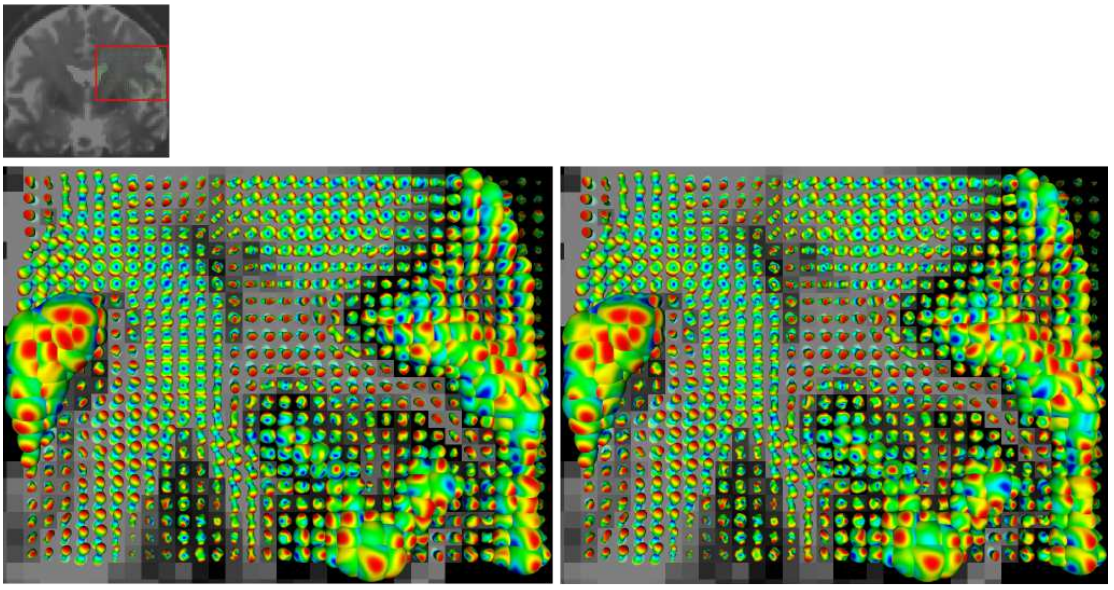

Figure 4.10: In-vivo Human Cerebral Dataset. EAPs computed from 4th order diffusion tensors estimated from the signal using (a) the Riemannian approach, and (b) the Ternary Quartic approach. The coronal slice shows a region of interest where three major fiber bundles are known to intersect. These are the cortico-spinal tract, the corpus callosum, and the superior longitudinal fasciculus.

estimated from the signal. In this region of interest three major fiber bundles are known to cross. These are the corpus callosum, top and left, the cortico-spinal tract, left and top to down, and the superior longitudinal fasciculus, traversing the plane

near the centre. Note the general agreement in shape, both angular structure and radial size, between the EAPs computed from the 4th order tensors estimated using the two different methods.

4.3.3 Discussion

In this section we presented an alternate approach for estimating 4th order GDTI1 diffusion tensors with a positive diffusion profile from the signal. In this approach we adopted the polynomial interpretation of HOTs, and reframed the problem of estimating tensors with positive diffusion as a problem of estimating positive polynomials from the signal. However, since results on polynomials only consider non-negative polynomials and not strictly positive polynomials, we had to consider the slightly weaker problem of estimating polynomials or tensors with non-negative diffusion profiles from the signal. However, in implementation, this turned out to only be a negligible concession, since due to numerical computations, computing exactly zero diffusion was a rarity. This approach also employed the Euclidean metric, which, as suggested in [67], is perhaps better suited for diffusion data than the affine invariant Riemannian metric.

Our proposed method for estimating non-negative homogeneous polynomials from the signal is based on Hilbert's famous theorem on non-negative ternary quartics, where he showed that non-negative ternary quartics could be written as a sum of three squares of homogeneous quadratic polynomials. Since this result is only for degree 4 homogeneous polynomials, our approach only considers estimating 4th order diffusion tensors with non-negative diffusion profiles. This is done by estimating the coefficients of the three quadratic forms from the signal, and then by computing the coefficients of the 4th order diffusion tensor from Hilbert's sum of squares, which in practice involves the Gram matrix.

Our approach is in the class of two other approaches that also use the result on ternary quartics. The three methods differ in the way the coefficients of the quadratic forms are estimated from the signal. We estimate all the coefficients separately in a vector form, while the two other methods estimate the coefficients in a matrix form. The matrix form leads to an ambiguity in the parameterization that results in an infinite solution space. However, this is overcome by one of the matrix methods by a **QR**-decomposition and by the other matrix method by an Iwasawa decomposition followed by a Cholesky parameterization of the leading minor of the matrix. Our formulation on the other hand naturally overcomes such ambiguities and is straightforward to implement. However, we estimate 18 unknowns from the signal, and then compute the 15 independent coefficients of the 4th order tensor from these unknowns. This implies three degrees of freedom that can be explored to apply further constraints. An interesting lead to follow is to try and distinguish between the 18 un-

knowns and their negative counterparts, since both result in the same 15 coefficients of the 4th order diffusion tensor.

In comparison to the family of Ternary Quartic methods, the only other approach for estimating 4th order GDTI1 diffusion tensors with a positive diffusion profile from the diffusion signal is the Riemannian approach we presented in the previous section. While, the Ternary Quartic approach can only deal with a non-negative diffusion, the Riemannian approach in comparison can deal with the stronger formulation of a positive definite diffusion profile. However, as it was discussed here, and shown in other papers, the Riemannian approach deals with the positivity constraint in a more constrained space than implied by the 4th order tensor model, whereas the Ternary Quartic approach solves the problem of non-negative diffusion in the correct space. In our experiments on synthetic data, we observed sharper angular profiles from the Ternary Quartic approach when compared to the results of the Riemannian approach, and suspected that this was due to the over-constraint of the latter approach. However, this needs to be investigated further before it can be confirmed.

We conducted experiments on synthetic data with known ground truth diffusion profiles, where we compared the Ternary Quartic approach to methods of estimating the 4th order diffusion tensor that do not take into consideration any constraints on the diffusion profile, to evaluate the impact of noise in the signal on the estimation process of the diffusion tensors. These experiments showed the importance of considering constraints like non-negativity on the diffusion profile, while estimating diffusion tensors of order 4 from noisy signals. This was in conformity with the experiments conducted in the previous section, which showed that the positivity constraint implied by the Riemannian method had a benevolent influence on the estimated tensors and their diffusion profiles. Further experiments on in-vivo human cerebral data again confirmed this, since only the Riemannian approach and the Ternary Quartic approach were able to estimate 4th order tensors with positive diffusion profiles. Both the standard Euclidean LS approach and the SH to HOT approach estimated tensors with negative diffusion profiles although negative diffusion is non-physical. Furthermore, the impact of non-negative and positive constraints on the diffusion profile on the EAPs computed from the tensors was shown in the in-vivo data experiment. This again indicated the importance of the non-negativity and the positivity constraints.

Finally we conducted experiments on a biological phantom with a known layout to consider the coherence of the geometry of EAPs computed from 4th order tensors estimated using the Ternary Quartic approach with the underlying fiber directions. The geometry of the EAPs was in concurrence with the underlying phantom layout, and also in agreement with the EAPs computed from tensors estimated using the Riemannian approach. This confirmed that it is possible to infer the underlying fiber directions from the angular structure of the EAPs computed from 4th order tensors estimated using the Ternary Quartic approach.

4.4 Discussion and Conclusion

In this chapter, we considered the GDTI1 model, which was proposed to accurately estimate the complex profile of the ADC in dMRI, in regions with heterogeneous fiber configurations. In such regions the popular DTI fails to correctly model the ADC. In GDTI1 Cartesian tensors of order higher than two were used to attain greater accuracy in the modelling of complex shaped ADCs. GDTI1 HOTs of order k were assumed to be symmetric since only their projections along vectors were used in the ADC modelling, and were assumed to be of even order since negative diffusion is non-physical. However, in spite of this design, the normal and standard method for estimating GDTI1 HOTs from the signal, namely the Euclidean LS approach doesn't guarantee an estimated HOT with a positive diffusion profile. Euclidean LS estimation, although linear and efficient can result in estimated HOTs with negative diffusion profiles.

In this chapter, we proposed two different approaches for estimating 4th order GDTI1 diffusion tensors with positive diffusion profiles and non-negative diffusion profiles respectively. In the first method, we considered the algebra of 4th order tensors to map symmetric 3D 4th order tensors to symmetric 6D 2nd order tensors. We then applied the Riemannian framework for the space of $\mathcal{S}ym_6^+$, to estimate 4th order diffusion tensors with strictly positive or positive definite diffusion profiles. In the second method, we considered the polynomial interpretation of the multi-linear form of HOTs, to reformulate the problem of estimating a HOT as a problem of estimating a polynomial. In the case of 4th order diffusion tensors, we were able to use Hilbert's theorem on non-negative ternary quartics to parameterize 4th order tensors as a sum of squares of quadratic forms. By estimating the coefficients of the quadratic forms, we were able to reconstruct 4th order diffusion tensors with non-negative diffusion profiles from the signal.

The Riemannian method we proposed, ensures a positive definite diffusion profile, but solves a problem more constrained than implied by the model. This can be understood from the fact that the 3D 4th order tensors were estimated in $\mathcal{S}ym_6^+$, as 6D 2nd order tensors, which implies that the Riemannian method ensures that the multi-linear form of the 4th order tensor is positive definite for all symmetric 3D 2nd order tensor. However, the GDTI1 model implies that the multi-linear form of the 4th order tensor needs to be positive definite for only rank deficient 3D 2nd order tensors of maximal rank one. Therefore, the Riemannian method ensures a positive diffusion profile, but the solution space is more constrained than the true solution space.

The second method we proposed – the Ternary Quartic method solves the problem in the correct space due to the appropriate polynomial parameterization. However, since the known polynomial results, e.g. Hilbert's theorem on ternary quartics, only guarantee non-negativity, this method considers the theoretically weaker problem of

a positive semi-definite or a non-negative diffusion profile. But this method also uses the Euclidean metric, which, as has been suggested in [67], is perhaps better suited for computing with diffusion data than the affine invariant Riemannian metric.

From the implementation and the results, we found that the shape of the ADCs and EAPs computed from tensors estimated using the Riemannian method to be similar to the shape of the ADCs and EAPs computed from tensors estimated using the Ternary Quartic method. We did, however, remark a swelling in the shapes of the tensors estimated using Riemannian method, which we suspected was the result of the over constraint. A more detailed analysis is, therefore, necessary to identify the sub-space spanned by the Riemannian approach, and also the quantify the impact of this sub-space on the estimated results. Finally, in the tests for negative diffusion profiles, we never came across zero diffusion from tensors estimated using the Ternary Quartic method, which is probably due to numerical computations. Therefore, we concluded that the concession of the weaker non-negativity constraint to be negligible in practice.

We experimented on synthetic and in-vivo human cerebral data using both the Riemannian framework and the Ternary Quartic approach to motivate the need for a positive or non-negative diffusion profile constraint. Both synthetic data experiments and in-vivo data experiments clearly indicated the gains of applying such constraints. We also presented the computation time to evaluate the increased complexity, and found this to be tractable. Finally we conducted tests on a biological phantom data with a known layout to evaluate whether it was possible to infer the underlying fiber directions from the geometry of the EAPs computed from the tensors estimated using the two approaches presented in this chapter. Our experiments indicated that this could be answered in the affirmative and that the geometry of the EAPs computed from the tensors estimated using the Riemannian framework and the Ternary Quartic approach could reveal the underlying fiber directions.

CHAPTER 5

FAST & ANALYTICAL EAP APPROXIMATION FROM A 4TH ORDER TENSOR

Contents

5.1 INTRODUCTION

Generalized Diffusion Tensor Imaging (GDTI1: section-3.4.2), was proposed to model the apparent diffusion coefficient (ADC) recovered by diffusion MRI (dMRI) when imaging the diffusion of water molecules in heterogeneous media like the cerebral white matter. Essentially, GDTI1 [44] uses higher order Cartesian tensors (HOTs) to model the spherical profile of the ADC. However, although the complex shape of the ADC reflects the complex geometry of the underlying tissue, it is well known that the geometry of the ADC doesn't correspond to underlying fiber directions [46]. This can be understood from the q-space formalism, where it can be seen that the ADC and the diffusion signal are in the Fourier domain of the diffusion EAP, which describes the probability of the diffusing particles. The geometry of the EAP is a direct indicator of the microstructure of the underlying tissue or fiber bundles.

But GDTI1 was proposed because it overcomes the limitation of diffusion tensor imaging (DTI) [30], which is inadequate at modelling the signal from regions with multiple fiber configurations. The HOT that is used in GDTI1 to model the spherical profile of the ADC, can model the signal and the ADC in such situations with greater accuracy. Therefore, the GDTI1 approach has been of considerable interest and has seen various developments. In particular a number of contributions were made to estimate 4th order HOTs in GDTI1 under the constraint of a positive diffusion profile, since negative diffusion is non-physical [65, 83, 66, 79].

However, in spite of the interests in HOTs to describe complex shaped ADCs, the tissue microstructure can only be inferred from the shape of the EAP. However, to compute the EAP from the HOT model of the ADC in GDTI1 is no easy task [84]. That is perhaps the reason why the GDTI1 approach has been overtaken by other methods that estimate the EAP or its characteristics directly from the signal, such as QBI, PAS-MRI, DOT, SD etc. [28, 85, 59, 58, 60, 86, 87].

In this section, we propose a modification to the original GDTI1 model under the q-space formalism, which allows us to compute a closed-form approximation of the EAP using Hermite polynomials. In this modified model we still estimate HOTs from the signal, but these HOTs don't represent the spherical profile of the ADC anymore. The HOTs are used to describe the signal over the entire q-space. We show that this approximation converges well to the true EAP. Also, we are still able to apply the constraint of a positive diffusion profile in our modified model while estimating the HOT from the signal before computing the EAP approximation. Finally since the solution is analytical, it is fast and can be implemented efficiently.

We first test this approach on a synthetically generated dataset that simulates crossing fibers. We compare the computation time of this method with a numerical discrete Fourier Transform scheme to recover the EAP from the original GDTI1 model. We show that with our modified approach we are able to recover the underlying fiber

layout and gain considerably in computation time. This is of relevance in visualization. We also conduct experiments on in-vivo human cerebral data to illustrate the applicability of this approach on real data.

5.2 Materials and Methods

We recall the signal $E(\mathbf{q}) = \frac{S(\mathbf{q})}{S_0}$, in GDTI1 [44] is modelled using a kth order tensor $\mathbf{D}^{(k)}$, which describes the spherical or angular profile of the ADC:

$$\begin{aligned} E(\mathbf{q})_k &= \exp\left(-4\pi^2 q^2 t \sum_{j_1=1}^{3}\sum_{j_2=1}^{3}\cdots\sum_{j_k=1}^{3} D^{(k)}_{j_1 j_2 \ldots j_k} g_{j_1} g_{j_2} \ldots g_{j_k}\right) \\ &= \exp\left(-4\pi^2 q^2 t \sum_{m+n+p=k} D^{(k)}_{mnp} g_1^m g_2^n g_3^p\right), \end{aligned} \tag{5.1}$$

where $\mathbf{q} = \gamma\delta\mathbf{G}/2\pi$ when $\mathbf{G}$ is the gradient vector, $t = (\Delta - \delta/3)$, and g_j are the components of the unit gradient vector $\mathbf{g} = \mathbf{G}/|\mathbf{G}|$. The second equality is a reinterpretation of the first by a rearrangement of the indices [65]. $k = 4$ gives the 4th order diffusion tensor model. We also recall that in the q-space formalism, the diffusion signal and the EAP are related by the Fourier Transform [25]:

$$P(\mathbf{r}) = \int E(\mathbf{q}) \exp\left(-2\pi i \mathbf{q}^T \mathbf{r}\right) d\mathbf{q}.$$

The q-space formalism entails the condition that $\delta \ll \Delta$, implying that $t \approx \Delta$.

For $k = 2$, $E(\mathbf{q})_2$ is the DTI model, whose Fourier Transform $P(\mathbf{r})_2$ is well known to also be a Gaussian, which corresponds to the free diffusion EAP (section-3.3.1). We denote by $P(\mathbf{r})_i$ the EAP computed from the Fourier Transform of $E(\mathbf{q})_i$. However, for general $k > 2$, closed-forms for the Cartesian Fourier Transform of $E(\mathbf{q})_k$ are hard to compute, since in Cartesian coordinates $E(\mathbf{q})_k$ isn't separable in q_1, q_2, q_3, the components of $\mathbf{q}$. In [84], where a method for recovering the EAP from GDTI1 is proposed, $P(\mathbf{r})_k$ is computed numerically by evaluating $E(\mathbf{q})_k$ more or less densely in q-space and by computing its fast Fourier Transform.

In this section, we propose to modify the original GDTI1 model by making Eq-5.1 separable in the Cartesian coordinate. This is done by realizing that GDTI1 in fact uses two orders $k1$ and $k2$ for the radial and the angular components respectively:

$$E(\mathbf{q})_{k1,k2} = \exp\left(-4\pi^2 q^{k1} \alpha t \sum_{m+n+p=k2} D^{(k2)}_{mnp} g_1^m g_2^n g_3^p\right) \tag{5.2}$$

$$= \exp\left(-4\pi^2 q^{k1-k2} \alpha t \sum_{m+n+p=k2} D^{(k2)}_{mnp} q_1^m q_2^n q_3^p\right), \tag{5.3}$$

where in GDTI1 $k1 = 2$ and $k2 = k$. In this formulation α is a constant with units m^{2-k1} that makes the exponent unit-free when $k1 \neq 2$, and $q = |\mathbf{q}|$. The first equality

is written in the components of the unit gradient vector $\mathbf{g}$, while the second equality is in the components of the reciprocal space vector $\mathbf{q}$. This reformulation of GDTI1, allows $E(\mathbf{q})$ to become separable in q_1, q_2, q_3 when $k1 = k2 = k$.

Although the original formulation of GDTI1 uses a Cartesian HOT, it was in truth written in spherical coordinates since the HOT $\mathbf{D}^{(k)}$, was evaluated only along the unit gradient vector $\mathbf{g}$. Alternately the spherical coordinates also become evident from the two separate orders $k1, k2$, for the radial and the angular parts. By equating the two orders $k1 = k2$, our modification converts the signal formulation to the Cartesian coordinates and recouples the radial and the angular parts. The HOT is now evaluated over the entire q-space. This reformulation allows us to compute an analytical Fourier Transform of $E(\mathbf{q})_{k,k}$ in the Cartesian coordinates.

It should be noted that the DOT method proposed in [60] computes the Fourier Transform of the GDTI1 model in spherical coordinates. However, in the DOT, the Cartesian HOT is replaced by the spherical harmonic (SH) basis to describe the complex shaped ADC, since the SHs are easier to manipulate in the spherical coordinates, and since they transform well under the Fourier Transform in spherical coordinates.

Interestingly, in spite of this reformulation, the signal in Eq-5.3 still retains a mono-exponential form parameterized by the diffusion HOT $\mathbf{D}^{(k_2)}$, like in the original formulation. In Eq-5.1 the negative logarithm of the signal is $b \cdot \mathrm{ADC}$, where $b = 4\pi^2 q^2 t$. In the modified model, if we denote $b' = 4\pi^2 \alpha t$, then:

$$\ln\left(E(\mathbf{q})_{k,k}\right) = -b' \cdot \widehat{\mathrm{ADC}} = -b' \sum_{m+n+p=k} D^{(k)}_{mnp} q_1^m q_2^n q_3^p.$$

This makes it evident, that we can again estimate the HOT $\mathbf{D}^{(k)}$ from the diffusion signal in such a way, that its diffusion profile is positive, i.e. $\widehat{\mathrm{ADC}} > 0$. Here, the diffusion profile $\widehat{\mathrm{ADC}}$ is no longer a function on the sphere, but rather a function on the entire q-space. However, from this equation, we also see that when $k = 4$, the methods that were developed to estimate a HOT with a positive diffusion profile for the GDTI1 model in Eq-5.1, can all be directly applied to the modified model in Eq-5.3, to estimate $\mathbf{D}^{(4)}$ with a positive diffusion profile constraint. Therefore, using the modified model in Eq-5.3, it is possible to estimate a 4th order HOT from the signal, which satisfies a positive diffusion profile, before computing the EAP from this HOT.

Our solution for the EAP from the modified HOT model pivots around the following property of the Fourier Transform:

$$\mathscr{F}\{x^n f(x)\} = \left(\frac{i}{2\pi}\right)^n \frac{d^n}{dt^n} \mathscr{F}\{f(x)\}(t),$$

where $\mathscr{F}$ stands for the Fourier Transform. If we employ $g(x) = e^{-2\pi^2 x^2}$ for $f(x)$, then its Fourier Transform is $G(t) = \mathscr{F}\{g(x)\}(t) = \frac{1}{\sqrt{2\pi}} e^{\frac{-t^2}{2}}$. However, the derivatives of

the Gaussian function $G(t)$, generate the Hermite polynomials $\frac{-d^n}{dt^n}e^{\frac{-t^2}{2}} = He_n(t)e^{\frac{-t^2}{2}}$. Therefore:

$$\mathscr{F}\{x^n e^{-2\pi^2 x^2}\}(t) = \left(\frac{i}{2\pi}\right)^n He_n(t)\frac{1}{\sqrt{2\pi}}e^{\frac{-t^2}{2}}. \tag{5.4}$$

The generalization to 3D is simple since the Gaussian function is separable in the variables.

To leverage this property of the Fourier Transform, and those of the Gaussian function, for computing a closed-form approximation of the EAP from $E(\mathbf{q})_{k,k}$, i.e. its Fourier Transform $P(\mathbf{r})_{k,k}$, we propose to expand $E(\mathbf{q})_{k,k}$ as a multivariate polynomial multiplied by a 3D Gaussian function:

$$E(\mathbf{q})_{k,k} \approx \left(\sum C_{l,s,u} q_1^l q_2^s q_3^u\right) \exp\left(-2\pi^2\beta(q_1^2+q_2^2+q_3^2)\right),$$

where β is a constant with units m^2 to render the exponent unit free, and the new coefficients $C_{l,s,u}$ in the polynomial expansion, contain the imaging parameter b', and the coefficients of the HOT $\mathbf{D}^{(k)}$. If this expansion were possible, then $E(\mathbf{q})_{k,k}$ would become separable in q_1, q_2, q_3.

Such an expansion can be achieved from a few manipulations and a Taylor expansion:

$$\begin{aligned} E(\mathbf{q})_{k,k} &= \exp\left(\left(-4\pi^2\alpha t \sum D^{(k)}_{mnp} q_1^m q_2^n q_3^p\right) + 2\pi^2\beta(q_1^2+q_2^2+q_3^2)\right) \times \\ &\quad \exp\left(-2\pi^2\beta(q_1^2+q_2^2+q_3^2)\right) \\ &= h(\mathbf{q}) \exp\left(-2\pi^2\beta(q_1^2+q_2^2+q_3^2)\right), \end{aligned}$$

where the summation in the first equality is over m, n, p such that $m+n+p = k$, as denoted in Eq-5.3, and $h(\mathbf{q}) = \exp\left(\left(-4\pi^2\alpha t \sum D_{mnp} q_1^m q_2^n q_3^p\right) + 2\pi^2\beta(q_1^2+q_2^2+q_3^2)\right)$. Since $h(\mathbf{q})$ is an exponential function $e^{X(\mathbf{q})}$, we define $h_n(\mathbf{q})$ as the nth order Taylor expansion of $h(\mathbf{q})$ in the variables q_1, q_2, q_3. Therefore $h_n(\mathbf{q})$ is a trivariate polynomial of degree $n-1$ plus an error term of degree n. Ignoring the error term, $h_n(\mathbf{q})$ has the required form $h_n(\mathbf{q}) = \sum_{l+s+u<n} C_{l,s,u} q_1^l q_2^s q_3^u$. Therefore we can define the nth order approximation of the signal:

$$\begin{aligned} E(\mathbf{q})^{(n)}_{k,k} &= h_n(\mathbf{q}) \exp\left(-2\pi^2\beta(q_1^2+q_2^2+q_3^2)\right) \\ &= \left(\sum_{l+s+u<n} C_{l,s,u} q_1^l q_2^s q_3^u\right) \exp\left(-2\pi^2\beta(q_1^2+q_2^2+q_3^2)\right). \end{aligned} \tag{5.5}$$

Since $h_n(\mathbf{q})$ is the Taylor's expansion of an exponential function $h(\mathbf{q})$, $h_n(\mathbf{q})$ converges to $h(\mathbf{q})$ uniformly over all $\mathbf{R}^3$ as n is made large. Therefore $E(\mathbf{q})^{(n)}_{k,k}$ converges to $E(\mathbf{q})_{k,k}$ uniformly over $\mathbf{R}^3$ as n is made large.

As $E(\mathbf{q})^{(n)}_{k,k}$ is separable in q_1, q_2, q_3, it is possible to compute a closed form for its

Cartesian Fourier Transform, which is also separable. Using the property in Eq-5.4:

$$P(\mathbf{r})_{k,k}^{(n)} = \frac{1}{(2\pi\beta)^{\frac{3}{2}}} \exp\left(\frac{-1}{2\beta}(r_1^2 + r_2^2 + r_3^2)\right) \times \left(\sum_{l+s+u<n} i^{l+s+u} C_{l,s,u} He_l(r_1) He_s(r_2) He_u(r_3)\right). \quad (5.6)$$

For large n, the approximation $P(\mathbf{r})_{k,k}^{(n)}$ converges to the true EAP $P(\mathbf{r})_{k,k}$. In practice we use $n = 5, 7, 9$.

We thus find a closed-form approximation of the EAP from the modified HOT model of the ADC in GDTI1. The solution is a polynomial multiplied by a Gaussian. Therefore, the polynomial can be interpreted as the correction to the free diffusion Gaussian EAP due to the complex heterogeneous medium.

An alternate explanation to this method, can be found from Eqs-5.5 & 5.6, which avoids modifying the GDTI1 model. Eqs-5.5 & 5.6 resemble closely the formulation of the signal in the expansion of the cumulant generating function (CGF) (Eq-3.33), and the approximation of the EAP in GDTI2 using the Gram-Charlier series (Eq-3.45) [45]. While in the CGF expansion, the signal is expanded in the standard polynomial basis with the cumulants as the coefficients, in Eq-5.5 the signal is in fact expanded in a subset of the standard polynomial basis. Since the Fourier Transform of a monomial multiplied by a Gaussian is a Hermite polynomial multiplied by a Gaussian, the EAP is approximated in GDTI2 in the Hermite polynomial (tensor) basis, with again the cumulants as the coefficients using the Gram-Charlier series. Likewise in Eq-5.6, the EAP is approximated in the Hermite polynomial (tensor) basis. A difference between this method and GDTI2 lies in the fact that while GDTI2 uses the entire polynomial (Hermite polynomial) basis to expand the signal (EAP), this method uses only a subset of these bases. Therefore, the coefficients $C_{l,s,u}$ are no longer the cumulants. Or, in other words, if the entire polynomial basis had been used here, then $C_{l,s,u}$ would have become the cumulants. Also, the coefficients $C_{l,s,u}$ aren't estimated directly from the signal, though they can be from Eq-5.5, but are computed from the coefficients of the HOT $\mathbf{D}^{(k)}$ and the Taylor expansion in Eq-5.5. Therefore, changing the order n of the approximation has an effect on the approximated EAP, since it adds or subtracts terms in Eq-5.6. However, as shown in the experiments, this does not affect the direction of the peaks of the approximate EAP. This interpretation shows that this method also belongs to the same family as GDTI2.

We program an efficient implementation of the proposed method through symbolic computation. Using Maple$^{\mathrm{TM}}$, and assuming Eq-5.3, we expand $E(\mathbf{q})_{k,k}$ into a Taylor series in the variables q_1, q_2, q_3 up to predefined orders $n = 5, 7, 9$. This expansion automatically computes for us the new coefficients $C_{l,s,u}$ from the coefficients of the HOT $\mathbf{D}^{(k)}$ (Eq-5.5). The EAP approximation $P(\mathbf{r})_{k,k}^{(n)}$, is then generated by again computing the Fourier Transform of $E(\mathbf{q})_{k,k}^{(n)}$ symbolically. The expansion of the EAP is

then converted to C-code using Maple$^{\text{TM}}$, which is compiled. This routine therefore takes as input the imaging parameters, namely t, and the coefficients of $\mathbf{D}^{(k)}$ that are estimated from the diffusion signal. α, β are taken to be equal to 1.

5.3 Experiments and Results

Although we developed the theory for arbitrary $k = k1 = k2$, for the following experiments we consider $k = 4$, i.e. $E(\mathbf{q})_{4,4}$ and $P(\mathbf{r})^{(n)}_{4,4}$. This is because, as we have seen, for $E(\mathbf{q})_{4,4}$ we can employ HOT estimation techniques to guarantee that the 4th order HOT has a positive diffusion profile ($\widehat{\text{ADC}} > 0$). In all the following the 4th order HOT $\mathbf{D}^{(4)}$ is estimated from Eq-5.2, with $k1 = k2 = 4$ using the method described in [79]. The estimation in [79] is described for Eq-5.1, which depends on the b-value $b = 4\pi^2 q^2 t$. We adapt this to Eq-5.2 by replacing the b-value by the imaging parameters $4\pi^2\alpha t$ and the ADC by the $\widehat{\text{ADC}}$.

We test the approach first on synthetic data, and then on in-vivo human cerebral data. The synthetic data is generated using the multi-tensor model described in Appendix-A.0.1. We use $\mathbf{D} = \text{diag}(1700, 300, 300) \times 10^{-6}$ mm^2/s, for the profile of a single fiber, and $\mathbf{D} = \text{diag}(700, 700, 700) \times 10^{-6}$ mm^2/s for the profile of an isotropic voxel. The diffusion signals are generated with a single shell acquisition scheme based on a b-value of 3000 s/mm^2. The gradient directions are considered isotropically spread out on the sphere along 81 encoding directions. Since the dataset is generated from the fixed b-value, we let $t = 50$ ms, which allows us to compute q.

In the synthetic data experiment, we consider two fiber bundles crossing or overlapping in a way that makes them converge and diverge. This changes their crossing angle in the region where they cross. The voxels outside the fiber bundles are generated using the isotropic diffusion profile. The layout of the synthetic data fibers, and the result of the estimated EAP approximations of order 7, from the 4th order HOT, $P(\mathbf{r})^{(7)}_{4,4}$, are presented in Fig-5.2. We see that the angular profiles of the EAP, evaluated at $|\mathbf{r}| = 20$ μm, are well aligned with the original fiber bundle layout – their peaks correspond. In the two zooms, we take a closer look at some of the voxels in the crossing regions. In the top zoom we see that the peaks of the angular profile of

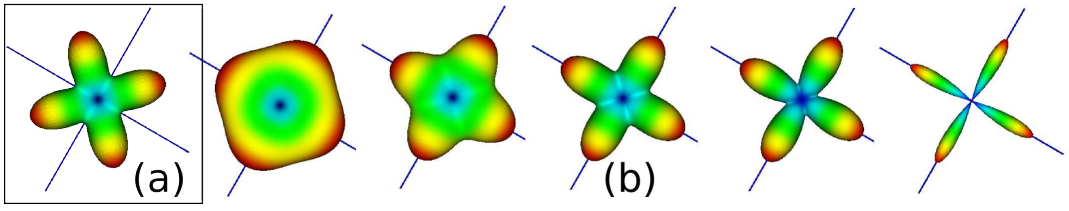

Figure 5.1: Spherical profiles of (a) the $\widehat{\text{ADC}}$ estimated from the modified GDTI1 with a 4th order tensor and (b) the EAP approximation $P(\mathbf{r})^{(7)}_{4,4}$ with increasing $|\mathbf{r}|$ from 12 μm to 20 μm.

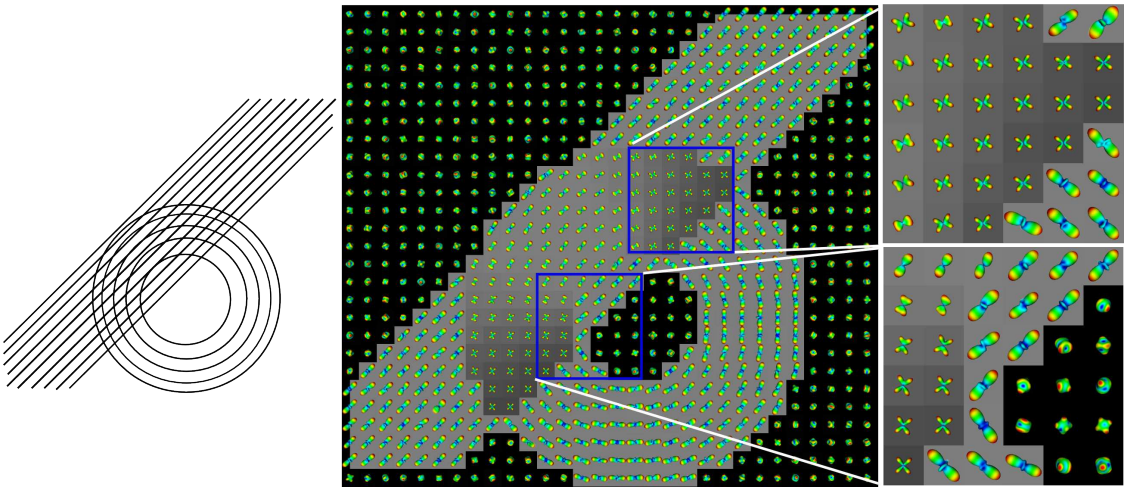

Figure 5.2: Synthetic dataset experiment. Left: Fiber bundle layout. Centre: $P(\mathbf{r})^{(7)}_{4,4}$. Right: Zoom into the regions with crossings – top: the changing angle between the fiber bundles is detected, bottom: three types of voxels, isotropic, single fiber, two fibers.

the EAP detect the changing angle between the converging or diverging fiber bundles. In the bottom zoom we see the three different types of voxels recovered by the EAP, namely the isotropic, the single fiber, and the two fibers crossing. Although the isotropic voxels also have peaks, the peaks of the EAPs representing crossings are far sharper.

Speed is of great utility in visualization. The closed-form of $P(\mathbf{r})^{(n)}_{4,4}$ makes it computationally efficient, especially since the expression for a fixed n can be hard coded and compiled. In the synthetic data experiment we compare this approach to a numerical Fourier Transform of the GDTI1 model. For visualization and comparison we consider the whole slice, which is partially seen in Fig-5.2, with 30×30 voxels. For the implementation of the numerical Fourier Transform we evaluate the GDTI1 model (Eq-5.1) on a $21 \times 21 \times 21$ Cartesian grid. We evaluate the numerically computed EAP on a coarse spherical mesh with 162 vertices. The computation time on our computer was 526 s. We then compute $P(\mathbf{r})^{(7)}_{4,4}$, but this time on a finer spherical mesh with 2562 vertices. The computation time on the same computer was 73 sec. Despite the finer mesh, $P(\mathbf{r})^{(7)}_{4,4}$ is about seven times faster than the regular discrete Fourier Transform. On the coarse mesh with 162 vertices, the computation time for $P(\mathbf{r})^{(7)}_{4,4}$ was about 10 s.

Fig-5.3 shows the effect of the Taylor expansion order n on the EAP approximation. The six images are zooms into a region where the two fiber bundles converge and cross. In the top row we present $P(\mathbf{r})^{(n)}_{4,4}$, with $n = 5, 7, 9$ evaluated for the probability radius $|\mathbf{r}| = 16$ μm. Increasing n adds more terms to the EAP approximation in Eq-5.6, which adds more corrections to the approximation, making it converge better to

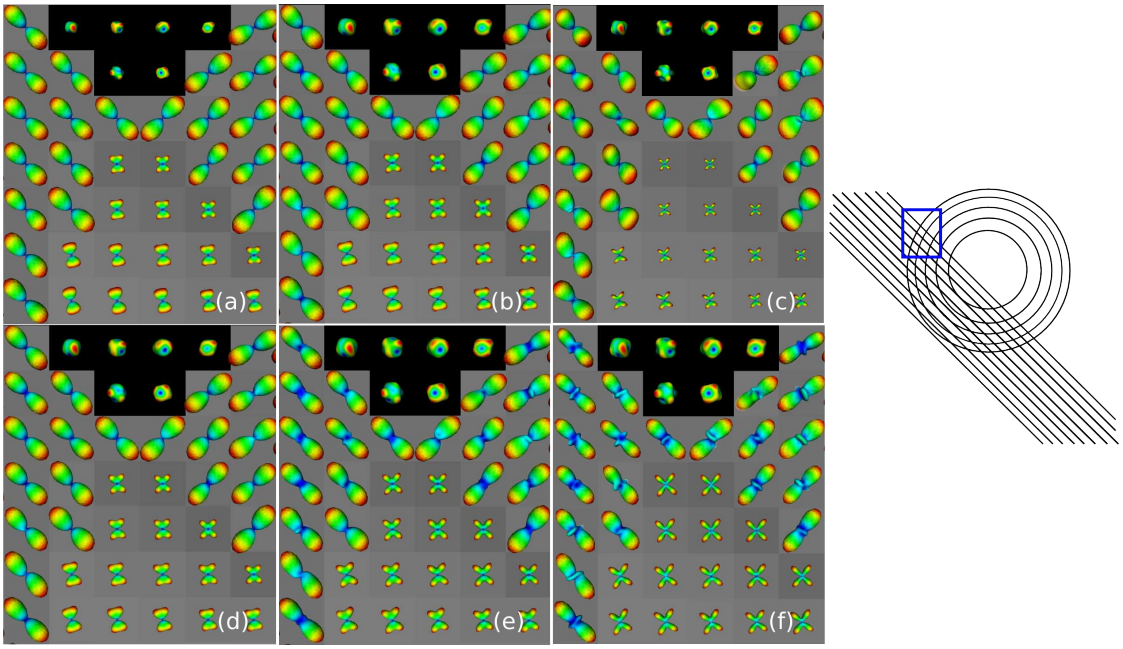

Figure 5.3: Effects of the approximating order n and the probability radius $|\mathbf{r}|$. In top-row $|\mathbf{r}|$ is fixed and we vary n. In bottom row n is fixed and we vary $|\mathbf{r}|$. Top row: $|\mathbf{r}| = 16$ μm: (a) $P(\mathbf{r})_{4,4}^{(5)}$, (b) $P(\mathbf{r})_{4,4}^{(7)}$, (c) $P(\mathbf{r})_{4,4}^{(9)}$. Bottom row: $n = 7$ $\left(P(\mathbf{r})_{4,4}^{(7)}\right)$: (d) $\equiv$ (b) $|\mathbf{r}| = 16$ μm, (e) $|\mathbf{r}| = 18$ μm, $|\mathbf{r}| = 20$ μm.

the true EAP. As the approximation $P(\mathbf{r})_{4,4}^{(n)}$, is corrected, it shows sharper peaks and narrower crossings for $n = 9$, than $n = 5$, for the same probability radius. However, this also increases the computation time. But the peaks of the lower order approximations seem to be well aligned with the higher order approximations. In other words, the peaks maintain their angular alignment, although they lose sharpness and the EAP loses angular resolution, and narrow crossings become harder to discern. However, the angular resolution can be recovered, and the peaks "sharpened" in the lower order approximations by increasing the probability radius, which saves computing time. This is shown in the bottom row, where we show $P(\mathbf{r})_{4,4}^{(7)}$ for the probability radius varying from $|\mathbf{r}| = 16$ μm$\ldots 20$ μm. These experiments reveal that the effect of the Taylor expansion order n is to underestimate the EAP in the approximation. Therefore, we use the order 7 approximation $P(\mathbf{r})_{4,4}^{(7)}$, as a good trade-off between convergence to the true EAP and computation time.

For the in-vivo human cerebral data, we use the dataset described in Appendix-A.0.3. However, in this case we make certain assumptions about the imaging parameters. This dataset was acquired using a twice refocussed Reese sequence [88], and not a standard PGSE sequence, with gradient durations $\delta_1 = 12.03$ ms, $\delta_2 = 19.88$ ms, $\delta_3 = 21.76$ ms, $\delta_4 = 10.15$ ms. As suggested in [89], Reese sequence parameters are sometimes adapted to the standard PGSE parameters with $\delta = \delta_1 + \delta_2$, and Δ as the time between the start of δ_1 and the start of δ_3. However, since the application times

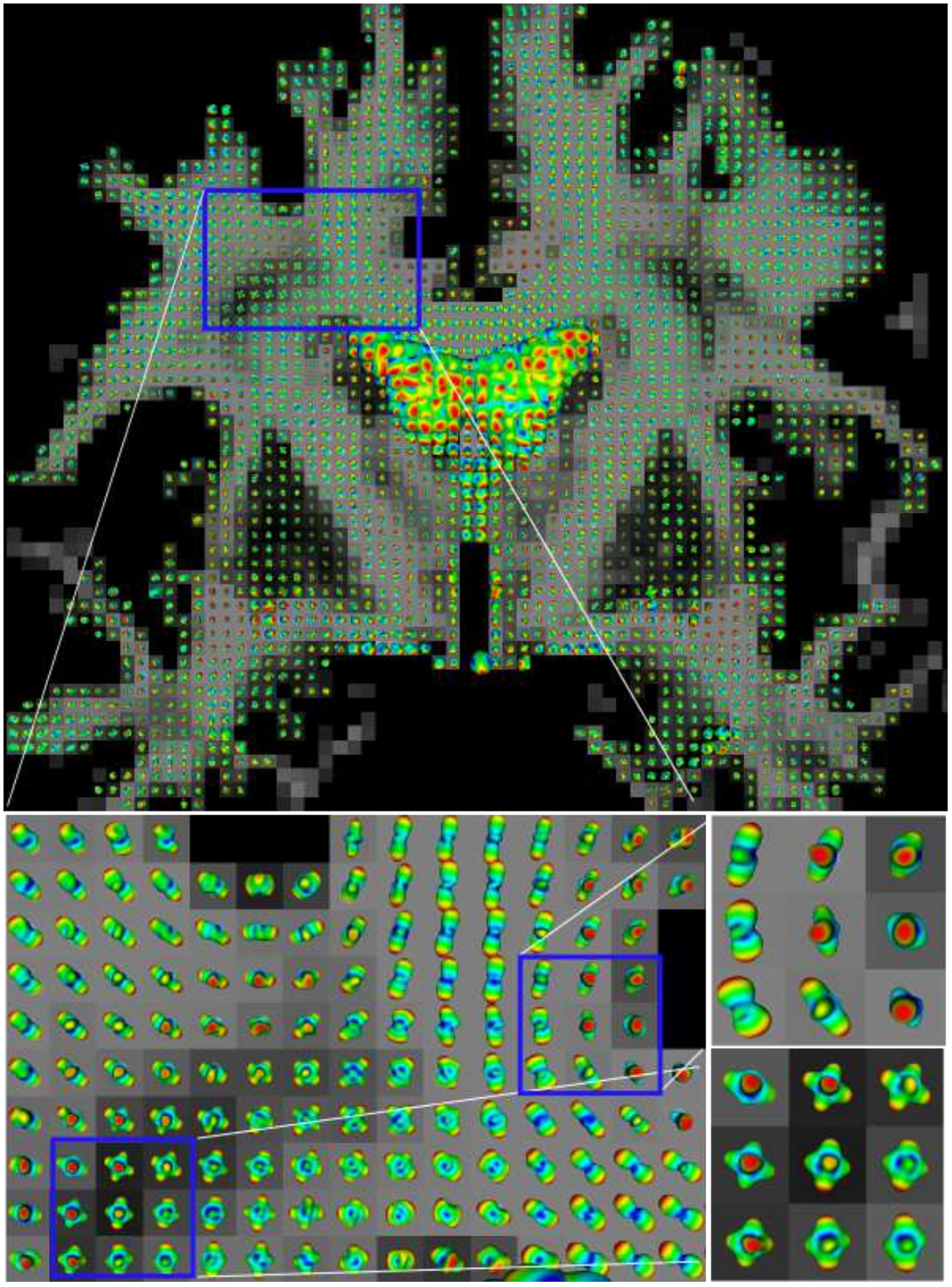

Figure 5.4: Real data. Coronal slice with the $P(\mathbf{r})^{(7)}_{4,4}$. The main zoom contains regions where three fiber bundles, namely the CC, the CST, and the SLF, intersect. The upper secondary zoom highlights the crossing between the CC and the cingulum due to partial voluming. The lower secondary zoom shows the main voxels, with three peaks that correspond to the crossing between the CC, the CST, and the SLF.

of δ_i were unknown, we assume $q^2 = b$, which implies $4\pi^2 t = 1$.

Fig-5.4, shows a coronal slice from the in-vivo dataset, where three fiber bundles are known to cross. In the plane horizontally and diagonally is the corpus callosum (CC), top to bottom is the cortico-spinal tract (CST) and going through the plane is the superior longitudinal fasciculus (SLF). The 4th order HOTs were approximated from this dataset. In Fig-5.4 are shown the estimated order 7 approximations $P(\mathbf{r})^{(7)}_{4,4}$ of the EAP. The zooms highlight the crossings between the major fiber bundles. In the main zoom is the region where the three fibers, the CC, the CST and the SLF, intersect each other. In the upper secondary zoom the crossing between the CC and the cingulum is highlighted, which occurs due to partial voluming. In the lower secondary zoom is seen the main voxels with three peaks, which correspond to the crossing between the three fiber families – the CC, the CST and the SLF.

5.4 Discussion and Conclusion

GDTI1 was developed to model complex ADC profiles which was an inherent shortcoming of DTI. GDTI1 uses HOTs of order k to model a complex ADC geometry. However, the shape of the ADC doesn't correspond to the underlying fiber directions. The microstructure of the tissue can be inferred from the geometry of the EAP, where in the q-space formalism the EAP and the diffusion signal are related by the Fourier Transform. But it's not easy to compute the EAP, $P(\mathbf{r})_k$, from the HOT model of the signal $E(\mathbf{q})_k$ in GDTI1.

We overcome this hurdle by modifying the ADC model of GDTI1, which allows us to approximate $E(\mathbf{q})$ by a multivariate polynomial approximation, and by proposing a novel closed-form approximation of $P(\mathbf{r})$ using Hermite Polynomials. The solution is a polynomial times a Gaussian, therefore the polynomial can be interpreted as the correction to the Gaussian EAP due to the inhomogeneous medium. An alternate explanation can be used to explain this method, where the signal is expanded in the polynomial basis, and the EAP is expressed in the Hermite polynomial basis, which establishes the similarity of the proposed method to GDTI2. Also, since the solution is analytical, it is fast, and the approximation converges well to the true EAP.

In case of an order 4 HOT, this method can be directly adapted to the methods proposed for estimating 4th order diffusion tensors with positive diffusion profiles. Therefore, it is possible to estimate a 4th order HOT with a positive diffusion profile using this modified model before approximating the EAP. The experiments show that estimating only the 15 coefficients of a 4th order HOT are enough to reveal the underlying fiber bundle layout. However, this is dependent on the order of the Taylor expansion used. Although the order of the expansion doesn't change the angular alignment of the peaks of the approximate EAP, it does affect its angular resolution or its capability of discerning narrow crossings. Increasing the order, increases the

corrections to the approximation, which improves this angular resolution. However, it also increases the computation time. The angular resolution can be recovered in lower order approximations, by increasing the probability radius, which saves computation time. However, this overall effect indicates, that the truncation in the Taylor expansion has the effect of underestimating the true EAP in the approximation.

CHAPTER 6

GEOMETRIC FEATURES FROM SPHERICAL DIFFUSION FUNCTIONS AND TRACTOGRAPHY

Contents

Overview

Spherical functions play a pivotal role in diffusion MRI for representing sub-voxel-resolution microstructural information of the underlying tissue. This information is encoded in the geometric shape of the spherical function. In this chapter we use a polynomial approach to extract geometric characteristics from spherical functions in diffusion MRI , such as the maxima, the minima and the saddle-points. We then use tools from differential geometry to quantify further details such as principal curvatures at the extrema. We propose new bio-markers like the Peak Fractional Anisotropy and Total Peak Fractional Anisotropy, to represent this rich source of information for characterizing cerebral white-matter. Finally as an application of our approach, we apply maxima-extraction to perform tractography, where we extend the standard Streamline tractography, and also the Tensorline tractography to work with generic spherical diffusion functions. We illustrate our method on the Orientation Distribution Function (ODF) estimated from synthetic and real data.

6.1 Introduction

In diffusion MRI (dMRI), while diffusion weighted images (DWIs) measure the diffusion of water molecules along single given directions, the reconstructed and integrated image is often represented as values on a sphere or as a spherical function in every voxel. The shape or geometric characteristics of these antipodally symmetric *spherical diffusion functions* (SDFs) provide a sub-voxel resolution microstructural information of the underlying tissue superior to the resolution of the raw DWIs. However, since the current spatial resolution, typically 2.5 mm^3 [90], of dMRI is coarse compared to the true scale of an axon, which is of the order of 1 μm, the SDF represents at best the average or dominant fiber direction of the underlying tissue locally, and is affected by partial voluming effects.

The geometric characteristics of several of these reconstructed SDFs have direct physical interpretations. The simplest example is DTI, where the spherical func-

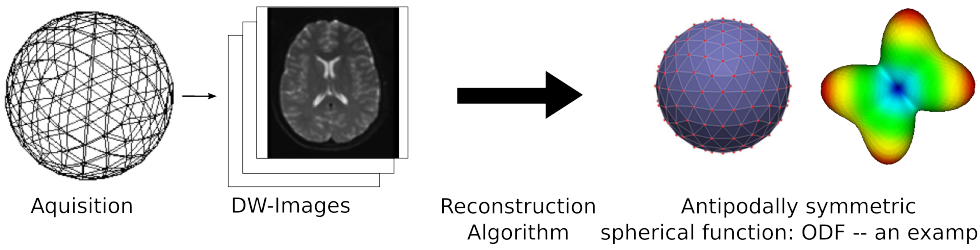

Figure 6.1: A *spherical diffusion function* (SDF) reconstructed from DWIs acquired along a set of gradient directions. The maxima of the ODF, an example of an SDF, indicate fiber bundles. It is, therefore, important to correctly estimate the maxima of these SDFs.

tion is an ellipsoid whose elongation indicates fiber bundle directions [30, 31]. The spectral decomposition of the diffusion tensor into its eigenvalues and eigenvectors represents the ellipsoid's geometry. These and derived scalars indicate tissue microarchitecture such as the dominant fiber direction, parallel and perpendicular diffusion, mean diffusion and Fractional Anisotropy (FA). However, DTI is limited in regions where multiple fibers cross, converge or diverge.

Therefore, a number of reconstruction techniques with SDFs with richer geometries and multiple peaks capable of discerning complex fiber configurations, such as crossings, have been recently proposed in dMRI. Some of these were presented in section-3.4. It is common to analytically represent an SDF in the *spherical harmonic* (SH) basis, such as analytical Q-Ball Imaging, or the *orientation distribution function* (ODF) [52, 53, 54], PAS-MRI [85], Spherical Deconvolution [59], or the DOT [60] to name a few. Another basis of choice is the *symmetric tensor* (ST) basis constrained to the sphere – DTI or GDTI1 (sec-3.4.2) for example [30, 44].

However, unlike in DTI, there exists no simple method for extracting all the geometric characteristics from these SDFs with multiple extrema. Since the maxima of certain SDFs indicate the underlying fiber directions, which is important in tractography, a number of algorithms have been proposed to extract only these. Examples consist of simple discrete mesh searches [3] and various optimization approaches [57, 59]. But these methods are all heuristic. Mathematically systematic approaches detecting the maxima and quantifying other geometric characteristics are few [91, 92, 93].

The discrete mesh search approach [3] heuristically searches for local maxima on a discretized version of the SDF by considering the SDF's values on the vertices of a discrete mesh of the sphere. Naturally, the precision of the maxima found by this approach is dependent on the refinement of the mesh. However, its execution time is also dependent on the mesh refinement. In other words, a finer mesh or discretization of the sphere improves the solution found by the finite search and is closer to the "correct" maximal direction which is the solution of the continuous spherical function, but it also increases the searching time of the algorithm quadratically [93]. In [3] typically an icosahedral tessellation of order 5, i.e. 1281 mesh vertices on a hemisphere, is used to execute the discrete mesh search, which corresponds to an angle of $\sim 4^o$ between vertices [3].

Numerical optimization techniques such as Newton-Raphson gradient descent in [59] and Powell's method in [57], on the other hand solve a continuous optimization problem to locate a maximum direction. However, such approaches are inherently limited to being local since the optimization is a local search, and are, therefore, dependent on the initialization. The SDFs have complex shapes, aren't convex (except for the case of the ellipsoid, which is trivial), and have many maxima. Therefore, different initial solutions could lead to different local basins of extrema, and a heuristic approach

would be necessary to restart the optimization routine for locating all the maxima of the SDF. For example, solutions from the finite difference search could be used to initialize and restart the optimization routine, which could then refine and improve the precision of the maximal directions.

In this chapter we present a homogeneous polynomial approach for extracting numerous geometric characteristics of an SDF. First we present a method for accurately extracting the maxima of any non-parametrically represented SDF described either in the SH basis or the ST basis. This is neither a heuristic approach, like a discrete mesh search, nor a local search like optimization. It guarantees that all the maxima are bracketed analytically, and then refined numerically to any degree of precision based on standard numerical schemes. This ensures that we can accurately extract *all* the maxima of an SDF without overlooking any. This approach can be considered the limiting case of the discrete mesh search with a complete mathematical framework like in an optimization approach, since it operates on the continuous SDF and locates its extrema based on the criterion $\nabla(\mathrm{SDF}) = \mathbf{0}$. But it is not dependent on initialization.

Next, using tools from differential geometry, we compute further geometric details like the principal curvatures at the maxima of the SDFs. While the maxima are a first order description, the principal curvatures provide a second order information, which can describe the "shape" of each maxima. To represent all this information in an integrated fashion, we propose the *peak fractional anisotropy* (PFA) measure to characterize each maxima of the SDFs. The PFA can be understood to be a kind of FA for each peak characterizing its geometry. We also propose the Total-PFA, which is a sum of all the PFAs of all the maxima of the SDF to characterize the entire SDF.

Finally as an application of the polynomial maxima extraction, we perform tractography on synthetic and real data. In the process we extend the classical DTI Streamline tractography [41]. We adapt the Streamline tractography to the multiple maxima that can be discerned by complex SDFs in regions with fiber crossings, allowing us to trace through such regions with greater accuracy than in DTI tractography. We also extend the well known Tensorline tractography [94, 95] to complex SDFs, to smooth out local kinks, which can make the fiber tracks unnaturally "wriggly" in plain Streamline tractography due to acquisition noise and partial voluming that make the estimated SDF field spatially irregular.

We illustrate all this on the diffusion ODF, both the ODF-T [51, 54] (Tuch), and the ODF-SA [55] (solid angle). The ODF-SAs are known to have sharper peaks and better angular resolution than the ODF-Ts. Both ODFs are non-parametric SDFs represented in the SH basis and are good generic SDFs for applying the maxima extraction method. However, this is only for illustration, and this approach can be performed on any other kind of SDF as mentioned earlier. We first experiment on synthetic

data generated from a multi-tensor model, then on in-vivo human cerebral data [96]. Using the modified Streamline and Tensorline tractography on the human dataset, we show marked improvements in detecting lateral radiations of the *corpus callosum* (CC).

6.2 MAXIMA EXTRACTION

Extracting the geometric characteristics of a generic SDF described either in the SH or the ST basis, can be broken down into three steps. First we represent the SDF as a *homogeneous polynomial* (HP) constrained to a sphere. Second, we formulate a constrained polynomial optimization problem for identifying all the stationary points or extrema of the SDF. Since the optimization problem can be seen as a root finding problem for a system of polynomials, we solve this system using a novel polynomial system solver instead of employing a local optimization approach. This solver allows us to analytically bracket all the real roots of the polynomial system without depending on an initial solution, and refine the roots numerically to a high precision to accurately detect all the extrema of the SDF. Third, we classify the extrema as maxima, minima and saddle-points and compute their principal curvatures to completely quantify all the extrema of the SDF.

6.2.1 From SHs to Tensors or Homogeneous Polynomials

The SHs form a complex complete orthonormal basis for square integrable functions on the unit sphere. Therefore, any SDF can be expanded in the infinite SH basis or approximated to any accuracy by a truncated series:

$$\text{SDF} = \sum_{l,m} c_{lm} Y_l^m(\theta, \phi), \tag{6.1}$$

where $Y_l^m(\theta, \phi)$ are the SHs, c_{lm} are the coefficients, and $\theta \in [0, \pi]$, $\phi \in [0, 2\pi)$. The SH of order l and degree m is defined as:

$$Y_l^m(\theta, \phi) = \sqrt{\frac{(2l+1)(l-m)!}{4\pi(l+m)!}} P_l^m(\cos\theta) e^{im\phi}, \tag{6.2}$$

where $m \leq |l|$, and $P_l^m(x)$ are the associated Legendre polynomials. Henceforth, for practical purposes, we shall only consider a truncated SH expansion. A modified, real, and symmetric SH basis is popularly used in dMRI to describe SDFs, since the diffusion function is real and assumed to be symmetric [3]:

$$Y_j(\theta, \phi) = \begin{cases} \sqrt{(2)} \cdot \text{Re}(Y_l^{|m|}(\theta, \phi)) & \text{if } m < 0 \\ Y_l^m(\theta, \phi) & \text{if } m = 0 \\ \sqrt{(2)} \cdot (-1)^{m+1} \text{Im}(Y_l^m(\theta, \phi)) & \text{if } m > 0 \end{cases},$$

where $j = (l^2 + l + 2)/2 + m$, and $Y_l^{-m}(\theta, \phi) = (-1)^m \overline{Y}_l^m(\theta, \phi)$, the complex conjugate of $Y_l^m(\theta, \phi)$. Henceforth, we will refer to the modified basis when referring to the SH basis.

An alternate basis for describing a symmetric spherical functions is the ST basis, which is based on Cartesian higher order tensors (HOT). In 3D an SDF in the ST basis can be approximated by a HOT or order-n by [44]:

$$\text{SDF} = \sum_{j_1=1}^{3} \sum_{j_2=1}^{3} \cdots \sum_{j_n=1}^{3} D^{(n)}_{j_1 j_2 \cdots j_n} g_{j_1} g_{j_2} \cdots g_{j_n},$$

where $D^{(n)}_{j_1 j_2 \cdots j_n}$ are the coefficients of the HOT $\mathbf{D}^{(n)}$, and g_{j_k} are the components of the unit norm vector $\mathbf{g} = [\sin\theta\cos\phi, \sin\theta\sin\phi, \cos\theta]^T = [g_x, g_y, g_z]^T$. This HOT representation can be rewritten in other forms by rearranging the terms:

$$\begin{aligned} \sum_{j_1=1}^{3} \sum_{j_2=1}^{3} \cdots \sum_{j_n=1}^{3} D^{(n)}_{j_1 j_2 \cdots j_n} g_{j_1} g_{j_2} \cdots g_{j_n} &= \sum_{r+s+t=n} D^{(n)}_{r,s,t} g_x^r g_y^s g_z^t \\ &= \sum_{j=1}^{N} \mu_j D_j \prod_{p=1}^{n} g_{j(p)}, \end{aligned}$$

where the first equality is from [65], which clearly indicates that a ST or order-n can be seen as a homogeneous polynomial of degree-n. The second equality is from [44], where the monomials $\prod_{p=1}^{n} g_{j(p)} = g_x^r g_y^s g_z^t$, with $r+s+t = n$ are factored together with their multiplicities μ_j, and D_j are the N independent coefficients of the ST, ($N = (n+1)(n+2)/2$). Therefore, a ST basis with a HOT of order-n is a rearranged form of a *homogeneous polynomial* (HP) with degree-n. In other words an SDF described in the ST basis, is basically written as a HP constrained to a sphere.

The passage from SHs to HPs constrained to a sphere can be understood from the spherical harmonic transform (SHT). The SH coefficients needed to describe an SDF, written as a HP, in the modified SH basis (Eq-6.1) can be calculated from the SHT:

$$c_k = \sum_{j=1}^{N} D_j \mu_j \int_{\Omega} \prod_{p=1}^{n} g_{j(p)} Y_k(\theta, \phi) d\Omega. \tag{6.3}$$

Since the SHT doesn't depend on the coefficients of the HP (or HOT) D_j, the SHT of the SDF can be seen as a dot product between the vector of unique HP coefficients and the vector of SHTs of the monomials. Therefore, computing m SH coefficients in the truncated SH expansion can be written as a matrix vector multiplication:

$$\mathbf{C} = \mathbf{M}\mathbf{d},$$

where $\mathbf{C} = [c_1, c_2, \cdots c_m]^T$, $\mathbf{d} = [D_1, D_2, \cdots D_n]^T$, and:

$$\mathbf{M} = \begin{pmatrix} \mu_1 \int_\Omega \prod_{p=1}^{n} g_{1(p)} Y_1(\theta,\phi) d\Omega & \dots & \mu_N \int_\Omega \prod_{p=1}^{n} g_{N(p)} Y_1(\theta,\phi) d\Omega \\ \vdots & \ddots & \vdots \\ \mu_1 \int_\Omega \prod_{p=1}^{n} g_{1(p)} Y_m(\theta,\phi) d\Omega & \dots & \mu_N \int_\Omega \prod_{p=1}^{n} g_{N(p)} Y_m(\theta,\phi) d\Omega \end{pmatrix}.$$

Therefore, there exists a linear transformation between the truncated SH basis and the HP basis. Further when $m = n$, $\mathbf{M}$ is a $n \times n$ square matrix that is invertible. Therefore, when the rank of the truncated SH expansion is equal to the degree of the HP, the two bases are linearly bijective, or they describe the same space of spherical functions. One can move between them by computing the transformation matrix $\mathbf{M}$. This was shown in [44, 75].

In other words, any SDF written either in the ST basis or the truncated SH basis can be rewritten equivalently in a HP polynomial basis constrained to the sphere, via a linear transformation.

6.2.2 Solving a Polynomial System

The problem of finding the maxima of an SDF written in either the SH basis or the ST basis can therefore be reformulated as a problem of optimizing a HP, $\mathrm{P}(\mathbf{x} = [x_1, x_2, x_3]^T)$, constrained to a sphere ($||\mathbf{x}||_2 = 1$):

$$\max_{\mathbf{x}} \mathrm{P}(\mathbf{x}) \quad \text{subject to} \quad \|\mathbf{x}\|_2^2 - 1 = 0. \tag{6.4}$$

The maximization problem could have been very well formulated in the spherical coordinates (SH basis). It would have then also had the advantage of being unconstrained. But the reason for converting to the constrained HP basis or to a Cartesian coordinate system is because we don't solve Eq-6.4 as an optimization problem, which is a local method and dependent on an initial solution. Instead we re-write it as a system of polynomials and use a novel polynomial system solver to recover all the extrema of $\mathrm{P}(\mathbf{x})$ at once.

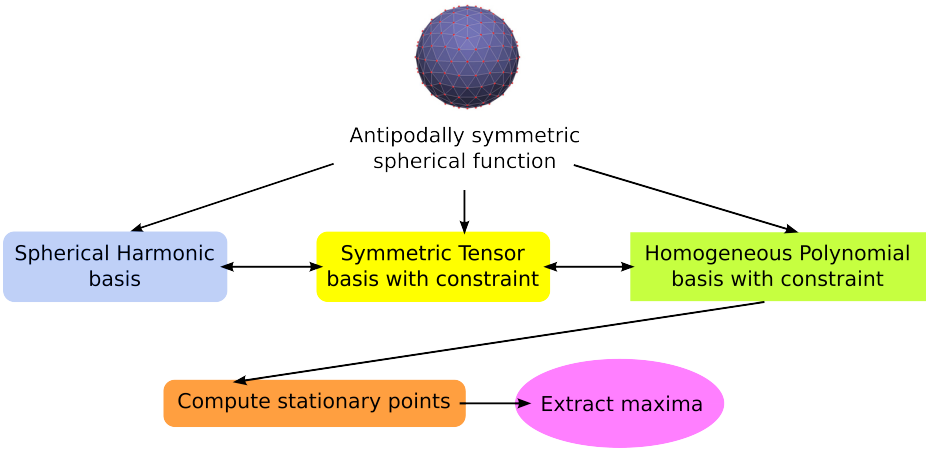

Figure 6.2: A *spherical diffusion function* (SDF) can be represented in three equivalent bases – spherical harmonics, symmetric tensor constrained to the sphere, or homogeneous polynomial (HP) constrained to the sphere. As a constrained HP it is possible to compute its stationary points to extract the maxima of the SDF.

Using Lagrange Multipliers, Eq-6.4 can be rewritten as an unconstrained functional:

$$\mathrm{F}(\mathbf{x}, \lambda) = \mathbf{P}(\mathbf{x}) - \lambda\,(\|\mathbf{x}\|_2^2 - 1). \tag{6.5}$$

From optimization theory, the maxima $\mathbf{x}^*$ (and its corresponding λ^*) of the SDF would have to satisfy $\nabla\mathrm{F}(\mathbf{x}^*, \lambda^*) = 0$:

$$\frac{\partial \mathrm{F}(\mathbf{x}^*, \lambda^*)}{\partial x_1} = \frac{\partial \mathrm{F}(\mathbf{x}^*, \lambda^*)}{\partial x_2} = \frac{\partial \mathrm{F}(\mathbf{x}^*, \lambda^*)}{\partial x_3} = \|\mathbf{x}^*\|_2^2 - 1 = 0. \tag{6.6}$$

Eq-6.6 is a system of HPs, $\{\mathrm{Q}_k(\mathbf{X} = [\mathbf{x}, \lambda]^T)\}$, which implies that $\mathbf{X}^* = (\mathbf{x}^*, \lambda^*)$ is a root of this system. Since the SDF is a real function, only the real roots of this system are of interest. Therefore, the maxima of the SDF can be extracted by finding the real roots of the polynomial system $\{\mathrm{Q}_k(\mathbf{X})\} = \mathbf{0}$. However, the condition $\nabla\mathrm{F}(\tilde{\mathbf{x}}, \tilde{\lambda}) = 0$ identifies all the stationary points or extrema of the SDF. Therefore, once the real roots of $\{\mathrm{Q}_k(\mathbf{X})\}$ are identified, they would have to be categorized into the maxima, minima, and saddle-points of the SDF.

To find the real roots of the polynomial system $\{\mathrm{Q}_k(\mathbf{X})\}$, we use the subdivision method for polynomial systems proposed and implemented by B. Mourrain & J.P. Pavone, described in [97]. This method makes use of the Bernstein basis and its geometric properties to analytically bracket all the real solutions of a system of polynomials inside a pre-defined domain of the problem space, $\mathbf{R}^4$. The solutions or roots, once bracketed, are then refined numerically using standard 1D root-solvers to any degree of precision.

The Bernstein polynomial basis is used to provide a constructive proof of Weierstrass approximation theorem, which states that a continuous function on the interval $[a, b]$ can be uniformly approximated by polynomial functions. In other words each of the polynomials in the system $\{\mathrm{Q}_k(\mathbf{X})\}$ can be accurately approximated in the Bernstein polynomial basis. In 1D, on the interval $[a, b]$, the Bernstein basis of degree-d are the $d + 1$ Bernstein polynomials:

$$\mathrm{B}_d^i(x; a, b) = \binom{d}{i} \frac{1}{(b-a)d}(x-a)^i(b-x)^{d-i}, \text{where} \quad i = 0..d.$$

A univariate polynomial can be decomposed in this basis in the same interval with coefficients B_i, as:

$$f(x) = \sum_{i=0}^{d} B_i \mathrm{B}_d^i(x; a, b).$$

By extension, using the tensor product "$\times$", of the Bernstein basis in each dimension, a multivariate polynomial, with four variables in our case, can be decomposed in the Bernstein basis in a domain $[a_1, b_1] \times [a_2, b_2] \times [a_3, b_3] \times [a_4, b_4]$, as:

$$\mathrm{Q}(\mathbf{X}) = \sum_{i_1=0}^{d_1} \sum_{i_2=0}^{d_2} \sum_{i_3=0}^{d_3} \sum_{i_4=0}^{d_4} B_{i_1,i_2,i_3,i_4} \quad \mathrm{B}_{d_1}^{i_1}(x_1; a_1, b_1) \times \mathrm{B}_{d_2}^{i_2}(x_2; a_2, b_2) \times \mathrm{B}_{d_3}^{i_3}(x_3; a_3, b_3) \times \mathrm{B}_{d_4}^{i_4}(x_4 = \lambda; a_4, b_4) \quad . \tag{6.7}$$

In our case, $\mathrm{Q}(\mathbf{X}) = \mathrm{Q}_k(\mathbf{X})$, and the initial domain for each polynomial in the system can be easily defined. Since the HP representing the SDF is constrained to the unit sphere, the initial domain of all the $\mathrm{Q}(\mathbf{X})$'s can be $[-1,1] \times [-1,1] \times [-1,1] \times [-K,K]$, for very large K. The system of HPs is converted to the Bernstein basis using exact arithmetic to avoid loss of precision. This operation is required only once, since later operations are performed only in the Bernstein basis.

The subdivision method uses the following properties of the Bernstein basis to find the roots of a system of Bernstein polynomials $\{\mathrm{Q}_k(\mathbf{X})\}$ [97].

De Casteljau's algorithm: De Casteljau's algorithm, is a fundamental algorithm that can subdivide the Bernstein representation of a univariate polynomial $f(x)$ into two Bernstein sub-representations in two sub-domains of the initial domain. This can be done repeatedly to sub-divide and refine a domain in 1D.

Descartes' theorem: Moreover, for a univariate polynomial in the Bernstein basis, Descartes' theorem states:

Theorem: *the number of real roots of* $f(x) = \sum B_i \mathrm{B}_d^i(x;a,b)$ *in* $]a,b[$ *is bounded by the number of sign changes of* $\{B_i\}$, $V(\{B_i\})$*, and is equal modulo 2.*

In other words, if the number of sign changes $V(\{B_i\}) = 0$ then $f(x)$ has no real roots in the interval $]a,b[$, if $V(\{B_i\}) = 1$ then $f(x)$ has one real root, and if $V(\{B_i\}) > 1$ then either $f(x)$ has no real roots or it has a number of real roots $]a,b[$. The end points a & b can be trivially tested to consider the interval $[a,b]$. This forms an *exclusion* test that is zero when $f(x)$ has no real roots in the interval $[a,b]$. Therefore, using Descartes' theorem and De Casteljau's algorithm, it is possible to reject intervals that don't contain any roots of $f(x)$ and progressively refine intervals that contain the roots. In other words, it is possible to analytically identify and subdivide intervals to bracket the real roots, of $f(x)$. Once a root has been bracketed or isolated, and the bracketing interval is small enough, or $V(\{B_i\}) = 1$, any standard numerical one dimensional root-finder of choice can be used to refine the real root with high precision.

Projection Lemma: For any multivariate Bernstein polynomial $\mathrm{Q}(\mathbf{X})$ (Eq-6.7), let the following functions be defined:

$$\begin{aligned} m_j(\mathrm{Q};x_j) &= \sum_{i_j}^{d_j} \min_{(0\le i_k\le d_k, k\neq j)} B_{i_1,i_2,i_3,i_4} \mathrm{B}_{d_j}^{i_j}(x_j;a_j,b_j) \\ M_j(\mathrm{Q};x_j) &= \sum_{i_j}^{d_j} \max_{(0\le i_k\le d_k, k\neq j)} B_{i_1,i_2,i_3,i_4} \mathrm{B}_{d_j}^{i_j}(x_j;a_j,b_j). \end{aligned}$$

Lemma: *For any* $\mathbf{X}$ *in the domain of definition, and for any dimension* $j = 1..4$*,* $m_j(\mathrm{Q};x_j) \le \mathrm{Q}(\mathbf{X}) \le M_j(\mathrm{Q};x_j)$.

From the lemma, the 1D Bernstein polynomials $m_j(\mathrm{Q}; x_j)$, and $M_j(\mathrm{Q}; x_j)$, can be seen as sandwiching the projection $q_j(\mathbf{X})$, of $\mathrm{Q}(\mathbf{X})$, along the jth dimension. This implies that if $\tilde{\mathbf{X}}$ were a root of $\mathrm{Q}(\mathbf{X})$ on a domain, then its jth coordinate $\tilde{x_j}$ would be sandwiched by the roots of $m_j(\mathrm{Q}; x_j)$ and $M_j(\mathrm{Q}; x_j)$ in that domain. Conversely, if in a certain domain, $m_j(\mathrm{Q}; x_j)$ and $M_j(\mathrm{Q}; x_j)$ don't have any roots by Descartes' theorem, then $\mathrm{Q}(\mathbf{X})$ doesn't have any roots in that domain either. This way Descartes' exclusion test can be extended to a multivariate Bernstein polynomial.

Further, it is possible to partially extend Descartes' exclusion test to a system of multivariate Bernstein polynomials $\mathbf{Q}(\mathbf{X}) = \{\mathrm{Q}_k(\mathbf{X})\}$ by defining:

$$\begin{aligned} \hat{m}_j(\mathbf{Q}; x_j) &= \sup\{m_j(\mathrm{Q}_k; x_j);\ k = 1..4\}, \\ \hat{M}_j(\mathbf{Q}; x_j) &= \inf\{M_j(\mathrm{Q}_k; x_j);\ k = 1..4\}. \end{aligned}$$

This implies that if the 1D Bernstein polynomials $\hat{m}_j(\mathbf{Q}; x_j)$ and $\hat{M}_j(\mathbf{Q}; x_j)$ don't have roots by Descartes' theorem along the jth dimension of a domain, then the system $\{\mathrm{Q}_k(\mathbf{X})\}$ has no roots in the domain.

Combining De Casteljau's algorithm and the powerful exclusion test allows to analytically subdivide and reject sub-domains by applying them along every dimension of the domain. This can be done in such a fashion that the rejected sub-domains are guaranteed to not contain any real roots of the polynomial system $\{\mathrm{Q}_k(\mathbf{X})\}$ (Eq-6.6). Once the intervals that were not rejected along every dimension are small enough, they are numerically refined to locate the roots along those dimensions in those intervals. However, theoretically, these roots (along given dimensions) are only roots of the projections $q_j(\mathbf{X})$ and may not be a root $\tilde{\mathbf{X}}$ of $\mathrm{Q}(\mathbf{X})$. An additionally test would be required to reject solutions to the above subdivision process that may not be real roots of the polynomial system $\{\mathrm{Q}_k(\mathbf{X})\}$. In practice, however, we have never come across such solutions, but simply testing for $\nabla\mathrm{F}(\tilde{\mathbf{X}}) = 0$ would provide such a test.

This is the essence of the subdivision method, however, the implementation in [97] also considers other aspects such as pre-conditioning and a reduction step to render the root finding more efficient and precise.

6.2.3 Categorizing the Extrema

Once all the stationary points of the polynomial system $\{\mathrm{Q}_k(\mathbf{X})\}$ or the extrema of the SDF have been quantified with high precision, these would have to be categorized into maxima, minima and saddle-points to identify the maxima of the SDF, which indicate fiber directions. This is done using the Bordered Hessian test [98].

Bordered Hessian In unconstrained multi-dimensional optimization theory a point $\tilde{\mathbf{x}}$, is considered an extremum of the functional $\mathrm{F}(\mathbf{x})$, when it satisfies $\nabla\mathrm{F}(\tilde{\mathbf{x}}) = 0$.

The extremum can be then categorized by evaluating the Hessian of the functional at the extremum $H\mathrm{F}(\tilde{\mathbf{x}})$. If $H\mathrm{F}(\tilde{\mathbf{x}})$ is positive definite, then $\tilde{\mathbf{x}}$ is a local minimum, if $H\mathrm{F}(\tilde{\mathbf{x}})$ is negative definite, then $\tilde{\mathbf{x}}$ is a local maximum, and if $H\mathrm{F}(\tilde{\mathbf{x}})$ has non-zero eigenvalues with mixed signs, then $\tilde{\mathbf{x}}$ is a saddle-point.

In constrained optimization, which is our case, the Hessian test is extended to the Bordered Hessian test to account for the constraints. Given an n dimensional functional $\mathrm{P}(\mathbf{x})$ to be maximized, subject to a set of m constraints $\mathbf{g}(\mathbf{x})$, the general Lagrangian functional is:

$$\mathrm{F}(\mathbf{x}, \boldsymbol{\lambda}) = \mathrm{P}(\mathbf{x}) + \boldsymbol{\lambda}^T \mathbf{g}(\mathbf{x}).$$

The Bordered Hessian of this functional is defined as:

$$\overline{H}\mathrm{F}(\mathbf{x}, \boldsymbol{\lambda}) = \begin{bmatrix} 0_{m\times m} & \nabla\mathbf{g}(\mathbf{x})_{m\times n} \\ \nabla\mathbf{g}(\mathbf{x})^T_{n\times m} & H\mathrm{F}(\mathbf{x}, \boldsymbol{\lambda})_{n\times n} \end{bmatrix}_{(m+n)\times(m+n)}, \tag{6.8}$$

where the Hessian of the Lagrangian functional is bordered by the Jacobian of the constraints $\nabla\mathbf{g}(\mathbf{x})$, and padded by a corner-block of zeros. In our case $n = 3$ and $m = 1$, therefore, the Bordered Hessian is a 4×4 matrix. The Bordered Hessian is rank deficient and cannot satisfy the definiteness conditions of the Hessian test. However, an extremum, $\tilde{\mathbf{X}} = (\tilde{\mathbf{x}}, \tilde{\boldsymbol{\lambda}})$, of the constrained optimization can be categorized using the following alternating sign tests [98]:

$$\begin{aligned} (-1)^m \det(\overline{H}_r\mathrm{F}(\tilde{\mathbf{X}})) &> 0 \text{ strict minimum}, \\ (-1)^r \det(\overline{H}_r\mathrm{F}(\tilde{\mathbf{X}})) &> 0 \text{ strict maximum}, \\ & r = m+1, ..., n, \end{aligned} \tag{6.9}$$

$$\text{where}: \quad \overline{H}_r\mathrm{F} = \begin{bmatrix} 0_{m\times m} & \nabla\mathbf{g}_{m\times r} \\ \nabla\mathbf{g}^T_{r\times m} & H\mathrm{F}_{r\times r} \end{bmatrix}_{(m+r)\times(m+r)}. \tag{6.10}$$

We consider an extremum to be a saddle-point, when it satisfies neither of the sign tests. This allows us to categorize an extremum as a maximum, or a minimum or a saddle-point.

Principal Curvatures There are other ways of categorizing an extremum $\tilde{\mathbf{X}}$ into a maximum, or a minimum. It can be done, for example, using differential geometry as proposed in [91] by computing the principal curvatures κ_1, κ_2 at the extremum. The extremum is then categorized from the signs of κ_1, κ_2:

- *Elliptical point ($\kappa_1 \cdot \kappa_2 > 0$)*: when κ_1, κ_2 have the same sign, the surface is locally convex.
  - *Maximum ($\kappa_1 > 0,\ \kappa_2 > 0$)*: when both κ_1, κ_2 are positive the surface is locally a maximum.

  - *Minimum ($\kappa_1 < 0,\ \kappa_2 < 0$)*: when both κ_1, κ_2 are negative the surface is locally a minimum.

- *Hyperbolic point ($\kappa_1 \cdot \kappa_2 < 0$)*: when κ_1, κ_2 have opposite signs, the surface is locally a saddle-point.

- *Parabolic point ($\kappa_1 \cdot \kappa_2 > 0$)*: when either κ_1 or κ_2 or both are zero, the surface is locally parabolic along the direction of the non-zero principal curvature. When both κ_1, κ_2 are zero the parabolic surface becomes planar.

The principal curvatures of a 2D surface S, described by its Cartesian parametric form $S(u, v)$, embedded in $\mathbf{R}^3$ can be computed from differential geometry [99]. The curvature of the surface S, at any point $p(u_0, v_0)$, can be intuitively understood as the rate of change of the normal vector to the surface at the point. This is described by the Gauss map, which defines a function on the normal vector, its derivative – the "shape operator", which measures the rate of change of this function or the normal vector, and whose eigenvectors are the principal curvatures, and the first & second fundamental forms, which help to compute the shape operator.

The Gauss map is a function from the surface S to the sphere S^2 – it maps the unit normal vector $\mathbf{n}$, at p, to the parallel normal vector $\mathrm{N}(p)$, in S^2, $\mathrm{N} : S \rightarrow S^2$. In other words $\mathrm{N}(p) = \mathbf{n}$. $\mathrm{N}(p)$ can be computed from two non-collinear vectors in the tangent plane of S at p, T_pS. In fact the partial derivatives of S, $S_u = \partial S(u, v)/\partial u$ and $S_v = \partial S(u, v)/\partial v$, define a local coordinate system of T_pS, and $\mathrm{N}(p) = S_u \times S_v / ||S_u \times S_v||$. Since $\mathrm{N}(p) = \mathbf{n}$, $T_{\mathrm{N}(p)}S^2 = T_pS$.

Further, $< \mathbf{n}, \mathbf{n} >= 1$, implies that $< \mathbf{n}_u, \mathbf{n} >=< \mathbf{n}_v, \mathbf{n} >= 0$, where $<, >$ represent the inner product, and the subscripts indicate partial derivatives. Therefore, the gradient of $\mathrm{N}(p)$ is in the tangent space T_pS. This implies that the derivative of the Gauss map is a function from the tangent space of S at p, to the corresponding tangent space on the sphere $d\mathrm{N} : T_pS \rightarrow T_{\mathrm{N}(p)}S^2$. The shape operator is defined as $\mathcal{S} = -d\mathrm{N}$.

The first fundamental form represents the metric in the tangent space induced by the curvature, it defines the inner product in the tangent plane at p, $I : T_pS \times T_pS \rightarrow \mathbf{R}$. It is represented by the symmetric matrix:

$$I = \begin{bmatrix} E & F \\ F & G \end{bmatrix},$$

where $E =< S_u, S_u >$, $F =< S_u, S_v >$, $G =< S_v, S_v >$. The inner product between any two vectors in the tangent plane can therefore be computed as $< x, y >= x^T I y$.

The second fundamental form defines the inner product $II(w) = - < d\mathrm{N}(w), w >$, $w \in T_pS$, and can be represented by the symmetric matrix:

$$II = \begin{bmatrix} L & M \\ M & N \end{bmatrix},$$

where $L =< \mathbf{n}_u, S_u >$, $M =< \mathbf{n}_u, S_v >=< \mathbf{n}_v, S_u >$, and $N =< \mathbf{n}_v, S_v >$, therefore, $II(w) = -w^T II w$. In practice, however, it is easier to compute the second partial derivatives of the surface rather than the derivatives of the normal. This can be used from the fact that $< \mathbf{n}, S_u >=< \mathbf{n}, S_v >= 0$, (since S_u & S_v are in the tangent plane), which implies that $L =< \mathbf{n}, S_{uu} >$, $M =< \mathbf{n}, S_{uv} >=< \mathbf{n}, S_{vu} >$, and $N =< \mathbf{n}, S_{vv} >$.

The matrix of the shape operator, or the Gauss map's derivative, can be computed from the first and the second fundamental forms:

$$d\mathrm{N} = -\mathcal{S} = -II \cdot I^{-1} = \frac{1}{EG - F^2} \begin{bmatrix} MF - LG & LF - ME \\ NF - MG & MF - NE \end{bmatrix}. \tag{6.11}$$

These are known as the Weingarten equations in matrix form. The principal curvatures of S at p are the eigenvectors of $\mathcal{S}$ computed at p. These can be derived from the trace $2H$, and the determinant K of $\mathcal{S}$, where:

$$H = \frac{GL - 2FM + EN}{2(EG - F^2)}, \tag{6.12}$$

$$K = \frac{LN - M^2}{EG - F^2}, \tag{6.13}$$

where in terms of the eigenvalues of $\mathcal{S}$, $H = (\kappa_1 + \kappa_2)/2$, and $K = \kappa_1 \cdot \kappa_2$. Therefore, H is known as the *mean curvature* and K is known as the *Gaussian curvature* of the surface. Therefore:

$$\kappa_1 = H + \sqrt{H^2 - K}, \tag{6.14}$$

$$\kappa_2 = H - \sqrt{H^2 - K}, \tag{6.15}$$

where $\kappa_1 \geq \kappa_2$. The principal curvatures of a surface S at p, can be therefore computed from the coefficients E, F, G, L, M, N, of the first and the second fundamental forms, which depend on the partial derivatives of S: $S_u, S_v, S_{uu}, S_{uv}, S_{vv}$, evaluated at p.

This can be used to compute the principal curvatures of the SDF at an extremum. Computing the principal curvatures is easier in the SH representation (Eq-6.1) of the SDF by considering $\theta = u,\ \phi = v$, instead of the HP or ST representations. But Eq-6.1 is the parametric representation of the SDF in spherical coordinates, and would have to be transformed to Cartesian coordinates:

$$\begin{aligned} \mathrm{SDF}_{sph} &= [\theta, \phi, r(\theta, \phi)]^T \qquad \Leftrightarrow \\ \mathrm{SDF}_{Cart} &= r(\theta, \phi)[\sin\theta\cos\phi, \sin\theta\sin\phi, \cos\theta]^T, \end{aligned} \tag{6.16}$$

where $r(\theta, \phi)$ is the value of the SDF at (θ, ϕ), and SDF_{Cart} is the surface S whose curvatures we want to compute.

The partial derivatives of SDF_{Cart} can be computed in terms of $r(\theta, \phi)$, and are simplified by the fact that the curvatures are being calculated only at an extremum

$\tilde{\mathbf{X}} = [\tilde{\theta}, \tilde{\phi}, r(\tilde{\theta}, \tilde{\phi})]^T$, where $\nabla S = 0$ (Eq-6.6), implying $r_\theta(\tilde{\theta}, \tilde{\phi}) = r_\phi(\tilde{\theta}, \tilde{\phi}) = 0$. Then the coefficients of the first and the second fundamental forms are:

$$\begin{array}{lllllll} E & = & r^2, & & L & = & r_{\theta\theta} - r, \\ F & = & 0, & & M & = & r_{\theta\phi}, \\ G & = & r^2 \sin^2\theta, & & N & = & r_{\phi\phi} - r\sin^2\theta, \end{array} \tag{6.17}$$

where $r = r(\theta, \phi)$. Since $r(\theta, \phi)$ is in the SH basis, following are the partial derivatives of SHs that can be computed from Eq-6.2 and the recursions they satisfy [100]:

$$\begin{array}{lcl} (Y_l^m)_\theta & = & \frac{-f_{lm}}{\sin\theta}\left[(l+1)\cos\theta P_l^m - (l-m+1)P_{l+1}^m\right] e^{im\phi}, \\ (Y_l^m)_\phi & = & (im)Y_l^m, \\ (Y_l^m)_{\theta\theta} & = & \frac{f_{lm}}{\sin^2\theta}[(l+1+(l+1)^2\cos^2\theta)P_l^m \\ & & -2\cos\theta(l-m+1)(l+2)P_{l+1}^m + (l-m+1)(l-m+2)P_{l+2}^m]e^{im\phi}, \\ (Y_l^m)_{\theta\phi} & = & \frac{-imf_{lm}}{\sin\theta}\left[(l+1)\cos\theta P_l^m - (l-m+1)P_{l+1}^m\right] e^{im\phi}, \\ (Y_l^m)_{\phi\phi} & = & -m^2 Y_l^m, \end{array} \tag{6.18}$$

where:

$$f_{lm} = \sqrt{\frac{(2l+1)(l-m)!}{4\pi(l+m)!}}.$$

Therefore, by combining Eqs-6.17,6.18, it is possible to compute the principal curvatures κ_1, κ_2 at an extremum of an SDF described in the SH basis. However, it should be noted that the spherical coordinates (Eq-6.16) have an ambiguity along the Z-axis, where $\theta = 0$ and ϕ can take on any value in its domain. Therefore, computing the partial derivatives of the SHs along the Z-axis or in its close neighbourhood would be numerically unstable. This can be verified from Eq-6.18, where partial derivatives with respect to θ are all divided by $\sin\theta$, which tends towards zero as $\theta \to 0$. Therefore, if an extremum is along or close to the Z-axis, the SH representation of the SDF would have to be rotated to take the extremum away from the Z-axis.

6.2.4 Experiments and Results

To test the proposed maxima extraction method, we use the ODF-T as the SDF. We consider a rank-4 SH expansion of the ODF-Ts and estimate these from various datasets. We conduct experiments on synthetic data generated from a multi-tensor model (sec-3.4.4), and on human cerebral data from [96]. The datasets are described in Appendix-A.

We use the synthetic dataset to test the precision and accuracy of our maxima extraction method. The synthetic dataset is generated with $\mathbf{D} = \mathrm{diag}(1390, 355, 355) \times 10^{-6}$ mm^2/s, for the single fiber profile, with a b-value of 3000 s/mm^2. No noise is added to the signal since the maxima extraction method plays no role in the estimation process of the SDF, it considers the SDF as is, and isn't affected by how it was estimated. It

	$ang(d, d^{'})^{o}$		$\|\|\nabla \mathrm{F}(d^{'})\|\|$		$\|\|\nabla \mathrm{F}(d)\|\|$	
	m	v	m	v	m	v
1-Fib	0.01	4.22e-05	2.07e-11	1.5e-21	4.9e-04	9.17e-08
2-Fib$_{90^{o}}$	0.025	3.85e-05	5.58e-11	1.76e-21	3.6e-03	2.48e-06

Table 6.1: (m=mean, v=variance). Measuring the precision of the maxima extraction on synthetic dataset. $||\nabla \mathrm{F}(d^{'})||$ indicates the amount of error in the maxima extraction process. $||\nabla \mathrm{F}(d)||$ indicates the amount of error in the estimation of ODF-Ts in the rank-4 SH basis. The first error is orders of magnitude smaller than the second error. This indicates the precision of the maxima extraction process.

only solves $\nabla \mathrm{F} = 0$ (Eq-6.6), where F describes the SDF, in our case the ODF-T, in a constrained HP basis. The test for precision is therefore based upon this criterion.

The idea is to use a set of known ground truth directions $\{d_i\}$ to generate the synthetic DWI signals and estimate the ODF-Ts from these DWIs. It is then possible to extract the maxima of these ODF-Ts, which give another set of directions $\{d_k^{'}\}$. Ideally, $\{d_i\}$ should be identical to $\{d_k^{'}\}$. We therefore proceed to comparing $\{d_k^{'}\}$ to $\{d_i\}$. This is only possible when $k = i$. When the two sets are comparable, we pair the computed directions with the ground truth directions such that their difference is minimized. Then we first compute the angle between d_i and $d_i^{'}$ in degrees which we denote as $ang(d_i, d_i^{'})^{o}$. If this angle is non zero, we proceed to quantify the errors.

Let the ODF-Ts be described in the constrained HP basis by the Lagrangian functional $\mathrm{F}(\mathbf{x})$. Therefore, the values of $||\nabla \mathrm{F}(d_i)||$ and $||\nabla \mathrm{F}(d_i^{'})||$ indicate the error of $\{d_i\}$ and $\{d_k^{'}\}$ not satisfying the extremum criterion $\nabla \mathrm{F} = 0$. However, these quantify two different errors. Since, $\{d_i^{'}\}$ are the stationary points of $\mathrm{F}(\mathbf{x})$, the value of $||\nabla \mathrm{F}(d_i^{'})||$ indicates the amount of error in the maxima extraction process, i.e. the conversion to the Bernstein basis, and the performance of the subdivision algorithm. Computing $||\nabla \mathrm{F}(d_i)||$ on the other hand indicates the amount of error in the problem formulation process, i.e. the estimation of the ODF-Ts in the rank-4 SH basis, and the conversion to the constrained HP basis of degree-4.

To compute these errors that quantify the precision of the maxima extraction process, we construct test cases with two types of fiber configurations and repeat the tests randomly one hundred times for each configuration. In the first configuration we consider only a single fiber in the voxel. In the second configuration we consider two fibers crossing perpendicularly in the voxel with equal weights. However, the ground truth directions are generated randomly for each test. From these repeated tests we generate statistics on $ang(d_i, d_i^{'})^{o}$, $||\nabla \mathrm{F}(d_i)||$, and $||\nabla \mathrm{F}(d_i^{'})||$. For the crossing fiber configuration, since two maxima are extracted, we only keep the greatest error between these two maxima.

The results are presented in Table-6.1. In all the tests the correct number of maxima were extracted ($i = k$). First from $ang(d, d^{'})^{o}$, which is of the order of 0.1^{o}, it is already obvious that the maxima extraction is numerically very precise – the extracted maxima are very good representatives of the ground truth fiber directions. Next, from the criterion $\nabla \mathrm{F} = 0$, which was solved to find the maxima of the SDF (ODF-T), it is clear that the maxima computation process, represented by the error $||\nabla \mathrm{F}(d^{'})||$, is numerically far more precise than the combined ODF-T estimation and conversion to the HP basis process, represented by the error $||\nabla \mathrm{F}(d)||$. In fact the first error is orders of magnitude smaller than the second error. Therefore, the maxima extraction not only brackets the extrema of the SDF analytically, but also extracts these extrema with high precision.

For the synthetic data we also illustrate the extraction of all the extrema and their classification using the Bordered Hessian. This is shown in Fig-6.3. We consider here three types of fiber configurations. These are the single fiber, two fibers crossing perpendicularly and three fibers crossing perpendicularly. In each of the cases the extrema are extracted from the ODF-T model of the SDF. These extrema are then classified as maxima, minima and saddle-points and are displayed using different colours. It is interesting to see that in the 1 fiber and 2 fiber cases, all the maxima, even the unimportant ones are correctly found. This is the expected behaviour of the subdivision method. However, in practice these maxima would have to be heuristically thresholded. The colour of the glyphs represent local anisotropy, with red indicating high anisotropy (or large function value – local maximum), and blue indicating low anisotropy (or small function value – local minimum). The extrema are colour coded with the maxima in thick yellow, minima in thin green, and saddle-points in fine blue.

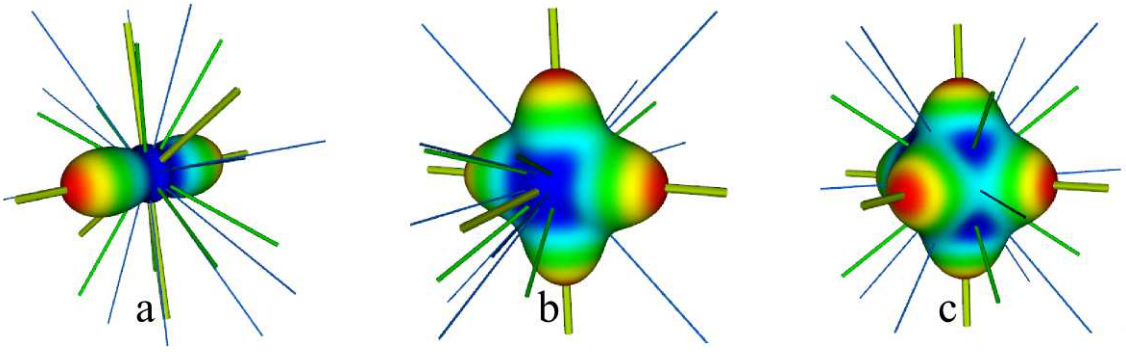

Figure 6.3: Extrema extraction & categorization from synthetic data. a) 1-fiber b) 2-fibers c) 3-fibers. Glyph-colour: red indicates high anisotropy (local maximum), blue indicates low anisotropy (local minimum). Line-colour: thick-yellow: Maxima, thin-green: Minima, fine-blue: Saddle points

Finally we present the results of maxima extraction on the in-vivo cerebral dataset. In this case we consider both the ODF-T and the ODF-SA SDF models, since ODF-SAs are known to be sharper than ODF-Ts. Therefore, we expect more crossings detected by the ODF-SA than by the ODF-T. We estimate both ODFs from the real dataset and consider rank-4 SH expansions. Only the maxima are extracted and shown in Fig-6.4. This shows a coronal slice, which is known to have fiber bundles crossing from three families – the corticospinal tract (CST), vertically in the plain, the corpus callosum (CC), horizontally and diagonally in the plain, and the superior longitudinal fasciculus (SLF), perpendicular to the plain (section-2.2.4, Fig-2.7).

In the left column of Fig-6.4 are the ODF-Ts, and in the right column are the ODF-SAs. Clearly the ODF-SAs have sharper peaks and a greater number of crossings. The top row shows a zoomed region, and a single voxel with all its extrema classified (with the same colour code as above). The bottom row shows the entire coronal slice, with only the maxima extracted from the ODFs. The glyph colour of the ODFs in the zoom follow the same colour code as above. Without this colour code, it is hard to make out the extrema of the ODF-T, which is highly smooth, or almost isotropic in comparison to the ODF-SA. But, as indicated by the extrema detection, it too has

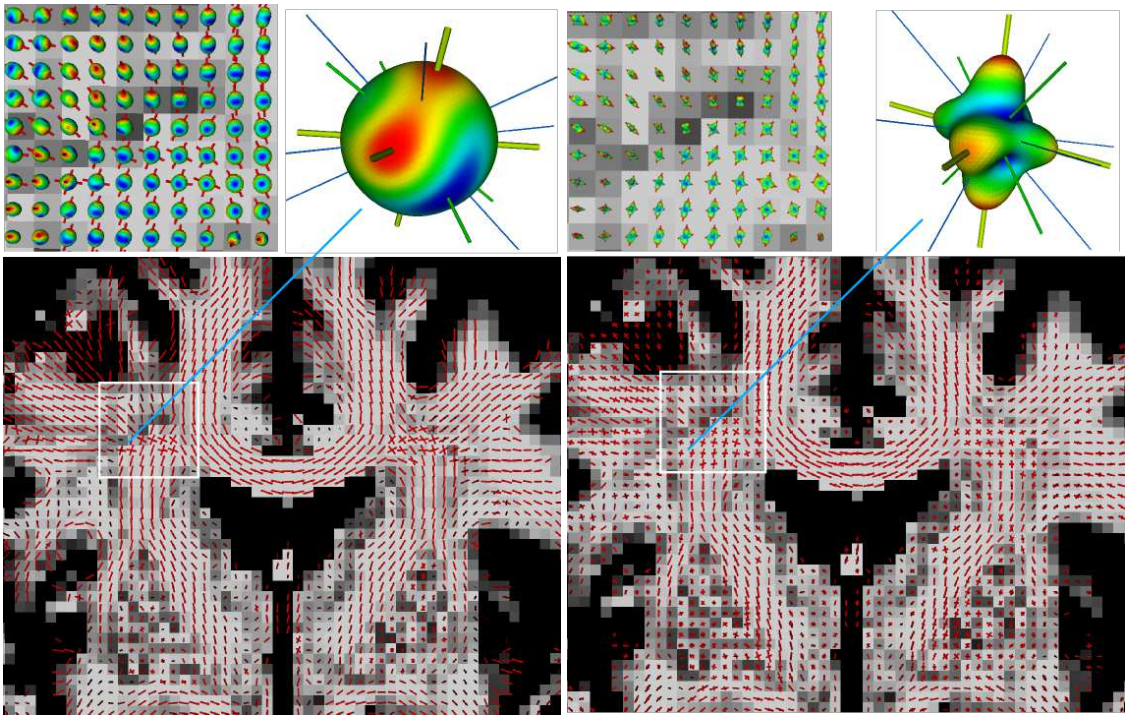

Figure 6.4: Real Data Crossings: Maxima from ODF-T (left-column) & ODF-SA (right-column) in rank-4 SH basis. Top-row: Zoomed region with ODFs and their maxima, and one voxel with an ODF and its classified extrema. Bottom: Coronal slice where the CST, the CC, and the SLF cross. Maxima from the ODFs shown by red lines. ODF-SAs have sharper peaks and detect more crossings than ODF-Ts.

three peaks, which is also indicated by the glyph colour code.

6.2.5 Discussion

We have shown a way of extracting the extrema, of classifying them as maxima, minima and saddle-points, and also of computing the principal curvatures at the extrema, for a very general class of SDFs expressed either in the SH basis or the ST basis. While the extrema were detected using an analytical bracketing method by the subdivision method in the Bernstein basis, they were then refined by standard 1D numerical solvers to a high degree of precision. This whole process was tested on synthetically generated multi-tensor data with known ground truth directions. These experiments confirmed that not only could the extrema be detected analytically, implying that none would be missed, but also that they could be extracted with high precision. Further, we also presented visually the correct classification of these extrema as maxima, minima and saddle-points. Finally we tested the maxima extraction on in-vivo cerebral data with both the ODF-T and the ODF-SA models. Although the ODF-SA has sharper peaks and detects a greater number of crossings, the maxima extraction was able to detect extrema from highly smooth ODF-Ts.

6.3 Peak Fractional Anisotropy

Although we showed in the previous section how to compute the principal curvatures at the extrema, we didn't use this information. We now proceed to an application of the principal curvatures at the maxima of an SDF. The extrema extracted from an SDF, represent first order descriptions of the SDF's shape, while the principal curvatures represent second order descriptions, and can further describe the shape of the extrema. This is a rich source of geometric information about any SDF. We propose the *peak fractional anisotropy* (PFA) measure to represent this information in an integrated fashion to characterize the extrema (maxima) of an SDF. We also characterize the entire SDF by the *Total-PFA*, which sums the PFA measures describing each maxima of the SDF over all the maxima of the SDF.

There are other methods in dMRI that use the principal curvatures of a peak of an SDF to quantify its shape. Seunarine et al. [101] proposed the *peak anisotropy* (PA) that measures the anisotropy of the cross-section of every peak of an SDF. It is computed as the FA of the shape operator $\mathcal{S}$ (section-6.2.3). In other words PA measures the spread of the peak since it computes the FA of the principal curvatures. Seunarine et al. use this measure of spread, on the peaks of the ODF-T and the PAS-MRI, in probabilistic tractography as a means of extracting more information from a peak, like fiber direction probabilities, than just its maximal direction.

Bloy and Verma in [91] experimentally study the relationship between the mean cur-

vature H, of a peak in the case of a single peak (SDF with only one maximum), and the FA of the tensor $\mathbf{D}$ that parameterizes the anisotropic free diffusion Gaussian EAP (Eq-3.17), which is used to generate the synthetic signal that is used to estimate the SDF. In their example, they consider the ODF-T.

In comparison to PA and mean curvature, the PFA we propose measures the anisotropy of an entire peak of an SDF. The PFA of a peak of a generic SDF can be compared conceptually to a geometric approach for extracting scalar bio-markers like the FA from DTI. While in DTI, FA was computed from the eigenvalues of the diffusion tensor, the PFA of a peak assigns to it a scalar value computed from its function value (maxima value) and principal curvatures, which describes the overall shape of the peak.

Since the PFA measures the anisotropy of each peak, the Total-PFA, which sums the PFAs of each peak of an SDF, is a quantity that measures the "starriness" of the SDF. In other words, Total-PFA emphasizes local anisotropy (of each peak) rather than overall anisotropy of the SDF. This differentiates Total-PFA from measures like *generalized anisotropy* (GA) [102] and *generalized fractional anisotropy* (GFA) [51]. Since GA and GFA both compute scalar indices of complex shaped SDFs from the variance of the SDFs function values, they are both insensitive to local elongations. In fact, they are invariant to the shuffling of the function values and can therefore have the same measure for different shapes when the shapes contain the same function values [103].

6.3.1 Materials and Methods

To compute the anisotropy of a peak of an SDF from its function value and principal curvatures, the idea is to fit to a peak an ellipsoid that can match the function value and principal curvatures of the peak. By parameterizing the fitted ellipsoid by three unknowns – its eigenvalues, it is then possible to compute the FA of this ellipsoid, which we designate as the PFA. Various models are possible for computing the PFA.

We call the simplest PFA the *ellipsoid PFA* (PFAe). Essentially, as just explained, we fit a canonically described ellipsoid at every maximum, such that the ellipsoid's principal radius equals the maximum's function value, and its principal curvatures equal the principal curvatures of the SDF at the maximum. This allows us to compute the eigenvalues, or principal radii, of the ellipsoid. The PFA is the FA of this ellipsoid. This is the PFAe corresponding to the maximum-peak.

Since we decided to illustrate these methods on two particular SDF models, namely the ODF-T and the ODF-SA, we propose two other PFAs, each corresponding to the underlying SDF model. If we consider anisotropic free diffusion, where the EAP is the oriented Gaussian (Eq-3.17), parameterized by the covariance tensor $\mathbf{D}$, then it is

possible to compute the ODF-T and the ODF-SA of this EAP analytically. Let these analytical ODFs be known as the FD-ODF-T and the FD-ODF-SA, where FD indicates free diffusion. These are also parameterized by the covariance tensor $\mathbf{D}$. When $\mathbf{D}$ is taken in its canonical representation, it only has three parameters, namely its eigenvalues along the coordinate axes. In such a case, it is simple to compute the function value and the principal curvatures of the analytical FD-ODF-T and FD-ODF-SA. By matching these to the maximum function value, and the principal curvatures of the peak of the SDF under consideration, it is possible to fit an FD-ODF-T or an FD-ODF-SA to the peak, and to estimate $\mathbf{D}$.

Naturally, the model of the analytical ODF has to match the model of the SDF, i.e. if the SDF were an ODF-T, we match a FD-ODF-T to each of its peaks, and similarly if the SDF were an ODF-SA, we match a FD-ODF-SA to each of its peaks. The FA of the covariance tensor $\mathbf{D}$ estimated in this fashion for a peak, defines the PFA of that peak based on the model. In other words if the SDF were an ODF-T, then the corresponding PFA for every peak is the *PFA-T*, and if the SDF were an ODF-SA, then the corresponding PFA for every peak is the *PFA-SA*.

We now compute these forms analytically. First we consider the PFAe. The canonical form of an ellipsoid is

$$\left(\frac{x}{\lambda_x}\right)^2 + \left(\frac{y}{\lambda_y}\right)^2 + \left(\frac{z}{\lambda_z}\right)^2 = \mathbf{x}^T\mathbf{D}\mathbf{x} = 1,$$

where $\mathbf{x} = [x, y, z]$, and $\mathbf{D} = \mathrm{diag}(\lambda_x, \lambda_y, \lambda_z)$. We consider this ellipsoid to be elongated along the X-axis, or $\lambda_x > \lambda_y, \lambda_z$. In this case, the maximum function value and principal curvatures of this ellipsoid can be computed to be:

$$\begin{aligned} \kappa_1 &= \frac{\lambda_x(3\lambda_z - 2\lambda_x)}{\lambda_z}; \quad \kappa_2 = \frac{\lambda_x(3\lambda_y - 2\lambda_x)}{\lambda_y}; \\ \mathcal{F} &= \frac{1}{\lambda_x}. \end{aligned} \tag{6.19}$$

To fit an ellipsoid to the maximum value $\tilde{\mathcal{F}}$ and principal curvatures $\tilde{\kappa_1}, \tilde{\kappa_2}$ of a peak of an SDF, it is necessary to solve the above equations for $\lambda_x, \lambda_y, \lambda_z$:

$$\begin{aligned} \lambda_x &= \frac{1}{\mathcal{F}}; \\ \lambda_y &= \frac{2}{\mathcal{F}(3 - \kappa_1\mathcal{F})}; \quad \lambda_z = \frac{2}{\mathcal{F}(3 - \kappa_2\mathcal{F})}. \end{aligned} \tag{6.20}$$

These formulae can be used to fit an ellipsoid to a peak of an SDF, and to compute the PFAe of the peak.

Next we consider the PFA-T. The analytical formula for the FD-ODF-T parameterized by a canonically represented covariance tensor $\mathbf{D} = \mathrm{diag}(\lambda_x, \lambda_y, \lambda_z)$ is found to be [104]:

$$\Psi_T(x, y, z) = \frac{1}{Z}\sqrt{\frac{1}{\frac{x^2}{\lambda_x} + \frac{y^2}{\lambda_y} + \frac{z^2}{\lambda_z}}}, \tag{6.21}$$

where all the constants have been absorbed into Z, the normalizing constant, since the ODF-T isn't a true marginal distribution, and $\Psi_T(x,y,z) = r(\theta,\phi)$ from the discussion on principal curvatures (section-6.2.3). The maximum function value and principal curvatures can again be computed analytically when Ψ_T is elongated along the X-axis. The quantities are found to be:

$$\kappa_1 = \frac{Z\sqrt{\lambda_x}}{\lambda_y}; \quad \kappa_2 = \frac{Z\sqrt{\lambda_x}}{\lambda_z}; \quad \mathcal{F} = \frac{\sqrt{\lambda_x}}{Z}. \tag{6.22}$$

Eq-6.22 implies that the λ_i can be computed uniquely only up to the constant Z. But since scaling the eigenvalues doesn't change the FA, we can fix $Z = 1$ and solve for $\lambda_x, \lambda_y, \lambda_z$:

$$\begin{aligned} \lambda_x &= \mathcal{F}^2; \\ \lambda_y &= \frac{\mathcal{F}}{\kappa_1}; \quad \lambda_z = \frac{\mathcal{F}}{\kappa_2}. \end{aligned} \tag{6.23}$$

These can be used for fitting a FD-ODF-T to each peak of any ODF-T, when its function value and principal curvatures $\tilde{\mathcal{F}}, \tilde{\kappa_1}, \tilde{\kappa_2}$, are known, making it possible to compute the peak's PFA-T from the λ_i.

Finally we consider the PFA-SA. The analytical formula for the FD-ODF-SA parameterized by the canonically represented covariance tensor $\mathbf{D} = \mathrm{diag}(\lambda_x, \lambda_y, \lambda_z)$ can be computed to be:

$$\Psi_{SA}(x,y,z) = \frac{1}{4\pi\sqrt{\lambda_x\lambda_y\lambda_z}} \left(\frac{1}{\frac{x^2}{\lambda_x} + \frac{y^2}{\lambda_y} + \frac{z^2}{\lambda_z}} \right)^{\frac{3}{2}}. \tag{6.24}$$

Again $\Psi_{SA}(x,y,z) = r(\theta,\phi)$ from the discussion on principal curvatures (section-6.2.3). Since this is a true marginal distribution, it doesn't have a normalizing constant. The formulae for the maximum function value and principal curvatures can again be computed analytically when Ψ_{SA} is elongated along the X-axis. We find:

$$\begin{aligned} \kappa_1 &= \frac{4\pi\lambda_y(3\lambda_x - 2\lambda_z)}{\lambda_x\sqrt{\lambda_y\lambda_z}}; \quad \kappa_2 = \frac{4\pi\lambda_z(3\lambda_x - 2\lambda_y)}{\lambda_x\sqrt{\lambda_y\lambda_z}} \\ \mathcal{F} &= \frac{\lambda_x^{3/2}}{4\pi\sqrt{\lambda_x\lambda_y\lambda_z}}, \end{aligned} \tag{6.25}$$

Interestingly, Eq-6.25 indicates that the function value and principal curvatures, at the maximum of a FD-ODF-SA, remain unchanged if the λ_i of the covariance tensor are multiplied by a constant. Therefore, again, Eq-6.25 can be solved for $\lambda_x, \lambda_y, \lambda_z$ only up to a scaling factor. However, since that doesn't change the computed FA, we consider the solution set:

$$\begin{aligned} \lambda_x &= 1; \\ \lambda_y &= \frac{3}{\kappa_2\mathcal{F} + 2}; \quad \lambda_z = \frac{3}{\kappa_1\mathcal{F} + 2}. \end{aligned} \tag{6.26}$$

These can be used for fitting a FD-ODF-SA to each peak of any ODF-SA, and to compute the PFA-SA of the peak from the λ_i.

The maxima extraction process and the computation of the principal curvatures allow us to naturally characterize each peak of an SDF from the various PFAs. We simply extend this characterization to the entire SDF by considering a weighted sum the PFAs for all its peaks. We designate this the Total-PFA (Total-PFAe, Total-PFA-T and Total-PFA-SA):

$$\text{TotalPFA} = \sum_{i=1}^{N} \mathcal{F}_i \cdot \text{PFA}_i.$$

Since the Total-PFA is a summation of all the local anisotropy measure from each peak, it is therefore an integrated measure of the overall peakedness of an SDF. It indicates how star-like the shape of the SDF is.

6.3.2 Experiments and Results

Although the PFA measures the anisotropy of each peak of an SDF from its function value and principal curvatures, to characterize the underlying cerebral tissue from the SDF's shape, this huge set of information has to be categorized between voxels and presented in a uniform fashion. However, since not all the SDFs in the voxels of a reconstructed dMRI image have the same number of peaks, it isn't straightforward to compare peaks of neighbouring SDFs.

It is possible to compare and visualize the primary or the most significant maximum of each SDF. The primary maximum indicates the major fiber bundle direction. Therefore, it is possible to visualize this direction and its coherency from the maximum's direction and its PFA. The more coherently the underlying fiber bundle is structured, the higher is the PFA, indicating greater anisotropy. The more fanned out is the fiber bundle structure, the lower the PFA, indicating lower anisotropy.

But this representation only conveys partial information of an SDF since it discards the information on its other peaks. Therefore, nothing can be said about the complexity of the underlying tissue's microstructure. However, since the Total-PFA integrates the anisotropy from all the peaks of an SDF into a single scalar, which measures the starriness or the peakedness of an SDF, it is well suited to characterize the microstructure complexity. But it must be noted, that the individual peak information can be handy in other situations, such as in tractography. The estimated covariance tensor $\mathbf{D}$ from the fitted ellipsoid (or FD-ODF-T or FD-ODF-SA) can be used to define probabilities and uncertainties along each peak.

We conduct experiments on the in-vivo cerebral dataset, and we consider both the ODF-T and ODF-SA models, since they're known to have peaks with different shapes. The ODF-SA has sharper peaks than the ODF-T, and it also detects a greater number

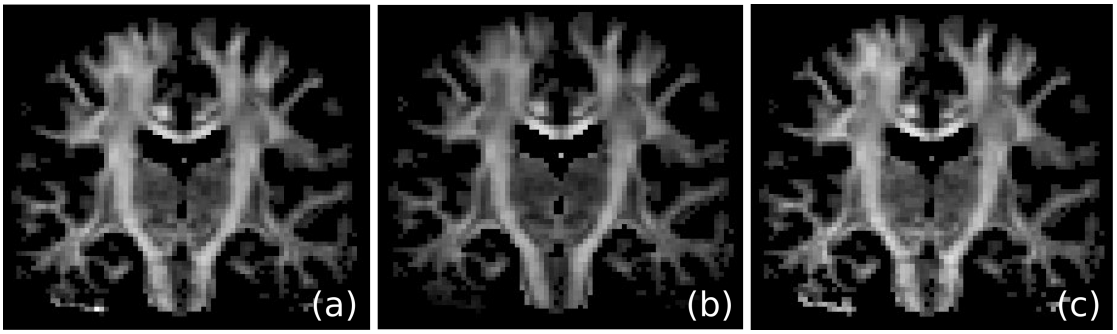

Figure 6.5: (a) FA, (b) GFA from ODF-T, (c) GFA from ODF-SA. FA measures anisotropy in DTI, however, DTI cannot detect crossings and loses anisotropy in regions with crossings. GFA is defined for SDFs with complex shapes, which can detect crossings. But since GFA is a measure based on the variance of the function's values, it cannot detect local anisotropies. Therefore, GFA presents a very similar contrast to FA – which is high in white matter and low in grey matter, but is also low in regions known to have crossings.

of crossings. However, the ODF-SA is also more sensitive to signal noise than the ODF-T. From the in-vivo cerebral dataset we estimate the ODF-Ts and the ODF-SAs, extract their maxima, and compute the PFA-T and PFA-SA of the two SDF images. We don't consider the PFAe scalar measure, since in these experiments the SDF models are known. PFAe can be useful on generic SDFs. Summing the PFAs for each peak, we also compute for the two SDF images their Total-PFA-T and the Total-PFA-SA respectively. Finally we also compute the GFA to compare against the results of the Total-PFA. The results are presented on coronal slices where there are known crossings between the CST and the CC in the plain, and the SLF going through the plain.

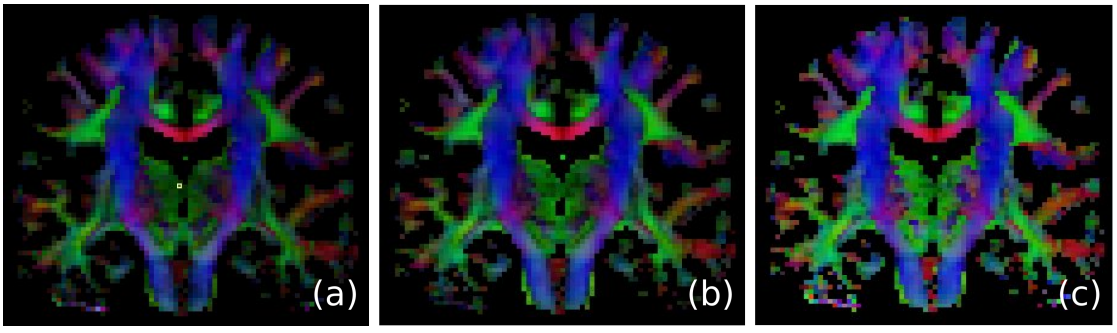

Figure 6.6: (a) Colour coded DTI major eigenvector, weighted by FA. (b) Colour coded ODF-T primary maximum, weighted by corresponding PFA-T. (c) Colour coded ODF-SA primary maximum, weighted by corresponding PFA-SA. In the colour code red represents X-axis, green represents Y-axis, blue represents Z-axis. The colour code indicates the direction of the eigenvector/maximum.

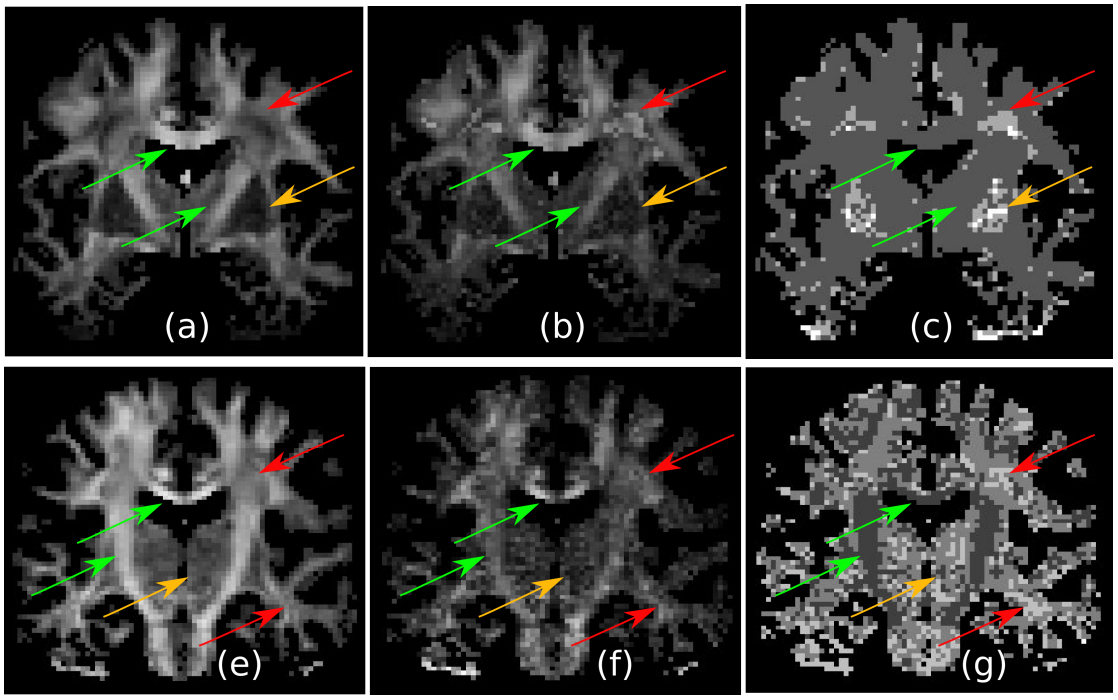

Figure 6.7: Total-PFA and GFA. Top-row: ODF-T, Bottom-row: ODF-SA. 1st column: GFA from (a) ODF-T and (e) ODF-SA. 2nd column: Total-PFA – (b) Total-PFA-T from ODF-T (f) Total-PFA-SA from ODF-SA. 3rd column: Number-of-maxima from (c) ODF-T and (g) ODF-SA. Total-PFA measures the starriness or peakedness of an SF and emphasizes local sub-voxel anisotropy. Green arrow indicates regions with no crossings (dark in 3rd col.) but high local anisotropy (bright in Total-PFA) like the CC and the CST. Red arrow indicates regions with many crossings (bright in 3rd col.) and with high local anisotropy (bright in Total-PFA) like where the CC, CST and SLF intersect. However, these regions have low GFA values. Orange arrow indicates regions with high crossings (bright in 3rd col.) but with low local anisotropy (dark in Total-PFA). These regions also have low GFA values. The ODF-SAs corresponding to the bottom-row can be seen in Fig-6.8.

First we compare the GFA to the FA. FA is defined for DTI, which has limitation in regions with fiber crossings. Therefore, it is known that FA is low in regions of the white matter where crossing fibers are present, even though the tissue has high anisotropy locally in multiple directions. GFA is defined on complex shaped SDFs that can detect such crossing fibers. However, since the GFA is computed from the variance of the SDF's function values, it too is insensitive to local anisotropy. This is seen in Fig-6.5, where the GFA is computed from both the ODF-T (b) and the ODF-SA (c). A DTI estimation was also computed from the in-vivo human dataset, which allows us to compute the FA (a). It is seen in Fig-6.5 that the GFA has a very similar contrast to the FA, in spite of the fact that ODF-Ts and ODF-SAs detect crossings (Fig-6.7).

Next we compare the primary maximum extracted from the ODF-Ts and ODF-SAs to the major eigenvector from DTI. This is shown in Fig-6.6. The eigenvector/maximum directions are colour encoded, where red indicates a direction along the X-axis, blue, along the Y-axis, and green, along the Z-axis. In Fig-6.6, (a) is the eigenvector from DTI weighted by the FA scalar measure, (b) is the primary maximum of ODF-T weighted by the corresponding PFA-T scalar measure, and (c) is the primary maximum of the ODF-SA weighted by the corresponding PFA-SA scalar measure. The overall colouring is similar between the three images, implying that the major eigenvector and the primary maxima agree. But the contrasts are different, since they represent different anisotropy measures.

Finally the results of Total-PFA are presented in Fig-6.7. Three types of scalar measures are presented in this figure to highlight the sensitivity of Total-PFA. The first column is the GFA, the second column is the Total-PFA, and the third column is an image where the contrast is the number of maxima in the ODF-Ts and ODF-SAs. The first row contains the results from ODF-Ts, and the second row contains results from ODF-SAs. The arrows indicate regions that highlight the sensitivity of Total-PFA.

The green arrows indicate regions where the ODF models have only a single maximum (dark in the number-of-maxima image: 3rd column), and where these single maxima display high anisotropy (bright in the Total-PFA: 2nd column). These are typically in the CC and the CST, and are also bright in the GFA (1st column). The orange arrows indicate regions where the ODF models have multiple peaks (bright in the 3rd column), and where these multiple maxima have low anisotropy (dark in the Total-PFA: 2nd column). These regions are dark in the GFA too (1st column). The red arrows indicate regions where the ODF models again have multiple peaks (again bright in the 3rd column), but this time these multiple maxima have high anisotropy (bright in the Total-PFA: 2nd column). However, these regions appear dark in the GFA (1st column), just like the regions indicated by the orange arrows in the GFA. These are typically regions with crossing fibers – like where the CC, the CST and the SLF intersect. Therefore, these are regions that tend to have high local anisotropy. The ODF-SAs corresponding to the Total-PFA results in Fig-6.7, bottom-row, can be seen in Fig-6.8.

This shows that Total-PFA, with its emphasis on sub-voxel local anisotropy can highlight regions of the underlying tissue that have complex microstructures. Since Total-PFA sums the PFAs of all the peaks of an SF, where the PFAs measure the individual anisotropy of the peaks, Total-PFA is able to discern between regions with multiple peaks and low peak anisotropies, which should intuitively correspond to globally isotropic SFs, and regions with multiple peaks and high peak anisotropies, which are regions with high local anisotropies along multiple directions. Such regions occur when fibers cross, and where the SDFs have pronounced star-like shapes

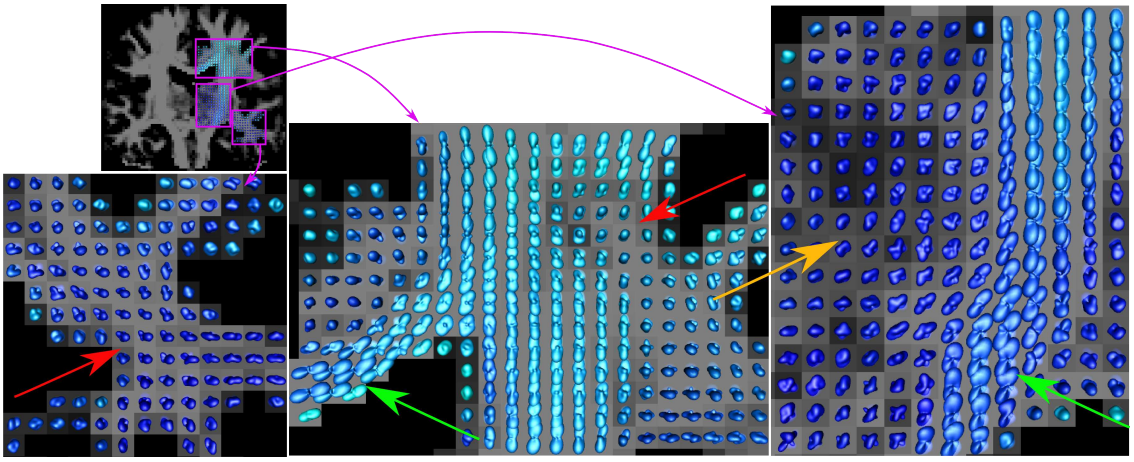

Figure 6.8: The ODF-SAs corresponding to the Total-PFA results shown in Fig-6.7 (bottom row).

6.3.3 Discussion

While the extrema represent a first order description of an SDF, the principal curvatures at the extrema provide second order information that further describe the extrema. In case of the maxima or peaks of an SDF, these geometric measures can be used to formulate an integrated measure of anisotropy for the peaks individually. This is called the PFA. Various types of PFAs can be computed. The simplest is the ellipsoid PFA that can be used for any SDF. For particular SDF models, such as the ODF-T and the ODF-SA, it is possible to compute more detailed PFAs – like the PFA-T and the PFA-SA. The PFA of a peak of an SDF, can be conceptually compared to the FA of a diffusion tensor.

Summing PFAs over the peaks of an SDF, it is possible to compute the Total-PFA. Again depending upon the PFA type, it is possible to compute the Total-PFAe, the Total-PFA-T and the Total-PFA-SA. Intuitively, the Total-PFA is a measure that emphasizes local sub-voxel anisotropy. In other words it measures the "starriness" or the peakedness of an SDF. In experiments conducted on in-vivo cerebral data, this is highlighted by the fact, that Total-PFA is able to discern between regions where SDFs have multiple peaks but with low peak anisotropy, and regions where SDFs have multiple peaks with high peak anisotropy.

When an SDF has multiple peaks with low peak anisotropy, it intuitively corresponds to global isotropy of the SDF's shape. The SDF has bumps, but is very rounded. When an SDF has peaks with high anisotropy, be it only a single peak or multiple peaks, the SDF's shape is intuitively highly non-spherical – elongated in the case of a single peak, and star-like in the case of multiple peaks. Therefore, Total-PFA can be thought of as a scalar that measures the *sphericity* of an SDF.

6.4 TRACTOGRAPHY

We have seen so far a way of extracting various geometric characteristics from a wide class of SDFs. However, SDFs in dMRI represent local voxel level information. This can be integrated spatially to reveal global structures in the cerebral white matter. As an application to our proposed method for maxima extraction, we perform tractography, to reconstruct such structures.

Tractography graphically reconstructs the connectivity of the cerebral white-matter by integrating along the direction indicated by the local geometry of the SDF. It is a modern tool that is unique in the sense that it permits an indirect dissected visualization of the brain in-vivo and non-invasively [40]. The underpinnings of tractography are also based on the fundamental assumption of dMRI – the diffusion of water molecules is hindered to a greater extent perpendicular to coherent fiber bundle structures than parallel to these. Therefore, following the geometry of the local diffusion function and integrating along reveals the continuous dominant structure of the fiber bundle. However, in spite of the gain due to its non-invasive nature, tractography can only infer such structures indirectly. Therefore, tractography is acutely sensitive to the local geometry and the error is cumulative. The correct estimation of the local geometry is crucial.

Deterministic tractography is a well established tool that has seen considerable success in researching neurological disorders [90]. Deterministic tractography begins from a seed point and traces along the dominant fiber direction by locally connecting the "fibers" or mathematically becoming tangent to these. Classically the major eigenvector of the diffusion tensor in DTI represent these "fibers" [105, 41, 95]. However, since DTI is ambiguous and cannot accurately describe the fiber directions in regions with complex fiber configurations, DTI tractography, in spite of its successful usage, is known to be prone to errors. Hence the trend in recent years to extend tractography to complex shaped SDFs that describe the underlying fiber directions more accurately [28, 48, 106].

Probabilistic tractography was proposed to address the reliability of deterministic tractography which remains sensitive to a number of parameters. The concept and output of probabilistic tractography is, however, subtly different from determinist tractography. While the latter attempts to find the connectivity between two regions, the former measures the likelihood that two regions are connected, or it provides a connectivity confidence. Given the capabilities and ambiguities of dMRI acquisition and reconstruction schemes of today, due to partial voluming, noise, etc., probabilistic tractography provides a more complete statement. However, in spite of this deterministic tractography has proved useful, and there exist probabilistic schemes that rely on deterministic tracking to compute confidence measures, such as in the probabilistic bootstrapping tractography on fODFs [107]. Therefore, improving deterministic

tractography is an important problem.

In this section we propose a deterministic tractography scheme based on the polynomial approach presented earlier for accurately extracting the maxima of any non-parametrically represented SDF. We extend the Streamline tractography and the Tensorline tractography, which were defined for DTI, to a generic class of SDFs that can have complex geometries capable of detecting fiber crossings. We illustrate our modified Streamline and Tensorline tractographies on ODF-SAs, and show improvements in detecting the lateral radiations of the CC, by tracing through regions where the CC intersects the CST and the SLF.

6.4.1 Materials and Methods

We adapt the Streamline tractography [41] to the multiple maxima that can be discerned by complex SDFs in regions with fiber crossings, allowing us to trace through such regions with greater accuracy than in DTI tractography. We also extend the well known Tensorline tractography [94, 95] to complex SDFs, to smooth out local kinks that can make the fiber tracks unnaturally "wriggly" in plain Streamline tractography due to acquisition noise and partial voluming which make the estimated SDF field spatially irregular. This is important, since a spatially irregular SDF field can cause kinks in the fiber important enough to violate the curvature threshold and stop the tracking algorithm.

Streamline tractography The continuous version of Streamline tractography [41] defined for DTI, considers a fiber tract as a 3D space curve parametrized by its arc-length, $\mathbf{r}(s)$, and describes it by its Frenet equation:

$$\frac{d\mathbf{r}(s)}{ds} = \mathbf{t}(s) = \epsilon_1(\mathbf{r}(s)), \tag{6.27}$$

where $\mathbf{t}(s)$ the tangent vector to $\mathbf{r}(s)$ at s is equal to the unit major eigenvector $\epsilon_1(\mathbf{r}(s))$ of the diffusion tensor at $\mathbf{r}(s)$. This implies that fiber tracts are locally tangent to the dominant eigenvector of the diffusion tensor at every spatial position. The differential equation Eq-6.27 along with the initial condition $\mathbf{r}(0) = \mathbf{r}_0$ means that starting from $\mathbf{r}_0$, a fiber can be traced by continuously integrating Eq-6.27 along the direction indicated locally by the major eigenvector of the diffusion tensor at that point.

However, integrating Eq-6.27 requires two things – first, a spatially continuous tensor (or SDF) field, and second, a numerical integration scheme. [41] proposed two approaches for estimating a spatially continuous tensor field from a discrete DTI tensor field, namely approximation and interpolation. They also proposed the Euler's method, the 2nd order Runge-Kutta method, and the adaptive 4th order Runge Kutta method as numerical integration schemes. Finally, for stopping they proposed four criteria – the tracts are within the image volume, the tracts are in regions with

FA value higher than a threshold, the curvature of a tract is smaller than a threshold, and that a tract is better aligned with the major eigenvector in the next spatial location than any of the two other eigenvectors.

We adapt this tractography algorithm to SDFs with multiple maxima by modifying Eq-6.27 to:

$$\frac{d\mathbf{r}(s)}{ds} = \eta_{\theta_{min}}(\mathbf{r}(s)),\ \mathbf{r}(0) = \eta_{max}(0) \tag{6.28}$$

where $\eta_i(\mathbf{r}(s))$ are all the unit maxima vectors of the SDF extracted by our method at $\mathbf{r}(s)$, η_{max} is the unit maximum vector whose function value is the largest amongst all the η_i, and $\eta_{\theta_{min}}$ is the unit maximum vector in the current step that is most collinear to the unit maximum vector followed by the integration in the previous step. Eq-6.28 and the initial condition state that at the starting point we begin integrating along the dominant maximum direction, and at each consecutive step we first extract all the maxima of the SDFs and choose the maximum direction most collinear to the maximum direction from the previous integration step, to move forward in the integration.

To choose the maximum direction most collinear to the previously chosen maximum direction, we compute the dot product between the previously chosen maximum direction and all the maxima of the current step, and consider the absolute values of the dot products. Hence, the maximum chosen for the next integration direction is the maximum whose absolute value of its dot product with the previously chosen maximum direction is the largest. Also to avoid erratic forward and backward steps during the integration, if the value of the dot product is negative, we flip the unit maximum direction to point it consistently along the fiber direction, just like in [41].

Since we require a continuous field of SDFs for integrating Eq-6.28, we consider the Euclidean interpolation of the SDFs, which is a simple interpolation of the coefficients of the SDFs in the SH basis [3], and is equivalent to the L2-norm interpolation of the SDFs, since the SHs form an orthonormal basis. For the numerical integration scheme we employ the 2nd order Runge-Kutta method due to its robustness and simplicity with an integration step of length 0.5mm.

For stopping we only use two criteria – the tracts are within the image volume, and tracts aren't allowed with high curvature, or the radius of curvature of tracts is smaller than 0.87mm. Currently we don't employ any stopping criteria based on anisotropy indices because such indices such as GFA for complex SDFs show similar contrasts to FA, and therefore have low values in regions with fiber crossings.

Tensorline tractography Since Streamline tractography traces fibers that are always tangent to the maxima of the local SDF, these fibers can be unnaturally "wriggly". Due to acquisition noise the estimated discrete SDF field is generally spatially irregular. Thus closely following the local maximum can cause the fiber to wriggle.

This effect can be important enough to violate the curvature criterion and cause the tracking algorithm to abort. Furthermore, partial voluming effects can also cause certain SDFs to lack maxima along the fiber direction, especially in voxels with fiber crossings, even when neighbouring SDFs may have maxima well aligned with the fiber direction. This can cause the tracking algorithm to suddenly deviate to another fiber track, violating again the curvature criterion.

DTI Tensorline tractography was proposed to specifically address these issues [94, 95]. ϵ_1 in Eq-6.27 was replaced by:

$$\mathbf{v}_{\text{out}} = f\epsilon_1 + (1-f)((1-g)\mathbf{v}_{\text{in}} + g\mathbf{D}\cdot\mathbf{v}_{\text{in}}), \tag{6.29}$$

where f, g are user defined weights, $\mathbf{v}_{\text{in}}, \mathbf{v}_{\text{out}}$ are the incoming and outgoing tangents respectively, $\mathbf{D}$ is the local diffusion tensor with ϵ_1 its unit major eigenvector, and $\mathbf{D}\cdot\mathbf{v}_{\text{in}}$ is the tensor deflection (TEND) [95] term. This implies that locally the fiber isn't completely tangent to the major eigenvector, but is the weighted sum of the major eigenvector, the TEND term where the entire diffusion tensor globally influences the fiber direction from the previous step $\mathbf{v}_{\text{in}}$, and $\mathbf{v}_{\text{in}}$ itself, which acts as an inertial factor to maintain the fiber's general trend. This smooths away unnatural kinks, and also helps to plough through regions with uncertainty, where $\mathbf{D}$ is oblate or spherical.

With general SDFs, $\mathbf{D}$ doesn't exist, but the SDFs have more complex geometries that are meant to better resolve the angular uncertainties in regions with crossings, implying that the TEND term can be ignored. Note that with the approach for measuring PFA for each peak, it is possible to measure an ellipsoid characterized by a symmetric positive definite 3×3 matrix $\mathbf{D}$ that can be used to compute an equivalent to the TEND term. But we do not consider this for the moment. Therefore, we adapt the Tensorline tractography to general SDFs with multiple maxima by replacing $\eta_{\theta_{min}}$ in Eq-6.28 by:

$$\mathbf{v}_{\text{out}} = f\eta_{\theta_{min}} + (1-f)\mathbf{v}_{\text{in}}, \tag{6.30}$$

with f a user defined weight, and with $\mathbf{v}_{\text{in}}, \mathbf{v}_{\text{out}}$ as defined above. Again $\mathbf{v}_{\text{in}}$ acts like an inertial factor to maintain the fiber's general trend, and Eq-6.30 smooths away kinks and helps to navigate regions with SDFs affected by partial voluming.

6.4.2 Experiments and Results

In the experiments we conduct for testing tractography with the maxima extraction we have proposed, we consider the ODF-SA model and the Tensorline algorithm. The ODF-SA model is used since it detects a greater number of crossings and its peaks are much sharper than the ODF-T model. These qualities are useful while tracing through regions that have known crossing fiber configurations. Also we use the Tensorline algorithm since it is a generalization of the Streamline tractography,

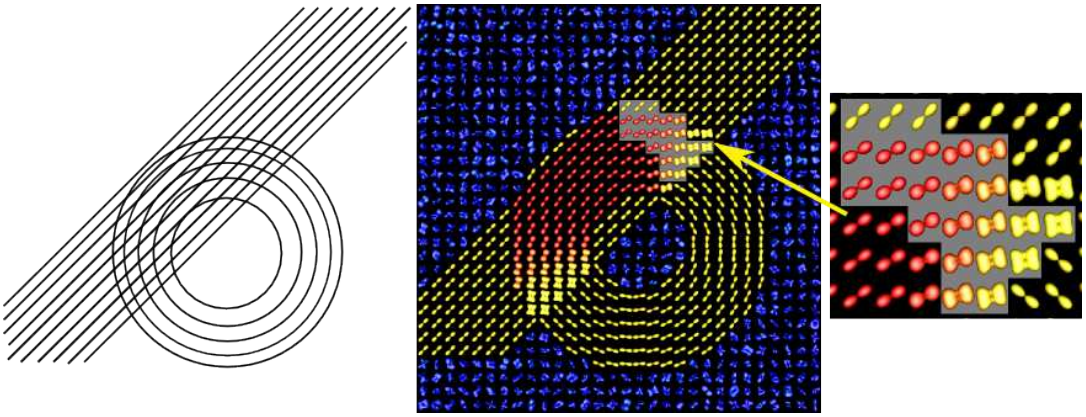

Figure 6.9: Synthetic dataset with fiber bundles converging and diverging. Left: Overlapping fiber layout. Centre: ODF-SAs estimated from dataset with seed voxel in grey. Right: zoom in seed voxels.

and is better suited while tracing through SDF images that haven't been spatially smoothed, which is our case. For comparison we also present DTI Streamline and Tensorline tractography.

We first conduct tests on a synthetic dataset, designed to have two overlapping fiber bundles first converge and then diverge. This is a more complex scenario than pure crossings, since converging and diverging creates a range of crossing angles between the two bundles. Such cases are hard to deal with because as the fibers progressively converge, the crossing angle is progressively reduced, until sooner or later the crossing angle is below the angular threshold of the SDF model. When this happens the SDF model, i.e. ODF-SA can no longer discern two fiber bundles, and therefore has only one peak that points between the two converging fibers.

The synthetic dataset is generated using the multi-tensor model (Appendix-A.0.1), where the profile for a single fiber is taken to be $\mathbf{D} = \mathrm{diag}(1700, 300, 300) \times 10^{-6}$ mm^2/s, for the single fiber profile, with a b-value of 3000 s/mm^2. We compare DTI Tensorline tracking and ODF-SA Tensorline tracking on this dataset. The ODF-SAs were estimated in a truncated rank-4 SH basis.

We also conduct tests on the in-vivo human cerebral dataset (Appendix-A.0.3). Again we consider ODF-SAs in a rank-4 SH basis and also DTI, which we estimate from this dataset. We use the Tensorline tractography on both these SDF models. We track specifically from seeds within the CC. It is well known that due to the important crossings between the lateral radiations of the CC and the CST it is difficult to track the lateral radiations of the CC. We use the ODF-SA and our modified tracking algorithm to specifically recover these lateral radiations of the CC. We also track the SLF which crosses the lateral radiations of the CC and the CST to validate our tracking method in regions where three fiber bundles cross.

In all the Tensorline tractography tests that were conducted we used the following weight factors. DTI Tensorline tractography was performed with $f = 0.3$ and $g = 0$ (Eq-6.29). These weights imply that the TEND term was ignored and only the inertia term $\mathbf{v}_{\text{in}}$ played a role. These weights were chosen to make the DTI Tensorline tracking comparable to the ODF-SA Tensorline tracking. The ODF-SA Tensorline tracking was performed with $f = 0.3$ (Eq.6.30).

The tractography results in the synthetic dataset are presented in Figs-6.9 & 6.10. Fig-6.9 shows the layout of the synthetically generated fiber bundles that overlap. By converging and diverging, they generate a range of crossing angles between the two fiber bundles. The estimated ODF-SA image is shown with the tractography seed voxels highlighted with a grey background. A zoom into the seed voxels clearly shows the changing crossing angles detected by the ODF-SAs.

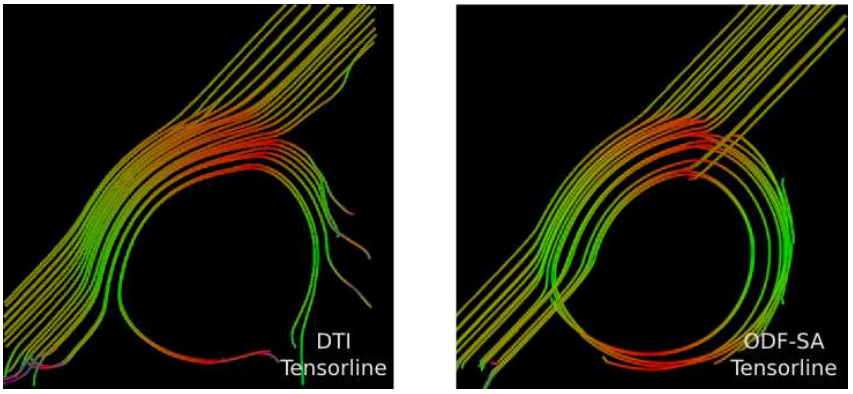

Figure 6.10: DTI and ODF-SA Tensorline fiber tracking on synthetic data. DTI fibers bend in regions with crossings, while ODF-SA fibers cross.

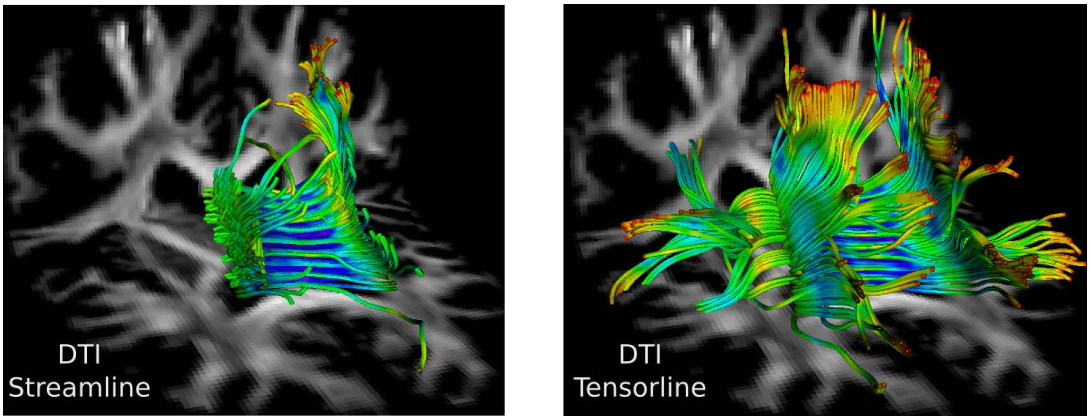

Figure 6.11: DTI Streamline and Tensorline tractography from seed regions inside the CC. Since the lateral radiations of the CC cross the CST in the CR, it is known that DTI Streamline tractography cannot recover these lateral radiations. DTI Tensorline tractography performs better and traces some fibers from the lateral radiations.

Fig-6.10 shows the results from the DTI Tensorline and the ODF-SA Tensorline tractographies. In the DTI tractography it is clear that there are no crossings. The tracked fibers bend or curve along their paths to account for the reduced anisotropy in the diffusion tensors in the regions with crossings (as seen in Fig-6.9). ODF-SA Tensorline tractography clearly shows fibers crossing between the two bundles. However, it too shows some bending and curving of its traced fibers. This happens where the converging and diverging fiber bundles create crossing angles that are below the threshold of the ODF-SA's angular resolution (as see again in Fig-6.9).

In the in-vivo dataset, we first conducted DTI Streamline and Tensorline tractography experiments for comparison. The results are presented in Fig-6.11. The tracking is seeded in regions within the CC. It is clear that DTI Streamline in unable to trace fibers through the regions where the CC crosses the CST in the *corona radiata* CR. None of the lateral radiations of the CC are recovered. In comparison DTI Tensorline tractography performs considerably better. A number of radial projections are recovered, showing that indeed Tensorline tractography is able to plough through regions with crossings.

ODF-SA Tensorline tractography with the proposed maxima extraction method is shown in Fig-6.12. It too was seeded in the same regions within the CC. Clearly ODF-

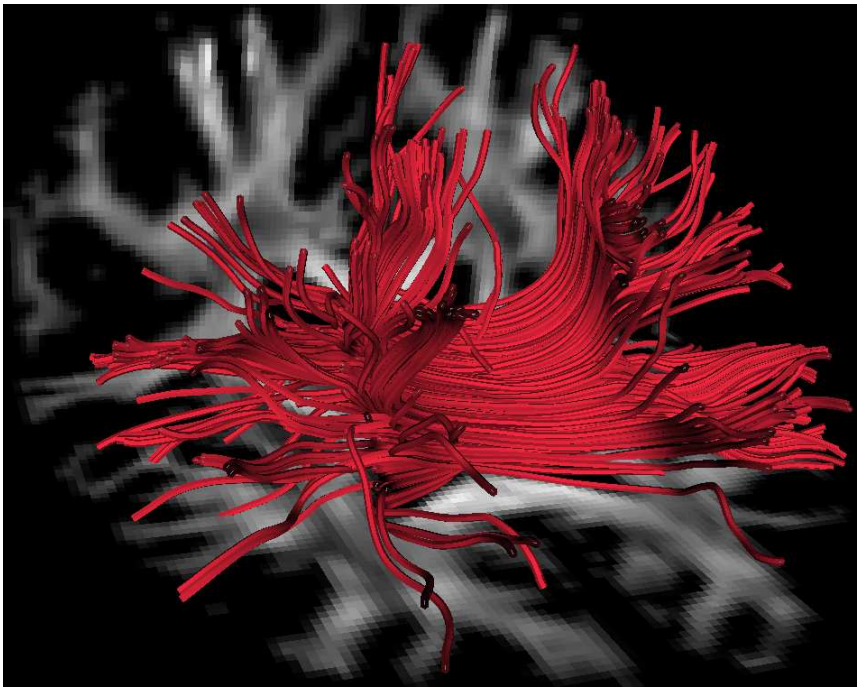

Figure 6.12: ODF-SA Tensorline tractography with the method of maxima extraction proposed in this chapter. Tracking was seeded in the CC like in Fig-6.11. A much richer distribution of the lateral radiations of the CC are traced through the region of crossings, where the CC intersects the CST in the CR.

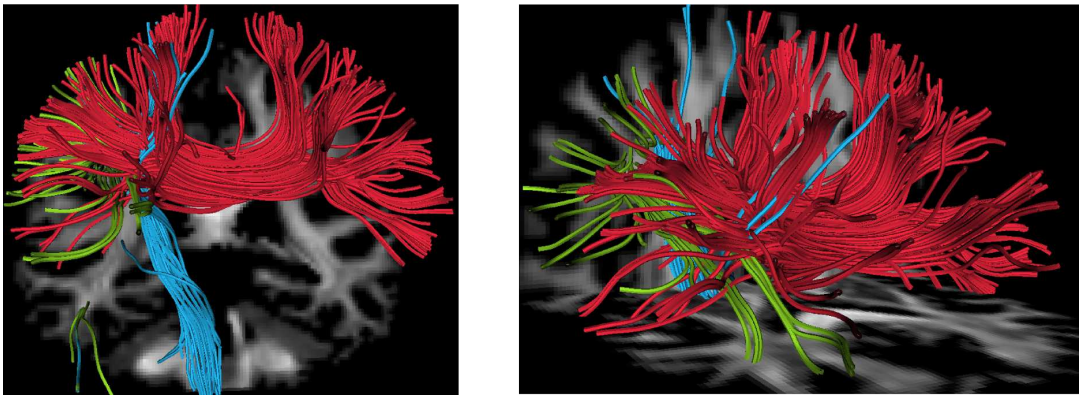

Figure 6.13: ODF-SA Tensorline tractography with the method of maxima extraction proposed in this chapter. Three fiber bundles are traced, starting from different seed regions. Red: seeds in the CC (left-right). Blue: seeds in the CST (superio-inferior). Green: seeds in the SLF (anterio-posterior). Zoom into crossing region in Fig-6.14.

SA Tensorline tractography is capable of tracing through the intersections between the CC and the CST. A much richer distribution of lateral radiations of the CC are recovered than in the DTI tractography experiments. The capacity of ODF-SA Tensorline tractography to trace through regions with crossings is further highlighted in Fig-6.13. Three fiber bundles that criss-cross are traced by seeding the tractography in different regions. In red are the fibers traced from seeds within the CC (left-right). In blue are the fibers traced from seeds within the CST (superio-inferior). In green are the fibers traced from seeds within the SLF (anterio-posterior). These three fiber

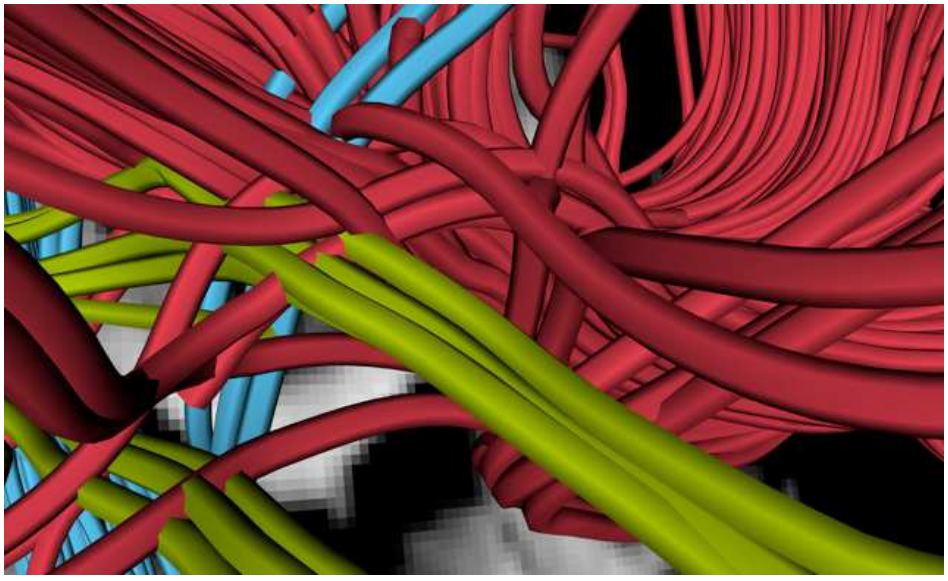

Figure 6.14: ODF-SA Streamline tractography with the method of maxima extraction proposed in this chapter. Zoom into the region where three fiber bundles cross. Red: CC (left-right). Blue: CST (superio-inferior). Green: SLF (anterio-posterior).

bundles intersect each other within the same region – a region that has been closely scrutinized in this chapter. In the section-6.2.4 we extracted the maxima of ODF-Ts and ODF-SAs within this region to show the presence of multiple maxima. In the section-6.3.2 we showed that the Total-PFA revealed this region to have a high number of crossings and high local anisotropy. In Fig-6.14 we see a zoom into this region with the results of the ODF-SA Tensorline tractography, where we clearly see the three fiber bundles – the CC, the CST and the SLF crossing.

6.4.3 Discussion

As an application of the polynomial approach for maxima extraction, we performed tractography on SDFs with complex shapes, namely the ODF-SA. To do this, we adapted the deterministic DTI Streamline and Tensorline tractography algorithms to SDFs that can detect crossings and can have multiple maxima. ODF-SA Tensorline tractography was chosen since ODF-SAs have sharp peaks which help to detect fiber bundle crossings, and since the Tensorline algorithm helps smooth out local kinks in the traced fibers that result from spatially irregular SDF estimation due to signal noise.

Experiments were conducted on a synthetically generated dataset and on the in-vivo human cerebral dataset. For comparison we also performed DTI Streamline and Tensorline tractography. From seed regions within the CC, DTI Streamline tractography wasn't able to recover the lateral radiations of the CC because of the crossing between the CC and the CST in the CR. A number of these radiations were recovered by the DTI Tensorline tractography. The best result was achieved by the ODF-SA Tensorline tractography where a rich distribution of lateral radiations were recovered. By also tracking from seed regions within the CST and the SLF, we were able to trace fibers through a region where all three fiber bundles – the CC, the CST, and the SLF, cross.

6.5 Conclusion

In dMRI, the partial and directional diffusion information in DWIs is integrated into a single function which represents diffusion in every voxel. This function reflects the microstructure of the underlying tissue. In the case of the cerebral white matter, this function reflects the underlying fiber bundle layout. This diffusion function is most often represented as a spherical diffusion function (SDF) whose geometry can be used to infer the underlying microstructure.

In this chapter we proposed a method for extracting many geometric features from SDFs. We proposed a polynomial approach for extracting all the extrema of a wide class of SDFs with complex shapes described either in the SH basis or the ST basis.

The extrema were bracketed analytically, ensuring that none were missed, and they were refined numerically, ensuring high precision in the results. The extrema were identified on the criterion of optimization theory, without any dependence on an initial solution. Therefore, the proposed approach is neither heuristic like a finite search on a discrete mesh, nor local, as is optimization. We also classified the extrema into maxima, minima and saddle points.

We further computed the principal curvatures at the extrema, and proposed the PFA to characterize the maxima of an SDF, which indicate fiber directions. We also proposed the Total-PFA which measures the peakedness or starriness of an SDF to characterize the complexity of the underlying tissue's microstructure. Using the Total-PFA, we were able to differentiate between regions (SDFs) with multiple peaks with low local anisotropy that indicates overall isotropy, and regions (SDFs) with multiple peaks with high local anisotropy that indicates sub-voxel level directional anisotropy.

As an application of the maxima extraction, we also performed tractography. We extended Streamline and Tensorline tractography to SDFs with multiple maxima, and were capable of recovering lateral radiations of the CC that cross the CST. We were also able to successfully track fibers through regions where three fiber bundles cross, namely the CC, the CST and the SLF.

CHAPTER 7

CONCLUSION

In this thesis we addressed a number of problems related to high order diffusion MRI (dMRI) reconstruction techniques. These techniques attempt to infer the microstructure of the cerebral white matter with greater accuracy than the popularly used diffusion tensor imaging (DTI). Although DTI has almost become the de facto dMRI reconstruction technique due to its mathematical simplicity, modest acquisition requirements and elegant interpretation, which has lead to powerful and practical applications, DTI is limited in regions with microstructural heterogeneity. Therefore, numerous higher order reconstruction techniques have been recently proposed in dMRI. Currently these techniques are gaining in popularity and are seeing increased applications, since they recover greater details of information from the complex microstructure of the cerebral white matter. Our contributions can be summarized as follows.

- We first examined the Generalized DTI (GDTI) model, which uses Cartesian tensors of order higher than two to model the apparent diffusion coefficient (ADC) in regions with microstructural heterogeneity with greater accuracy than DTI, and addressed the problem of estimating 4th order tensors with a positive diffusion profile, since negative diffusion is non-physical. We proposed two independent methods for achieving this.
  - The first method we proposed was based on the algebra of 4th order tensors, where we mapped symmetric 3D 4th order Cartesian tensors to symmetric 6D 2nd order Cartesian tensors by studying the symmetry properties of the 4th order tensors. This isometrically isomorphic map allowed us to apply the Riemannian metric for the space of symmetric positive definite (SPD) 6×6 matrices to these 6D 2nd order tensors to confine all matrix operations to SPD matrices. This allowed us to estimate 4th order GDTI diffusion tensors with positive diffusion profiles.
  - The second method we proposed was based on the polynomial interpretation of higher order tensors (HOTs), where using Hilbert's theorem on

ternary quartics we were able to parameterize the estimation of 4th order GDTI diffusion tensors to guarantee non-negative diffusion profiles.

Comparing the two methods theoretically we observed that the Riemannian approach ensured positive definite diffusion profiles, but solved a problem more constrained than implied by the GDTI model, while the ternary quartic approach solved the correct problem, but only ensured non-negativity. However, from the experiments we observed that the results of the Riemannian approach were similar to the results of the ternary quartic approach and that due to numerical computations we never came across exactly zero diffusion in the diffusion profiles of the tensors estimated using the ternary quartic approach.

- Next we addressed the problem of estimating the high order diffusion propagator from HOTs, since the ADC modelled by HOTs in the GDTI model describes the effects of the microstructural heterogeneity in the signal space or the Fourier space (q-space). Therefore, it is necessary to compute the diffusion propagator from these HOTs to infer the geometry of the microstructure, since the propagator represents the effects of the microstructural heterogeneity in the real space.
  - We proposed an analytical approximation of the propagator from a modified GDTI model. We showed that the approximation converges well to the true diffusion propagator and since it is analytical, it is fast and can be implemented efficiently. We also showed from the results that it is possible to infer the geometry of the microstructure from the angular structure of the approximate propagator.
- Finally we addressed the problem of extracting the complex information recovered by the higher order models by interpreting the geometry of their reconstructed diffusion functions. The diffusion functions of higher order dMRI models are often represented as generic functions on the sphere whose complex shapes indicate sub-voxel resolution geometric details of the underlying microstructure.
  - We first proposed a complete method for the exact detection of all the maxima for a wide class of spherical functions, since the maxima often indicate fiber directions.
  - We showed that this could be used to trace fibers through regions with crossing fiber configurations.
  - Further, by extracting more geometric features from these spherical functions, we proposed a sub-voxel resolution anisotropy measure, which we named the peak fractional anisotropy (PFA). By integrating the PFA for all the maxima of an individual spherical function, we also proposed the Total-PFA for characterizing the cerebral white matter.

All our contributions were based on the uniting underlying mathematical framework of Cartesian tensors. Cartesian tensors provide an alternate function basis to the popularly used Spherical Harmonic (SH) basis for describing reconstructed diffusion functions. This is an important alternative. While the SH basis with its spherical coordinate approach is better suited for describing angular functions and angular characteristics of the underlying white matter, like the angular moments of the diffusion propagator, which reveal axon fiber directions, the Cartesian tensors or multivariate polynomials provide a Cartesian coordinate approach to the problem, and these are better suited for computing Cartesian characteristics such as moments or cumulants of the diffusion propagator, which can be used to quantify the anisotropy of the white matter. The angular profile of the Cartesian tensors can also reveal fiber directions.

In addition to this Cartesian coordinate approach for estimating the EAP, in collaboration with Jian Cheng and other colleagues, we have also proposed an analytical spherical coordinate approach for estimating the EAP by modelling the diffusion signal and the EAP in two complete orthonormal bases that form Fourier Transform pairs in the spherical coordinates. The use of this Fourier basis-pair to analytically estimate the EAP in the spherical coordinates is called the spherical polar Fourier imaging (SPFI: section-3.4.5) [64, 108]. This Fourier basis-pair can also be used to estimate the ODF analytically, which we have proposed in [109, 110]. Finally we have also proposed a Riemannian framework for computing on ODFs described in any complete orthogonal basis [111, 112].

In collaboration with Julien Cohen-Adad and other colleagues, we have also contributed in developing Q-Ball metrics and comparing these against DTI metrics for assessing the integrity of a spinal cord after injury and for identifying lesions. Experiments were conducted on cat spinal cords and results were presented in [113, 114].

Perspectives:

Cartesian tensors provide a multivariate polynomial basis for describing the diffusion signal and the propagator in a Cartesian coordinate system. This relates the diffusion propagator to the diffusion signal via the Cartesian form of the Fourier Transform, which is separable, is considerably better studied and easier to manipulate than the spherical form of the Fourier Transform. However this is the approach taken by all recent dMRI reconstruction techniques that attempt to estimate the diffusion propagator from the signal (section-3.4.5). There are only few reconstruction techniques which take advantage of the Cartesian Fourier Transform, e.g. Generalized DTI 2 (GDTI2) (section-3.4.2), the approach proposed in [115] and the approach we have proposed in chapter-5. Diffusion Kurtosis Imaging (DKI) (section-3.4.4) is also closely related, since it models the diffusion signal in the multivariate polynomial basis.

All these methods have, however, mathematically incomplete formulations. They either do not consider a complete functional basis or an orthogonal functional basis. These two properties are highly desirable. GDTI2 and DKI theoretically consider the complete multivariate polynomial basis (with cumulants as coefficients) for modelling the signal. However, since in practice a truncated basis is required, (order four in both the cases), the fact that the multivariate polynomial basis isn't orthogonal implies that the estimated coefficients or the "cumulants" are necessarily biased or influenced by the other coefficients. This raises the problem of estimating the cumulants correctly. We have begun addressing this problem and preliminary results were presented in [116]. The methods in [115] and in chapter-5 do not consider complete functional bases for modelling the signal, which restricts the types of signal functions that can be estimated in these incomplete functional bases.

Therefore, the Cartesian approach with the multivariate polynomial basis opens up a rich set of problems for choosing the right basis for correctly estimating the required parameters from the diffusion signal (such as cumulants). The Cartesian approach has promising possibilities, since both the Cartesian Fourier Transform and the field of multivariate polynomials are historically well studied domains.

APPENDIX **A**

DATASETS

A.0.1 Synthetic dataset

To conduct controlled experiments with known ground truths, we use a multi-tensor approach to generate synthetic DWIs [106]. The EAP corresponding to a single fiber is taken to be an anisotropic free diffusion Gaussian distribution, parametrized by a covariance tensor $\mathbf{D} = \mathrm{diag}(\lambda_x, \lambda_y, \lambda_z)$ in its canonical coordinates. $\mathbf{D}$ is rotated using rotation matrices to orient the fiber in space. We generate the signal DWIs for the single fiber by considering the q-space formalism and taking the Fourier Transform of the Gaussian EAP, which results in the anisotropic Stejskal-Tanner signal equation (Eq-3.25). Multiple crossing fibers are simulated by considering an EAP that is the weighted sum of free diffusion Gaussians, where each Gaussian represents a fiber oriented in space. The signal DWIs for a multi-fiber or crossing-fiber is derived easily in the same fashion as $S(\mathbf{g}_i) = \sum_{k=1}^{N} w_k e^{-b\mathbf{g}_i^T \mathbf{D}_k \mathbf{g}_i}$, such that $\sum_k w_k = 1$, $\mathbf{D}_k = \mathbf{R}_k^T \mathbf{D} \mathbf{R}_k$ with $\mathbf{R}$ a rotation matrix, $S(\mathbf{g}_i)$ represents the DWI along the ith gradient direction, and N are the number of fibers crossing in the voxel.

A.0.2 Biological Rat phantom dataset

The biological phantom [117] was created at the McConnell Brain Imaging Center (BIC), McGill University, Montréal, Canada. MR images were acquired on a 1.5T Sonata MR scanner using a knee coil. It was created from two excised Sprague-Dawley rat spinal cords embedded in 2% agar. The acquisition was done with a single-shot spin-echo planar sequence with twice-refocused balanced gradients, designed to reduce eddy current effects. The dataset was acquired with 90 gradient directions, on a single q-shell with a b-value of 3000 s/mm^2, $q = 0.35\ \mu m^{-1}$, TR= 6.4 s, TE= 110 ms, FOV 360 x 360 mm^2 , 128 x 128 matrix, 2.8 mm isotropic voxels and four signal averages per direction. The SNR of the S_0 image was estimated to be approximately 70 for the averaged phantom, and around 10 for the cord at b-value of 3000 s/mm^2.

A.0.3 In-vivo Human dataset, Max Planck Institute (MPI), Leipzig, Germany

This in-vivo human cerebral dataset [96] was acquired with a whole-body 3T Siemens Trio scanner, with an 8-channel array head coil and maximum gradient strength of 40 mT/m. The DWIs were acquired using spin-echo echo planar imaging (EPI) (time repetition [TR] = 12 s, echo time [TE] = 100 ms, 128 x 128 image matrix, FOV = 220×220 mm^2, 72 slices with 1.7mm thickness (no gap) covering the whole brain). The diffusion weighting was isotropically distributed along 60 encoding directions, with a b-value of 1000 s/mm^2. Seven images without any diffusion weightings were placed at the beginning of the sequence and after each block of ten DWIs as anatomical reference for offline motion correction. Random variations in the data were reduced by averaging 3 acquisitions, resulting in an acquisition time of about 45 minutes. The SNR in the white matter of this S_0 image was estimated to be approximately 37. The motion correction for the DWIs was combined with a global registration to T1 anatomy images. The gradient direction for each volume was corrected using rotation parameters. The registered images were interpolated to the new reference frame with an isotropic voxel resolution of 1.72 mm.

A.0.4 In-vivo Human dataset, NeuroSpin/CEA, Paris, France

This human brain dataset was acquired on a 1.5T scanner using 41 gradient directions, with a b-value of 700 s/mm^2 with TR = 1.9 s,TE = 93.2 ms, 128 x 128 image matrix, 60 slices, with voxel dimensions of 1.875mm x 1.875mm x 2mm. This dataset is from a public HARDI database that can be found in [118].

APPENDIX **B**

PUBLICATIONS OF THE AUTHOR

Book chapters

- A. Ghosh and R. Deriche
  From second to higher order tensors in diffusion MRI, Tensors in Image Processing and Computer Vision, Advances in Pattern Recognition, Chapter 9. Springer London, May 2009, Editors: Santiago Aja-Fernández, Rodrigo de Luis García, Dacheng Tao, and Xuelong Li, 2009.

Conference papers

- A. Ghosh, M. Descoteaux, and R. Deriche
  Riemannian Framework for estimating Symmetric Positive Definite 4th Order Diffusion Tensors, In Medical image computing and computer-assisted intervention – MICCAI, pages 858-865, 2008.

- A. Ghosh, E. Tsigaridas, M. Descoteaux, P. Comon, B. Mourrain, and R. Deriche
  A polynomial based approach to extract the maxima of an antipodally symmetric spherical function and its application to extract fiber directions from the orientation distribution function in diffusion MRI, In Proceedings of Workshop on Computational Diffusion MRI, MICCAI, 2008.

- A. Ghosh, M. Moakher, and R. Deriche
  Ternay quartic approach for positive 4th order diffusion tensors revisited, In 2009 IEEE International Symposium on Biomedical Imaging: From Nano to Macro, pages 618-621, June 2009.

- A. Ghosh and R. Deriche
  Fast and closed-form ensemble-average-propagator approximation from the 4th-order diffusion tensor, In 2010 IEEE International Symposium on Biomedical Imaging: From Nano to Macro, pages 1105-1108. IEEE Press, April 2010.

- A. Ghosh and R. Deriche
Extracting geometrical features & peak fractional anisotropy from the ODF for white matter characterization, In 2011 IEEE International Symposium on Biomedical Imaging: From Nano to Macro, April 2011.

- A. Ghosh and R. Deriche
Extracting geometrical features & peak fractional anisotropy from the ODF for white matter characterization, In 2011 IEEE International Symposium on Biomedical Imaging: From Nano to Macro, April 2011.

- J. Cheng, A. Ghosh, T. Jiang, and R. Deriche
A Riemannian framework for orientation distribution function computing, In Medical Image Computing and Computer Assisted Intervention (MICCAI), pages 911-918, September 2009.

- J. Cheng, A. Ghosh, T. Jiang, and R. Deriche
Model-free and analytical EAP reconstruction via spherical polar fourier diffusion MRI, In Medical Image Computing and Computer-Assisted Intervention - MICCAI, volume 6361, pages 590-597, 2010.

- J. Cheng, A. Ghosh, R. Deriche, and T. Jiang
Model-free, regularized, fast, and robust analytical orientation distribution function estimation, In Medical Image Computing and Computer-Assisted Intervention - MICCAI, volume 6361 of Lecture Notes in Computer Science, pages 648-656, 2010.

Conference abstracts

- A. Ghosh, M. Descoteaux, and R. Deriche
4th order diffusion tensor estimation and application, In Proceedings ISMRM, volume 16, page 3321, 2008.

- A. Ghosh, E. Tsigaridas, M. Descoteaux, and R. Deriche
A polynomial based approach to extract fiber directions from the ODF and its experimental validation, In Proceedings ISMRM, volume 17, page 1389, 2009.

- A. Ghosh, E. Özarslan, and R. Deriche
Challenges in reconstructing the propagator via a cumulant expansion of the one-dimensional q-space MR signal, In Proceedings ISMRM, May 2010.

- A. Ghosh and R. Deriche
Unraveling the ODF: Extracting its maxima & other geometric characteristics for bio-markers & tractography in diffusion MRI, In Proceedings 2010: Medical Imaging: Perspectives on Perception and Diagnostics, IIT Delhi, India, December 2010.

- J. Cohen-Adad, A. Ghosh, H. Leblond, M. Descoteaux, R. Deriche, H. Benali, and S. Rossignol
  Comparison of DTI and Q-Ball imaging metrics in a cat model of spinal cord injury, In 14th Annual Meeting of the Organization for Human Brain Mapping (HBM), San Fransisco, USA, July 2009.

- J. Cohen-Adad, H. Leblond, A. Ghosh, M. Descoteaux, R. Deriche, H. Benali, and S. Rossignol
  Evaluation of Q-Ball metrics for assessing the integrity of the injured spinal cord, In Proceedings ISMRM, volume 17, page 639, 2009.

- J. Cheng, A. Ghosh, T. Jiang, and R. Deriche
  Riemannian median and its applications for orientation distribution function computing, In Proceedings ISMRM, 2010.

- J. Cheng, A. Ghosh, T. Jiang, and R. Deriche
  Fast, model-free, analytical diffusion PDF profile estimation from the DWI signals, In 16th Annual Meeting of the Organization for Human Brain Mapping, Barcelona, June 2010.

- J. Cheng, A. Ghosh, T. Jiang, and R. Deriche
  Fast, model-free , analytical ODF reconstruction from the q-space signal, In 16th Annual Meeting of the Organization for Human Brain Mapping, Barcelona, June 2010.

Bibliography

[1] C. Lenglet. *Geometric and Variational Methods for Diffusion Tensor MRI Processing*. PhD thesis, Universite de Nice - Sophia Antipolis, December 2006.

[2] C. Poupon. *Détection des faisceaux de fibres de la substance blanche pour l'étude de la connectivité anatomique cérébrale.* PhD thesis, Ecole Nationale Supérieure des Télécommunications, December 1999.

[3] M. Descoteaux. *High Angular Resolution Diffusion MRI: From Local Estimation to Segmentation and Tractography*. PhD thesis, Universite de Nice - Sophia Antipolis, February 2008.

[4] V. Prckovska. *High Angular Resolution Diffusion Imaging. Processing & Visualization.* PhD thesis, Eindhoven University of technology, October 2010.

[5] H. Johansen-Berg and T. E. Behrens. *Diffusion MRI, From quantitative measurement to in vivo neuroanatomy*. Elsevier, 1st edition, April 2009.

[6] H. Gray. *Gray's Anatomy of the Human Body*. LEA and FEBIGER, 1918.

[7] C. R. Noback, D. A. Ruggiero, R. J. Demarest, and N. L. Strominger. *The Human Nervous System: Structure and Function*. Humana Press, March 2005.

[8] R. Nieuwenhuys, R. Nieuwenhuys, and J. Voogd. *The Human Central Nervous System: A Synopsis and Atlas*. Springer, December 1988.

[9] B. Pakkenberg, D. Pelvig, L. Marner, M. J. Bundgaard, H. J. G. Gundersen, J. R. Nyengaard, and L. Regeur. Aging and the human neocortex. *Experimental Gerontology*, 38(1-2):95–99, 2003. Proceedings of the 6th International Symposium on the Neurobiology and Neuroendocrinology of Aging.

[10] D. A. Drachman. Do we have brain to spare? *Neurology*, 64, 2005.

[11] T. H. Williams, N. Gluhbegovic, and J. Jew. *The human brain: dissections of the real brain*. Virtual Hospital, 1997.

[12] F. Bloch. Nuclear induction. *Physical Review*, 70:460–474, 1946.

[13] E. Purcell, H. Torrey, and R. Pound. Resonance absorption by nuclear magnetic moments in a solid. *Physical Review*, 69:37–38, 1946.

[14] E. Hahn. Spin echoes. *Physical Review*, 80:580–594, 1950.

[15] H. Y. Carr and E. M. Purcell. Effects of diffusion on free precession in nuclear magnetic resonance experiments. *Physical Review*, 94:630–638, May 1954.

[16] P. Lauterbur. Image formation by induced local interactions: examples employing nuclear magnetic resonance. *Nature*, 242:190–191, 1973.

[17] P. Mansfield. Multi-planar image formation using nmr spin echoes. *Journal of Physics C*, 10:55–58, 1977.

[18] J. Crank. *The Mathematics of Diffusion*. Oxford University Press, 2nd edition, 1975.

[19] A. Einstein. Investigations on the theory of the Brownian movement. *Ann. der Physik*, 1905.

[20] E. Ozarslan. *Developments in Diffusion Weighted Magnetic Resonance Imaging (MRI) with Applications to Neural Tissue*. PhD thesis, University of Florida, 2004.

[21] H. C. Torrey. Bloch equations with diffusion terms. *Phys. Rev.*, 104(3):563–565, November 1956.

[22] E. O. Stejskal and J. E. Tanner. Spin diffusion measurements: Spin echoes in the presence of a time-dependent field gradient. *The Journal of Chemical Physics*, 42(1):288–292, 1965.

[23] E. O. Stejskal. Use of Spin Echoes in a Pulsed Magnetic-Field Gradient to Study Anisotropic, Restricted Diffusion and Flow. *The Journal of Chemical Physics*, 43(10):3597–3603, 1965.

[24] L. Minati and W. P. Węglarz. Physical foundations, models, and methods of diffusion magnetic resonance imaging of the brain: A review. *Concepts in Magnetic Resonance Part A*, 30A(5):278–307, 2007.

[25] P. T. Callaghan. *Principles of nuclear magnetic resonance microscopy*. Oxford University Press, Oxford, 1993.

[26] M. G. Kendall and A. Stuart. *The Advanced Theory of Statistics*, volume 1. Charles Griffin & Company Ltd, London, 3rd edition, 1947.

[27] P. J. Basser. Relationships between diffusion tensor and q-space MRI. *Magnetic Resonance in Medicine*, 47:392–397, 2002.

[28] D. Tuch. *Diffusion MRI of Complex Tissue Structure*. PhD thesis, Harvard University and Massachusetts Institute of Technology, 2002.

[29] P. J. Basser. Diffusion primer. `http://users.fmrib.ox.ac.uk/~karla/reading_group/lecture_notes/TheoryofDiffusion.pdf`.

[30] P. J. Basser, J. Mattiello, and D. LeBihan. Estimation of the effective self-diffusion tensor from the NMR spin echo. *Journal of Magnetic Resonance*, B(103):247–254, 1994.

[31] P. J. Basser, J. Mattiello, and D. LeBihan. MR diffusion tensor spectroscopy and imaging. *Biophysical Journal*, 66(1):259–267, 1994.

[32] C. Chefd'hotel, D. Tschumperlé, R. Deriche, and O. Faugeras. Constrained flows on matrix-valued functions : application to diffusion tensor regularization. In *Proceedings of ECCV'02*, June 2002.

[33] C. Chefd'hotel, D. Tschumperlé, R. Deriche, and O. Faugeras. Regularizing flows for constrained matrix-valued images. *J. Math. Imaging Vis.*, 20(1-2):147–162, January 2004.

[34] Z. Wang, B. C. Vemuri, Y. Chen, and T. H. Mareci. A constrained variational principle for direct estimation and smoothing of the diffusion tensor field from complex DWI. *IEEE Transactions on Medical Imaging*, 23(8):930–939, 2004.

[35] P. Fletcher and S. Joshi. Principal geodesic analysis on symmetric spaces: Statistics of diffusion tensors. In *Proc. Computer Vision Approaches to Medical Image Analysis*, Prague, May 2004.

[36] M. Moakher. A differential geometric approach to the geometric mean of symmetric positive-definite matrices. *SIAM J. Matrix Anal. Appl.*, 26(3):735–747, April 2005.

[37] X. Pennec, P. Fillard, and N. Ayache. A Riemannian Framework for Tensor Computing. *International Journal of Computer Vision*, 66(1):41–66, January 2006. A preliminary version appeared as INRIA Research Report 5255, July 2004.

[38] P. J. Basser. Inferring microstructural features and the physiological state of tissues from diffusion-weighted images. *NMR in Biomedicine*, 8:333–344, 1995.

[39] C. Westin, S. Maier, H. Mamata, A. Nabavi, F. Jolesz, and R. Kikinis. Processing and Visualization for Diffusion Tensor MRI. *Medical Image Analysis*, 6(2):93–108, June 2002.

[40] M. Catani, R. J. Howard, S. Pajevic, and D. K. Jones. Virtual in vivo interactive dissection of white matter fasciculi in the human brain. *NeuroImage*, 17:77–94, 2002.

[41] P. J. Basser, S. Pajevic, C. Pierpaoli, J. Duda, and A. Aldroubi. In vivo fiber tractography using DT-MRI data. *Magnetic Resonance in Medicine*, 44(4):625–632, October 2000.

[42] P. Hagmann, L. Jonasson, P. Maeder, J.-P. Thiran, V. J. Wedeen, and R. Meuli. Understanding Diffusion MR Imaging Techniques: From Scalar Diffusion-Weighted Imaging to Diffusion Tensor Imaging and Beyond. *RadioGraphics*, 26:S205–S223, 2006.

[43] L. Frank. Characterization of anisotropy in high angular resolution diffusion-weighted MRI. *Magnetic Resonance in Medicine*, 47(6):1083–1099, 2002.

[44] E. Ozarslan and T. H. Mareci. Generalized diffusion tensor imaging and analytical relationships between diffusion tensor imaging and high angular resolution diffusion imaging. *Magnetic Resonance in Medicine*, 50(5):955–965, November 2003.

[45] C. Liu, R. Bammer, and M. E. Moseley. Generalized Diffusion Tensor Imaging (GDTI): A Method for Characterizing and Imaging Diffusion Anisotropy Caused by Non-Gaussian Diffusion. *Israel Journal of Chemistry*, 43:145–154, 2003.

[46] D. Tuch, T. Reese, M. Wiegell, N. Makris, J. Belliveau, and V. Wedeen. High Angular Resolution Diffusion Imaging Reveals Intravoxel White Matter Fiber Heterogeneity. *Magnetic Resonance in Medicine*, 48(4):577–582, 2002.

[47] V. J. Wedeen. Mapping fiber orientation spectra in cerebral white matter with Fourier transform diffusion MRI. In *In Proc. of the 8th Annual Meeting of ISMRM*, page 82, 2000.

[48] V. J. Wedeen, P. Hagmann, W.-Y. I. Tseng, T. G. Reese, and R. M. Weisskoff. Mapping complex tissue architecture with diffusion spectrum magnetic resonance imaging. *Magn. Reson. Med.*, 54(6):1377–1386, 2005.

[49] J. D. Schmahmann, D. N. Pandya, R. Wang, G. Dai, H. E. D'Arceuil, A. J. de Crespigny, and V. J. Wedeen. Association fibre pathways of the brain: parallel observations from diffusion spectrum imaging and autoradiography. *Brain*, I30:630–653, 2007.

[50] J. H. Jensen, J. A. Helpern, A. Ramani, H. Lu, and K. Kaczynski. Diffusional Kurtosis Imaging: the quantification of non-Gaussian water diffusion by means of magnetic resonance imaging. *Magnetic Resonance in Medicine*, 53(6):1432–1440, June 2005.

[51] D. Tuch. Q-ball imaging. *Magnetic Resonance in Medicine*, 52(6):1358–1372, 2004.

[52] A. Anderson. Measurements of fiber orientation distributions using high angular resolution diffusion imaging. *Magnetic Resonance in Medicine*, 54:1194–1206, 2005.

[53] C. Hess, P. Mukherjee, E. Han, D. Xu, and D. Vigneron. Q-ball reconstruction of multimodal fiber orientations using the spherical harmonic basis. *Magnetic Resonance in Medicine*, 56:104–117, 2006.

[54] M. Descoteaux, E. Angelino, S. Fitzgibbons, and R. Deriche. Regularized, Fast, and Robust Analytical Q-Ball Imaging. *Magnetic Resonance in Medicine*, 58:497–510, 2007.

[55] I. Aganj, C. Lenglet, G. Sapiro, E. Yacoub, K. Ugurbil, and N. Harel. Reconstruction of the orientation distribution function in single and multiple shell Q-ball imaging within constant solid angle. *Magnetic Resonance in Medicine*, 64(2):554–566, 2010.

[56] A. Tristan-Vega, C. F. Westin, and S. Aja-Fernandez. A new methodology for the estimation of fiber populations in the white matter of the brain with the Funk-Radon transform. *NeuroImage*, 49:1301–1315, 2010.

[57] K. M. Jansons and D. C. Alexander. Persistent angular structure: new insights fom diffusion magnetic resonance imaging data. *Inverse Problems*, 19:1031–1046, 2003.

[58] B. Jian and B. C. Vemuri. A unified computational framework for deconvolution to reconstruct multiple fibers from diffusion weighted MRI. *IEEE Trans. Med. Imaging*, 26(11):1464–1471, 2007.

[59] J. D. Tournier, F. Calamante, D. Gadian, and A. Connelly. Direct estimation of the fiber orientation density function from diffusion-weighted MRI data using spherical deconvolution. *NeuroImage*, 23:1176–1185, 2004.

[60] E. Özarslan, T. M. Shepherd, B. C. Vemuri, S. J. Blackband, and T. H. Mareci. Resolution of complex tissue microarchitecture using the diffusion orientation transform (DOT). *NeuroImage*, pages 1086–1103, 2006.

[61] M. Descoteaux, R. Deriche, D. Le Bihan, J.-F. Mangin, and C. Poupon. Multiple q-shell diffusion propagator imaging. *Medical Image Analysis*, July 2010.

[62] E. Ozarslan, C. Koay, T. M. Shepherd, S. J. Blackband, and P. J. Basser. Simple harmonic oscillator based reconstruction and estimation for three-dimensional q-space MRI. In *ISMRM 17th Scientific Meeting and Exhibition*, page 1396, 2009.

[63] H.-E. Assemlal, D. Tschumperlé, and L. Brun. Efficient and robust computation of PDF features from diffusion MR signal. *Medical Image Analysis*, 13(5):715–729, 2009. Includes Special Section on the 12th International Conference on Medical Imaging and Computer Assisted Intervention.

[64] J. Cheng, A. Ghosh, T. Jiang, and R. Deriche. Model-Free and Analytical EAP Reconstruction via Spherical Polar Fourier Diffusion MRI. In *Medical Image Computing and Computer-Assisted Intervention - MICCAI*, volume 6361, pages 590–597, 2010.

[65] A. Barmpoutis, B. Jian, and B. C. Vemuri. Symmetric positive 4th order tensors & their estimation from diffusion weighted MRI. In *Information Processing in Medical Imaging (IPMI 2007)*, pages 308–319, 2007.

[66] A. Barmpoutis, M. S. Hwang, D. Howland, J. R. Forder, and B. C. Vemuri. Regularized positive-definite fourth-order tensor field estimation from DW-MRI. *NeuroImage*, 45(1 sup.1):153–162, March 2009.

[67] O. Pasternak, N. Sochen, and P. J. Basser. The effect of metric selection on the analysis of diffusion tensor MRI data. *NeuroImage*, 49(3):2190–2204, 2010.

[68] V. Arsigny, P. Fillard, X. Pennec, and N. Ayache. Log-Euclidean metrics for fast and simple calculus on diffusion tensors. *Magnetic Resonance in Medicine*, 56(2):411–421, August 2006. PMID: 16788917.

[69] M. Moakher. Fourth-order cartesian tensors: Old and new facts, notions and applications. *The Quarterly Journal of Mechanics and Applied Mathematics*, 61(2):181–203, 2008.

[70] M. Moakher. The Algebra of Fourth-Order Tensors with Application to Diffusion MRI. In D. Laidlaw and J. Weickert, editors, *Visualization and Processing of Tensor Fields*, Mathematics and Visualization, pages 57–80. Springer Berlin Heidelberg, 2009. 10.1007/978-3-540-88378-4_4.

[71] A. Ghosh, M. Descoteaux, and R. Deriche. Riemannian framework for estimating symmetric positive definite 4th order diffusion tensors. In *Medical image computing and computer-assisted intervention - MICCAI*, volume 5241 of *Lecture notes in computer science*, pages 858–865, New-York, USA, 2008. Springer.

[72] P. J. Basser and S. Pajevic. Spectral decomposition of a 4th-order covariance tensor: Applications to diffusion tensor MRI. *Signal Processing*, 87:220–236, 2007.

[73] P. Fillard. *Traitement Riemannien des tenseurs pour l'IRM de diffusion et l'anatomie algorithmique du cerveau*. PhD thesis, Université de Nice Sophia-Antipolis, February 2008.

[74] L. R. Frank. Characterization of anisotropy in high angular resolution diffusion-weighted MRI. *Magn. Reson. Med*, 47:1083–1099, 2002.

[75] M. Descoteaux, E. Angelino, S. Fitzgibbons, and R. Deriche. Apparent diffusion coefficients from high angular resolution diffusion imaging: Estimation and applications. In *SPIE Medical Imaging*, San Diego, February 2006.

[76] M. Descoteaux, E. Angelino, S. Fitzgibbons, and R. Deriche. Apparent diffusion coefficients from high angular resolution diffusion imaging: Estimation and applications. *Magnetic Resonance in Medicine*, 56:395–410, 2006.

[77] A. Barmpoutis and B. C. Vemuri. A unified framework for estimating diffusion tensors of any order with symmetric positive-definite constraints. In *Proceedings of ISBI10: IEEE International Symposium on Biomedical Imaging*, pages 1385–1388, 14-17 April 2010.

[78] W. Rudin. Sums of squares of polynomials. *The American Mathematical Monthly*, 107(9):pp. 813–821, 2000.

[79] A. Ghosh, M. Moakher, and D. Rachid. Ternay quartic approach for positive 4th order diffusion tensors revisited. In *IEEE International Symposium on Biomedical Imaging: From Nano to Macro*, pages 618–621, June 2009.

[80] V. Powers and B. Reznick. Notes towards a constructive proof of Hilbert's theorem on ternary quartics. *Quadratic forms and their applications (Dublin 1999), Contemp. Math.*, 272(9), 2000.

[81] B. Jian and B. C. Vemuri. Metric Learning Using Iwasawa Decomposition. *Computer Vision, IEEE International Conference on*, 0:1–6, 2007.

[82] W. H. Press, B. P. Flannery, S. A. Teukolsky, and W. T. Vetterling. *Numerical Recipes in C: The Art of Scientific Computing*. Cambridge University Press, 2nd edition, October 1992.

[83] A. Ghosh, M. Descoteaux, and R. Deriche. Riemannian framework for estimating symmetric positive definite 4th order diffusion tensors. In *Medical Image Computing and Computer-Assisted Intervention (MICCAI)*, pages 858–865, 2008.

[84] E. Ozarslan, B. C. Vemuri, and T. H. Mareci. Fiber orientation mapping using generalized diffusion tensor imaging. In *IEEE International Symposium on Biomedical Imaging: Nano to Macro*, pages 1036–1039 Vol. 1, April 2004.

[85] D. C. Alexander. Maximum Entropy Spherical Deconvolution for Diffusion MRI. In *Image Processing in Medical Imaging*, pages 76–87, 2005.

[86] B. Jian, B. C. Vemuri, E. Ozarslan, P. R. Carney, and T. H. Mareci. A novel tensor distribution model for the diffusion-weighted MR signal. *NeuroImage*, 37:164–176, 2007.

[87] B. Jian and B. C. Vemuri. Multi-fiber reconstruction from diffusion MRI using mixture of wisharts and sparse deconvolution. In *Proceedings of the 20th international conference on Information processing in medical imaging*, IPMI'07, pages 384–395, Berlin, Heidelberg, 2007. Springer-Verlag.

[88] T. G. Reese, O. Heid, R. M. Weisskoff, and V. J. Wedeen. Reduction of eddy-current-induced distortion in diffusion MRI using a twice-refocused spin echo. *Magnetic Resonance in Medicine*, 49(1):177–182, January 2003.

[89] P. A. Cook, Y. Bai, N. S. Gilani, K. K. Seunarine, M. G. Hall, G. J. Parker, and D. C. Alexander. Camino: Open-Source Diffusion-MRI Reconstruction and Processing. In *14th Scientific Meeting of the International Society for Magnetic Resonance in Medicine*, page 2759, May 2006.

[90] O. Ciccarelli, M. Catani, H. Johansen-Berg, C. Clark, and A. Thompson. Diffusion-based tractography in neurological disorders: concepts, applications, and future developments. *Lancet Neurol*, 7(8):715–27, 2008.

[91] L. Bloy and R. Verma. On computing the underlying fiber directions from the diffusion orientation distribution function. In *MICCAI '08: Proceedings of the 11th international conference on Medical Image Computing and Computer-Assisted Intervention - Part I*, pages 1–8, Berlin, Heidelberg, 2008. Springer-Verlag.

[92] A. Ghosh, E. Tsigaridas, M. Descoteaux, P. Comon, B. Mourrain, and R. Deriche. A polynomial based approach to extract the maxima of an antipodally symmetric spherical function and its application to extract fiber directions from the orientation distribution function in diffusion MRI. In *Proceedings of Workshop on Computational Diffusion MRI, MICCAI*, 2008.

[93] I. Aganj, C. Lenglet, and G. Sapiro. ODF maxima extraction in spherical harmonic representation via analytical search space reduction. In T. Jiang, N. Navab, J. P. W. Pluim, and M. A. Viergever, editors, *Medical Image Computing and Computer-Assisted Intervention (MICCAI)*, volume 6362 of *Lecture Notes in Computer Science*, pages 84–91. Springer, 2010.

[94] D. M. Weinstein, G. L. Kindlmann, and E. C. Lundberg. Tensorlines: Advection-diffusion based propagation through diffusion tensor fields. *Visualization Conference, IEEE*, 0:40, 1999.

[95] M. Lazar, D. Weinstein, J. Tsuruda, K. Hasan, K. Arfanakis, M. Meyerand, B. Badie, H. Rowley, V.Haughton, A. Field, and A. Alexander. White matter

tractography using diffusion tensor deflection. In *Human Brain Mapping*, volume 18, pages 306–321, 2003.

[96] A. Anwander, M. Tittgemeyer, D. Y. von Cramon, A. D. Friederici, and T. R. Knosche. Connectivity-based parcellation of broca's area. *Cerebral Cortex*, 17(4):816–825, 2007.

[97] Bernard Mourrain and Jean-Pascal Pavone.

[98] E. Im. Hessian sufficiency for bordered Hessian. *Res. Lett. Inf. Math. Sci.*, 8:189–196, 2005.

[99] M. P. Do-Carmo. *Differential Geometry of Curves and Surfaces*. Prentice Hall, 1st edition, February 1976.

[100] E. J. Garboczi. Three-dimensional mathematical analysis of particle shape using x-ray tomography and spherical harmonics: Application to aggregates used in concrete. *Cement and Concrete Research*, 32(10):1621–1638, October 2002.

[101] K. K. Seunarine, P. A. Cook, M. G. Hall, K. V. Embleton, G. J. M. Parker, and D. C. Alexander. Exploiting peak anisotropy for tracking through complex structures. *Computer Vision, IEEE International Conference on*, 0:1–8, 2007.

[102] E. Ozarslan, B. C. Vemuri, and T. H. Mareci. Generalized Scalar Measures for Diffusion MRI Using Trace, Variance and Entropy. *Magnetic Resonance in Medicine*, 53(4):866–876, 2005.

[103] E. Ozarslan, L.-C. Chang, C. Pierpaoli, and P. J. Basser. Roughness: A reshuffling-variant differential geometric index for DWI. In *ISMRM 15th Scientific Meeting and Exhibition*, page 1517, 2007.

[104] M. Descoteaux, E. Angelino, S. Fitzgibbons, and R. Deriche. A Linear and Regularized ODF Estimation Algorithm to Recover Multiple Fibers in Q-Ball Imaging. Technical Report 5768, INRIA Sophia Antipolis, November 2005.

[105] S. Mori, B. Crain, V. Chacko, and P. V. Zijl. Three-dimensional tracking of axonal projections in the brain by Magnetic Resonance Imaging. *Annals of Neurology*, 45(2):265–269, February 1999.

[106] M. Descoteaux, R. Deriche, T. R. Knosche, and A. Anwander. Deterministic and Probabilistic Tractography Based on Complex Fibre Orientation Distributions. *IEEE Transactions on Medical Imaging*, 28(2):269–286, 2009.

[107] B. Jeurissen, A. Leemans, D. K. Jones, J. D. Tournier, and J. Sijbers. Probabilistic fiber tracking using the residual bootstrap with constrained spherical deconvolution. *Human Brain Mapping*, 2010.

[108] J. Cheng, A. Ghosh, T. Jiang, and R. Deriche. Fast, model-free, analytical diffusion PDF profile estimation from the DWI signals. In *16th Annual Meeting of the Organization for Human Brain Mapping, Barcelona*, June 2010.

[109] J. Cheng, A. Ghosh, R. Deriche, and T. Jiang. Model-Free, Regularized, Fast, and Robust Analytical Orientation Distribution Function Estimation. In *Medical Image Computing and Computer-Assisted Intervention - MICCAI*, volume 6361 of *Lecture Notes in Computer Science*, pages 648–656. Springer, 2010.

[110] J. Cheng, A. Ghosh, T. Jiang, and R. Deriche. Fast, Model-Free , Analytical ODF Reconstruction from the q-Space Signal. In *16th Annual Meeting of the Organization for Human Brain Mapping, Barcelona*, June 2010.

[111] J. Cheng, A. Ghosh, T. Jiang, and R. Deriche. A Riemannian Framework for Orientation Distribution Function Computing. In *Medical Image Computing and Computer Assisted Intervention (MICCAI)*, September 2009.

[112] J. Cheng, A. Ghosh, T. Jiang, and R. Deriche. Riemannian Median and Its Applications for Orientation Distribution Function Computing. In *Proceedings ISMRM*, 2010.

[113] J. Cohen-Adad, A. Ghosh, H. Leblond, M. Descoteaux, R. Deriche, H. Benali, and S. Rossignol. Comparison of DTI and Q-Ball imaging metrics in a cat model of spinal cord injury. In *14th Annual Meeting of the Organization for Human Brain Mapping (HBM), San Fransisco, USA*, July 2009.

[114] J. Cohen-Adad, H. Leblond, A. Ghosh, M. Descoteaux, R. Deriche, H. Benali, and S. Rossignol. Evaluation of q-ball metrics for assessing the integrity of the injured spinal cord. In *Proceedings of International Society of Magnetic Resonance in Medicine (ISMRM)*, volume 17, page 639, 2009.

[115] A. Barmpoutis, B. C. Vemuri, and J. R. Forder. Fast displacement probability profile approximation from HARDI using 4th-order tensors. In *Proceedings of ISBI: IEEE International Symposium on Biomedical Imaging*, pages 911–914, 14 - 17 May 2008.

[116] A. Ghosh, E. Özarslan, and R. Deriche. Challenges in reconstructing the propagator via a cumulant expansion of the one-dimensional q-space MR signal. In *Proceedings ISMRM*, May 2010.

[117] J. Campbell, K. Siddiqi, V. Rymar, A. Sadikot, and B. Pike. Flow-based fiber tracking with diffusion tensor q-ball data: Validation and comparison to principal diffusion direction techniques. *NeuroImage*, 27(4):725–736, October 2005.

[118] C. Poupon, F. Poupon, L. Allirol, and J.-F. Mangin. A database dedicated to anatomo-functional study of human brain connectivity. In *Twelfth Annual Meeting of the Organization for Human Brain Mapping (HBM)*, 2006.